Quantum theory of plasmons in nanostructures

Ph.D. Thesis

Kirsten Andersen

Center for Atomic-scale Materials Design
Department of Physics
Technical University of Denmark

May 2015

DTU Physics
Department of Physics

CAMd
Center for Atomic-scale Materials Design

Preface

This thesis is submitted in candidacy for the Ph.D. degree in physics from the Technical University of Denmark. The work was carried out a at Center for Atomic-scale Materials design (CAMD) at the Department of Physics in the period September 2011 to May 2015, under supervision of professor Kristian S. Thygesen and professor Karsten W. Jacobsen. The Ph.D. project was funded by an internal scholarship from DTU.

I am very grateful for the guidance and inspiration given by my supervisors, and for all the time and effort they have invested in my project. Thank you Kristian for your good ideas and for our many interesting discussion, and Karsten for your valuable contributions and deep knowledge within so many topics in physics.

Also, I would like to thank: Simone for his collaboration on the modelling of heterostructures, and my master students, Kristian Lund, Felipe and Line, for their contributions to this thesis, their ideas and good questions.

Morten Gjerding, Mohnish, Filip, and Morten for proofreading. Jens Jørgen, Filip, and Morten Gjerding for always being glad to discuss code developing issues, and to Jun Yan for explaining plasmons and the response code in the beginning of my project. Ole and Marcin for their help with computers and software, and Marianne for her assistance with administrative stuff.

The people at CAMD for good times and bad jokes, who not already mentioned: Per, Chris, Anja, Ivano, Elvar, Korina, Kristian Ørnsø, Martin, Niels, Chengjun, Manuel, Ulrik, Keld, Falco, Jan and Jakob.

Lastly, thank you Morten for never allowing me to doubt myself, and Agnes for always bringing a smile to my face.

Kirsten Andersen
Copenhagen, May 2015

Abstract

In this thesis, *ab initio* quantum-mechanical calculations are used to study the properties of plasmons in nanostructures that involve atomic length-scales. The plasmon is an electronic excitation that corresponds to oscillations in the electron charge density in metals, often visualized as water ripples in a pond where the water represents a sea of free electrons. Plasmons on metal surfaces and in nanostructured materials, such as metal nanoparticles and atomically thin two-dimensional materials, have several technological applications due to their ability to confine light on nanoscale.

For a theoretical description of plasmon in such materials, where the electrons are heavily confined in one or more directions, a quantum mechanical description of the electrons in the material is necessary. In this thesis, the *ab initio* methods Density functional theory (DFT) and linear response time-dependent DFT are applied to calculate the properties of plasmons in nanostructures in different dimensions. In order to identify and visualize localized plasmon modes, a method for calculating plasmon eigenmodes within the *ab initio* framework has been developed. In the studied materials, quantum mechanical effects such as coupling to single-electronic transitions, electron spill-out from the surface, tunneling, and spatial non-locality, are shown to alter the plasmon excitations.

The studied systems include two-dimensional materials, such as thin metal films, monolayer transition metal dichalcogenides, and graphene. Here, also van der Waals heterostructures (vdWh), which are stacks of different two-dimensional materials, are considered. A new multi-scale approach for calculating the dielectric-function of vdWh, which extends *ab initio* accuracy to the description of hundreds of atomic layers, is presented. Also, one-dimensional plasmons are studied in the case of atomically thin nanowires and edge-states of MoS_2.

Resume

Ab initio kvantemekaniske beregninger er i denne afhandling blevet anvendt til at udforske egenskaberne af plasmoner i nanostrukturer på atomar skala. Plasmonen er en exciteret elektrontilstand, hvor der opstår svingninger i elektrontætheden. Dette visualiseres ofte som bølger i en vandoverflade, hvor vandet repræsenterer de frie elektroner i et metal. Plasmoner på metaloverflader og i nanomaterialer, såsom nanopartikler af atomart-tynde todimensionelle materialer, har mange teknologiske anvendelsesmuligheder på grund af deres evne til at indsnævre lys på nanometer-skala.

Den teoretiske beskrivelse af plasmoner i sådanne materialer, hvor elektronerne er begrænset til at have en meget lille rummelig udstrækning i en eller flere retninger, kræver en kvantemekanisk beregning af elektronernes egenskaber. I denne afhandling bliver de kvantemekaniske metoder, tæthedsfunktionalteori og lineær responsteori, brugt til at beregne plasmonernes egenskaber i nanomaterialer af forskellig dimensioner. Beregningerne for de undersøgte systemer viser at kvantemekaniske effekter påvirker plasmonen betydeligt. Disse effekter inkluderer kobling til elektroniske enkelpartikel overgange, elektronernes endelige udstrækning fra metal-overflader, tunnelering mellem partikler og rummelig ikke-lokalitet.

De udforskede systemer inkluderer todimensionelle materialer såsom tynde metalfilm, overgangsmetal-dichalcogenider og grafen. Her er også van der Waals heterostrukturer (vdWh), som består af forskellige todimensionelle materialer stablet ovenpå hinanden, blevet undersøgt. Der præsenteres en ny metode til at beregne den dielektriske funktion af sådanne strukturer, hvor *ab initio* præcision kan opnås for strukturer bestående af hundredvis af lag. Derudover er endimensionelle plasmoner på atomar-skala blevet undersøg i tynde nanotråde og kanttilstande på MoS_2.

List of papers

Paper I

Spatially resolved quantum plasmon modes in metallic nano-films from first-principles.
Kirsten Andersen, Karsten W. Jacobsen, and Kristian S. Thygesen, Phys. Rev. B 86, 245129 (2012)

Paper II

Plasmons in metallic monolayer and bilayer transition metal dichalcogenides.
Kirsten Andersen and Kristian S. Thygesen, Phys. Rev. B 88, 155128 (2013)

Paper III

The dielectric genome of van der Waals heterostructures.
Kirsten Andersen, Simone Latini, and Kristian S. Thygesen, submitted (2015).

Paper IV

Visualizing hybridized quantum plasmons in coupled nanowires: From classical to tunneling regime.
Kirsten Andersen, Kristian L. Jensen, N. Asger Mortensen, and Kristian S. Thygesen, Phys. Rev. B 87, 235433 (2013)

Paper V

Plasmons on the edge of MoS_2 nanostructures.
Kirsten Andersen, Karsten W. Jacobsen, and Kristian S. Thygesen, Phys. Rev. B 90, 161410(R) (2014).

Contents

Chapter 1

Introduction

The plasmon is a fundamental type of electronic excitation that corresponds to oscillations in the electron charge density. The plasmon is often visualized as water ripples in a pond where the water represents the sea of free electrons in the metal. Thus, this resonance always involves more than one electron, i.e. it is *collective*, and is driven by the Coulomb interaction between them. Therefore, the energy can be significantly larger than the excitation energy of the individual electrons, typically several electron volts depending on the free-electron density of the metal and the strength of the interaction.

While the plasmon in bulk metals is of minor technological importance, plasmons on metal surfaces, in two-dimensional materials, in metallic wires, and in nanoparticles have several applications. The purpose of this thesis is to obtain a better theoretical understanding of plasmons in such materials, under the general term nanostructures, in the limit where atomic length scales are relevant. Here, the picture of a free-electron sea does no longer apply, and one must turn to a quantum mechanical desciption of the electrons. In the following, an introduction to the applicability of plasmons in the context of plasmonics is given, together with a motivation for including quantum mechanical effects in the theoretical description.

1.1 Plasmonics

A desirable property of the plasmon on surfaces and nanostructure is its ability to couple to light and thereby confine optical fields to length-scales much smaller than the wavelength of light [1]. This is favorable for nanoelectronic applications where a challenge is to carry digital information at high efficiency, while the components are miniaturized in order to increase the number of transistors on a microprocessor [2]. While optical fibers can carry data with high capacity, the size of optical cables are typically three orders of magnitude larger than electronic components such as nanoscale electronic transistors, making the technologies incompatible. Here, plasmons can be used to merge photonics and

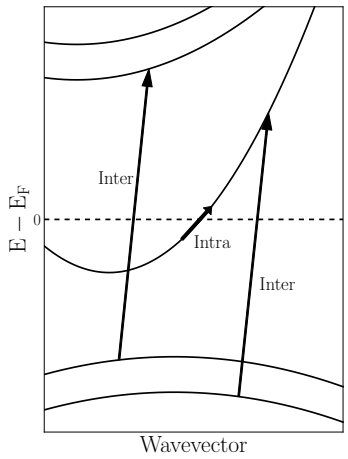

Figure 1.1: Sketch of a simplified bandstructure, showing the wavevector dependence of the electron energy levels. Intraband transitions originates from low-energy transitions within the metallic band that crosses the Fermi level. Interband transitions takes place between different electronic bands.

electronics at the nanoscale [3, 4], integrating optics and electronics on the same microchip [5]. Also, coupling of localized surface plasmons in metal particles to optical fields can be used to improve the performance of solar cells [6] and for chemical sensing [7, 8]. For example surface enhanced raman spectroscopy relies of the large enhancement of the electric field on the proximity of metal particles and aggregates due to plasmons [9].

1.2 Plasmons and quantum effects

For the theoretical description of plasmons, the main convention has been to use classical electrodynamics. Typically these approaches successfully accounts for resonances in metallic structures larger than around 10 nm [10]. As the progress in nanotechnology has made it possible to structure and characterize materials down to the atomic scale, the study of plasmons below the 10 nm size-range is possible. In this limit, purely classical approaches are found to fail for various reasons as explained in the following. An alternative theoretical approach used within this thesis, is provided by *ab initio* (from first principles) methods where the atomic structure and quantum mechanical properties of the electrons are taken into account.

As the size of a structure approaches the atomic scale, quantum mechanical effects begin to play a larger role. Here, quantum size effects emerges when the continuum of electronic energies become increasingly discretized with decreasing particle size. The increased spacing between the single-particle energy levels will

generally result in an increase (commonly referred to as blueshift) of the plasmon energy compared to larger particles, together with increased broadening of the ressonance [10]. Another quantum effect with size-dependent importance is the spill-out of electrons from the metal surface. When a structure is small, there is a relative larger effect of spill-out that decreases the effective electron density available for the plasmon resonance. This leads to a decrease (redshift) in plasmon energy, arguing from the standard relation between plasmon energy and electron density [11]. Experiments have revealed a blueshift on the localized surface plasmon resonance in silver nanoparticles with decreasing particle size in disagreement with classical models [12] [13] [14]. The description of noble metals, such as silver, is complicated by the coupling of the plasmon to localized transitions associated with the *d*-band of the metal. This leads to a shift of the plasmons, which could also play a role for blueshift with decreasing size, as will be discussed further in Chapter 4.

The case of silver is an example that also bound (non-metallic) electrons in a material can affect the plasmons. The discrete energy levels of electrons forms a continuum of states in extended materials. Here, the energy levels can be pictured as energy bands, where the energy evolves with the wave-vector. From this perspective, one can distinguish bewteen single-particle excitations originating from intraband (within the same electronic band) or interband transitions (between different electronic bands). A sketch of a simplified bandstructure is shown in Fig. 1.1, where both intra- and interband transitions are indicated. The intraband transitions are those which contributes to the plasmon, which can be viewed as a linear combination of electron-hole pairs. The interband transitions can couple to the plasmons and result in energy shifts and Landau damping. Therefore, a quantum mechanical approach is necessary for predicting the properties of plasmons in non-simple metals and new plasmonic materials. This effect is found to play a large role for several of the materials studied in this thesis.

Another property, not taken into account by classical models, is the spatial non-locality of the response that leads to a wave-vector dependence of the plasmon energy, generally termed dispersion. In principle, this is not a strict quantum mechanical effect, and non-locality can also be accounted for by hydrodynamic models [15]. To get a quantitatively correct result; however, an *ab initio* description is generally required.

Lastly, the tunneling of electrons between particles becomes important at very small particle separation. Classical models return a diverging enhancement of the electric field within the particle gap when the separation tends towards zero. This, clearly unphysical effect, breaks down with the inclusion of tunneling. This sets an upper limit for the electric field enhancement [16], where the maximal enhancement is found at small, but finite separations. Also, accounting for the atomic structure of the interface has been found to affect the onset of tunneling within a theoretical description of such systems [17].

In this work, the described quantum effects are included through quantum mechanical calculation of the dielectric function, using the methods density func-

tional theory and linear response theory described in Chapter 2. A disadvantage of *ab initio* methods is their high computational cost, where calculations generally requires a supercomputer. Since the cost grows quickly with the number of atoms in the unit cell, these approaches are generally not applicable to structures larger than 10 nm at maximum. In this limit, classical electrodynamics and semi-classical models, such as the hydrodynamic approximation [15, 18], generally work well, where quantum approaches can be applied to understand special cases such as dimers of small separation. On the other hand, in the case of materials structured on the atomic scale, *ab initio* methods are of high relevance. There is an increasing interest in such materials; for example two-dimensional (2D) materials.

1.3 2D materials

In my view the main contribution of *ab initio* methods to this field, is the ability to predict the properties of new materials. Here, the growing interest in atomically thin 2D materials, initialized by the discovery of graphene [19], has lead to the extraction of for example monolayer MoS_2 [20]. Graphene plasmonics has appeared as a field of it's own [21], since graphene can hosts highly confined plasmons that propagate with low loss [22] and can be tuned by the degree of doping [23]. Here, quantum theory an ab initio calculations have provided a better understanding of the plasmon excitations and screening in this material [24] [25].

Also, *ab initio* calculations have been applied to predict the existence of many other 2D materials [26], leaving a whole library of 2D materials to select for desired properties. Metallic 2D materials that are predicted to host plasmons [27] has also been found to exist [28]. These materials could be of high importance for future nanoelectronics, where recent advances in stacking different 2D materials on top of each other to form van der Waals heterostructures [29], has given even more possibilities for tailoring the electronic properties.

It is also interesting to study the properties of 2D systems from a fundamental perspective, since plasmons behave qualitatively and quantitatively different from the 3D counterpart. In this thesis, Chapter 4 and 5 is devoted to the study of plasmons in 2D materials, discussing the fundamental properties and applying an *ab initio* approach to different structures. An additional contribution, a new theoretical approach for calculating the dielectric function of van der Waals heterostructures is presented in Chapter 5, where *ab initio* accuracy is extended to much larger structures with a multi-scale approach.

The strongest possible confinement of a propagating plasmon is obtained for one-dimensional materials, where confinement to the atomic scale has been observed [30]. In this thesis, also the fundamental properties of plasmons in 1D is discussed and *ab initio* approaches applied to a few one-dimensional systems.

1.4 Spatially resolved plasmons

A main contributions of this thesis is a new method within the *ab initio* framework to investigate the spatial form of plasmons. This is of relevance for nanostructures, where several plasmon modes of different symmetry and localization can exist. Here, common macroscopic approaches for the dielectric function are not sufficient to identify all the resonances of the system, and the information already present in the microscopic dielectric function must be utilized. As discussed in Chapter 3, the plasmon *eigenmodes* can be defined through an eigenvalue equation for the dielectric matrix.

The study of the spatial form of plasmons are further motivated by the progress in electron microscopy the last decade that has made it possible to resolve the plasmon losses with atomic precision. Since plasmons in nanoparticles generally interacts strongly with light, the excitations of interest are commonly probed with optical microscopy. Plasmons in very small particles below 10 nm on the other hand interact more weakly with light, making observation of plasmon in these structures more challenging.

Another common approach is to use electron energy loss spectroscopy (EELS), where the energy lost by fast electrons traveling through a sample provides information about the excitations within the sample. The cross-section for probing plasmons is large with this method, where energy-loss below 50 eV is typically due to excitations of plasmons. [31]. While spatial resolution of optical microscopes is limited by the diffraction limit to approximately half the wavelength of light, the small de Broglie wavelength of fast electrons enable spatial resolution below 1 Å[32]. This is obtained by performing EELS within a transmission electron microscope where the electron beam is focused on this length scale. By scanning over the structure, the energy losses can be mapped in real space, thus providing spatial resolution of the plasmon excitations.

For example, this technique has been applied to small metal nanoparticles, where a different response is obtained when probing the bulk and surface of the particle due to the localized surface plasmon [33, 14]. For metallic nanorods, several discrete plasmon modes where identified as standing waves along the rods [34, 35]. In a study on defects in graphene [36], it was shown that spatial information can be obtained down to atomic scale, where the difference in the response due to single defects could be resolved. An expression for the spatially resolved EELS from quantum theory is derived in Chapter 3 and applied to the study of a few systems within the thesis.

1.5 Outline

To conclude this introduction, a brief description is provided for the following chapters:

Chapter 2 gives an introduction to the theoretical and methodological foundation for the thesis by a description of density functional theory and linear

response theory that are used to obtain a quantum mechanical description of the dielectric function.

Chapter 3 presents the developed approach for calculating and visualizing plasmons in confined structures from quantum theory. The main contribution is the definition of an eigenvalue equation for the dielectric matrix that enables the identification of the plasmon eigenmodes of an electronic system. Secondly, an equation for the spatially resolved EELS is derived from ab initio.

Chapter 4 discusses the properties of plasmons in 2D materials, where the results for the plasmon eigenmodes in metallic 2D systems are presented, including thin metal films and monolayer transition metal dichalcogenides.

Chapter 5 presents the developed quantum electrostatic heterostructure (QEH) model for effectively calculating the dielectric function of van der Waals heterostructures that are stacks of different 2D materials.

Chapter 6 discusses the properties of plasmons confined to 1D, where the results for plasmons in thin nanowires and edge states on MoS_2 are presented.

Chapter 7 gives a brief summary and discussion of the results of the thesis as a whole.

Chapter 2

Theory

The purpose of this Chapter is to introduce the reader to the theoretical concepts and methods used within the thesis. Section 2.1 is devoted to the problem of obtaining the electronic structure of materials, with an emphasis on density functional theory that used to calculate single-particle electronic states. In Section 2.2, linear response theory, that is used to calculate the dielectric function and plasmon properties, is described.

2.1 The electronic structure problem

Most of the physical and chemical properties of matter are governed by the electronic structure. The key equation for obtaining the electron energy and wave function is the electronic Schrödinger equation:

$$\hat{H}_e \Psi(\mathbf{R}, \mathbf{r}) = E(\mathbf{R}) \Psi(\mathbf{R}, \mathbf{r}), \tag{2.1}$$

with the electronic Hamiltonian, $\hat{H}_e$. The Born Oppenheimer approximation and the adiabatic approximation has been applied to decouple the electronic part of the Hamiltonian from the nuclear part, where the many-body wave function, $\Psi(\mathbf{R}, \mathbf{r})$, is still a function of electronic and nuclear coordinates, $\mathbf{r}$ and $\mathbf{R}$ respectively. Also the electron energy, $E(\mathbf{R})$, depends on the nuclear coordinates, which defines a potential energy surface for the atomic positions. The electronic Hamiltonian for a system of N_e electrons and N_α stationary nuclei is written (in atomic units):

$$\hat{H}_e = -\frac{1}{2} \sum_{i=1}^{N} \nabla_i^2 - \sum_{\alpha}^{N_\alpha} \sum_{i}^{N_e} \frac{Z_\alpha}{|\mathbf{R}_\alpha - \mathbf{r}_i|} + \sum_{i,j<i}^{N_e} \frac{1}{|\mathbf{r}_i - \mathbf{r}_j|}, \tag{2.2}$$

where the three terms are the kinetic energy, the electron-nuclei interaction and the electron-electron repulsion respectively. The nuclei set up a potential felt by the electrons, and the electron-nuclei interaction can thus be written as a generalized external potential, $V_{\text{ext}}(r)$.

Since the electron-electron interaction couples all the electronic degrees of freedom, the Schrödinger equation cannot be directly factorized to a set of single-particle equations, and the complexity increases rapidly with the number of electrons. Therefore exact solutions can only be obtained for simple systems, such as the homogeneous electron gas and very small molecules [37]. Thus, further approximations are necessary in order to describe the electronic structure of physical systems with several atoms and electrons. A solution is provided by Density functional theory (DFT), that uses the electron density as a parameter, instead of the many-body wave function, which reduces the degrees of freedom significantly.

2.1.1 Density functional theory

The theoretical foundation of DFT is that the energy is uniquely determined by the electron density, as proven by Hohenberg and Kohn and stated in their first theorem: [38]

> The external potential $v_{\text{ext}}(\mathbf{r})$ is uniquely determined by the electronic density, to within an additive constant.

Hence, it is not possible to define two different external potentials that results in the same density. The energy can therefore be written as a functional of the electron density, n:

$$E[n(\boldsymbol{r})] = F[n(\boldsymbol{r})] + \int v_{ext}(\boldsymbol{r}) n(\boldsymbol{r}) d\boldsymbol{r}, \tag{2.3}$$

where the first term is the universal part that contains the kinetic energy and electron-electron coupling, $F[n] = \langle \Psi | \hat{T} + \hat{U}_{ee} | \Psi \rangle$, and the second term depends on the external potential. DFT is in principle exact provided that the correct form of $F[n]$ is known. In practice both components of $F[n]$ are difficult to evaluate as exact functionals of the density. The electron-electron interaction can be split into several terms of increasing importance, where the largest contribution is the Hartree energy, that accounts for the classical Coulomb repulsion between the electrons:

$$E_{\text{Hartree}} = \frac{1}{2} \int \int \frac{n(\boldsymbol{r}) n(\boldsymbol{r}')}{|\boldsymbol{r} - \boldsymbol{r}'|} d\boldsymbol{r} d\boldsymbol{r}'. \tag{2.4}$$

However, only including the Hartree term will overestimate the interaction energy, since the position of the electrons are correlated such that the probability for finding two electrons in close vicinity of each other is smaller than for large separations. This is accounted for by including the exchange and correlation energies, where approximate expressions are commonly found.

The exchange part stems from the fermionic nature of electrons, that requires the electronic wave function to be anti-symmetric with respect to interchanging of two electronic coordinates. The consequence is that two electrons cannot be found in the same state in terms of spin and position, known as Pauli's

exclusion principle. Including the Hartree and exchange energies corresponds to the Hartree-Fock approximation, where the electron wave function can be written as a single Slater determinant.

The missing part is the correlation energy, written as the difference between the exact and Hartree-Fock energy: $E_C = E_0 - E_{\mathrm{HF}}$, and is the smallest of the contributions but the one hardest to evaluate. It accounts for the correlation of electrons due to the Coulomb repulsion, and therefore also affects electrons with different spins. Both the exchange and correlation energy are negative, since both effects keep the electron out of each others way and thereby reduces the Coulomb repulsion. Several approximations for exchange-correlation functionals exists, where the most important are described in the following subsection.

Another challenge is the kinetic energy, where an expression must i obtained in terms of the density. A solution was provided by Kohn and Sham in 1965 [39], using a reference system of non-interacting electrons, with the same density as the interacting system. The kinetic energy is evaluated in terms of the one-electron orbitals, that are found as solutions to the single-particle Kohn-Sham equations. The one-electron Kohn-Sham Hamiltonian is written:

$$\hat{H}_{KS} = -\frac{1}{2}\nabla^2 + v_{\mathrm{eff}}(\boldsymbol{r}), \tag{2.5}$$

where $v_{\mathrm{eff}}(\boldsymbol{r})$ is an effective local potential that results in the same density as the interacting system, given by:

$$v_{\mathrm{eff}}(\boldsymbol{r}) = v_{ext}(\boldsymbol{r}) + v_{\mathrm{Hartree}}[n](\boldsymbol{r}) + v_{xc}[n](\boldsymbol{r}), \tag{2.6}$$

$$v_{xc}[n](\boldsymbol{r}) \equiv \frac{\partial \tilde{E}_{xc}[n]}{\partial n(\boldsymbol{r})}. \tag{2.7}$$

Then the Kohn-Sham equations must be solved self-consistently, where the single-particle energies, ϵ_i are given by:

$$\Big(-\frac{1}{2}\nabla_i^2 + v_{\mathrm{eff}}(\boldsymbol{r})\Big)\phi_i(\boldsymbol{r}) = \epsilon_i\phi(r),, \tag{2.8}$$

and the total electron density is determined from the wave functions:

$$n(\boldsymbol{r}) = \sum_{n=1}^{N} |\phi(\boldsymbol{r})|^2. \tag{2.9}$$

Thus, these equations can be solved in an iterative cycle, where the electronic density is updated in order to decrease the total energy.

The total electron energy functional (also called the Hohenberg-Kohn energy functional [40]) is written in terms of the non-interacting kinetic energy, $T_S[n]$:

$$E[\rho] = T_S[n] + E_{\mathrm{Hartree}}[n] + E_{ext} + \tilde{E}_{xc}[n], \tag{2.10}$$

The difference between the exact and the non-interacting kinetic energy, $T[n]$ and $T_s[n]$ respectively, is added to the exchange-correlation energy, for example though the principle of adiabatic connection[37], such that:

$$\tilde{E}_{xc}[n] = E_{xc}[n] + T[n] - T_s[n]. \tag{2.11}$$

The ground state density is found by minimizing the total energy, as states by the second Hohenberg-Kohn theorem:

> The variational energy is minimized for the ground state density, such that the density that minimizes the energy is the ground state density.

Therefore the Kohn-Sham equations are solved in iterate steps in order to minimize the total energy, until a chosen convergence-criteria is met. Here the single-particle Kohn-Sham energies enters as Lagrange multipliers, and they are therefore not formally justified as single-particle energies. Even though the Kohn-sham states cannot be mathematically defined as electron addition or removal energies, as is the case of Hartree Fock [40], experience have shown that the Kohn-Sham energies and wave functions usually gives a qualitatively correct picture. For example the Kohn-Sham energies generally gives a qualitative correct description of band structures, but where the size of the band gap is usually underestimated.

In the energy functional Eq. 2.11, all the unknown information has been but into the exchange-correlation functional, $\tilde{E}_{xc}[n]$, that must be approximated. In the following two fundamental approaches is presented.

2.1.2 Exchange-correlation functionals

The simplest approximation to exchange-correlation is the Local Density Approximation (LDA) where the solution for the homogeneous electron gas (HEG) is used:

$$E_{\mathrm{xc}}^{\mathrm{LDA}}[n] = \int n(\boldsymbol{r})\epsilon_{\mathrm{xc}}^{\mathrm{HEG}}[n(\boldsymbol{r})], \tag{2.12}$$

where $\epsilon_{\mathrm{xc}}^{\mathrm{HEG}}[n(\boldsymbol{r})]$ is the HEG result for the exchange-correlation energy density. This approximation is in particular justified for systems where the electron density varies slowly in space. Yet, the performance for more non-homogeneous systems is better than one might expect, since the spherically averaged exchange-correlation hole is usually similar to the exact one. In general, LDA tends to overestimate bond energies and underestimate excitation energies such as band gaps [37].

A more sophisticated approach is the Generalized Gradient Approximation (GGA), where the inhomogeneity of the density is taken into account. This is done by including the gradient of the density in the expression for the exchange-correlation functional:

$$E_{xc}[n] = \int n(\boldsymbol{r})\epsilon_{xc}[n(\boldsymbol{r}), \nabla n(\boldsymbol{r})], \tag{2.13}$$

where ϵ_{xc} is the exchange-correlation energy density. Several GGA type functionals has been proposed, such as the widely used Perdew, Burke and Ernzerhof

(PBE) functional [41]. GGA functionals improves the description of binding energies and bond length compared to LDA, and slightly improves on band gap energies.

A general error produced by both functionals, is that the exchange-correlation potential decays exponentially rather with r than having the correct $-e^2/r$ dependence. Therefore, the description of systems involving weak bonds such as hydrogen bonds and van der Waals interactions is deficient, while strongly bound systems (covalent, ionic and metallic bonding) are often well-described. In order to obtain a more accurate description of the quasi-particle band gap and optical excitations, higher order methods that builds on top of ground state DFT, such as the GW approximation [42] and the Bethe-Salpeter equation [43] can be applied.

2.1.3 Electronic structure calculations

For this thesis density functional theory calculations has been performed with the electronic structure code GPAW [44]. The code builds upon the projector augmented-wave (PAW) method where the all-electron wave function is decomposed into a smooth pseudo wave function describing the valance electrons, and a frozen core where the core electrons are constrained to match the reference shape of the isolated atom. The advantage of the frozen core approximation is that it reduces computational costs, while a good description of the valence electrons is still obtained. The all-electron and pseudo valance wave functions are related through a linear transformation, expressed in terms of projector functions [45].

GPAW allows for a both a grid-based and plane-wave representation of the pseudo wave functions, together with the atomic centered linear combination of atomic orbitals (LCAO) mode. For systems with periodic boundary conditions the plane-wave representation is often advantageous in terms of computational cost. Also plane-wave mode is more convenient when the result is given as input to a linear response calculation, where also the response functions are represented in a plane-wave basis (see Section 2.2.3).

The GPAW code supports periodic and non-periodic boundary conditions in different directions, and several exchange-correlation functionals are implemented. Computational costs is reduced by parallelization, where k-points, spins, bands, (and domains in grid-based mode) are distributed over several processors. Also many-body methods for obtaining a better description of excited states are implemented [46, 47], where linear response time-dependent DFT [48] has been used to calculate the dielectric function and plasmon properties, as described in the following section.

2.2 Linear response theory

In this section the general concept of linear response theory in introduced, and it is explained how this approach can be used together with DFT to calculate

the dielectric function. The dielectric function is a main quantity for describing the electronic screening and excitations of a material, including the plasmon resonances.

When a material is subject to an external perturbation, such as an optical field or fast electrons, it will respond in a manner that depends on the nature of the perturbation. Linear response theory states that [49]:

> For weak external perturbations the response of the material will be proportional to the strength of the perturbation.

The relation of proportionality between the perturbation and the response is expressed in terms of a correlation function, where examples are given in the following. In order to describe the electronic excitations, the first step is to calculate the response in the electron density due to an external electric potential.

2.2.1 The density response function

The density response function, $\chi(\mathbf{r}, \mathbf{r}', t - t')$, often called the electric susceptibility, accounts for the changes from the ground-state density at position $\mathbf{r}$ and time t, due to an external potential $v_{\text{ext}}(\mathbf{r}', t')$:

$$\delta n(\mathbf{r}, t) = \int d\mathbf{r}' \int dt' \chi(\mathbf{r}, \mathbf{r}', t - t')\, v_{\text{ext}}(\mathbf{r}', t'). \tag{2.14}$$

Since the response is generally non-local in space and time, the response at $(\mathbf{r}, t)$ will depend on the perturbation at other positions $\mathbf{r}'$ and the perturbations at previous times, $t' < t$. Thus, χ is a retarded correlation function that only accounts for perturbations at times before the observation time, and it is assumed that the perturbation is turned on adiabatically at $t' = -\infty$. From the Kubo formula [50, 49], χ is obtained as a density-density correlation function in terms of the density operator $\hat{n}(r, t)$ as:

$$\chi(\mathbf{r}, \mathbf{r}', t - t') = -i\theta(t - t')\langle[\hat{n}(\mathbf{r}, t), \hat{n}(\mathbf{r}', t')]\rangle_0, \tag{2.15}$$

where the equilibrium average, $\langle\rangle_0$, of the commutator is taken.

Since only the time difference $(t - t')$ enters in the response function, the expression is conveniently transformed to Fourier (frequency) space, assuming that the external potential oscillates periodically with time, $v_{\text{ext}}(\mathbf{r}', t') = v_{\text{ext}}(\mathbf{r}')e^{i\omega t'}$:

$$\delta n(\mathbf{r}, \omega) = \int d\mathbf{r} \chi(\mathbf{r}, \mathbf{r}', \omega) v_{\text{ext}}(\mathbf{r}', \omega). \tag{2.16}$$

Eq. (2.16) contains the full density response function, whereas the non-interacting density response function, χ^0, gives the density response due to the total potential within the material:

$$\delta n(\mathbf{r}, \omega) = \int d\mathbf{r} \chi^0(\mathbf{r}, \mathbf{r}', \omega) v_{\text{tot}}(\mathbf{r}', \omega). \tag{2.17}$$

The non-interacting counterpart is useful since it can be expressed in terms of singe-particle wave functions, ψ, energies, ϵ, and occupation numbers, f: [51]

$$\chi^0(\mathbf{r},\mathbf{r}',\omega) = \sum_{\mathbf{k},\mathbf{q}}^{\mathbf{BZ}} \sum_{n,n'} (f_{n\mathbf{k}} - f_{n'\mathbf{k}+\mathbf{q}}) \frac{\psi^*_{n\mathbf{k}}(\mathbf{r})\psi_{n'\mathbf{k}+\mathbf{q}}(\mathbf{r})\psi_{n\mathbf{k}}(\mathbf{r}')\psi^*_{n'\mathbf{k}+\mathbf{q}}(\mathbf{r}')}{\omega + \epsilon_{n\mathbf{k}} - \epsilon_{n'\mathbf{k}+\mathbf{q}} + i\eta}, \tag{2.18}$$

where n refers to band index and $\mathbf{k}$ to wave-vector. The difference in occupation $(f_{n\mathbf{k}} - f_{n'\mathbf{k}+\mathbf{q}})$ ensures that only transitions from occupied to unoccupied electronic states will contribute to the sum in Eq. (2.18). The parameter η is formally a positive infinitesimal that ensures the correct decay of the density response function for $t - t' \to \infty$, but also serves as a broadening parameter that gives a finite spectral width to the peak in the imaginary part of χ^0.

Since χ^0 is expressed in terms of non-interacting electronic states, it can be calculated on the basis of the Kohn-Sham eigenstates obtained from a DFT calculation. This approach in known as linear response time-dependent DFT (TDDFT), which is used in this thesis.

The full and non-interacting density response functions are related through the Dyson equation [52]:

$$\chi(\mathbf{r},\mathbf{r}',\omega) = \chi^0(\mathbf{r},\mathbf{r}',\omega) + \int d\mathbf{r}_1 d\mathbf{r}_2 \chi^0(\mathbf{r},\mathbf{r}',\omega)\Big(v_c(\mathbf{r}_1,\mathbf{r}_2) + f_{xc}(\mathbf{r}_1,\mathbf{r}_2,\omega)\Big)\chi(\mathbf{r}_2,\mathbf{r}',\omega), \tag{2.19}$$

$$f_{xc}(\mathbf{r}_1,\mathbf{r}_2,\omega) = \frac{\delta v_{xc}(\mathbf{r}_1,\omega)}{\delta n(\mathbf{r}_2,\omega)}, \tag{2.20}$$

where $v_c = \frac{1}{|\mathbf{r}_1 - \mathbf{r}_2|}$ is the Coulomb (Hartree) potential and f_{xc} is the exchange-correlation kernel that depends of the response to the exchange-correlation potential. The simplest choice is to neglect the exchange-correlation at this level and set $f_{xc} = 0$, so that the only contribution to the kernel is the Coulomb potential. This is known as the random phase approximation (RPA), which is generally a good approximation for the description of plasmons, typically giving results for plasmon energies within 5 % of the experimental value [48]. In terms of the magnitude of the dielectric function, RPA tends to underestimate the screening. However, this error is often cancelled by the underestimation of the band gap of a DFT calculation on the LDA or PBE exchange-correlation level.

Exchange correlation effects can be included by using the Adiabatic local density approximation (ALDA) where f_{xc} is expressed as a functional of the local density. Including exchange-correlation effects generally decreases the plasmon energy, and leads to an increase in the calculated dielectric constant.

2.2.2 The dielectric function

The dielectric function is the main quantity for describing the dielectric properties of a material, such as electronic screening and plasmon resonances. It is a

retarded correlation function in the same manner as the density response functions, and relates the total potential within the material to an external potential on the form $v_{\text{ext}}(\mathbf{r})e^{i\omega t}$:

$$v_{\text{ext}}(\mathbf{r},\omega) = \int d\mathbf{r}'\epsilon(\mathbf{r},\mathbf{r}',\omega)v_{\text{tot}}(\mathbf{r}',\omega), \tag{2.21}$$

where the total potential is the sum of the external and induced potential: $v_{\text{tot}} = v_{\text{ext}} + v_{\text{ind}}$. Within the RPA, ϵ can be obtained directly from the non-interacting density response function:

$$\epsilon(\mathbf{r},\mathbf{r}',\omega) = \delta(\mathbf{r}-\mathbf{r}') - \int d\mathbf{r}'' v_c(\mathbf{r},\mathbf{r}'')\chi^0(\mathbf{r}'',\mathbf{r}',\omega). \tag{2.22}$$

As for the density response functions, the dielectric function is non-local in space and time, such that the response depends on the perturbation also at other positions at previous times.

For homogeneous systems, where the response is only a function of $(\mathbf{r}-\mathbf{r}')$, the non-locality can be translated into a wave-vector (q) dependence of the dielectric function. For a homogeneous metal, the homogeneous electron gas, the wave functions that enters in Eq. (2.18) takes the form of plane waves with wave-vector $\mathbf{k}$ such that the following expression is obtained [40]:

$$\epsilon(\mathbf{q},\omega) = 1 + \frac{8\pi e^2}{q^2 V}\sum_{\mathbf{k}} \frac{f(\mathbf{k}) - f(\mathbf{k}+\mathbf{q})}{E(\mathbf{k}+\mathbf{q}) - E(\mathbf{k}) - \hbar\omega - i\eta}, \tag{2.23}$$

commonly referred to as the Lindhard dielectric function. In the long wavelength limit, $q \to 0$, this expression can be reduced to (going to second order in q):

$$\epsilon(q\to 0,\omega) = 1 - \frac{\omega_p^2}{(\omega+i\eta/\hbar)^2} - \frac{3}{5}\frac{\omega_p^2}{(\omega+i\eta/\hbar)}v_F^2 q^2 - .... \tag{2.24}$$

Here ω_p is the bulk plasmon frequency: $\omega_p^2 = ne^2/m\epsilon_0$, also obtained from Drude theory [53, 54] where a non-interacting sea of electrons is assumed. The plasmon frequency is seen to have a square-root dependence on the free-electron density, $\omega_p \propto \sqrt{n}$.

By setting $q = 0$ in Eq. (2.24), the Drude results for the dielectric function is obtained, where the spatial non-locality is completely neglected:

$$\epsilon_{\text{Drude}}(\omega) = 1 - \frac{\omega_p^2}{\omega(\omega+i/\tau)}. \tag{2.25}$$

The parameter $\tau = \hbar/2\eta$ can be interpreted as the time between scattering events between electrons and cores in the Drude model.

The magnitude and sign of the dielectric function reflects how the system responds to external fields. For $\epsilon > 1$ the total potential within the material is smaller than the external potential, i.e. the electric field is screened by the material. When $\epsilon \approx 0$ on the other hand, the total potential will be much larger

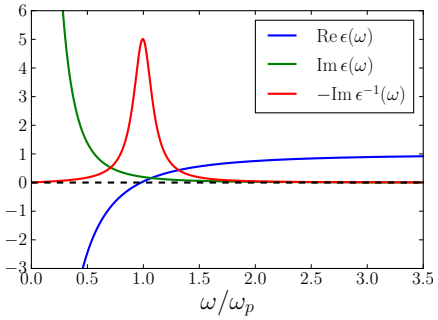

Figure 2.1: Drude result for the dielectric function, Eq. (2.25) with $\eta = 0.2\omega_p$, showing the real and imaginary parts as well as the loss function, $\mathrm{Im}\,\epsilon^{-1}$, that peaks at the plasmon frequency, ω_p. At $\omega \approx \omega_p$ the real part of ϵ is zero, such that a eigen-resonance of the electron system is excited at this frequency and $v_{\mathrm{tot}} >> v_{\mathrm{ext}}$.

than the external potential, which corresponds to that an eigen-resonance of the system is excited, such as the plasmon. The Drude result for the dielectric function satisfies that $\mathrm{Re}\,\epsilon = 0$ close to the plasmon frequency, as seen in Fig. 2.1. At the plasmon frequency there is also a peak in the electron energy loss-function, given by [40]:

$$\mathrm{EELS}(\omega) = -\mathrm{Im}\,\epsilon^{-1} = \frac{\epsilon_2}{\epsilon_1^2 + \epsilon_2^2}, \tag{2.26}$$

in therms of the real and imaginary parts, ϵ_1 and ϵ_2. Thus, having a peak in the loss function requires that both the real part and imaginary parts are small. The imaginary part is directly related to the losses within the material, and therefor accounts for the damping of the plasmon.

When the non-locality is taken into account by restoring the q-dependence of the dielectric function in Eq. (2.24), also the plasmon frequency acquires a wave-vector dispersion [40]:

$$\omega(q) = \omega_p + \frac{3v_{\mathrm{F}}^2}{10\omega_p}q^2 + ..., \tag{2.27}$$

where the plasmon energy increases slowly with q. Off course, materials are generally not homogeneous due to the atomic structure. In the following, the case of periodic systems is considered.

2.2.3 GPAW implementation

In GPAW linear response TDDFT is implemented for periodic systems, where the density response function is written in plane wave representation, $\chi_{\mathbf{G}\mathbf{G}'}(\mathbf{q}, \omega)$, in a basis of the reciprocal lattice vectors, $\mathbf{G}, \mathbf{G}'$, and in terms of the wave-vector

$\mathbf{q}$ restricted within the first Brillouin zone. In this manner, inhomogeneities within the unit cell is accounted for by the expansion in $\mathbf{G}, \mathbf{G}'$, also known as local field effects. $\chi_{\mathbf{G}\mathbf{G}'}(\mathbf{q})$ is related to $\chi(\mathbf{r}, \mathbf{r}')$ by the inverse Fourier transform:

$$\chi(\mathbf{r}, \mathbf{r}', \omega) = \frac{1}{\Omega} \sum_{\mathbf{q}}^{\mathrm{BZ}} \sum_{\mathbf{G}\mathbf{G}'} e^{i(\mathbf{q}+\mathbf{G})\cdot\mathbf{r}} \chi_{\mathbf{G}\mathbf{G}'}(\mathbf{q}, \omega) e^{-i(\mathbf{q}+\mathbf{G}')\cdot\mathbf{r}'}, \tag{2.28}$$

the same applying to the noninteracting counterpart, χ^0. As explained previously, the non-interacting density response function, χ^0, can be expressed in terms of single-particle electronic states. When combining Eq. (2.28) and Eq. (2.18), the expression for χ^0, first derived by Adler [55] and Wiser [56], is obtained:

$$\chi^0_{\mathbf{G}\mathbf{G}'}(\mathbf{q}, \omega) = \frac{1}{\Omega} \sum_{\mathbf{k},\mathbf{q}}^{\mathrm{BZ}} \sum_{n,n'} (f_{n\mathbf{k}} - f_{n'\mathbf{k}+\mathbf{q}}) \frac{\rho_{n\mathbf{k},n'\mathbf{k}+\mathbf{q}}(\mathbf{G}) \rho^*_{n\mathbf{k},n'\mathbf{k}+\mathbf{q}}(\mathbf{G}')}{\omega + \epsilon_{n\mathbf{k}} - \epsilon_{n'\mathbf{k}+\mathbf{q}} + i\eta}, \tag{2.29}$$

where ρ is the charge-density matrix given by:

$$\rho_{n\mathbf{k},n'\mathbf{k}+\mathbf{q}}(\mathbf{G}) = \langle \psi_{n\mathbf{k}}(\mathbf{r}) | e^{i(\mathbf{q}+\mathbf{G})\cdot\mathbf{r}} | \psi_{n'\mathbf{k}+\mathbf{q}}(\mathbf{r}) \rangle. \tag{2.30}$$

In linear response TDDFT the Kohn-Sham eigenvalues, wave functions and occupations obtained from a DFT calculation are inserted in Eq. (2.29) and (2.30). The RPA result for the dielectric matrix, Eq. (2.22), is written in plane-wave representation as:

$$\epsilon_{\mathbf{G}\mathbf{G}'}(\mathbf{q}, \omega) = \delta_{\mathbf{G},\mathbf{G}'} - \frac{4\pi}{|\mathbf{q}+\mathbf{G}|^2} \chi^0_{\mathbf{G}\mathbf{G}'}(\mathbf{q}, \omega), \tag{2.31}$$

where the Coulomb kernel $K_{\mathbf{G}}(\mathbf{q}) = \frac{4\pi}{|\mathbf{q}+\mathbf{G}|^2}$ is the Fourier transform of the Coulomb potential in three dimensions, that is diagonal in reciprocal space. Often the symmetrized version of the dielectric matrix used:

$$\epsilon_{\mathbf{G}\mathbf{G}'}(\mathbf{q}, \omega) = \delta_{\mathbf{G},\mathbf{G}'} - 4\pi \frac{1}{|\mathbf{q}+\mathbf{G}|} \chi^0_{\mathbf{G}\mathbf{G}'}(\mathbf{q}, \omega) \frac{1}{|\mathbf{q}+\mathbf{G}'|}, \tag{2.32}$$

which gives the same result as the non-symmetrized version in terms of macroscopic averages and resonance energies. However, when any spatial information of the resonances is extracted from the dielectric function, it is important to use the non-symmetrized version, Eq. (2.31). The symmetry of the dielectric matrix will be explored further in Chapter 3, where the theory for plasmon eigenmodes is presented.

For the calculation of optical and electron energy loss spectra the macroscopic dielectric function is typically used. This quantity gives the averaged response to a constant external perturbation, and is obtained by integrating over both spatial coordinates, which corresponds to choosing the $\mathbf{G} = \mathbf{G}' = 0$ components in reciprocal space:

$$\epsilon_M(\omega, \mathbf{q}) = \frac{1}{\epsilon^{-1}_{\mathbf{G}=0,\mathbf{G}'=0}(\mathbf{q}, \omega)}. \tag{2.33}$$

Taking the macroscopic component of the inverse dielectric matrix (instead of taking $\epsilon_{\mathbf{G}=0,\mathbf{G}'=0}$ directly) ensures that local field effects are included. This means that even though the external perturbation has no spatial variation, the system can respond on the microscopic scale by involving oscillations with finite wavelengths. This can again have an effect on the macroscopically averaged response.

The absorption spectra that corresponds to the absorption of light can be obtained as:

$$\mathrm{Abs}(\omega) = \mathrm{Im}\,\epsilon_M(\mathbf{q} \to 0, \omega). \tag{2.34}$$

Since the photon carries vanishing momentum, $\mathbf{q} \to 0$, the transition is close to vertical in $\mathbf{q}$-space. The electron energy loss spectrum corresponds to the energy lost by fast electrons probing the material:

$$\mathrm{EELS}(\mathbf{q}, \omega) = -\mathrm{Im}\,\epsilon_M^{-1}(\mathbf{q}, \omega). \tag{2.35}$$

I Fig. 2.1 with the Drude result, it was shown that the loss function has a peak at the plasmon frequency.

As will be discussed in the Chapter 3, the macroscopic dielectric function is not always useful for the study of nanostructures.

2.2.4 Details of implementation and convergence

For the linear response TDDFT implementation in GPAW, the non-interacting density response function is in practice obtained from a Hilbert transform of the spectral function [57], which reduces computational cost. The latest implementation of the code performs the Hilbert transform on a nonlinear frequency grid with a denser sampling at low frequencies.

A calculation must be converged with respect to several parameters. The spectral function is obtained from a sum over the Kohn-Sham states, where also unoccupied states must be included, typically several tens of eV above the Fermi level depending on the energy range of the resonances studied. Another important parameter is the energy cutoff for the plane waves, $\mathbf{G}, \mathbf{G}'$, that determines the size of the dielectric matrix, and thereby to how small wavelengths local-field effects are included. As a rule of thumb, unoccupied states must be included up to the energy cutoff value, which also requires a frequency grid that extend up to this energy.

Also the result must be converged with respect to the number of k-points, the frequency grid spacing, and the broadening parameter η, where η must be sufficiently large to smear out the discretization introduced by the finite grid spacing and the finite number of k-points. In order to resolve narrow resonances, it is necessary to use a small value of η where the number of k-points and frequency points must be increased.

For systems of lower dimensionality, such as 2D and 1D systems, the calculation must be converged with respect to the amount of vacuum in the unit cell,

that separates the repeated images. However, the separation required to decouple the Coulomb potential of the repeated unit cells can be much larger than the separation required to avoid overlap of the single-particle states in the ground state calculation. This can be seen as the Coulomb kernel $K_{\mathbf{G}}(\mathbf{q}) = \frac{4\pi}{|\mathbf{q}+\mathbf{G}|^2}$ diverges for small $\mathbf{q}+\mathbf{G}$. Therefore it is generally necessary to truncate the Coulomb Kernel in the relevant directions [58, 59]. Here the amount of vacuum must take up at least half of the unit cell, so that the truncation length equal to $L/2$, where L is the length of the unit cell, will not truncate the potential within the structure. In 2D, an expression for the Coulomb kernel, truncated along the z-direction can be written:

$$V^{2D}_{\mathbf{G},G_z}(\mathbf{q}_\parallel) = \frac{4\pi}{|\mathbf{G}^2 + \mathbf{q}_\parallel^2|}\big[1 - \cos(G_z L/2)\big], \tag{2.36}$$

which has been applied to the study of 2D materials such as monolayer MoS_2 and other transition metal dichalcogenides, graphene and monolayer hexagonal boron nitride, studied in Chapter 4 and 5.

For the one-dimensional systems studied in Chapter 6, different versions for the truncated kernel has been used. One solution is to use a cylindrical cutoff, as done in Paper IV. However, this form of truncation is disadvantageous when the 1D system has different widths along the two perpendicular directions, such as the MoS_2 nanoribbon studied in Paper V. Here the Wigner Seitz truncated kernel is used [60], that truncated the potential in all directions at a length scale $\frac{1}{2}\, a_i\, n_{\mathrm{kpts},i}$, where a_i is the length of the unit cell in the given direction, $i = \{x, y, z\}$, and $n_{\mathrm{kpts},i}$ is the number of k-points along the given direction.

2.3 Summary

In this chapter is was described how the dielectric function can be calculated from a quantum mechanical approach. Single-particle electron states from Kohn-Sham DFT is used to calculate the non-interacting density response function, directly related to the dielectric function. The relation of the dielectric function to the plasmon excitations and the macroscopic absorption and EELS spectra was explained. As will be discussed in the following chapter, macroscopic approaches are not always sufficient for studying nanostructures, which are far from macroscopic. Therefore new approaches for studying plasmons in confined geometries are presented.

Chapter 3

Quantum theory of plasmon eigenmodes

One of the main contributions of this thesis is a new method for calculating and visualizing plasmon modes of nanostructures from *ab initio*, see enclosed Paper I. In Section 3.1 the motivation for developing the method and its relevance is discussed, and in Section 3.2 a more thorough derivation of the theory is given together with a description of the GPAW implementation of the method. In Section 3.3 an expression for the spatially resolved electron energy loss spectrum is derived.

3.1 Calculating the dielectric response of nanostructures

In Section 2.2 it was described how the dielectric function can be used to calculate excitation spectra of materials, such as the optical absorption spectrum and electron energy loss spectrum. The convention is to use the macroscopic dielectric function, see Eq. (2.33), that gives the averaged response over the structure. However, for the description of nanostructures that is spatially confined along one or more directions, there can be several drawbacks in using this approach.

If the super-cell used for the calculation contains vacuum, the result for the dielectric constant will depend on the amount of vacuum in the cell, since the dielectric function (or the inverse, strictly speaking) is averaged over the entire super-cell [58]. This does not change the peak positions of the spectra, but changes the magnitude of the dielectric function. A solution is to consider the response to a macroscopic perturbation, but only average the response over the volume of the structure for the definition of the dielectric constant:

$$\frac{1}{\epsilon_M(\mathbf{q},\omega)} = \frac{1}{V}\int_V d\mathbf{r} \int_{-\infty}^{\infty} d\mathbf{r}' \epsilon_{\mathbf{q}}^{-1}(\mathbf{r},\mathbf{r}',\omega), \tag{3.1}$$

where the dielectric function for a particular momentum transfer, $\mathbf{q}$, is considered.

Another challenge for the description of plasmons in nanostructures is that a material of lower dimensionality can host several types of plasmons with different symmetries. Such plasmon modes can be thought of as *eigenmodes* of the resonating electron systems. For a bulk metal there is typically only one plasmon mode, corresponding to longitudinal waves in the electron charge density (neglecting interband plasmons at higher energies). When a surface is introduced to the material, another solution associated with the surface of the metal, the surface plasmon, will emerge.

As more surfaces are introduced there will be plasmon modes that resembles standing waves of the coupled electron system, including modes with odd symmetry across the structure. The symmetry and energy of such modes can often be predicted with classical theory, such as Mie theory for the interaction of light with particles [61, 62] or semi-classical approaches such as hydrodynamic models [15, 18] for metallic structures of different spatial forms. However, as discussed in Section 1.2, a quantum mechanical description is often desirable when small length scales are involved, and for more complicated electronic structures.

The macroscopic dielectric function obtained from TDDFT is often not sufficient to capture all the plasmon resonances in nanomaterials, where modes with odd symmetry will have *zero* weight in the macroscopic loss spectra. Also, with the presence of several modes, it is difficult to distinguish between modes close in energy. As an example, the macroscopic loss spectrum of a thin film of sodium is shown in Fig. 3.1, showing two main resonances at approximately 4 and 6 eV, corresponding to the surface and bulk resonances of Na. There is a small tail on the surface plasmon peak around 5 eV, indicating the presence of an additional resonance that cannot be accessed with the macroscopic approach.

These challenges calls for new methods for the calculation of the dielectric response of nanostructures from *ab initio*, that can resolve and characterize resonances with different symmetries. This information is already present in the microscopic dielectric function, where the definition of an eigenvalue equation for the dielectric matrix makes it possible to define plasmon eigenmodes of the system, see enclosed Paper I. In the next sections a more throughout derivation of the theory is provided together with a description of the GPAW implementation.

3.2 Eigenvalue equation for the dielectric matrix

The presented method utilizes the deeper lying structure of the dielectric function, to find the plasmon eigenmodes of the system through an eigenvalue equation. Consider a system to which an external potential of the form $v_{\text{ext}}(\mathbf{r}, \omega) = v(\mathbf{r})e^{i\omega t}$ is applied. Recall that the dielectric function relates the total potential to the external potential to linear order:

$$v_{\text{ext}}(\mathbf{r}, \omega) = \int d\mathbf{r}' \epsilon(\mathbf{r}, \mathbf{r}', \omega) v_{\text{tot}}(\mathbf{r}', \omega), \tag{3.2}$$

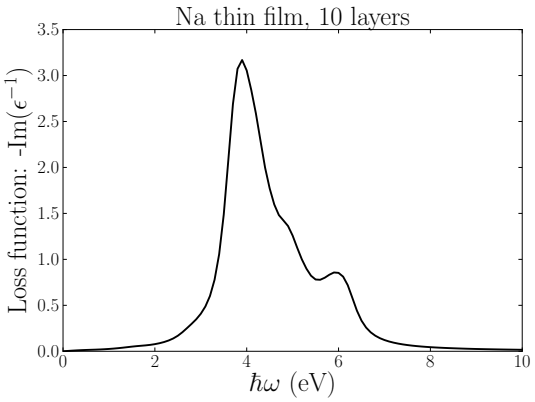

Figure 3.1: Electron energy loss spectrum of a sodium slab with 10 atomic layers. Two main resonances is seen in the spectrum, corresponding to the bulk and surface plasmon of sodium, found at approximately 4 and 6 eV respectively. An additional resonance that cannot be resolve is also seen at approximately 5 eV.

where the total potential equals the sum of the external and induced potential: $v_{\text{tot}}(\mathbf{r},\omega) = v_{\text{ext}}(\mathbf{r},\omega) + v_{\text{ind}}(\mathbf{r},\omega)$. If the external perturbation excites an eigen-resonance of the system, the response will be large compared to the perturbation: $\frac{v_{\text{tot}}(\mathbf{r}',\omega)}{v_{\text{ext}}(\mathbf{r},\omega)} \gg 1$, resulting in a small dielectric function. It is seen that in the limit $\epsilon \to 0$, a finite induced potential can exist in the limit of an infinitesimal external potential, which is used to define the criterion for having an eigen-resonances of the system:

$$\int \epsilon(\mathbf{r},\mathbf{r}',\omega)\phi_{\text{ind}}(\mathbf{r}',\omega)d\mathbf{r}' = 0, \tag{3.3}$$

where a self-sustained induced potential $\phi_{\text{ind}}(\mathbf{r}',\omega)$ exists. There can in principle exist several potentials, ϕ_{ind}, that satisfies Eq. (3.3). The equation can be solved by expressing it as an eigenvalue equation for the dielectric function in terms of the eigenvalues $\epsilon_n(\omega_n)$ and eigenvectors $\phi_n(\mathbf{r}',\omega)$:

$$\int \epsilon(\mathbf{r},\mathbf{r}',\omega_n)\phi_n(\mathbf{r}',\omega_n)d\mathbf{r}' = \epsilon_n(\omega_n)\phi_n(\mathbf{r},\omega_n), \tag{3.4}$$

where the true eigen-resonances are found for eigenvalues that satisfy: $\epsilon_n(\omega_n) = 0$.

Generally, this equation can not be exactly satisfied, due to a finite imaginary part of the eigenvalues: $\epsilon_n(\omega_n) = \text{Re}\,\epsilon_n(\omega_n) + i\Gamma_n(\omega_n)$, that accounts for the damping and screening of resonances, for example due to single-particle transitions. In terms of the inverse dielectric function, the finite imaginary part corresponds to having the poles of $\epsilon^{-1}(\mathbf{r},\mathbf{r}',\omega_n)$ in the complex frequency plane at negative imaginary frequencies. On the real frequency axis the resonances

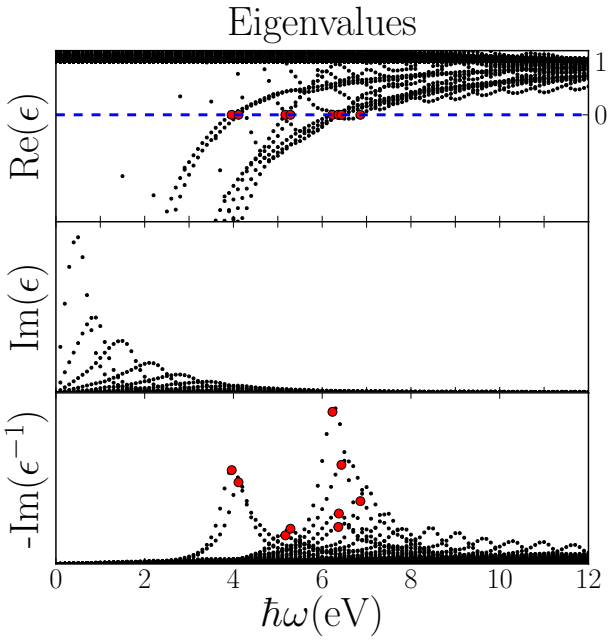

Figure 3.2: Eigenvalues of the dielectric matrix calculated for a thin film of Na (10 layers). The real part of the eigenvalues (upper panel), reveals several solutions for $\mathrm{Re}\,\epsilon = 0$ marked in red, corresponding to different plasmon eigenmodes. The imaginary part of the eigenvalues (middle panel) has peaks at the single-particle transitions that contributes to the plasmon modes. The eigenvalue loss spectrum (lower panel) has peaks at the plasmon energies, that coincides with the solutions for $\mathrm{Re}\,\epsilon = 0$ (red points) due to the low degree of damping in this material.

will give rise to peaks with a finite width. For the definition of plasmon eigenmodes we therefore require that only the real part of the eigenvalue goes to zero:

$$\mathrm{Re}\,\epsilon_n(\omega_n) = 0, \tag{3.5}$$

for the definition of a plasmon eigenmode.

3.2.1 Eigenvalue curves

The eigenvalues can be plotted as a function of frequency (ω), referred to as the eigenvalue curves or the eigenvalue spectrum. As an example, the result is shown for a 10 layer Na thin film in Fig. 3.2, the same structure as used for the macroscopic loss spectrum in Fig. 3.1. The eigenvalue spectrum is seen to form several distinct curves that evolves continuously with frequency, where some of the curves satisfy the condition $\mathrm{Re}\,\epsilon = 0$ at particular frequencies. The majority

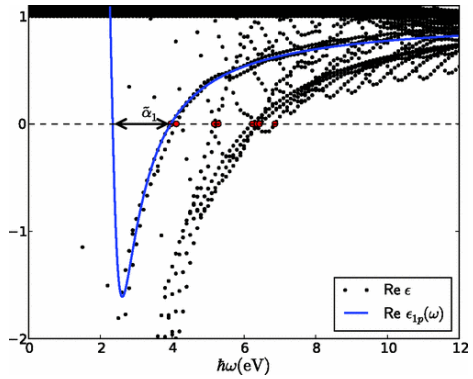

Figure 3.3: Eigenvalue curves for $\mathrm{Re}\,\epsilon$, where the single-pole model given in Eq. (3.6) has been fitted to one of the curves.

of the eigenvalues takes the value $\mathrm{Re}\,\epsilon \approx 1$, corresponding to eigenstates of the dielectric function that does not respond to external fields, and are not related to plasmon resonances. The number of eigenvalue curves is determined by the energy cutoff for the reciprocal lattice vectors, $\mathbf{G}, \mathbf{G}'$ that determines the size of the dielectric matrix, see section 3.2.4 for details on the GPAW implementation.

The eigenvalue curves fulfill the condition $\mathrm{Re}\,\epsilon = 0$ two times; Firstly when the real part crosses from positive to negative values and again when the curves recrosses to positive values (This is difficult to see in Fig. 3.2 for the first eigenvalue curves where the first crossing occurs very abruptly). A similar behavior is obtained with of a singe-pole model for the dielectric function:

$$\epsilon_{1p}(\omega) = 1 - \frac{\alpha}{\omega - \omega_0 + i\gamma}, \tag{3.6}$$

where ω_0 is the frequency for exciting single-particle transitions, γ is the damping factor and α is the strength of the plasmon mode. This form corresponds to the Lorentz dielectric function for bound charge carriers [40].

In Fig. 3.3 the single-pole model has been fitted to a chosen eigenvalue curve. The first solution to $\mathrm{Re}\,\epsilon = 0$ corresponds to the resonance at $\omega = \omega_0$ and is associated with single-particle transitions, that are also seen as peaks in the imaginary part of the eigenvalue. In this case the excitations corresponds to single-particle transitions involving the metallic bands. The second solution for $\mathrm{Re}\,\epsilon = 0$ corresponds to the plasmon resonance of the interacting electron system. This gives rise to peaks in the eigenvalue loss spectrum shown in the lower panel of Fig. 3.2.

For a low degree of damping, the zero-crossing point of the real part corresponds to the plasmon frequency and coincides with the peaks in $-\mathrm{Im}\epsilon_n^{-1}(\omega)$. When there is more damping in the system, the plasmon energy can be obtained from the condition:

$$-\mathrm{Im}\,\epsilon_n(\omega_m)^{-1} \text{ is a local maximum.} \tag{3.7}$$

From the model Eq. (3.6) it can be seen that the larger the value of α, the more the plasmon will shifted to higher energy compared to the single-particle transitions at ω_0. This is related to a high *strength* of the plasmon; there is much energy stored in the Coulomb potential that couples the charges, such that the collective excitation is found at significantly higher energy than the single-particle excitations. The magnitude of α obtained by fitting the model to the individual eigenvalue curves, can therefore be used as a measure for the plasmon strength or weight. A more general approach to find the plasmon strength in the cases where the eigenvalues is not well described by the single-pole model is to integrate the peaks in $\mathrm{Im}\,\epsilon_n^{-1}$ over a limited range of frequencies.

The symmetry and spatial form of the eigenmode solutions is given by the eigenvectors of the dielectric function, discussed in the following.

3.2.2 Spectral representation and symmetry

Since the dielectric function is non-Hermitian, the eigenvalues are complex and the eigenfunctions are non-orthogonal. Viewing the dielectric function at a particular frequency as a matrix, $\underline{\underline{\epsilon}}$, it is diagonalized by a non-singular matrix U [63]:

$$U^{-1}\,\underline{\underline{\epsilon}}\,U = D, \tag{3.8}$$

to yield the diagonal matrix, D, with the eigenvalues along the diagonal. The column vectors of U are the eigenvectors, ϕ_n, while the row vectors of the inverse, U^{-1}, consists of the dual basis eigenvectors, $(\phi^n)^*$, that satisfy the orthogonality relation: $\langle\phi^n|\phi_m\rangle = \delta_{n,m}$. When U and U^{-1} are applied to the left and right side of Eq. (3.8) respectively, the spectral representation of $\underline{\underline{\epsilon}}$ is obtained:

$$\underline{\underline{\epsilon}} = U\,D\,U^{-1}. \tag{3.9}$$

Since the dielectric function gives the response to potentials, the right side eigenvectors must correspond to electric potentials. Also it can be shown (see Appendix in Paper I) that the dual eigenvectors corresponds to charge densities, $\phi^n = \rho_n$, that are related to the potential eigenvectors through the Poisson equation:

$$\nabla^2\phi_n(\mathbf{r},\omega) = -4\pi\rho_n(\mathbf{r},\omega). \tag{3.10}$$

Thus the eigenvectors of potentials and density obtained at a particular frequency, ω_i are orthogonal to each other:

$$\langle\rho_n(\omega_i)|\phi_m(\omega_i)\rangle = \delta_{n,m}. \tag{3.11}$$

Note that plasmon eigenmodes at different frequencies does not satisfy this exactly. The dielectric function is written in spectral representation in terms of eigenvalues, and the potential and density eigenvectors:

$$\epsilon(\mathbf{r},\mathbf{r}',\omega) = \sum_n \epsilon_n(\omega)\phi_n(\mathbf{r},\omega)\rho_n^*(\mathbf{r}',\omega). \tag{3.12}$$

The eigenvectors therefore allows for direct visualization of the induced density and potential associated with the plasmon eigenmodes as described in the following section.

3.2.3 Visualizing plasmon eigenmodes

From the previous section follows that for the plasmon solutions of the eigenvalue problem in Eq. (5.9) the corresponding right and left side eigenvectors corresponds to the induced potential and density of the plasmon eigenmode respectively. This allows for the characterization of the nature of the plasmon mode, for example, if it is a bulk or surface plasmon.

As an example, the result for a thin film of Na is shown in Fig. 3.4, revealing several modes of surface and bulk character, and even or odd symmetry. The surface plasmons are split into even and odd combinations of the two surfaces, and the bulk modes are quantisized due to the final width of the slab, with an energy that increases with the number of nodes in the induced potential.

The results are discussed in more detail in the relation to plasmons in two-dimensional (2D) systems in Chapter 4. The approach has been applied to several other 2D systems, 2D heterostructures, and 1D materials.

3.2.4 GPAW implementation

The method is implemented in GPAW within the dielectric response module [48, 57]. Here, the non-symmetrized dielectric matrix is obtained in Bloch representation from the non-interacting density response function, Eq. (2.31). The eigenvalue equation in Eq. (5.9) is solved by diagonalizing the dielectric matrix:

$$\sum_{G'} \epsilon_{\mathbf{G},\mathbf{G}'}(\mathbf{q},\omega)\phi_{\mathbf{G}'}(\mathbf{q},\omega) = \epsilon_n(\mathbf{q},\omega)\phi_{\mathbf{G}}(\mathbf{q},\omega), \tag{3.13}$$

where $\mathbf{q}$ is the momentum transfer associated with the excitation. The equation is solved for each ω on the frequency grid for a given value of $\mathbf{q}$ to yield the eigenvalues $\epsilon_n(\mathbf{q},\omega_n)$ and the reciprocal space eigenvectors $\phi_{\mathbf{G},n}(\mathbf{q},\omega_n)$. The dimensions of the dielectric matrix, and thus the number of eigenvalues and -vectors, equals the number of reciprocal lattice vectors. The dual eigenvectors that corresponds to the induced density eigenfunctions, $\rho_{\mathbf{G},n}$, is obtained by inverting the matrix $\Phi_{\mathbf{G},\mathbf{G}'}$, that contains the column vectors $\phi_{\mathbf{G},n}(\mathbf{q},\omega_n)$ (the matrix corresponds to U in Eq. (3.8)).

The plasmon eigenmodes are identified as eigenvalue curves where the real part crosses from negative to positive values. Since the eigenvalues are calculated on a discrete frequency grid, the one-to-one connection of the eigenvalue points for each curve is ensured by computing the overlap of the eigenvectors at neighboring frequencies. The eigenvalues for a given frequency, ω_i is paired with the eigenvalue at ω_{i+1} that maximizes the overlap $\langle\rho_n(\omega_i)|\phi_m(\omega_{i+1})\rangle$.

The eigenvectors that corresponds to the solutions $\mathrm{Re}\,\epsilon_n(\mathbf{q},\omega_n) = 0$, are

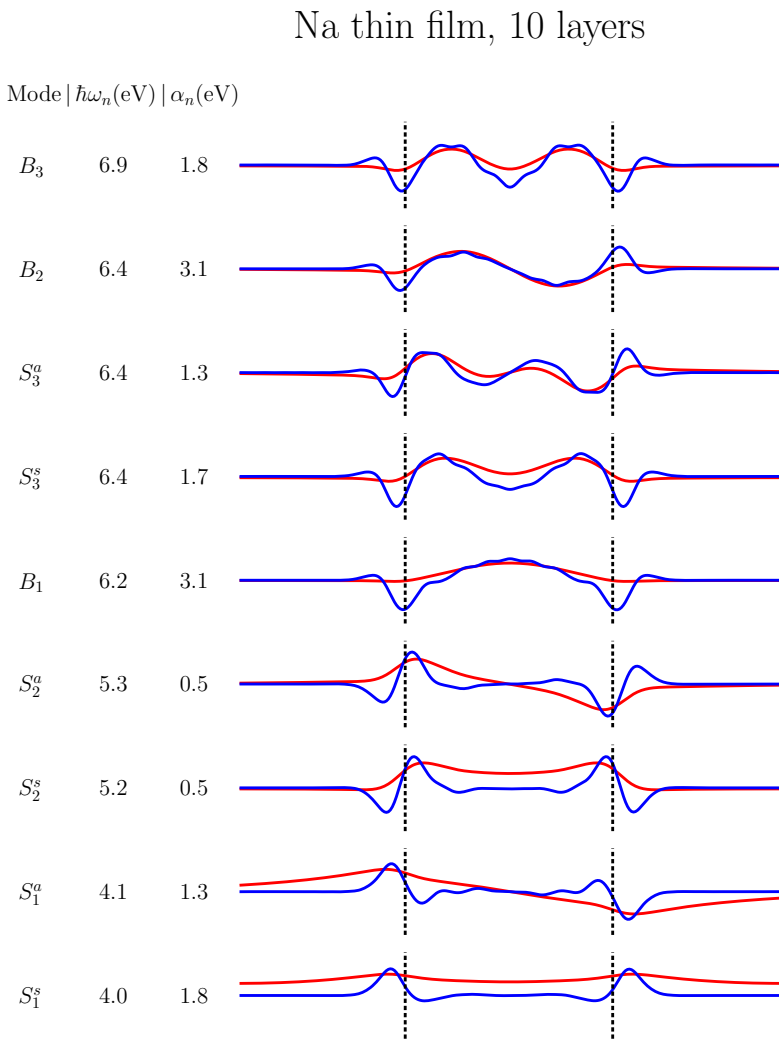

Figure 3.4: Spatial form of the induced density (blue) and induced potential (red) of the plasmon eigenmodes corresponding to each of the solutions for $\mathrm{Re}\,\epsilon = 0$ for a Na thin film, the eigenvalues shown in Fig. 3.2. The variation is plotted perpendicular to the film, where the dashed lines indicate the position of the surface atoms, and has a $\cos(q_\parallel \cdot \mathbf{r}_\parallel)$ variation parallel to the film, with $q_\parallel = 0.1\text{Å}^{-1}$. The modes are label according to surface, S, or bulk, B, character, and order, $\{1, 2, 3, ..\}$. Furthermore the surface plasmons split into symmetric and anti-symmetric combinations, labeled $\{s, a\}$.

obtained in real space as their inverse Fourier transform:

$$\phi_n(\mathbf{r},\mathbf{q},\omega_n) = \sum_{\mathbf{G}} e^{i(\mathbf{G}+\mathbf{q})\cdot\mathbf{r}}\phi_{\mathbf{G},n}(\mathbf{q},\omega_n), \tag{3.14}$$

$$\rho_n(\mathbf{r},\mathbf{q},\omega_n) = \sum_{\mathbf{G}} e^{i(\mathbf{G}+\mathbf{q})\cdot\mathbf{r}}\rho_{\mathbf{G},n}(\mathbf{q},\omega_n). \tag{3.15}$$

This yields complex-valued eigenvectors, that accounts for the time-evolution of the oscillation. The time-evolution is governed by the phase-factor $e^{i\omega_n\delta t}$, such that the rotation of the eigenvectors in the complex plane during the time δt is given by:

$$\phi_n(\mathbf{r},\mathbf{q},\omega_n,t_0+\delta t) = e^{i\omega_n\delta t}\phi_n(\mathbf{r},\mathbf{q},\omega_n,t_0). \tag{3.16}$$

Therefore the eigenvectors are rotated in the complex plane in order to minimize the imaginary part: $\mathrm{Im}\int e^{i\delta 2\pi}\phi_n(\mathbf{r})d\mathbf{r}$, which can typically be made quite small in this way.

The method has been implemented within the `DielectricFunction` module, that is used in the following manner:

```
from gpaw.response.df import DielectricFunction
df = DielectricFunction(calc='groundstate.gpw')
r, w, eigenvalues, w0, eigen0, vind, nind =\
df.get_eigenmodes(q_c=[n / nktpsX, 0, 0])
```

First, the `DielectricFunction` object is defined, where the DFT ground state calculation is given as input. Also at this stage parameters such as plane wave cutoff and the frequency grid should be defined. The method `get_eigenmodes()` is called to obtain the plasmon eigenmodes. The method takes the parameter `q_c` that represents the momentum transfer in reduced coordinates that is restricted to an integer value divided by the number of k-points in the given direction. The returned quantities are described in Table 3.1.

Table 3.1: Description of the quantities returned by `get_eigenmodes()`, return in the listed order. The shape of the arrays is given in parenthesis, where nG is the number of $\mathbf{G}$ vectors. nSol are the number of solutions to $\mathrm{Re}\,\epsilon = 0$.

`r`	real space grid, (1, n$\mathbf{r}$)
`w`	frequency grid, (nw)
`eigenvalues`	all eigenvalues of the dielectric matrix, (nw $\times$ nG)
`w0`	list of frequencies satisfying Re $\epsilon_n = 0$, (nSol)
`eigen0`	eigenvalues at Re $\epsilon_n = 0$, (nSol)
`vind`	induced potential for the solutions Re $\epsilon_n = 0$, (nSol $\times$ n$\mathbf{r}$)
`nind`	induced density for the solutions Re$\epsilon_n = 0$, (nSol $\times$ n$\mathbf{r}$)

3.3 Electron energy loss spectroscopy

As explained in the introduction, obtaining spatial information about plasmon excitations is further motivated by the advances in electron microscopy, where spatial resolution of the electron energy loss spectron (EELS) can be obtained with transmission electron microscopy (TEM) [31].

In EELS the specimen is probed by fast electrons, typically in the energy range 50 - 400 keV [32]. Upon interacting with the specimen a small fraction of the electrons loses energy and are slightly deflected from their original path, generally termed inelastic scattering. Measuring the energy loss and angular deflection of the scattered electrons provides information of the electronic excitations of the specimen. At high energy losses above approximately 100 eV, the energy loss is primary due to emission of core electrons, whereas in the low loss regime below 50 eV, also known as valence-EELS, the loss is mainly due to excitation of plasmons.

Recent advance in scanning transmission electron microscopy (STEM) has enabled the performance of EELS with a highly focused electron beam. Since the de Broglie wavelength of electrons at the relevant velocities is very small (below a tenth of an Angstrom), the electron beam can be focused to spot sizes in the order of 1 Å[32]. This allows for spatially resolved loss spectra, where the real-space form of plasmon oscillations can be measured below nm precision. This is of particular relevance to nanoparticles and nanostructures, where the losses can have spatial variation. For example the spatial form of plasmon losses has been studied in silver nanoparticles, [14], atomic defects in graphene [36], and metallic nanorods [34, 35].

The plasmon eigenmode analysis returns the eigen-resonances of the system, but does not provide information about how the modes couples to external perturbations. In order to supplement this method, an expression for the spatially resolved EELS in terms the density response function is derived.

3.3.1 Theoretical description

In the low-loss regime, the electron beam can be assumed to be a small perturbation such that the transition rate for the energy-loss process can be calculated with first order perturbation theory, i.e. Fermis golden rule [40]:

$$\frac{d\Gamma_{i\to f}}{dt}(\omega) = \frac{2\pi}{\hbar}\sum_f |\langle\psi_f|\hat{H}'|\psi_i\rangle|^2\delta(E_f - E_i - \hbar\omega), \tag{3.17}$$

here written as the general expression for the transition rate for going from the initial to final state, $\psi_{i/f}$, due to a perturbation $\hat{H}'$. In the case of an electron interacting with a specimen, the states $\psi_{i/f}$ contains both the state of the specimen and the electron. This expression can be rewritten in terms of the screened interaction $W(\mathbf{r}, \mathbf{r}', \omega)$ and a probe electron in initial and final state

$\tilde{\psi}_{i/f}(\mathbf{r})$: [51]

$$P_{i\to f}(\omega) = 2\int d\mathbf{r}\int d\mathbf{r}'\tilde{\psi}_f^*(\mathbf{r}')\tilde{\psi}_i(\mathbf{r}')\tilde{\psi}_f(\mathbf{r})\tilde{\psi}_i^*(\mathbf{r})\mathrm{Im}\,W(\mathbf{r},\mathbf{r}',\omega)\delta(E_f - E_i - \hbar\omega), \tag{3.18}$$

where $P_{i\to f}$ is the probability for the electron to exchange energy, ω, with the sample. The screened interaction is related to the density response function, χ, through:

$$W(\mathbf{r},\mathbf{r}',\omega) = \int d\mathbf{r}_1\int d\mathbf{r}_2\frac{\chi(\mathbf{r}_1,\mathbf{r}_2,\omega)}{|\mathbf{r}-\mathbf{r}_1||\mathbf{r}'-\mathbf{r}_2|}. \tag{3.19}$$

To simplify the treatment in the following, the probe electron is described as a point charge that moves at constant velocity, thus we are not considering the wavefunction of the incoming electron. Instead we use an expression solely in terms of the potential associated with the electron. In terms of external potential, ϕ_{ext} the probability becomes:

$$P(\omega) \propto \mathrm{Im}\int\int d\mathbf{r}d\mathbf{r}'\phi_{ext,f}(\mathbf{r},\omega)\,\chi(\mathbf{r},\mathbf{r}',\omega)\phi_{ext,i}(\mathbf{r}',\omega). \tag{3.20}$$

Here, the density response function can be obtained from linear response theory.

In order to describe the case of spatially resolved EELS, we use an external potential of a point charge moving with velocity $\boldsymbol{v}_e$ at position $\mathbf{R}_e(t) = \mathbf{r}_0 + \boldsymbol{v}_e t$, that hits the sample in $\mathbf{r}_0$:

$$\phi_{ext}(\mathbf{r},t) = \frac{1}{|\mathbf{r}-\mathbf{R}_e(t)|}. \tag{3.21}$$

3.3.2 Plane wave representation

In the following an expression for Eq. (3.20) in terms of the density response function in plane wave representation is derived. The Fourier transform of the external potential is given by the usual $1/\mathbf{G}^2$ form of the Coulomb potential, translated by $\mathbf{R}_e(t)$:

$$\phi_{ext}(\mathbf{G},t) = \int d\mathbf{r}\frac{1}{|\mathbf{r}-\mathbf{R}(t)|}e^{-i\mathbf{G}\cdot\mathbf{r}} = \frac{4\pi}{\mathbf{G}^2}e^{-i\mathbf{G}\cdot\mathbf{R}_e(t)}, \tag{3.22}$$

and the Fourier transform to ω-space is given by:

$$\phi_{ext}(\mathbf{G},\omega) = \int dt\frac{4\pi}{\mathbf{G}^2}e^{-i\mathbf{G}\cdot\mathbf{r}_0}e^{i(\omega-\mathbf{G}\cdot\boldsymbol{v}_e)t} = \frac{4\pi}{\mathbf{G}^2}e^{-i\mathbf{G}\cdot\mathbf{r}_0}\delta(\omega-\mathbf{G}\cdot\boldsymbol{v}_e). \tag{3.23}$$

Thus the external potential can be written as a sum of Fourier components with wavevector $\mathbf{G}$:

$$\phi_{ext}(\mathbf{r},\omega) = \sum_{\mathbf{G}}\frac{4\pi}{\mathbf{G}^2}e^{i\mathbf{G}\cdot(\mathbf{r}-\mathbf{r}_0)}\delta(\omega-\mathbf{G}\cdot\boldsymbol{v}_e). \tag{3.24}$$

It can be assumed that the relative changes in energy and momentum upon interacting with the sample is small, such that the electron moves with uniform

velocity in the medium. In principle the outgoing beam is slightly deflected, where the total energy and momentum of the electrons in the specimen and the beam must be conserved.

Inserting the above relation in Eq. (3.20) together with the relation for the inverse Fourier transform of $\chi_{\mathbf{G}\mathbf{G}'}(\mathbf{q},\omega)$ given in Eq. (2.28), yields the probability for energy loss with the beam hitting the sample at position $\mathbf{r}_0$:

$$P(\mathbf{r}_0,\omega) \propto \mathrm{Im} \int\int d\mathbf{r}d\mathbf{r}' \sum_{\mathbf{G}_1} \frac{4\pi}{\mathbf{G}_1^2} e^{i\mathbf{G}_1\cdot(\mathbf{r}-\mathbf{r}_0)} \delta(\omega - \mathbf{G}_1\cdot\boldsymbol{v}_e)$$
$$\sum_{\mathbf{q}}^{\mathrm{BZ}} \sum_{\mathbf{G}\mathbf{G}'} e^{i(\mathbf{q}+\mathbf{G})\cdot\mathbf{r}} \chi_{\mathbf{G}\mathbf{G}'}(\mathbf{q},\omega) e^{-i(\mathbf{q}+\mathbf{G}')\cdot\mathbf{r}'} \sum_{\mathbf{G}_2} \frac{4\pi}{\mathbf{G}_2^2} e^{i\mathbf{G}_2\cdot(\mathbf{r}'-\mathbf{r}_0)} \delta(\omega - \mathbf{G}_2\cdot\boldsymbol{v}_e). \tag{3.25}$$

The integration over $(\mathbf{r},\mathbf{r}')$ gives the delta functions: $\int d\mathbf{r} e^{i(\mathbf{G}_1+\mathbf{q}+\mathbf{G})\cdot\mathbf{r}} = \delta_{\mathbf{G}_1,-(\mathbf{q}+\mathbf{G})}$, $\int d\mathbf{r}' e^{i(\mathbf{G}_2-(\mathbf{q}+\mathbf{G}))\cdot(\mathbf{r}')} = \delta_{\mathbf{G}_2,(\mathbf{q}+\mathbf{G})}$, such that a simplified, general expression for the energy loss probability can be obtained:

$$P(\mathbf{r}_0,\omega) \propto \mathrm{Im} \sum_{\mathbf{q}}^{\mathrm{BZ}} \sum_{\mathbf{G}\mathbf{G}'} e^{i(\mathbf{q}+\mathbf{G})\cdot\mathbf{r}_0} \frac{4\pi}{|\mathbf{q}+\mathbf{G}|^2} \chi_{\mathbf{G}\mathbf{G}'}(\mathbf{q},\omega) \frac{4\pi}{|\mathbf{q}+\mathbf{G}'|^2} e^{-i(\mathbf{q}+\mathbf{G}')\cdot\mathbf{r}_0}$$
$$\delta\big(\omega + (\mathbf{q}+\mathbf{G})\cdot\boldsymbol{v}_e\big)\, \delta\big(\omega - (\mathbf{q}+\mathbf{G}')\cdot\boldsymbol{v}_e\big). \tag{3.26}$$

It is seen that the expression is basically the imaginary part of the inverse Fourier transform of the screened interaction:

$$W_{\mathbf{G},\mathbf{G}'}(\mathbf{q},\omega) = \frac{4\pi}{|\mathbf{q}+\mathbf{G}|^2} \chi_{\mathbf{G}\mathbf{G}'}(\mathbf{q},\omega) \frac{4\pi}{|\mathbf{q}+\mathbf{G}'|^2}, \tag{3.27}$$

at the beam position, $\mathbf{r}_0$

3.3.3 Normal beam

The equation can be simplified further by assuming a thin specimen with a finite extend in the (x,y)-plane that is probed by a normal beam with a velocity in the z-direction: $\boldsymbol{v}_e = \hat{\mathbf{e}_z} v_e$. The delta function $\delta\big(\omega-(\mathbf{q}+\mathbf{G}')\cdot\boldsymbol{v}_e\big)$ in Eq. (3.28), will then only involve the z-component of $\mathbf{q}+\mathbf{G}'$. Since the velocity of the electrons in TEM is typically very large, it is a valid assumption that ω/v_e is sufficiently small so that only the $G_z' = 0$ components couples to the beam, which also restricts q to the plane of the material, $\mathbf{q} = \mathbf{q}_\parallel$. The same argument can be applied to set $G_z = 0$, such that Eq. (3.28) can then be simplified to:

$$P(\mathbf{r}_0,\omega) \propto \mathrm{Im} \sum_{\mathbf{q}_\parallel}^{\mathrm{BZ}} \sum_{\mathbf{G}_\parallel\mathbf{G}'_\parallel} e^{i(\mathbf{q}_\parallel+\mathbf{G}_\parallel)\cdot\mathbf{r}_0} \frac{4\pi}{|\mathbf{q}_\parallel+\mathbf{G}_\parallel|^2} \chi_{\mathbf{G}_\parallel\mathbf{G}'_\parallel}(\mathbf{q}_\parallel,\omega)$$
$$\frac{4\pi}{|\mathbf{q}_\parallel+\mathbf{G}'_\parallel|^2} e^{-i(\mathbf{q}_\parallel+\mathbf{G}'_\parallel)\cdot\mathbf{r}_0}. \tag{3.28}$$

In practice the scattered electrons will be deflected at different angles, depending on the amount of momentum transferred to the specimen. Thus collecting scattered electrons at a particular angle, at a given energy loss, makes it possible to obtain the momentum-resolved and spatially resolved loss spectrum. This can be done by moving the collection aperture away from the majority signal [64], where a disadvantage of such an approach is that the strength of the signal will be greatly reduced.

3.4 Summary

In this chapter it was shown how plasmons in nanostructures can be obtained and visualized from a quantum mechanical approach. In the following chapters the eigenmode analysis is applied to different structures, where quantum mechanical effects are found to play a large role for the systems studied. As an additional tool for visualizing the response, an expression for the spatially resolved EELS was obtained. This has been applied to the study of thin metal films in Chapter 4, and edge states of an MoS_2 nanoribbon in Chapter 6.

Chapter 4

Plasmons in 2D materials

Plasmons in two-dimensional (2D) materials are of large interest for plasmonic application, where for example graphene plasmonics has emerged as a field of its own [23, 21, 22]. In this Chapter the methods described in Chapter 3 for calculating and visualizing plasmons in nanostructures is applied to study different 2D systems, including thin metal films and metallic transition metal dichalcogenides. As will be shown in the following, the plasmon in 2D behaves qualitatively and quantitatively different than plasmons in bulk materials. Also, quantum mechanical effects such as electron spill-out and band-structure effects are shown to play a large role for the plasmons in the studied systems.

4.1 General properties of plasmons in 2D

In bulk (3D) metals the plasmon has a finite energy in the long-wavelength limit, $q \to 0$, in spite of being a longitudinal wave [49], see for example Eq. (2.24). This reflects the long-ranged nature of the Coulomb interaction between electrons, that can maintain collective behaviour over large distances in 3D. For comparison, the energy of longitudinal phonon modes, where there is no long-range coupling, goes to zero in the long-wavelength limit. The finite energy and strength of the plasmon for $q \to 0$ also emerges from the RPA expression for the dielectric function:

$$\epsilon(\mathbf{q}, \omega) = \mathrm{I} - V(\mathbf{q})\chi^0(\mathbf{q}, \omega), \tag{4.1}$$

where local field effects are neglected in Eq. (4.1). For small q the non-interacting density response function, χ^0, is proportional to q^2 [65]. The scaling can for example be seen from applying $\mathbf{k} \cdot \mathbf{p}$ perturbation theory to the charge density matrices, that enters in the expression for χ^0 in Eq. (2.29).

$$\langle \psi_{n\mathrm{k}}(\mathbf{r}) | e^{i\mathbf{q}\cdot\mathbf{r}} | \psi_{n'\mathrm{k}+\mathbf{q}}(\mathbf{r}) \rangle_{\mathbf{q}\to 0} = -i\mathbf{q} \cdot \frac{\langle \psi_{n\mathrm{k}}(\mathbf{r}) | \nabla | \psi_{n'\mathrm{k}}(\mathbf{r}) \rangle}{\epsilon_{n'\mathrm{k}} - \epsilon_{n\mathrm{k}}}, \quad \text{for } n \neq n' \tag{4.2}$$

where a factor of q is obtained for each of the two terms, leading to a q^2 dependence of χ^0. Expression 4.2 only applies to interband transitions, and for metals the intraband contributions must also be considered. In this case also a q^2 dependence is also obtained for finite frequencies[1] [65, 66].

The divergence of the Coulomb potential, $V_{3D}(q) = \frac{4\pi}{q^2}$, exactly cancels the q-dependence in the product $V\chi^0$, which goes towards a constant value. Therefore ϵ can take a value different from one so that it is possible to satisfy $\epsilon_{3D}(q \to 0, \omega_p) = 0$, thus meeting the criterion for a having a plasmon resonance.

Also for the surface-plasmon, that exist on the surface of a semi-infinite material, the Coulomb potential is sufficiently strong to sustain a finite plasmon energy for low q, leading to the limit $\omega_s(q = 0) = \omega_p/\sqrt{2}$. (Not to be confused with the surface plasmon polariton that goes to zero as $\omega_s = qc$ in the retarded regime[51]).

For a 2D metal the behavior is qualitatively different, since the Coulomb potential in this case is equal to $V_{2D}(q) = \frac{2\pi}{q}$. This means that in the long wavelength limit, the product $V\chi^0$ goes to zero, so that the dielectric function is unity:

$$\epsilon_{2D}(q \to 0) = 1. \tag{4.3}$$

Therefore the 2D plasmon will have energy and weight that goes to zero for $q \to 0$. For the 2D homogeneous electron gas the plasmon dispersion relation for low q has been shown to be [67]:

$$\omega_{2D}^2(q \to 0) = \frac{ne^2}{2m_e^*\epsilon_0}q + \frac{3v_F^2}{8\pi\epsilon_0}q^2, \tag{4.4}$$

giving a $\sqrt{q}$ dependence of the leading term. This means that the 2D plasmon energy can be tuned with the value of q, opposed to the bulk and (nonretarded) surface plasmon that has an almost constant energy in the low-q regime.

For 2D insulators the weakening of the Coulomb potential for $q \to 0$ means that the ability of electrons to screen external or internal charges is greatly reduced. This can lead to a large increase in exciton binding energies, as found for monolayer MoS_2 [68]. This 2D transition of layered semiconductors is explored further in Chapter 5.

4.2 Thin metal films

In this Section the properties of plasmons in thin metal films are studied. This type of system serve as quasi 2D metal with a finite width. Here the role of quantum effects and spatial confinement can be studied, while the results can be compared to classical models for the plasmon energy. This system is also useful to evaluate the performance of the eigenmode analysis presented in the previous chapter, since the introduction of surfaces leads to the presence of several plasmon eigenmodes.

[1] Note that this does not hold in the static limit ($\omega = 0$) where χ^0 is constant at low q, which leads to a $1/q^2$ divergence of the dielectric function in 3D [40].

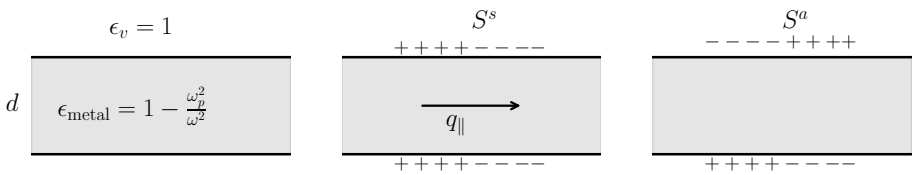

Figure 4.1: Classical model for the surface plasmons in a thin metal film, yielding a symmetric, S^s, and anti-symmetric, S^a, surface plasmon, where the sign of the induced charge on the two surfaces are in and out of phase respectively. The energy-dispersion of the modes with the parallel momentum transfer, $q_\parallel$ is given in Eq. (4.5)

4.2.1 Classical model

A classical expression for the energy versus q-dispersion of the surface plasmons in metal films can be derived. Consider a metal film of width, d, and a Drude form of the dielectric function within the metal, $\epsilon_M = 1 - \omega_p^2/\omega^2$. The interfaces with vacuum is abrupt where $\epsilon_v = 1$, see Fig. 4.1. In this case the induced density of the surface plasmon is a delta function at the surface. Solving Laplace's equation, $\nabla^2\phi = 0$, for the two regions and matching the electric fields at the surface, leads to two solution for the surface plasmons of the film [69]:

$$\omega_{a/s}(q_\parallel d) = \omega_p \left(\frac{1 \pm e^{-q_\parallel d}}{2} \right)^{\frac{1}{2}}. \tag{4.5}$$

The plasmon frequencies are written in terms of the bulk plasmon frequency, ω_p, and the product of the in-plane momentum transfer and the width of the film, $q_\parallel d$. Since the potential associated with the surface plasmon decays as e^{-qz} perpendicular to the surface, the surfaces will be coupled to a higher extend for low q or small d. The two plasmon modes corresponds to the symmetric, in-phase, oscillation of the two surfaces, and the anti-symmetric out-of phase oscillation of the two surfaces, see Fig. 4.1. In the long wavelength limit the symmetric mode goes to zero as: $\omega_s(q_\parallel) = \omega_p \sqrt{\frac{q_\parallel d}{2}}$, while the anti-symmetric mode approaches the bulk plasmon frequency as: $\omega_a(q_\parallel) = \omega_p \sqrt{1 + \frac{q_\parallel d}{2}}$. The energy curves obtained from this model is plotted together with quantum results in Fig. 4.4.

4.2.2 *Ab initio* calculations for sodium thin films

The theoretical approach for calculating plasmon eigenmodes in nanostructures, described in Chapter 3, was applied to the study of thin metal films and published in Paper I. In this Section the results are discussed in further detail in relation to plasmons in 2D systems.

Ab initio calculations were performed for thin slabs of sodium (Na), with the number of atomic layers equal to: $3, 6, 10$ and 20, corresponding to slab widths

of 6.3, 12.6, 21 and 42 Å respectively. Since Na is a simple metal with close to free-electron like behavior, this system can be used to investigate quantum size effects on the surface plasmons by comparing to the classical model described above.

Plasmon eigenmodes

The eigenvalues of the dielectric matrix for a 10 layer film was presented in Fig. 3.2, and yielded several solutions for $\mathrm{Re}\,\epsilon = 0$. The modes for a 20 layer slab is shown in Fig. 4.2, with the induced potential and density shown in red and blue respectively. The modes have been labeled according to character, where S and B refers to surface and bulk modes respectively. Symmetry is indicated by s/a, and the order by integers $\{1, 2, 3, ..\}$. The modes are plotted for increasing energy from bottom to top, where two lowest energy solutions is the symmetric and anti-symmetric first-order surface plasmons, S_1^s, S_1^a, also found by the classical model. Here the induced density of the surface modes is seen to be located just outside the surface.

In addition to the first order surface plasmon, our quantum approach predicts the presence of two higher order surface plasmons, S_2 and S_3, that also split in a symmetric and anti-symmetric combinations. Our finding of a second order mode is in good agreement with previous theoretical and experimental findings. Tsuei et al. [70] observed an additional peak in the electron energy loss spectrum of Na at roughly 5 eV for off-specular scattering. The theoretical prediction of such mode for simple metals was first given by Bennet [71] using a hydrodynamical model with a diffuse density distribution at the surface, a finding later supported by TDDFT calculation for Jellium slabs [72]. This mode, situated at $\omega \approx 0.8\omega_p$, has been named the multipole surface plasmon, since the charge density was found to integrate to zero normal to the surface. For the second order surface mode found in this study, S_2, the induced density is also found to integrate to zero perpendicular to the film, which is not the case for the first order mode. It was previously argued that this mode is only found theoretically when the spill-out of electrons from the surface is taken into account, as is also done in this case.

For the S_2 mode it is also observed that the peak in the induced density is spatially shifted closer to the surface. Interestingly, we predict from our quantum description the existence of an additional, weak subsurface mode, here termed S_3. This mode is found at roughly same energy as the bulk plasmon mode, why it will be difficult to observe in the normal loss spectra.

However, we find that the S_2 mode is visible the theoretical spatially resolved loss spectra, Fig. 4.3, shown as a contour plot in energy and probe position, z, perpendicular to the film. The spectrum is calculated as inverse Fourier transform of the screened interaction, $W_{\mathbf{G},\mathbf{G}'}(\mathbf{q},\omega) = \frac{4\pi}{|\mathbf{q}+\mathbf{G}|^2}\chi_{\mathbf{G}\mathbf{G}'}(\mathbf{q},\omega)\frac{4\pi}{|\mathbf{q}+\mathbf{G}'|^2}$, in the coordinate z_0, see Eq. (3.28). Again the surface plasmon at approximately 4 eV is seen to be localized outside the surface, while the weight of the bulk resonances just above 6 eV is largest below the third atomic layer. A separate weak resonance, corresponding to the S_2 mode, can be distinguished in the

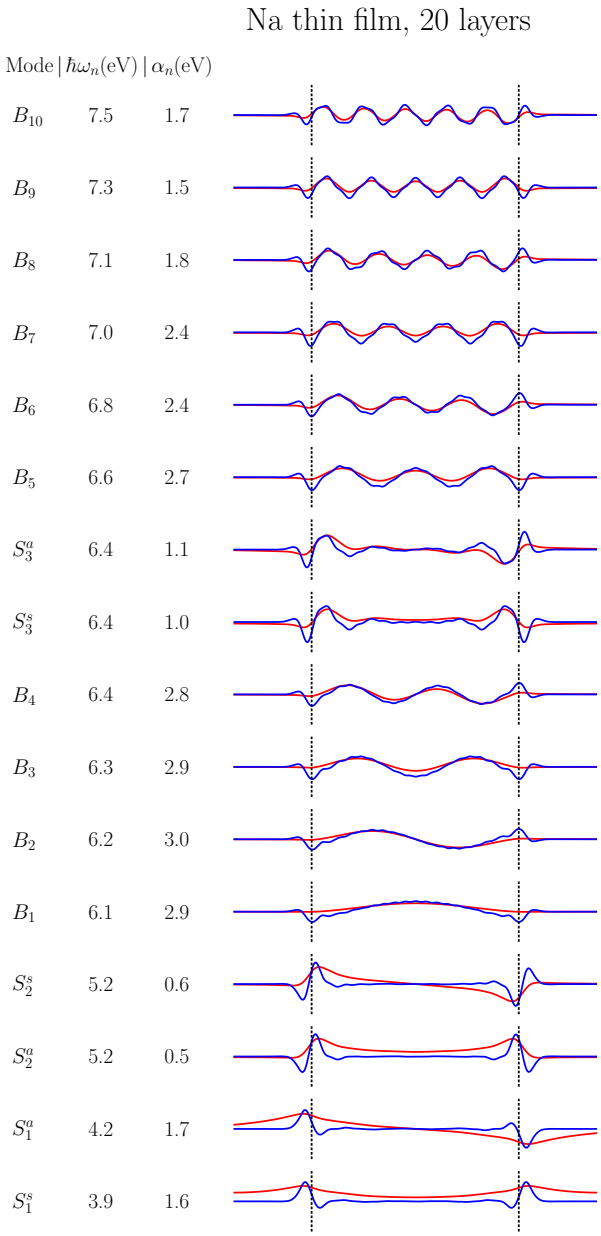

Figure 4.2: Plasmon eigenmodes of a Na thin film with 20 atomic layers. The modes have been labeled according to character, where S and B refers to surface and bulk modes respectively, s/a refers to symmetric/anti-symmetric, and the integers $\{1, 2, 3, ...\}$ represents the order of the mode. The energy, $\hbar\omega_n$, and strength, α_n, is also given for each mode.

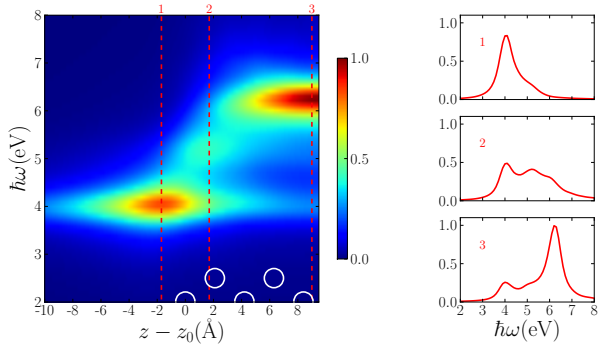

Figure 4.3: (a) Spatially resolved electron energy loss spectrum of a 10 layer film at $q_\parallel = 0.1\text{Å}^{-1}$, shown as a contour plot on the z-axis and the energy axis, revealing the extend of the modes in space and energy. (b) The loss spectrum obtained at three different positions, outside the surface (1), just below the surface (2) and in the middle of the film (3).

spectrum, localized just below the surface between the first and second atomic layer.

Surface plasmon dispersion

In Fig. 4.4 the dispersion of the energy with parallel momentum transfer of the regular surface plasmon modes are compared quantitatively to the classical result from Eq. (4.5). Since the degree of coupling between the two surfaces is directly related to the slab width, the thinner films produce a larger splitting of the modes at a given $q_\parallel$. The symmetric, S_1^s, mode goes to zero for $q_\parallel \to 0$ as expected for a 2D plasmon, and is in good agreement with the classical model, also for very thin film thicknesses. For larger $q_\parallel$ the quantum result continues to increase in energy, due to the wave-vector dependence of the surface plasmon mode, whereas the classical model neglects the spatial non-locality and converges towards classical surface plasmon energy $\omega_p/\sqrt{2}$.

The quantum result for the anti-symmetric mode S_1^a, on the other hand, shows large deviation from the classical model, also in the $q_\parallel \to 0$ limit. Here the energy is increasingly downshifted compared to the classical result with decreasing width of the film. While the classical result converges to the bulk plasmon frequency, ω_p, the quantum result appears to converge towards a lower energy. This disagreement is not due to the neglect of non-locality in the classical model; including only this effect should produce a blue-shift of the plasmon resonance due to the confinement.

When reaching the atomic-scale regime, our results show that another quantum effect play a larger role. We attribute the deviation to the electron-spill out from the surfaces, where the relative effect on the plasmon increases with

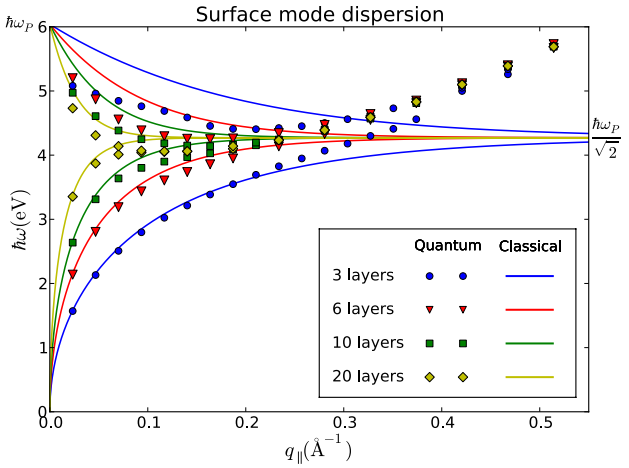

(a)

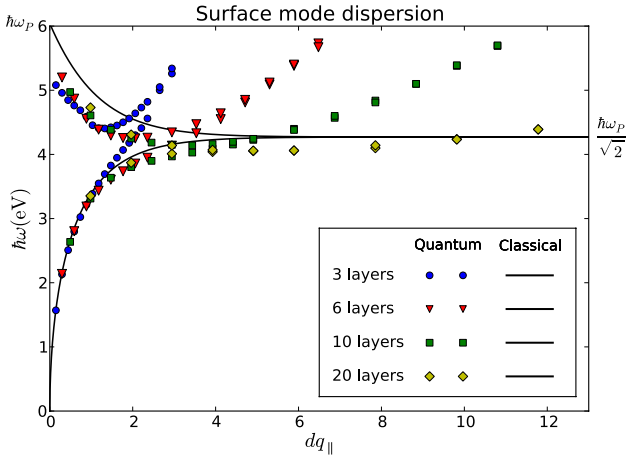

(b)

Figure 4.4: (a) Energy dispersion of the surface plasmon eigenmodes of Na thin films plotted as a function of in-plane momentum transfer, $q_\parallel$, for different number of layers, and compared to the classical result (solid lines). The lower and upper branch corresponds to the S_1^s and S_1^a mode respectively, visualized in Fig 4.2. (b) Same results as in (a) plotted against the dimensionless parameter $q_\parallel d$, where the classical result is independent of film thickness.

decreasing film thickness. The spill-out leads to a decrease in the free-electron density, which is expected to give a decrease in plasmon energy; exactly as observed for the anti-symmetric mode. The surface plasmon energy dispersion has also been plotted versus the dimensionless parameter, $q_{\parallel}d$, see Fig. 4.4b, from where it appears that for a 20 layer film, corresponding to a width of approximately 4 nm, the antisymmetric mode has not yet converged to the classical result.

The red-shift of the antisymmetric resonance with decreasing particle size contradicts the observed blue-shift in the surface plasmon resonance of silver nanoparticles compared to classical models [13, 14]. However, this effect stems from the more complicated response of noble metals as discussed in the next subsection.

4.2.3 Silver thin films

In order to study plasmons in non-simple metals, the *ab initio* approach was also applied to study thin films of silver (Ag). Silver is a noble metal and the best performing candidate for plasmonic applications, due to a very low degree of damping at optical frequencies [73]. The behavior of plasmons in Ag is qualitatively different than for simple metals, since the occupied d-states of Ag, located approximately 4 eV below the Fermi level, gives rise to single-particle transitions that couples to the plasmons [74]. For example this leads to a surface plasmon resonance that is shifted from approximately 6.3 eV (calculated from the free-electron density) down to a value of 3.7 eV found experimentally. In Fig. 4.5 the macroscopic loss function is plotted for an 18 layer film together with the single-particle spectrum given by $\mathrm{Im}\chi^0$. For the calculations on Ag, the GLLB-SC exchange-correlation functional [75] was used, since this has been found to give an improved description of the d-states [74]. In the response calculation an energy cutoff of (50, 50, 100) eV was used, and unoccupied bands were included 35 eV above the Fermi level.

In Fig. 4.6 the eigenvalue curves for Na and Ag films of similar widths are compared. The presence of interband transitions around 4 eV clearly affects the eigenvalue curves, such that for Ag the two curves associated with the surface plasmon resonances are split into two peaks at approximately 3.8 and 7.5 eV. Here, the eigenmode analysis allows us to identify both peaks as the surface plasmon. The effect, that a localized resonance can split a single plasmon resonance into two peaks, is conceptually similar to the Newns-Anderson model for chemisorption of atoms and molecules on metal surfaces. Here, energetically localized d-states in the metal leads to splitting of the chemisorption levels into bonding and anti-bonding states [76, 77].

As argued by Liebsch et. al [11], the observed blue-shift of the localized surface plasmon resonance (LSPR) of silver nanoparticles with decreasing particle size can be explained by a size-dependent degree of coupling of the surface plasmon to the $4d \rightarrow 5s$ transitions that are localized within the surface. For smaller particles the LSPR is to a higher extent localized outside the surface, leading to a reduced screening of the plasmon and a resulting blue-shift of the

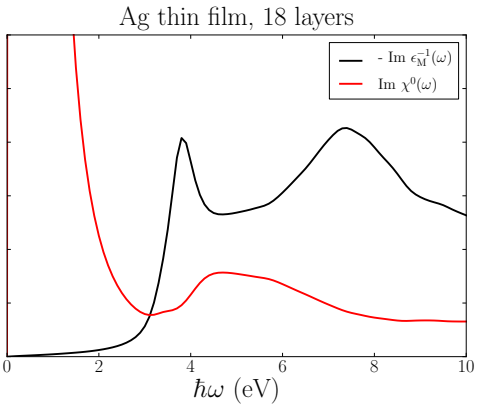

Figure 4.5: Macroscopic loss spectrum (black) of a 18 layer Ag film with a width of approximately 4 nm. The single-particle spectrum $\mathrm{Im}\,\chi^0(\omega)$ is also shown (red), and is seen to have a small peak at 4-6 eV, due to transitions from the occupied 4*d*-states. The effect of these transitions is to shift the surface plasmon down from a classical value of 6.3 eV to below 4 eV.

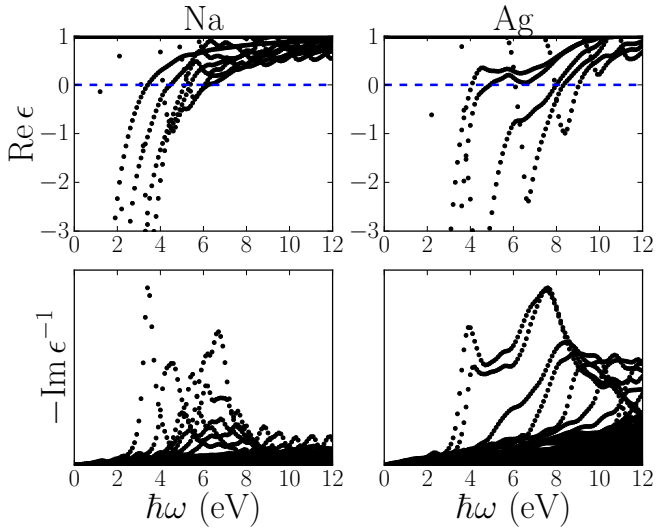

Figure 4.6: Comparison of the eigenvalue curves of 6 layer Na(110) and Ag(111) thin films. In both cases the two first solutions for $\mathrm{Re}\,\epsilon = 0$ corresponds to the symmetric and antisymmetric surface plasmon. The result for Ag looks qualitatively different due to the coupling to the $4d \rightarrow 5s$ transitions.

energy.

The enhanced screening below the surface can also explain why we do not find any higher order surface plasmons for Ag; Since these resonances are localized further within the surface they are screened to a higher extend that the case of Na.

4.3 Plasmons in metallic transition metal dichalcogenides

In this Section, plasmons in monolayer metallic transition metal dichalcogenides (TMDCs), which is particular type of 2D material, is studied. Since the discovery of the 2D semi-metal graphene[19] there has been a large interest in other 2D materials, leading to the extraction of monolayer hexagonal boron nitride [78] and MoS_2 [20].

TMDCs is a class of materials with the chemical formula MX_2, where M is a transition metal, and X is a chalcogen, i.e., a group 16 element such as S, Se and Te. They exist in bulk as layered materials that consists of 2D crystals coupled by weak and dispersive van der Waals forces. From here the individual layers can be extracted, similarly to how graphene in obtained from graphite. Even though semiconducting TMDCs such as MoS_2 have received most attention due to their potential for atomic scale transistors and their light-emitting properties, metallic monolayer TMCDs such as $TaSe_2$ have also been extracted [28]. Due to the presence of a metallic band with a finite density of states at the Fermi level of these materials, intrinsic 2D plasmons will be present in the absence of doping. As will be presented in the following, the quantum mechanical behavior of the electrons has a large impact of the plasmon in these materials.

In the attached Paper II, our study of six metallic TMDCs in monolayer form is presented. Metallic structures were obtained by choosing transition metals from group 5, where the valence is decreased by one with respect to Mo and W. This leads to the presence of a half-filled band that stems from hybridization of the d-state of the transition metal with the p_z states of the chalcogen. In the presented study we have investigated TMDC consisting of the metals: $\{V, Nb, Ta\}$ and the chalcogens: $\{S, Se\}$, leading to six different combinations.

We find that the electronic structure is very similar for these six materials; see Fig. 4.7 showing the electronic bandstructure for VS_2 and $TaSe_2$. Both materials have a metallic band with a bandwidth of approximately 1 eV, and with the remaining bands producing a gap of approximately 2.5 - 3 eV. As a general trend, we observe a small increase in bandwidth and energy gap with increasing size of the transition metal, going from V to Ta.

For the study of plasmons in the monolayer structures, the electron energy loss spectrum was calculated from the macroscopic dielectric constant ϵ_M:

$$\mathrm{EELS}(\mathbf{q},\omega) = -\mathrm{Im}\epsilon_M^{-1}(\mathbf{q},\omega), \tag{4.6}$$

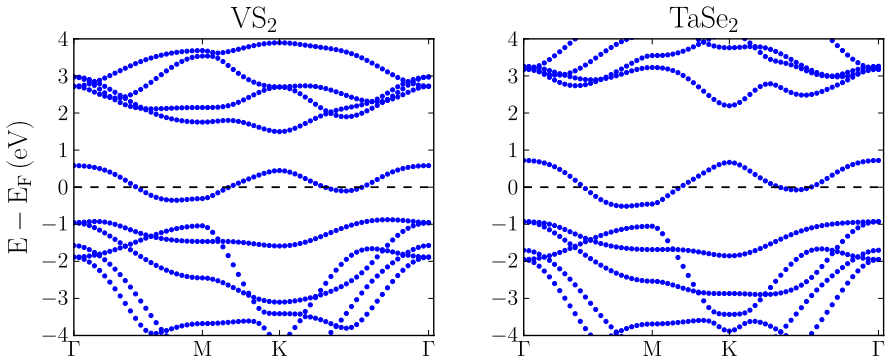

Figure 4.7: Bandstructure of VS_2 and $TaSe_2$, illustrating the very similar electronic properties. Both structures are metallic due to the half-filled electronic bands crossing the Fermi level.

which yielded the same result as the eigenmode analysis for the plasmon modes, since for the monolayer structures only a single mode with even symmetry across the slab was found to exist at low energy. An example of an electron energy loss spectrum is shown in Fig. 1 (right panel) in Paper II, for a range of parallel momentum transfers. As the plasmon energy increases, the spectral weight of the plasmon peak decreases significantly. This behavior is repeated for the other materials, as shown in Fig. 4.8, where the plasmon energy reaches a plateau for large momentum transfers as the strength continues to decrease. The calculated dispersions are in good agreement with a similar ab initio study on $NbSe_2$ and TaS_2 [27].

The plasmon energy is observed to increases with the size of the transition metal, producing a clear trend. For example, values of approximately 0.7 eV and 1.1 eV are reached for VS_2 and TaS_2 respectively. This result contradicts the trend one would expect from a classical treatment, where the plasmon energy should be proportional to the square-root of the free-electron density, $\omega_p \propto \sqrt{n}$. Since the heavier species have larger in-plane lattice constants, but the same number of metallic electrons per atom, the density of the metallic electrons is lower for TaS_2 than for VS_2, which should result in a lower plasmon frequency.

This behavior is not observed, since the plasmon resonances at larger q are largely dominated by screening and damping by interband transitions, as observed for the Ag thin films. This conclusion follows from our detailed analysis, where the density response function is divided into two parts originating from the intra- and interband transitions respectively:

$$\chi^0_{\mathbf{G},\mathbf{G}'}(\mathbf{q},\omega) = \chi^{0,\mathrm{Intra}}_{\mathbf{G},\mathbf{G}'}(\mathbf{q},\omega) + \chi^{0,\mathrm{Inter}}_{\mathbf{G},\mathbf{G}'}(\mathbf{q},\omega). \tag{4.7}$$

In practice the intraband part is calculated by only including the single metallic band in the response calculations, since this is the only contribution to intraband transitions. This returns the unscreened plasmon, and allows for comparison

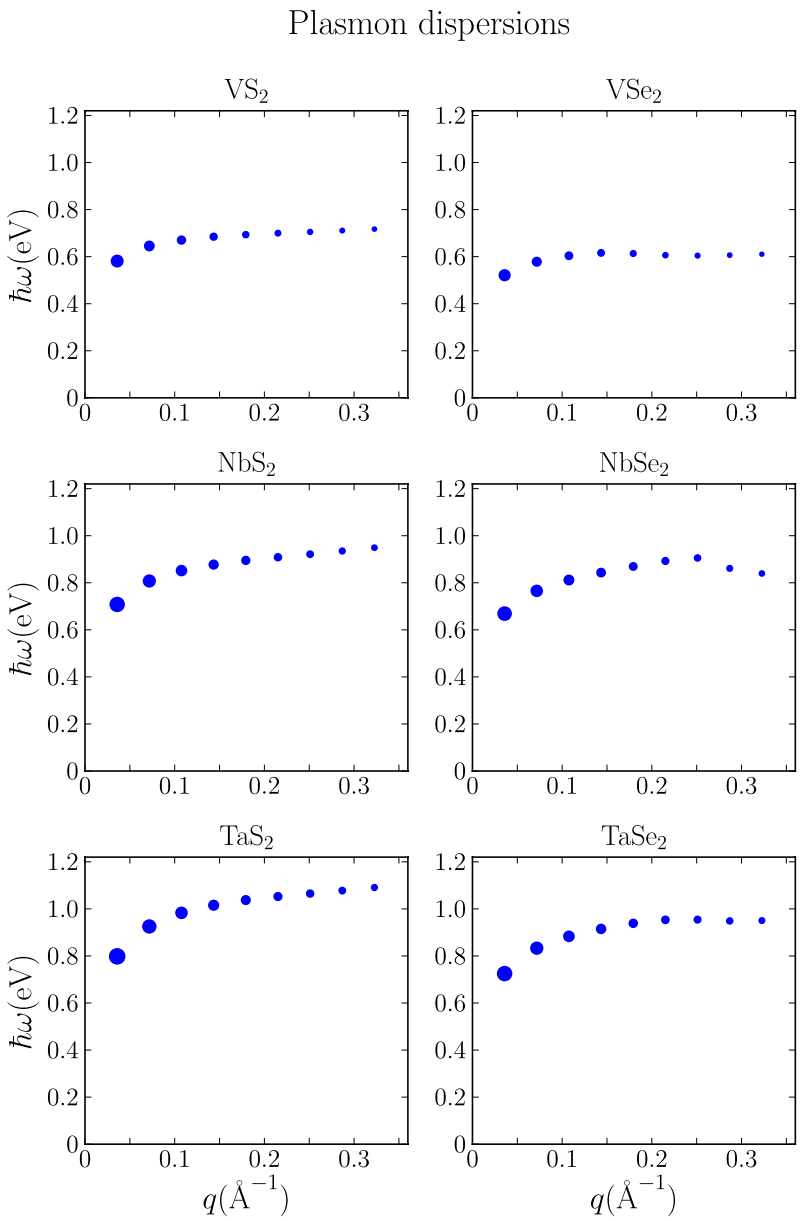

Figure 4.8: Plasmon energy dispersion of the six TMDC in the $\Gamma - M$ direction. The spectral weight (strength) of the modes, given as the integral under the loss peak, is indicated by size of the markers, and is found to decrease significantly with q.

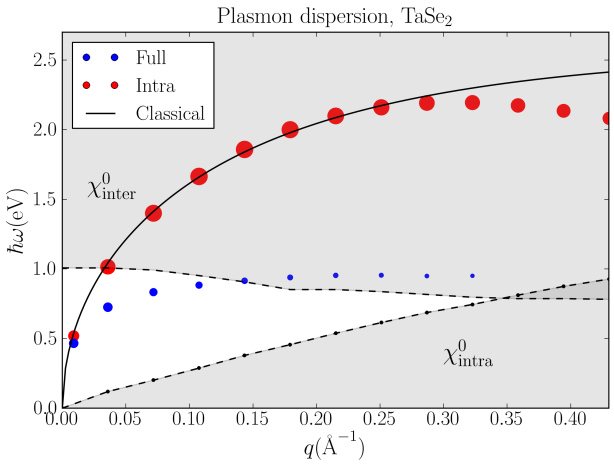

Figure 4.9: Plasmon dispersion calculated from the full response function (blue dots) and from a response function including only intraband transitions (red dots). The result of a classical model for the plasmons in a 2D film is shown for comparison. The shaded areas indicate the dissipative regions of Landau damping by inter and intraband transitions, respectively.

with the full, screened result. As seen in Figure. 4.9 where the two results are compared for $TaSe_2$, the effect of including the interband transitions is a significant downshift in energy and damping of the plasmon mode; Already at $q_\parallel = 0.15\text{Å}^{-1}$ the plasmon energy is decreased by a factor of two and the weight by a factor of ten.

The intraband plasmon is seen to be well described by the classical expression for a symmetric mode in a thin film, given in Eq. (4.5), where the effective mass of the electrons in the metallic band, $m^* \approx 2m_e$, is used in the expression for the plasmon energy: $\omega_p^2 = \frac{ne^2}{m^*\epsilon_0}$. The width of the layer has been approximated as $d = \frac{3}{2}d_{\text{Se}-\text{Se}}$, where $d_{\text{Se}-\text{Se}}$ is the perpendicular separation of Se atoms. A very good fit is obtained until $q_\parallel = 0.25\,\text{Å}^{-1}$ from where the plasmon dispersion is negative due to the finite bandwidth of the metallic bands. Another observation is that in the optical limit, $q \to 0$, it is now more clear that the energy goes to zero as expected for 2D materials.

In order to map the regions in (q, ω) space where Landau damping is present, the single-particle transitions are obtained from $\text{Im}\chi^{0,\text{Intra}}$ and $\text{Im}\chi^{0,\text{Inter}}$, and shown in gray in Fig. 4.9. Interband transitions is present from 1 eV, due to transitions between the occupied states and the metallic band. When the plasmon enters this dissipative region it is heavily damped, and shifted to energies close to the edge of the interband region. From this argument, the different plateaus for the plasmon energy of the materials are determined by the energy onset for the interband region; an effect that completely masks the decrease in free-electron density for the heavier transition metals.

To conclude this Chapter, the quantum mechanical approach and spatial analysis was applied to the study of plasmons in 2D materials, and the transition towards the atomic-size regime. Quantum mechanical effects such as electron spill-out and screening by single particle transitions were found to have a large impact on the plasmon resonances. In the following Chapter the study of 2D materials is continued in the context of van der Waals heterostructures,that are stacks of different 2D materials. Due to computational challenges with modelling this types of systems, a new multi-scale approach for calculating the dielectric function is presented.

Chapter 5

Van der Waals heterostructures

In this chapter, a new framework for calculating the dielectric function of van der Waals heterostructures (vdWh) is presented as an additional method contribution to this thesis. This approach builds upon the methods described in Chapter 2 and 3, but makes it possible to extend *ab initio* precision to the description of larger structures for this particular type of system.

Van der Waals heterostructures is a new class of materials, where the stacking of different 2D crystals, such as graphene, hexagonal boron nitride (hBN) and transition metal dichalcogenides (TMDCs), is used to tailor the electronic properties. This approach has already been used to enhance light-matter interactions for photovoltaic devices [79], for graphene plasmonics [22] and light emitting diodes [80]. In the review article by Geim and Grigoieva [29], they picture the 2D layers as discrete LEGO® bricks, that can be assembled to form any type of combination.

In the enclosed Paper III, we show that the conceptual picture also applies to the theoretical description of the dielectric properties van der Waals heterostructures, where the response functions of the entire heterostructure can be calculated from the response functions of the monolayers. The relevance of this new approach is emphasized by that full ab initio calculations for these structures are often impossible. Firstly, the difference in lattice constants of the layers means that one must use a large in-plane unit cell which contains many atoms, or strain some of the layers which returns an inaccurate description. Secondly, calculations for several layers will also contain too many atoms, rendering ab initio calculations impossible.

In the following Section 5.1, the principles of the developed Quantum Electrostatic Heterostructure (QEH) model is described, where a more detailed description of the method can be found in the supplemental material for Paper III. The model has been applied to the study of plasmon eigenmodes in graphene/hBN heterostructures, where the results are presented in Section 5.2.

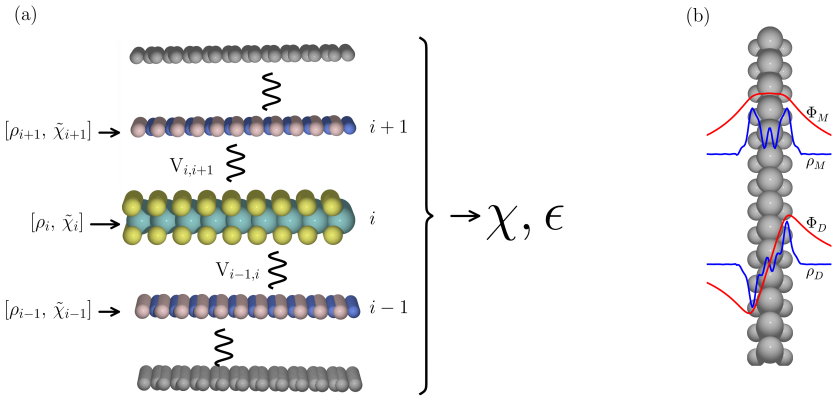

Figure 5.1: Overview of the Quantum Electrostatic Heterostructure (QEH) model. The density response function and the dielectric function of the heterostructure are calculated from the dielectric building blocks of the individual layers assuming a purely electrostatic interaction between the layers. The dielectric building blocks are calculated *ab initio* for the isolated layers, and comprise the monopole and dipole components of the density response function, $\tilde{\chi}^{M/D}$, and electron density, $\rho^{M/D}(z)$, induced by a constant and linear applied potential, respectively. (b) Monopole and dipole induced densities (blue) together with the associated potentials (red) for monolayer MoS2.

5.1 The Quantum Electrostatic Heterostructure (QEH) model

We have developed a method with *ab initio* accuracy for calculation of the dielectric function of 2D heterostructures, with a computational cost that is significantly reduced compared a full quantum calculations.

In our approach, full *ab initio* response calculations are performed for the individual monolayers of the structures. Secondly the coupling between the layers are accounted for on a electrostatic level, in order to obtain the dielectric function of the full heterostructure, see sketch of the model in Fig. 5.1. This approach utilizes that the 2D layers are only weakly bonded to each other through van der Waals forces. Therefore it is a good approximation that the electronic structure of the individual layers is only slightly modified by the neighboring layers, so that the hybridization of electronic states is negligible.

In order to work with the response for the individual layers, it is more convenient to work with the density response function, χ, since this will be localized on the layer. Therefore the (inverse) dielectric function is obtained from the density response function in the RPA:

$$\epsilon^{-1}(\mathbf{r}, \mathbf{r}', \omega) = \delta(\mathbf{r} - \mathbf{r}') + \int \frac{1}{|\mathbf{r} - \mathbf{r}''|} \chi(\mathbf{r}'', \mathbf{r}', \omega) d\mathbf{r}'', \tag{5.1}$$

where the interacting density response function, χ, is obtained from the non-interacting counterpart from the Dyson equation:

$$\chi(\mathbf{r},\mathbf{r}',\omega) = \chi^0(\mathbf{r},\mathbf{r}',\omega) \; + \int\int d\mathbf{r}_1 d\mathbf{r}_2 \chi^0(\mathbf{r},\mathbf{r}_1,\omega)\frac{1}{|\mathbf{r}_1-\mathbf{r}_2|}\chi(\mathbf{r}_2,\mathbf{r}',\omega). \quad (5.2)$$

A key step of the QEH model is to split Eq. (5.2) into two parts, as is generally valid as shown in the supplemental for Paper III. Here, the Coulomb interaction is divided into an intra layer and interlayer part: $V = \tilde{V}+V^I$. In the first part, the density response function for the monolayers where only the intra-layer coupling is included, is obtained from a full *ab initio* response calculation. In practice the Dyson equation is solved in Bloch space with a 2D truncated Coulomb potential, the expression given in Eq.(2.36). The macroscopic average is then taken in the plane of the layer, so that the response function, $\chi(z,z',q_\parallel,\omega)$, is expressed solely in terms of the perpendicular coordinate, z,z', the frequency, ω, and the magnitude of the in-plane momentum transfer, $q_\parallel$, assuming isotropic materials.

5.1.1 Dielectric building blocks

For each layer, the response is further condensed into a *dielectric building block*, that consist of the monopole and dipole component of the response function:

$$\tilde{\chi}_{i\alpha}(q_\parallel,\omega) = \int z^\alpha \chi_i(z,z',q_\parallel,\omega) z'^\alpha dz dz'. \quad (5.3)$$

where $\alpha = 0, 1$ for the monopole and dipole components, respectively. Thus, z^α corresponds to a perturbing potential with constant or linear variation across the layer. Also the induced density $\rho_{i\alpha}(z,q_\parallel)$, that accounts for the spatial form of the response, is included in the dielectric building block. It is normalized such that:

$$\int \tilde{\chi}_i(z,z',q_\parallel,\omega) z'^\alpha dz' = \tilde{\chi}_{i\alpha}(q_\parallel,\omega)\rho_{i\alpha}(z,q_\parallel). \quad (5.4)$$

We have found that generally the frequency dependence of $\rho_{i\alpha}$ can be neglected, while $\tilde{\chi}$ is highly frequency dependent. For the systems studied we have found that the monopole/dipole basis is sufficient, but the method can in principle be extended to include higher order moments with $\alpha > 1$.

In the second part of the QEH model the density response function of the full heterostructure is obtained by solving the Dyson equation that couples the dielectric building blocks via the inter-layer Dyson equation. The equation is written (omitting the $q_\parallel$ and ω variables for simplicity):

$$\chi_{i\alpha,j\beta} = \tilde{\chi}_{i\alpha}\delta_{i\alpha,j\beta} \; + \tilde{\chi}_{i\alpha} \sum_{k\neq i,\gamma} V_{i\alpha,k\gamma}\, \chi_{k\gamma,j\beta}, \quad (5.5)$$

Where the Coulomb matrices are defined as:

$$V_{i\alpha,k\gamma}(q_\parallel) = \int dz \rho_{i\alpha}(z,q_\parallel)\Phi_{k\gamma}(z,q_\parallel). \quad (5.6)$$

$\Phi_{k\gamma}$ is the potential of the induced density, $\rho_{k\gamma}$, which we calculate on a uniform grid by solving a 1D Poisson equation. Note that we leave out the self-interaction terms in Eq. (5.5) since the intralayer Coulomb interaction is already accounted for by the uncoupled $\tilde{\chi}_{i\alpha}$. The (inverse) dielectric function of Eq. (5.1) in the monopole/dipole basis becomes

$$\epsilon^{-1}_{i\alpha,j\beta}(q_\parallel,\omega) = \delta_{i\alpha,j\beta} + \sum_{k\gamma} V_{i\alpha,k\gamma}(q_\parallel)\,\chi_{k\gamma,j\beta}(q_\parallel,\omega). \tag{5.7}$$

5.1.2 Plasmon eigenmodes

In order to calculate the plasmon eigenmodes, the same form of eigenvalue equation as presented in Chapter 3 is defined for the dielectric matrix of the heterostructure, Eq. (5.7):

$$\sum_{j\beta} \epsilon_{i\alpha,j\beta}(q_\parallel,\omega) f_{n,j\beta}(q_\parallel,\omega) = \epsilon_n(q_\parallel,\omega) f_{n,i\alpha}(q_\parallel,\omega), \tag{5.8}$$

which returns the eigenvalues, $\epsilon_n(q_\parallel,\omega)$, and eigenvectors, $f_{n,i\alpha}(q_\parallel,\omega)$ of the dielectric matrix in the monopole/dipole basis. A plasmon eigenmode fulfills that:

$$\mathrm{Re}\sum_{j\beta} \epsilon_{i\alpha,j\beta}(q_\parallel,\omega) f_{n,j\beta}(q_\parallel,\omega) = 0, \tag{5.9}$$

corresponding to $\mathrm{Re}\epsilon_n(q_\parallel,\omega) = 0$. In practice, the plasmon energies are identified from the peaks in the eigenvalue loss-spectrum $-\mathrm{Im}\epsilon_n^{-1}(q_\parallel,\omega)$ since this includes the finite imaginary part which can shift the plasmon energy.

The right-hand eigenfunctions, $f_{n,i\alpha}$, give the induced potential of the plasmon in the basis of $\phi_{i,M/D}$. The left eigenfunctions, $f^n_{i\alpha}$, correspond to the induced density of the plasmon in the basis of $\rho_{i,M/D}$. The induced density can be expended in terms of the induced densities of the monolayers, $\rho_i(z,q_\parallel)$, to get their spatial form:

$$\rho_n(z,q_\parallel) = \sum_{i\alpha} f^n_{i\alpha}\rho_{i\alpha}(z,q_\parallel), \tag{5.10}$$

with the corresponding induced potential:

$$\phi_n(z,q_\parallel) = \sum_{i\alpha} f^n_{i\alpha}\Phi_{i\alpha}(z,q_\parallel). \tag{5.11}$$

5.1.3 GPAW implementation

The QEH model has been implemented as a separate module in GPAW, available from the homepage [81]. The dielectric building blocks are calculated with the method, `get_chi_2D` that takes a list of pickle files with the density response function, obtained from *ab initio*, of the layer at different momentum transfers, $q_\parallel$. This is used in the following manner:

```
from gpaw.response.qeh import get_chi_2D
q, w, chi_M, chi_D, z, drho_M, drho_D = get_chi_2D(filenames, name)
```

Table 5.1: Description of the quantities returned by the method `get_chi_2D()` that together defines the dielectric building block of a monolayer.

`q`	momentum transfer array, (nq)
`w`	frequency grid, (nw)
`chi_M`	monopole density response function, (nq × nw)
`chi_D`	dipole density response function, (nq × nw)
`z`	real space grid along z-direction, (nz)
`drho_M`	monopole induced density, (nq × nz)
`drho_D`	dipole induced density, (nq × nz)

The method returns the quantities described in table 5.1, that are saved to the pickle file `<name>-chi.pckl` that should be given as input to the QEH module. When unit cells of different sizes has been used for the calculations on different layers (which is usually the case due to differences in lattice constants), the q-grids will generally be different. Therefore the result must be interpolated to the same q-grid before given as input to the QEH module.

For semiconducting layers where the response function evolves smoothly with q, standard interpolation routines such as 2D spline interpolation is generally a good approach. For layers where the peaks in Imχ shifts largely with the value of q however, more sophisticated approaches are necessary. This is for example the case for metallic layers, where the plasmon frequency changes rapidly with q as seen in the previous chapter (since χ is an interacting response function, the imaginary part will have peaks at the plasmon energies)

The QEH class is used in the following manner:

```
from gpaw.response.qeh import QEH
HS = QEH(structure=['3H-MoS2','2BN', 'graphene',
                    '2BN', '3H-MoS2'],
         d=d   # layer distances
         )
eig, z, rho_z, phi_z, omega0 = HS.get_plasmon_eigenmodes()
```

where the example above calculates the plasmon eigenmodes of one layer of graphene sandwiched between two layers of hBN and three layers of MoS2 on each side. The distance array, `d`,should be an array with the interlayer distances within the structure. Also methods to calculate the macroscopic dielectric function and the screened potential for excitons have been implemented. See appendix A for the details of the QEH class and the associated methods.

5.1.4 Database of dielectric building blocks

A database with the dielectric building blocks of several 2D materials has been created within the computational materials repository, available from the home-

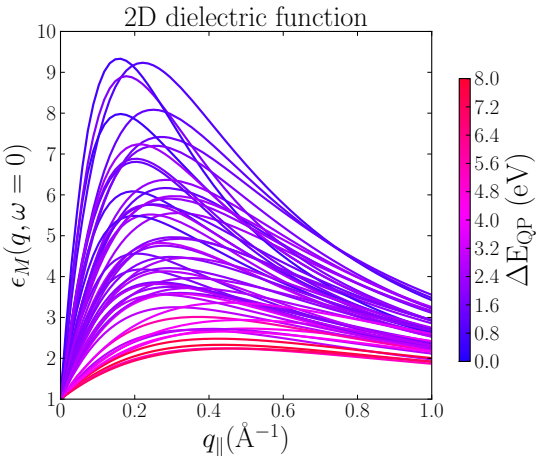

Figure 5.2: 2D dielectric function of the 51 semiconducting monolayer transition metal dichalcogenides and oxides. The color indicates the quasi-particle band gap calculated from the GW-approximation [26].

page [82]. The materials consist of 51 semiconducting transition metal dichalcogenides and oxides predicted to be stable by a recent *ab initio* study [26], monolayer hBN and graphene at 11 different doping levels from 0 to 1.0 eV. The details of the calculations for the 2D materials is given in the supplemental material for Paper III. A broad range of values for the dielectric function of the semiconducting 2D layers is obtained, as seen in Fig. 5.2. The dielectric function is found to be larger for low band gap semiconductors, the value of the quasi-particle band gap indicated in color. The band gaps were calculated with the GW approximation in Ref. [26]. In the optical limit, $q_\parallel \to 0$ the dielectric functions goes to one for all the 2D materials, due to the nature of the Coulomb potential in 2D (see discussion in Section 4.1).

5.1.5 Benchmark calculation on multilayer MoS_2

In order to test the performance of the method, the macroscopic dielectric function in the static limit ($\omega = 0$) of multilayer MoS_2 has been calculated with the QEH model and compared to the *ab initio* result for bilayer and bulk MoS_2. The macroscopic result is obtained by averaging the dielectric function over the width of the structure, in correspondence with the definition in Eq.(3.1).

The result is shown in Fig. 5.3, where the dielectric function is seen to increase with the number of layers. This illustrates the weakening of the Coulomb potential in 2D structures, where the screening is greatly reduced. At $q \to 0$ the dielectric function goes to one as expected for a 2D semiconductor, as discussed in Chapter 4, meaning that there is no screening of macroscopic fields in this limit. This takes place for all the structures with a finite width, L, that behaves

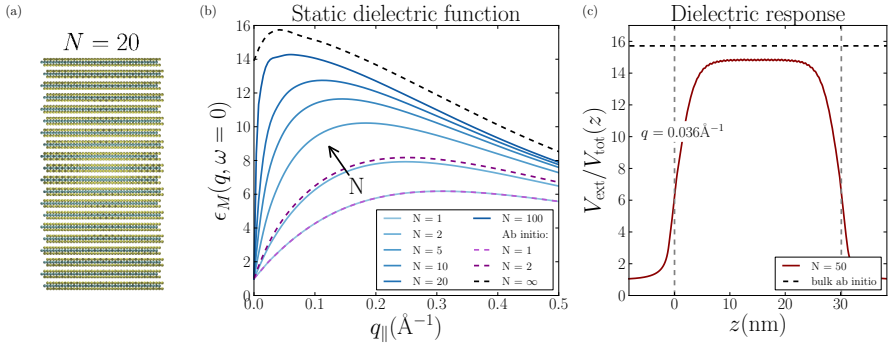

Figure 5.3: The transition of the dielectric function of MoS2 from 2D to 3D. a) Atomic structure of multilayer MoS2. b) The macroscopic dielectric function in the static limit, $\epsilon_M(q_\parallel, \omega = 0)$, as a function of in-plane momentum transfer for different number of layers, N. The dielectric function increases monotonically with N, and converges slowly towards the dielectric function of bulk MoS_2 obtained from *ab initio*. Also, there is excellent agreement with the *ab initio* result for bilayer MoS_2. c) Spatial variation in the dielectric response across 50 layers of MoS_2, compared to the dielectric function of bulk MoS_2 obtained from an *ab initio* calculation.

as 2D materials for $q_\parallel << 1/L$.

There is very good agreement with the *ab initio* results, which verifies that the effect of hybridization of electronic state between the layers has a negligible impact on the dielectric properties. Since the band gap in bilayer and bulk MoS_2 is known to be slightly smaller than for the monolayer, the model is expected to slightly underestimate the dielectric function; However, for $N = 2$ however the difference is very small. When the number of layers is increased, the dielectric function converges very slowly towards the bulk *ab initio* result, which is not yet reached at $N = 100$. The slow convergence is partially due to that the response of the structure has a large spatial variation across the structure, see Fig. 5.3 (c), such that the contribution from the edges leads to a decrease in the macroscopic result. Increasing the slab thickness beyond 50 layers brings the QEH result even closer to the bulk result in the middle of the slab, but a small underestimation remains originating from the difference in the band structures of the monolayer and bulk systems.

As seen in Fig. 4 in Paper III, the QEH model also enabled us to include the substrate effects on the exciton in WS_2, in good agreement with experiments. The presence of a substrate is seen to result in a decrease in exciton binding energy, due to screening of the electron-hole interaction. The magnitude of screening depends on the dielectric function of the substrate, where MoS_2 leads to a larger reduction in binding energy than hBN.

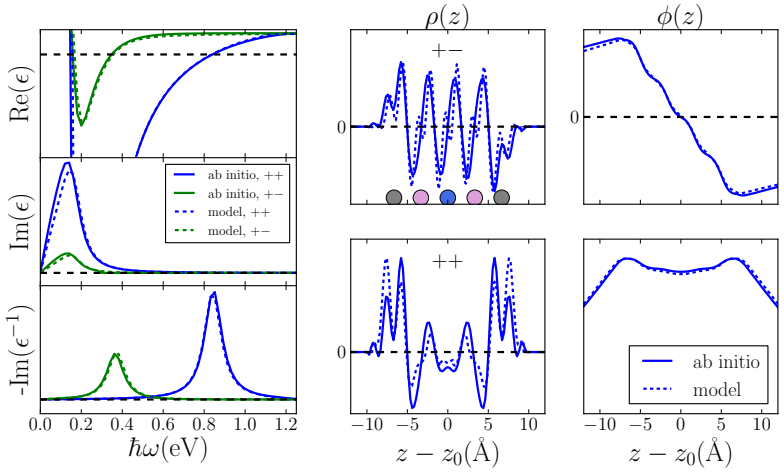

Figure 5.4: Plasmon eigenmode analysis for two layers of doped graphene separated by three layers of hBN calculated with full *ab initio* and the QEH model (dashed lines). a) Eigenvalue curves of the dielectric matrix that satisfy $\mathrm{Re}\,\epsilon = 0$, resulting in two plasmon eigenmodes corresponding to the antisymmetric (+-) and symmetric (++) combination of the two graphene layers, the induced densities $\rho(z)$ and potentials $\phi(z)$ shown in (b). The QEH model is seen to almost perfectly reproduce the eigenvalues and eigenvectors, justifying the QEH approach.

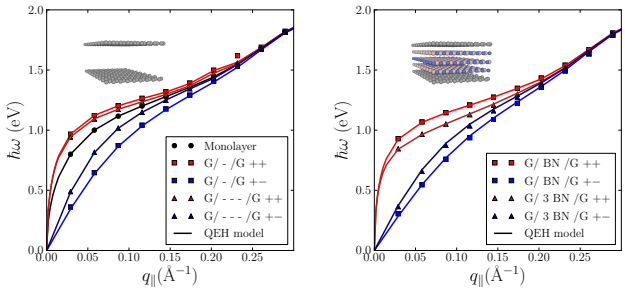

Figure 5.5: Plasmon dispersion of the two hybridized modes ($++$ / $+-$) in a graphene / BN / graphene heterostructure. The markers represent the *ab initio* results and the solid lines represents the result of the heterostructure model. In a) the graphene sheets are separated by vacuum corresponding to 1 and 3 layers of BN, and compared to the plasmon dispersion of the single plasmon in monolayer graphene. In b) the graphene layers are separated by BN.

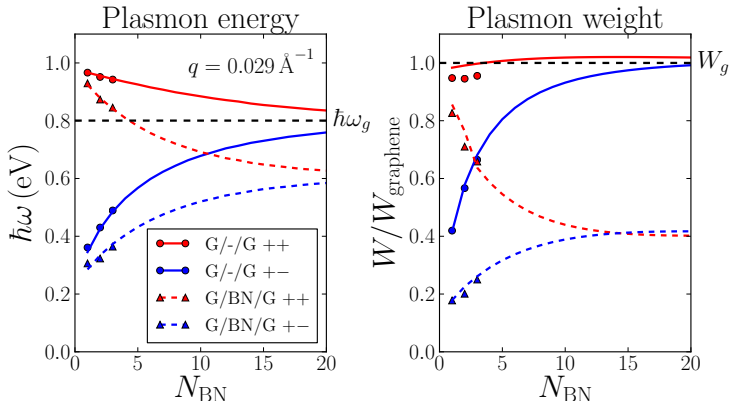

Figure 5.6: Energy (a) and weight (b) of the two hybridized plasmon modes as a function of the number of BN layers separating the the graphene layers, for a low momentum transfer of $q_{\parallel} = 0.029\text{Å}^{-1}$. The weight is normalized to result for the doped plasmon in monolayer graphene, $W_{graphene}$, and the energy is compared to the monolayer plasmon energy $\hbar\omega_0$, indicated as horizontal dashed lines. The points represent the *ab initio* result, and the lines the results of the QEH model.

5.2 Plasmons in graphene@hBN heterostructures

An important consideration regarding plasmon in 2D materials is how the substrate introduces further screening. In the previous chapter we saw how the presence of single-particle transitions energetically close to the plasmon resonance can lead to a large shift in energy. In the following the impact of single-particle transitions in neighboring layers on the 2D plasmon is studied, by using a system of two graphene sheets separated by up to 20 layers of hBN, see insert Fig. 5.5. When two graphene sheets are present the plasmon modes of the two structures can *hybridize* to form new collective modes of the system, as explained by plasmon hybridization theory [83]. This effect is conceptually similar to the hybridization of molecular orbitals [84], except that it is governed by the long ranged Coulomb potential that couples the resonances of the two systems.

Plasmons in graphene on hBN were recently found to propagate with low loss [22], and the close to perfect lattice match between the two layers enables full *ab initio* calculations for the thinnest heterostructures. We considered doped graphene that has a finite density of states at the Fermi level. This gives rise to 2D plasmons with energies in the regime 0-2 eV, that goes to zero in the optical limit as is characteristic for plasmons in 2D metals.

We calculate the effect of hBN on the plasmons using the QEH model for up to 20 layers of hBN and compare to full *ab initio* calculations for 1-3 layers of hBN. The plasmon eigenmode analysis yields two eigenvalue curves that satisfy $\text{Re}\,\epsilon = 0$, shown in Fig. 5.4a in the case of three layers of hBN separating the

sheets. The two solutions corresponds to the symmetric (++) and antisymmetric (+−) combinations of the graphene plasmons as previously found for two freestanding graphene sheets [85]. The induced density and potentials of the two eigenmodes are shown in Fig. 5.4b. The QEH model is seen to perfectly reproduce the *ab initio* results for the dielectric eigenvalues, plasmon energy, and weight, where the latter is defined as the peak under the loss function $-\mathrm{Im}\epsilon^{-1}(q_{\parallel},\omega)$. The densities and potentials of the plasmon eigenmodes are also reproduced fairly accurately by the model. The relatively large amount of electron density located on the hBN during the plasma oscillation reflects that the hBN layers screens the potential associated with the plasmons.

In Fig. 5.5 the plasmon dispersion is shown for 1 and 3 layers of BN and the corresponding amount of vacuum, comparing the *ab initio* to the QEH results. As seen in (a) the symmetric and antisymmetric mode is shifted to higher and lower energy respectively, compared to the plasmon in monolayer doped graphene. When hBN is included (b) all plasmon energies are slightly downshifted, the change perfectly reproduced by the model.

The change due to hBN is also apparent from Fig. 5.6 where the energy and weight is plotted for up to 20 layers of hBN at a low parallel momentum transfer. The redshift and damping of the plasmons due to hBN is seen to increase with the number of layers, and is almost saturated at 20 layers. Here the two graphene sheets are nearly decoupled and the symmetric and antisymmetric modes are close to degenerate in energy and weight. Since the electric field of the plasmon is more long-ranged for small $q_{\parallel}$, the effect of hBN is largest in this regime. Thus, for larger $q_{\parallel}$ the decrease in weight of the plasmon is not so pronounced, still leaving hBN as a high-quality substrate for graphene plasmonics.

In conclusion, the good agreement between the *ab initio* results and the model reflects that the hybridization of electronic states between the layers is also negligible in the case of graphene and hBN. Thus, the QEH model is found to perform very well for a description of the dielectric function of layered 2D semiconductors as well as plasmons in graphene heterostructures. Therefore the model can be applied to study the effects of different substrates on plasmons, excitons and band gaps, with more than 50 different semi-conducting 2D materials being available from the database.

Chapter 6

Plasmons confined to 1D

In the previous chapters plasmons in several 2D structures have been studied. In this chapter the case of one-dimensional (1D) plasmons in the atomic scale limit is considered, where the lower limit for confinement of propagating plasmons is reached.

Plasmons in 1D has mostly been studied in quasi-1D materials such as metallic nanowires of diameter of 50 to 100 nm hosting propagating surface plasmon polaritons [86, 87]. However, also a few examples of 1D plasmons confined to the atomic scale have been observed in the case of self-assembled atomic chains on semiconducting substrates [30, 88]. In condensed matter physics the idealized 1D electron gas is known as a Luttinger liquid [89, 90]. In this limit, the quasi-particle picture of electronic excitations breaks down, and plasmons obtain a special status as the only resonances of the system [49]. Luttinger liquid behavior has for example been observed in carbon nanotubes [91] and in nanowires fabricated by cleaved edge overgrowth [92].

In this chapter plasmons in different types of 1D systems is studied; In Section 6.2 thin nanowires below 2 nm in diameter are shown to host several plasmon eigenmodes where quantum mechanical effects and non-local response have a large impact on some of the plasmon modes. The results have been published in Paper IV. In this contexts we have also studied the hybridized plasmon modes of two nanowires at small separations, affected by tunneling between the two wires. In Section 6.3 the existence of 1D plasmons on the edges of a MoS_2 nanoribbon is predicted, the results published in Paper V.

First, some general properties of the idealized 1D system is discussed in the following Section.

6.1 Properties of plasmons in 1D

In Chapter 4, we saw that plasmons in 2D systems behave qualitatively and quantitatively different than plasmons in bulk materials, due to the weakening of the Coulomb potential in 2D. This argument can be extended to account for

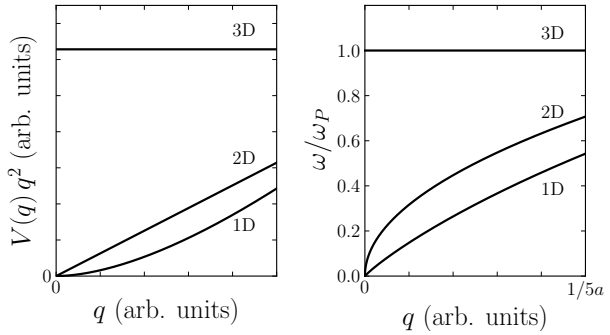

Figure 6.1: Comparison of the behavior of the Coulomb potential and plasmon frequency in the limit of low q for the 3D, 2D and 1D electron gas. The Coulomb potential (left panel) is plotted as $V(q)q^2$ where q^2 accounts for the dependence of χ^0. For the plasmon energies the expressions used are: $\omega_{3D} = \omega_P$, $\omega_{2D}(q) = \sqrt{\frac{ne^2}{2m_e^*\epsilon_0}q}$, and $\omega_{1D}(q) = qv_F\sqrt{1+\frac{4K_0(qa)}{\pi v_F}}$. Inspired by Fig. 1 in Ref. [66] .

the behavior of plasmons in 1D, where the Fourier transform of the Coulomb potential is written (in atomic units) as [49]:

$$V_{1D}(q) = \int_{-\infty}^{\infty} \frac{1}{|x|} \mathrm{e}^{-iqx} dx. \tag{6.1}$$

However, this expression diverges when the electrons are confined strictly in 1D. The divergence can be handled by allowing a finite width of the 1D system [66], a, resulting in a cutoff for the integration at small distances:

$$V_{1D}(q) = 2\int_{a}^{\infty} \frac{1}{|x|} \mathrm{e}^{-iqx} dx = 2K_0(qa). \tag{6.2}$$

K_0 is the modified Bessel function of the second kind of order zero. In the limit of low momentum transfers, $q << a$, the expression can be simplified to to $V_{1D}(q) = -2\ln(qa)$. Since the Coulomb potential diverges slower than the decay of the density response function to zero, $\chi^0(q) \propto q^2$, the plasmon energy and weight will go to zero for $q \to 0$, qualitatively similar to the behavior of plasmons in 2D systems, where the plasmons energy and weight does also go zero. The quantitative difference is that in 1D the Coulomb potential diverges slower than in 2D, so that not only the product $V(q)\chi^0(q)$ goes to zero for $q \to 0$ but also the derivative:

$$\frac{\delta}{\delta q} V_{1D}(q)\chi^0(q) \;\propto\; -\frac{\delta}{\delta q}\ln(qa)q^2 = \tag{6.3}$$

$$-\,q[1+2\ln(qa)] \to 0 \quad \text{for} \quad q \to 0. \tag{6.4}$$

The behavior of the Coulomb potential in 3D, 2D and 1D is illustrated in Fig. 6.1, where $V(q)q^2$ is plotted as a function of q, and the quantitative differences between 1D and 2D systems is seen.

6.1.1 1D plasmon dispersion

In order to obtain an expression for the plasmon dispersion in 1D, a simple model for the non-interacting density response function, χ^0, is constructed by assuming a single linear band with Fermi velocity v_F. At a given q, only the poles: $\omega_0 = \pm q v_F$ contributes to χ^0, leading to the expression:

$$\chi_0(q,\omega) = \frac{q}{\pi}\left(\frac{1}{\omega - qv_F + i\eta} - \frac{1}{\omega + qv_F + i\eta}\right), \tag{6.5}$$

$$= \frac{q}{\pi}\frac{2qv_F}{(\omega + i\eta)^2 - (qv_F)^2}, \tag{6.6}$$

where η accounts for energy broadening. Using the RPA, the dielectric function is obtained as: $\epsilon(q,\omega) = 1 - V_{1D}(q)\chi_0(q,\omega)$, where $V_{1D}(q)$ is the 1D Coulomb potential. The dielectric function has poles close to the single-particle energies, $\omega_0 = \pm q v_F$, while the inverse dielectric matrix has poles at the collective excitations of the system, i.e. the plasmons. By casting the inverse dielectric matrix on the form:

$$\epsilon^{-1}(q,\omega) = 1 + \frac{\alpha}{\omega - \omega(q) + i\eta} - \frac{\alpha}{\omega + \omega(q) + i\eta}, \tag{6.7}$$

the plasmon frequency, $\omega(q)$, is found to be:

$$\omega(q) = qv_F\sqrt{1 + \frac{2V(q)}{\pi v_F}}, \tag{6.8}$$

in the limit of $\eta = 0$. This expression is identical to the eigenenergies obtained from the interacting Tomonaga-Luttinger model [49], where the interaction parameter is set equal to the 1D Coulomb interaction. Also this expression was obtained as the long-wavelength limit of the full RPA result in 1D [93]. Thus, the 1D plasmon dispersion goes as $\omega(q) \approx q\sqrt{\ln(qa)}$ compared to the $\sqrt{q}$ relation in 2D.

In Fig. 6.1, the behavior of the plasmon energy in 3D, 2D and 1D is also summarized, illustrating the quantitative differences between 2D and 1D. Only the terms below second order in q has been included in the plasmon energy, leaving the 3D plasmon dispersion-less.

As shown in the following, Section 6.2, where the results for plasmons in metallic nanowires are presented, several plasmon eigenmodes exist in 1D systems with a finite width, where only the mode without cylindrical variation will behave as the ideal 1D plasmon.

6.2 Metallic nanowires

As a simple model of a 1D system, thin metal wires of widths below 2 nm were studied. The results were published in enclosed Paper IV, where the plasmon eigenmodes of single wires is discussed in the first part of the paper. This system

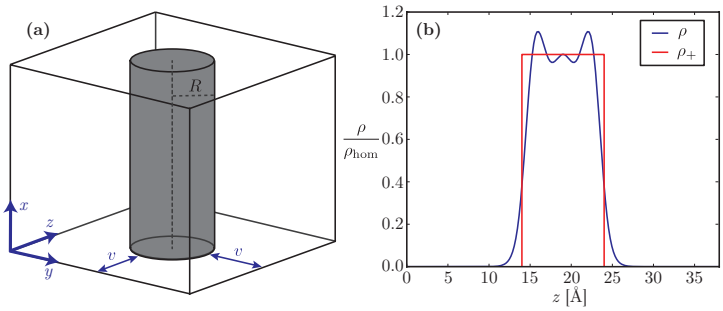

Figure 6.2: a) Sketch of the unit cell with a Jellium nanowire with radius R. b) Cross-sectional view of the fixed positive background density used for the Jellium approximation (red) and the converged electron density (blue). The densities are plotted relative to the free electron density of bulk Na, ρ_{hom}.

enables the study of the fundamental properties of atomic-scale plasmons in 1D, and to access the impact of non-local response and quantum mechanical effects such as electron spill-out on the plasmon properties.

The treatment was simplified by using a Jellium description of the metal where the atomic structure is neglected. In the Jellium approximation, the atomic nuclei are replaced by a homogeneous positive background. In order to describe a nanowire, the background charge density is terminated abrupt at the edges of the nanowire, as shown in Fig. 6.2. The electronic density is calculated self-consistently with DFT and is found to spill out from the nanowire edge as seen in Fig. 6.2(b). Therefore, this description enables the study nanowires with perfect cylindrical symmetry, where the quantum mechanical behavior of the electrons are still accounted for. However, the Jellium description is only a good approximation for simple-metals with free-electron like behavior, and in the present work the electron density of Na is used.

The eigenmode analysis described in Chapter 3, was applied to calculate the plasmon eigenmodes of wires of radius, R, from 1 Å to 8 Å. The analysis returns several solutions, where Fig. 3 in Paper IV shows the complete set of modes for $R = 2$ Å, 5 Å and 7.5 Å. As an example the induced potential and density of the surface modes for $R = 7.5$ Å is shown in Fig. 6.3. The induced density is clearly localized at the surface, and extends to the spill-out region outside the Jellium perimeter. The modes are labeled according to their order, $m = \{0, 1, 2, ...\}$, that accounts for the angular symmetry $e^{im\theta}$, so that for an increasing order, the density and potentials have an increasing number of standing waves along the wire perimeter. Each of the modes with $m > 0$, are found as a degenerate pair rotated by an angle of $\pi/(2m)$ with respect to each other. This degeneracy is also obtained by a group theoretical analysis, where these modes with $m > 0$ belongs to the doubly degenerate E_{mg} and E_{mu} irreducible representations of the point group $D_{\infty h}$ [94]. The $m = 0$ mode on the other hand has no angular variation, and belongs to the non-degenerate irreducible representation, A_{1g}.

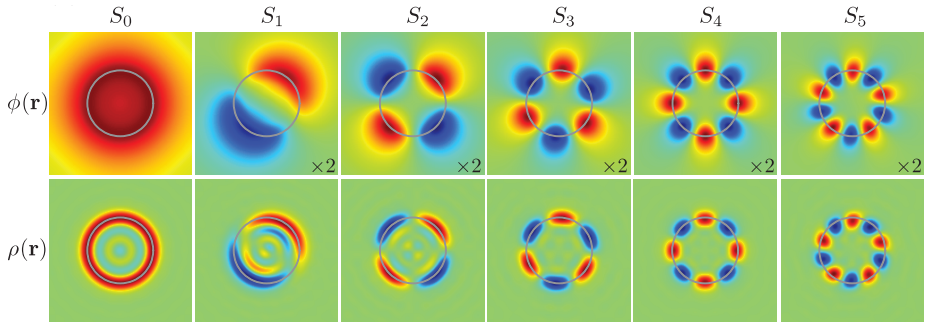

Figure 6.3: Cross-sectional view of the surface plasmon modes of a nanowire with radius $R = 7.5\,\text{Å}$, showing the induced potential, ϕ, and induced density, ρ. The modes are labeled according to their order, $m = \{0, 1, 2, ...\}$, and have $e^{im\theta}$ angular symmetry. For $m > 0$, the modes are found as degenerate pairs, as predicted by group-theory. In the direction parallel to the wire, x, the modes have a $e^{iq_\parallel x}$ variation.

As can be seen from Figure 3 in Paper IV, the number of surface modes decreases with decreasing radius of the wire, and for $R = 2.5\,\text{Å}$ only the S_0 and S_1 modes are found to exist. Or, to be more precise; the higher order modes exist as eigenvalues of the dielectric matrix, but $\text{Re}\,\epsilon_n = 0$ is never satisfied due to a high degree of damping. This can be explained in terms of Landau damping, where the plasmon enters the regime of single-particle transitions at high momentum transfers. Here the perpendicular oscillations of the modes leads to a larger effective q for the resonances with $m > 0$: $q_{eff}^2 = q_\parallel^2 + q_\perp^2$, where $q_\perp$ increases with m. Thus there is a lower limit for the wavelength that can be sustained by the plasmon modes, in this case found to be approximately $\lambda_{\text{min}} \approx 10$ Å.

The eigenmodes-analysis was also used to obtain the dispersion of the plasmon energy with respect to momentum transfer and radius, see Fig. 6.4. The results are compared to the classical expression for a surface mode of order m [95]:

$$\omega_m^2 = \omega_\text{P}^2\, q_\parallel R\, I'_m(q_\parallel R) K_m(q_\parallel R). \tag{6.9}$$

Here I_m and K_m are the modified Bessel function of first and second kind of order m, and ω_P is the bulk plasmon frequency determined by the free-electron density as $\omega_\text{P} = \sqrt{\frac{ne^2}{m\epsilon_0}}$. Since the Drude expression for the dielectric function, Eq. (2.25), that does not account for spatial non-locality is used in this classical model, the plasmon frequency is a function of the dimensionless product $q_\parallel R$ only. Thus, the wavelength dependence in neglected, and the plasmon energy approaches the surface plasmon energy, ω_s for high $q_\parallel R$.

The deviations between the quantum results and the classical model as shown in Fig. 6.4 can be explained by two main effects: 1) Electron spill-out that leads to a decrease in the electron density and a redshift in plasmon energy. This effect

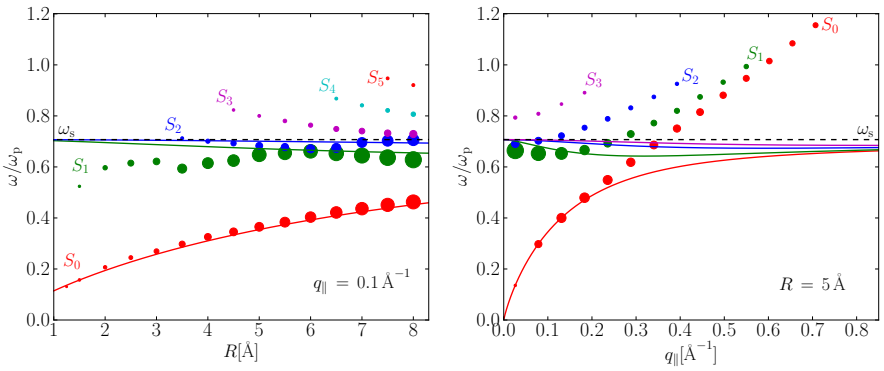

Figure 6.4: Plasmon energy dispersion for the surface modes as a function of: (a) Wire radius for a fixed momentum transfer of 0.1 Å^{-1}. (b) Momentum transfer for $R = 5$Å. The diameter of the markers indicates the strength of the plasmon modes. The result is compared to the classical model (solid lines) stated in Eq. (6.9). For the zero-order surface mode, S_0, there is a good agreement with the classical result at low $q_\parallel$, while for the other modes non-locality and electron spill-out leads to deviation from the classical result.

was also observed for the thin Na films studied in Chapter 4. 2) The wave-vector dependence of the plasmon energy that leads to a blueshift in plasmon energy with increasing q. At low momentum transfers, the zero-order mode is very well captured by the classical model, whereas the S_1 mode is redshifted due to the electron spill-out. For the higher order modes however, the increase in q_{eff} leads to an overall blueshift of the plasmon energy. The deviation due to the inclusion of non-locality is also present at high momentum transfers, where the quantum result produces a close to linear dispersion with q, that is not produced by the classical model due to the use of a local Drude dielectric function.

6.2.1 Plasmon hybridization in a nanowire dimer

The plasmon eigenmode analysis was also applied to visualize how the plasmon eigenmodes of a nanowire dimer, see Fig. 6.5, evolves with decreasing separations between the wires. When two wires are present, the plasmon modes of the two structures can hybridize to form new collective modes of the system. An example of hybridization of plasmons in 2D materials was given in Chapter 5, in the case of graphene@hBN heterostructures.

For plasmonic applications such as chemical sensing and spectroscopy, a desired property of plasmonic particles is the ability to confine light to the nanoscale [6]. In this context dimer structures are of large interest, since a particular strong enhancement can be obtained when two or more particles are in close proximity, with amplitude that increases with decreasing separation [96]. At very small separations, the increase breaks down due to non-local effects

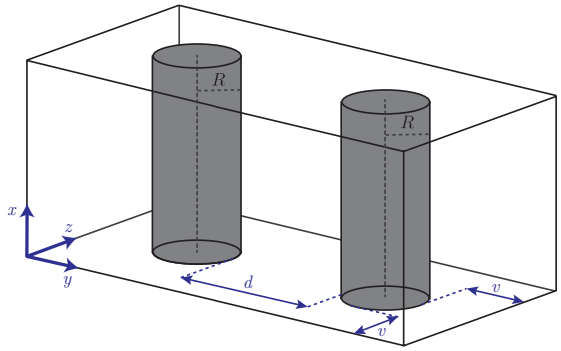

Figure 6.5: Sketch of the nanowire dimers at separation d.

[18] and tunneling of electrons between the particles [97, 98]. The crossover for tunneling is marked by the emergence of a charge-transfer plasmon (CTP), that stems from the flow of charges between the particles. Classical models produce an unphysical divergence in the electric field enhancement at small separations. Thus more advanced approaches such as extended hydro-dynamical models or quantum approaches are needed. Several other theoretical studies on nanoparticle and nanowire dimers have been reported, using either a classical description [99], semi-classical hydrodynamical approaches [100, 18], and *ab initio* approaches [101, 102].

In order to decrease computational cost, calculation were done for thin wires with $R = 2.5$ Å. At this width only the S_0 and the two degenerate S_1 modes exist, which also simplifies the description. This leads to the presence of six modes for the dimer structure. The modes are shown in Fig. 6.6a for the induced potential of the plasmons at $d = 2$ nm, where the shape of the modes are not altered by quantum effects. The modes are labeled according to even and odd symmetry as $++$ and $+-$ respectively, and the S_1 modes are furthermore characterized by vertical, v or horizontal, h, polarization.

The S_0^{+-} and S_1^{h++} modes with dipole character are the wire analogues to the bonding dimer plasmon (BDP) of nanoparticle dimers that has a large cross-section for coupling to optical fields. In Fig. 7 in Paper IV the modes are plotted for $d = 8$, 2 and 1 Å. Here the plasmon eigenmode analysis enabled the visualization of how quantum mechanical and non-local effects alters the spatial shape of the hybridized modes as the two wires approach each other. The S_0^{+-} and S_1^{h++} modes are in particular affected, and both are quenched at small separation and replaced by a charge transfer plasmon.

The energies of the hybridized modes are held against the results of a classical model for a nanowire dimer (the expression stated in appendix, Paper IV). The energies are plotted as a function of separation, d, in Fig. 6.6. At separations above approximately 8 Å, the classical model captures the splitting of the S_0 modes particularly well. At lower separations the S_1^{h++}, S_1^{v+-} and S_1^{v+-} modes starts to blueshift and deviate from the classical model that predicts a continuing

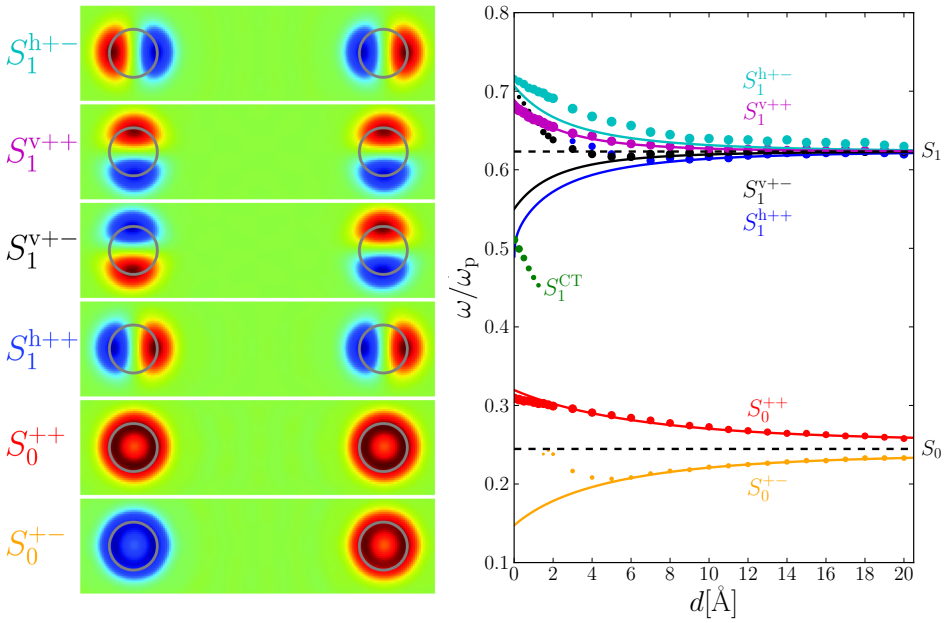

(a) (b)

Figure 6.6: (a) Induced density of the hybridized plasmon modes of a nanowire dimer at 2 nm separation of the Jellium surfaces. (b) The mode energy as a function of separation, d. For decreasing d, the modes split in energy, and at small separations, $d < 2$ Å the flow of charges between the wires leads to the emergence of the charge-transfer plasmon, S_1^{CT} at the expense of the S_+^{+-} and S_1^{h+-} modes that are quenched at small separations. This transition is clearly marked as a jump in the plasmon energy. However, already at separations below approximately 6 Å, the plasmon dispersion deviates from the classical result (solid lines) due to weak tunneling and potentially non-local effects.

redshift for vanishing separations. These three modes are more largely affected since opposite charges on the two structures comes into close contact at small separations.

At small separations the facing of opposite charges on the two wires is accompanied by a rapid drop in the electric potential across the interface. There is a limit to how rapid this drop can be, which gives rise in an induced potential of the hybridized plasmon modes that are modified already at 8 Å separations, potentially due to non-local effects. For decreasing separations also tunneling of electrons between the two wires will have a gradually increasing impact on the modes.

The emergence of the strong tunneling regime is marked by the replacement of the S_0^{+-} and S_1^{h++} modes with the charge-transfer plasmon, S^{CT}, just below 2 Å separation. While the altering of the modes has been continuous until this point, this shift is discontinuous. This is also apparent from the rapid shift in energy, as seen in Fig. 6.6.

To conclude this section, we have seen that the quasi-1D systems such as metallic nano wires of finite width can host several plasmon eigenmodes of different symmetry. The spill out of electrons from the surface and the wave-vector dependence of the plasmon energy resulted in deviations from the classical result. For the nanowire dimer, the plasmon eigenmode analysis was applied to visualize the transition of the eigenmodes from two separate wires towards the tunneling regime.

6.3 Edge-states of a MoS_2 nanowire

As another example of plasmons in a 1D system, we have predicted the existence of 1D plasmons on the edges of a zigzag MoS_2 nanoribbon, the results presented in Paper V.

A MoS_2 nanoribbon of zigzag type has two types of edges, see illustration in Fig. 6.7a. These edges are also present on MoS_2 nanoparticles where they are referred to as the S- and Mo-edge [103], where the Mo edge is generally found to be fully or partially covered with sulfur. Even though MoS_2 is a semiconductor, these edges have been found to host metallic states [104, 105].

The performed DFT calculation also predicts the existence of metallic edge states, where the obtained band structure, see Fig. 6.7b, reveals bands crossing the Fermi level. Each of these states are associated with the edges, where (I) is localized at the S-dimer on the S-edge, (II) on the Mo-atom on the Mo-edge, and (III) on the S-dimer on the Mo-edge. State (III) has a particular large Fermi-velocity and a large band-width of more than 2 eV.

When the eigenmode analysis is applied to this system, three plasmon eigenmodes are obtained, see Fig. 6.7c, where a one to one relation between single-particle states and the plasmon modes is found (shown in color). The induced density of the plasmon modes is highly localized perpendicular to the nanoribbon, and oscillates in the direction parallel to the ribbon, with wave vector $q_\parallel$. The potential and density of the modes are shown in a cross-sectional view in

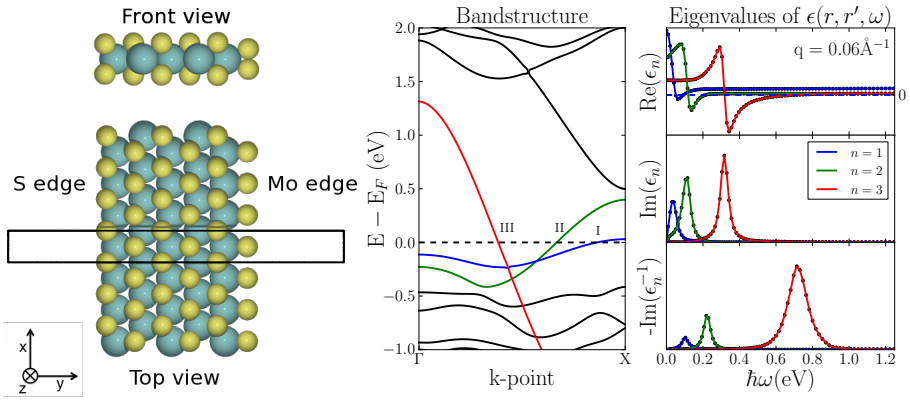

Figure 6.7: a) Sketch of the MoS_2 nanowire used for the calculations. b) DFT bandstructure of the MoS_2 nanoribbon, revealing three metallic edge states (I)-(III). The remaining bands produce a band gap of approximately 2 eV. (c) Eigenvalues of the dielectric matrix, having three solutions for $\mathrm{Re}\,\epsilon = 0$ at low energies. Each of the solutions stems from one of the metallic bands (relation shown in color), and corresponds to a plasmon eigenmode localized on one of the edges.

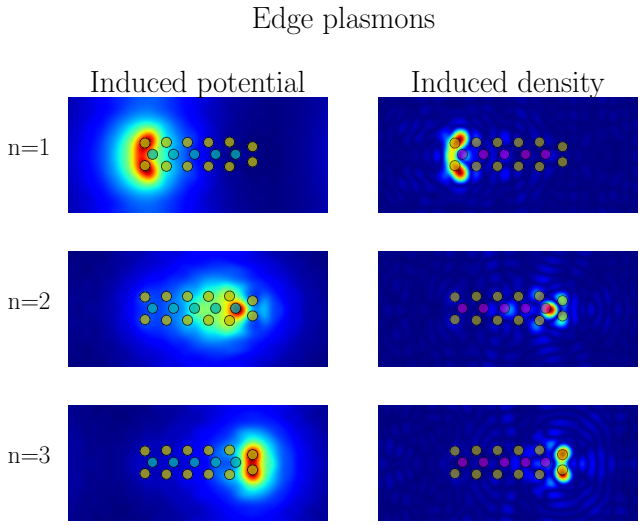

Figure 6.8: Induced potential and density of the three edge plasmons. The solution $n = 3$ stems from the electronic band (III), and is highly localized on the S-dimers on the Mo-edge (to the right). (The ripples in the induced density is due to a finite number of plane-waves in the representation of ϵ).

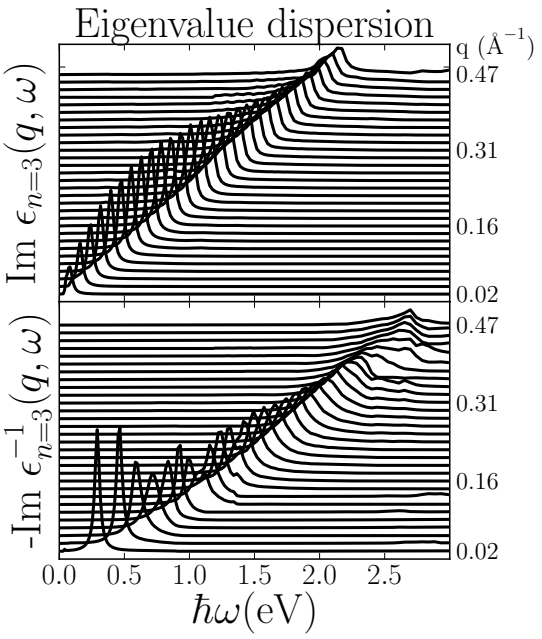

Figure 6.9: Waterfall plot of the eigenvalue dispersion with q. The single particle spectrum (Imϵ_n) shows a linear dispersion with $q_\parallel$, since the transitions stems from the almost linear electronic band (III), see Fig. 6.7b(a). The peaks of the plasmon resonances($-$Imϵ_n^{-1}) are shifted to higher energies due to the collective behaviour of the resonance. As q increases the plasmon is damped, resulting in broadening and reduced weight of the peak.

Figure. 6.8. In particular, the solution $n = 3$ originating from the metallic state (III) is highly localized at the edge; Thus, it is a 1D plasmon localized on the atomic scale.

In order to study the origin of this plasmon closer, a waterfall plot of the eigenvalue single-particle spectrum ($\mathrm{Im}\,\epsilon_n$), and the eigenvalue loss spectrum ($-\mathrm{Im}\,\epsilon_n^{-1}$) is shown in Fig. 6.9. The single particle transitions stem from the nearly linear electronic band (III), and the peak energy grows linearly with q, in correspondence with the 1D model for the density response function, Eq. (6.5). The weight of the transitions, defined as the area under the loss peak, approaches zero as $q \to 0$ as expected. The plasmon resonances seen in the lower panel is shifted to higher energies compared to the single-particle spectrum, reflecting a significant degree of collective behavior, where a large portion of the energy is stored in the collective motion of the electrons. For increasing q, the resonance is broadened due to damping, that stems from coupling to interband transitions and screening of the Coulomb potential.

In Fig. 6.10 the dispersion of the plasmon energy with q is plotted together

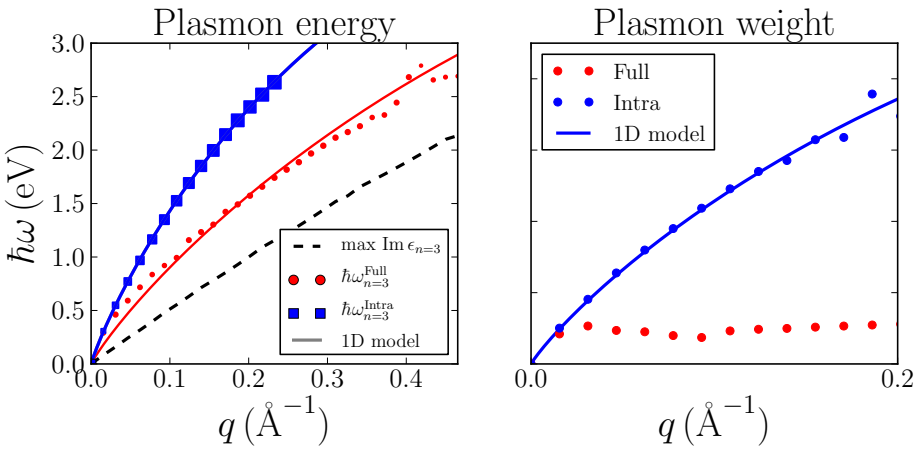

Figure 6.10: Plasmon energy and weight of the edge plasmon at the S-dimers of the Mo-edge ($n = 3$), comparing the full result (red) to the undamped intra-band plasmon (blue). The undamped plasmon is in good agreement with the 1D model, Eq. (6.8), while the full result cannot be described with this model due to a screening of the plasmon that is (q, ω)-dependent.

with the single-particle energies. Shown is also the dispersion of the undamped plasmon plasmon, that is obtained by only including the single metallic band (III) in the response calculation, see Eq. (4.7). The inclusion of all the remaining bands in the full result clearly leads to a decrease in plasmon energy and weight (the weight calculated as the integral over the loss peak).

The results have been fitted to the 1D RPA model, Eq. (6.8), where the 1D Coulomb interaction is written as: $V(q) = V_0 2|\ln(qa)|$, with a being the width of the 1D system and V_0 a system dependent interaction strength. The quality of the fit to the undamped result is excellent. In order to fit to the full result, the same value for a is used. This returns an interaction strength that is decreased by a factor of three compared to the undamped result. However, as seen from the poor quality of the fit to the full result, the change in plasmon energy cannot be accounted for by a mere decrease in V_0.

This also follows from considering the plasmon weights, also shown in Fig. 6.8, where the full result stays almost constant as q increases, while weight of the undamped plasmon increases in good correspondence with the 1D model. Clearly, this cannot be captured by a mere change in V_0. Therefore the change should be accounted for by the general case of a (ω, q)-dependent screening of the Coulomb potential: $V(q, \omega) = \epsilon^{-1}(q, \omega) 2|\ln(qa)|$. This behaviour is qualitatively similar to the damping of 2D plasmons in metallic transition metal dichalcogenides, see Section 4.3, where including inter-band transitions also lead to a downshift in the energy and weight of the plasmon.

Another question is whether these edge states could be identified experimentally with spatially resolved EELS. The theoretical spectrum has been calculated

using the approach described in 3.3, assuming a normal beam that excites plasmons with wave vector, q_x, parallel to the ribbon. Also the dependence on beam position along x is neglected, such that the scattering probability is a function of beam position along y:

$$P(y_0, q_x, \omega) \propto -\operatorname{Im} \sum_{G_y, G'_y} \frac{e^{iG_y y_0}}{q_x^2 + G_y^2} \, \chi_{G_y, G'_y}(q_x, \omega) \, \frac{e^{-iG'_y y_0}}{q_x^2 + G_y'^2}. \tag{6.10}$$

Here it is assumed that the signal can be resolved with respect to momentum transfer, q_x, which is challenging in practice due to the loss in signal when only a part of the signal is collected. The spectrum is shown in Fig. 6.11 for two different magnitudes of momentum transfer, as a contour plot versus energy and beam position perpendicular to the wire edges, y_0. For low momentum transfers the Coulomb potential is long ranged, which leads to a strong but also spatially smeared out signal from the S-dimers on the Mo-edge due to the edge plasmon. At higher momentum transfers the signal is more localized, and shifted to higher energy due to the strong wave-vector dependence of the plasmon energy in 1D. Also a weak signal from the other two edge plasmons is visible at lower energy. Provided that the long-ranged contributions at low momentum transfers can be filtered out from the experimental spectrum, we predict that it should be possible to verify the existence of a 1D resonance at the edge using spatially resolved EELS.

To conclude this section, we have proposed another material for hosting 1D plasmons, where the eigenmode analysis enabled the spacial visualization of the different plasmon modes as edge-states. We found that a particular edge configuration (the S-dimers on the Mo-edge) lead to a plasmon highly localized on the edge. By investigating the effects of the damping of the plasmon, electronic transitions associated within the MoS_2 ribbon was found to introduce damping of the plasmon. Finally the clear signature of the edge plasmon in the spatially resolved electron energy loss spectrum was demonstrated.

6.4 Summary

In summary, the properties of plasmons in 1D was studied in different systems, where quantum mechanical effects were found to have a large impact on the plasmon modes in several cases. For 1D systems at a finite width, the plasmon eigenmode analysis identified several plasmon eigenmodes that deviates from the classical result due to electron spill-out and non-local response. Also the hybridized plasmon of a nanowire dimer was found to be altered at small separations due to non-local response and electron tunneling between the wires. In the case of the edge states on MoS_2 nanowires we have proposed an atomic-scale system for hosting 1D plasmons of atomic-scale confinement. Here the edge plasmon can be understood as a 1D excitations that is screened by the electrons within the MoS_2 sheet, leading to deviations from the idealized 1D result. From the theoretical loss spectrum we predict that this resonance could be observed with spatially resolved EELS.

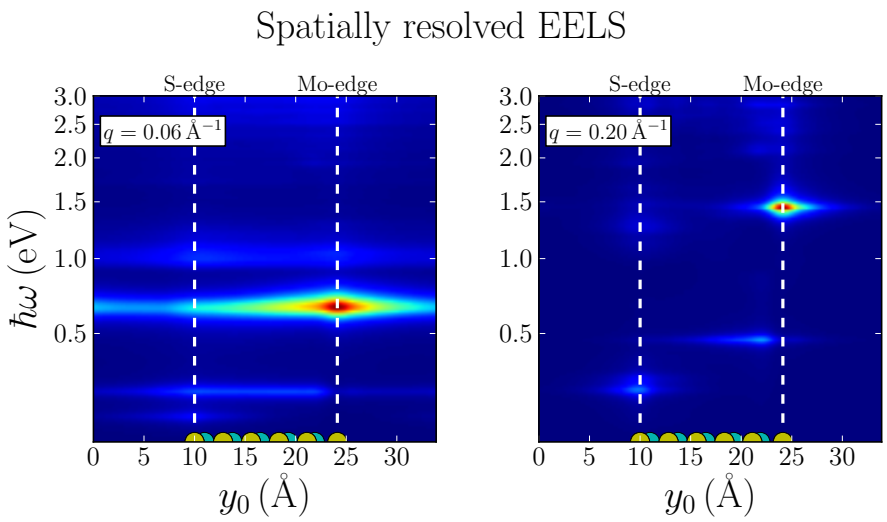

Figure 6.11: Spatially resolved electron energy loss spectrum calculated for two different values of momentum transfer q_x . We observe a strong signal associated with the S-dimer plasmon at the Mo edge, while the two other plasmon modes give a weaker response. At low momentum transfers, the signal is less localized due to the long range of the Coulomb potential.

Chapter 7

Conclusion

In the presented work, *ab initio* quantum theory has been applied to study the properties of plasmons atomic-scale nanostructures, and furthermore the need for a quantum mechanical description of the plasmon in these structures was demonstrated. Density functional theory (DFT) and linear response time-dependent DFT were used to calculate the non-local, dynamical dielectric function on top of a quantum mechanical description of single-particle electronic states. A method for identifying the plasmon as eigenmodes of the electronic system was presented, where an eigenvalue equation for the dielectric matrix was defined. This enabled the visualization of localized plasmon modes and characterization with respect to symmetry, which is not possible by standard macroscopic definitions of the dielectric function.

The eigenmode approach identifies the eigen-resonances of the electron system; i.e. it does not provide information on how the modes will couple to external perturbations. To supplement this method, an expression for the spatially resolved electron energy loss spectrum has been derived, which enables us to predict the probability for exciting a resonance with a highly localized electron beam. For example, this was used to predict a localized signal associated with a one-dimensional plasmon on the edge of MoS_2. Another important concern, which has not been adressed in this thesis, is how a plasmon will couple to light. Accounting for this coupling requires a more comprehensive extension of the theoretical description.

Quantum mechanical effects, such as coupling to single-particle transitions, electron spill-out, tunneling, and spatial non-locality have been found to modify the behavior of the plasmon in the studied systems. In the case of nanostructured simple metals, where sodium thin films and Jellium nanowires were studied, an increasing redshift in the plasmon energy with respect to classical models were found with decreasing size of the structures. This can be explained by the electron-spill out from the surface, that leads to a decrease in electron density available for the plasmon resonance. This finding contradicts experimental observations for silver nanoparticles where a blueshift with decreasing particle size was observed. However, the calculations for silver thin films revealed a qualita-

tively different behavior of the surface plasmon due to coupling to single-particle transitions, originating from the d-band of silver. A size-dependent strength of this coupling can also be used to explain the blueshift observed in experiments.

Changes in the energy and weight of the plasmon mode due to interband transitions were observed in several cases. For example, the 2D plasmons in monolayer transition metal dichalcogenides was found to deviate significantly from the undamped result. Here, the plasmon energy reached a plateau at higher momentum transfers completely dominated by the onset of interband transitions. Also for the one-dimensional plasmon on a particular edge-configuration of MoS_2, the plasmon deviated from the ideal 1D behavior due to a (q, ω)-dependent screening originating from the MoS_2 sheet. Substrate induced damping of the plasmon does also take place, as observed for graphene/hBN heterostructures, where the hybridized plasmons modes of two graphene sheets was slightly shifted in energy when hBN was inserted between the graphene layers.

The main disadvantage of *ab initio* methods is their high computational cost that limits these calculations to a finite number of atoms. Thus, a quantum mechanical treatment of the dielectric function could favorable be used together with semi-classical models, where larger structures can be described, while still including relevant quantum effects.

As a new approach for studying van der Waals heterostructures with quantum mechanical accuracy, but at lower computational cost, the Quantum electrostatic heterostructure (QEH) model has been presented. In this calculational scheme, the dielectric function of the heterostructures are calculated from the *ab initio* response function of the individual layers through an electrostatic interlayer coupling. The QEH model, together with a database containing the dielectric building blocks of more than 50 2D materials, can be applied to predict the effects of substrates on the electronic excitations in these materials.

Appendix A

The Heterostructure class

The following is printed from the python implementation of the QEH module, where a description of the input parameters and associated methods is given.

```
class Heterostructure:
    """This class defines dielectric function of heterostructures
        and related physical quantities."""
    def __init__(self, structure, d,
                 include_dipole=True, d0=None,
                 wmax=10, qmax=None):
        """Creates a Heterostructure object.

        Parameters:
        structure: list of str
            Heterostructure set up. Each entry should consist of number of
            layers + chemical formula.
            For example: ['3H-MoS2', graphene', '10H-WS2'] gives 3 layers of
            H-MoS2, 1 layer of graphene and 10 layers of H-WS2.
        d: array of floats
            Interlayer distances for neighboring layers in Ang.
            Length of array = number of layers - 1
        d0: float
            The width of a single layer in Ang, only used for monolayer
            calculation. The layer separation in bulk is typically a good
            measure.
        include_dipole: Bool
            Includes dipole contribution if True
        wmax: float
            Cutoff for frequency grid (eV)
        qmax: float
            Cutoff for wave-vector grid (1/Ang)
        """

    def get_chi_matrix(self):
```

```
        """
        Dyson equation: chi_full = chi_intra + chi_intra V_inter chi_full

        Returns:
            chi_qwij
        """

    def get_eps_matrix(self, step_potential=False):
        """
        Get dielectric matrix as: eps^{-1} = I + V chi_full

        step_potential: Bool
            If True: Use step function average of the Coulomb potential.

        Returns:
            eps_qwij
        """


    def get_macroscopic_dielectric_function(self, direction = 'x',
                                            layers=None):
        """
        Calculates the averaged  dielectric matrix over the structure in the
        static limit \omega = 0

        Parameters:
        direction : 'x' or 'z'
            'x' for q parallel to the layers,
            'z' for q perpendicular to the layers in the q_z -> 0 limit
        layers: array of integers
            list with index of specific layers to include in the average

        Returns:
            list of q-points, dielectric function
        """

    def get_response(self, dipole=False):
        """
        Get the induced density and potential due to constant perturbation
        obtained as: rho_ind(r) = \int chi(r,r') dr'

        dipole: Bool
            use dipole perturbation if True

        Returns:
            z grid, induced density, induced potential, layer positions
        """

    def get_plasmon_eigenmodes(self):
        """
```

```
Diagonalize the dieletric matrix to get the plasmon eigenresonances
of the system.

Returns:
    Eigenvalue array (shape Nq x nw x dim), z-grid, induced densities,
    induced potentials, energies at zero crossings.
"""
```

Bibliography

[1] S. A. Maier and H. A. Atwater, "Plasmonics: Localization and guiding of electromagnetic energy in metal/dielectric structures," *Journal of Applied Physics*, vol. 98, p. 011101, 2005.

[2] G. E. Moore *et al.*, "Cramming more components onto integrated circuits, 1965," *Electronics Magazine*, p. 4, 1965.

[3] E. Ozbay, "Plasmonics: Merging photonics and electronics at nanoscale dimensions," *Science*, vol. 311, pp. 189–193, 2006.

[4] H. A. Atwater, "The promise of plasmonics," *Scientific American*, vol. 296, pp. 56–62, 2007.

[5] J. Heber, "Plasmonics: Surfing the wave," *Nature News*, vol. 461, pp. 720–722, 2009.

[6] H. A. Atwater and A. Polman, "Plasmonics for improved photovoltaic devices," *Nature Materials*, vol. 9, pp. 205–213, 2010.

[7] K. A. Willets and R. P. Van Duyne, "Localized surface plasmon resonance spectroscopy and sensing," *Annu. Rev. Phys. Chem.*, vol. 58, pp. 267–297, 2007.

[8] E. M. Larsson, C. Langhammer, I. Zorić, and B. Kasemo, "Nanoplasmonic probes of catalytic reactions," *Science*, vol. 326, pp. 1091–1094, 2009.

[9] K. Kneipp, Y. Wang, H. Kneipp, L. T. Perelman, I. Itzkan, R. R. Dasari, and M. S. Feld, "Single molecule detection using surface-enhanced Raman scattering (SERS)," *Physical Review Letters*, vol. 78, p. 1667, 1997.

[10] F. J. G. de Abajo, "Microscopy: Plasmons go quantum," *Nature*, vol. 483, pp. 417–418, 2012.

[11] A. Liebsch, "Surface-plasmon dispersion and size dependence of Mie resonance: Silver versus simple metals," *Physical Review B*, vol. 48, p. 11317, 1993.

[12] F. Ouyang, P. Batson, and M. Isaacson, "Quantum size effects in the surface-plasmon excitation of small metallic particles by electron-energy-loss spectroscopy," *Physical Review B*, vol. 46, p. 15421, 1992.

[13] J. Tiggesbäumker, L. Köller, K.-H. Meiwes-Broer, and A. Liebsch, "Blue shift of the mie plasma frequency in Ag clusters and particles," *Physical Review A*, vol. 48, p. R1749, 1993.

[14] J. A. Scholl, A. L. Koh, and J. A. Dionne, "Quantum plasmon resonances of individual metallic nanoparticles," *Nature*, vol. 483, pp. 421–427, 2012.

[15] S. Raza, G. Toscano, A.-P. Jauho, M. Wubs, and N. A. Mortensen, "Unusual resonances in nanoplasmonic structures due to nonlocal response," *Physical Review B*, vol. 84, p. 121412, 2011.

[16] J. Zuloaga, E. Prodan, and P. Nordlander, "Quantum description of the plasmon resonances of a nanoparticle dimer," *Nano Letters*, vol. 9, pp. 887–891, 2009.

[17] P. Zhang, J. Feist, A. Rubio, P. García-González, and F. Garcia-Vidal, "Ab initio nanoplasmonics: The impact of atomic structure," *Physical Review B*, vol. 90, p. 161407, 2014.

[18] N. A. Mortensen, S. Raza, M. Wubs, T. Søndergaard, and S. I. Bozhevolnyi, "A generalized non-local optical response theory for plasmonic nanostructures," *Nature Communications*, vol. 5, 2014.

[19] K. Novoselov, A. K. Geim, S. Morozov, D. Jiang, M. Katsnelson, I. Grigorieva, S. Dubonos, and A. Firsov, "Two-dimensional gas of massless dirac fermions in graphene," *Nature*, vol. 438, pp. 197–200, 2005.

[20] K. F. Mak, C. Lee, J. Hone, J. Shan, and T. F. Heinz, "Atomically thin MoS_2: A new direct-gap semiconductor," *Physical Review Letters*, vol. 105, p. 136805, 2010.

[21] A. Grigorenko, M. Polini, and K. Novoselov, "Graphene plasmonics," *Nature Photonics*, vol. 6, pp. 749–758, 2012.

[22] A. Woessner, M. B. Lundeberg, Y. Gao, A. Principi, P. Alonso-González, M. Carrega, K. Watanabe, T. Taniguchi, G. Vignale, M. Polini, *et al.*, "Highly confined low-loss plasmons in graphene–boron nitride heterostructures," *Nature Materials*, 2014.

[23] L. Ju, B. Geng, J. Horng, C. Girit, M. Martin, Z. Hao, H. A. Bechtel, X. Liang, A. Zettl, Y. R. Shen, *et al.*, "Graphene plasmonics for tunable terahertz metamaterials," *Nature Nanotechnology*, vol. 6, pp. 630–634, 2011.

[24] E. Hwang and S. D. Sarma, "Dielectric function, screening, and plasmons in two-dimensional graphene," *Physical Review B*, vol. 75, p. 205418, 2007.

[25] J. Yan, K. S. Thygesen, and K. W. Jacobsen, "Nonlocal screening of plasmons in graphene by semiconducting and metallic substrates: First-principles calculations," *Physical Review Letters*, vol. 106, p. 146803, 2011.

[26] F. Rasmussen and K. S. Thygesen, "Computational 2D materials database: Electronic structure of transition metal dichalcogenides and oxides," *Journal of Physical Chemistry C*, 2015. Accepted.

[27] P. Cudazzo, M. Gatti, and A. Rubio, "Local-field effects on the plasmon dispersion of two-dimensional transition metal dichalcogenides," *New Journal of Physics*, vol. 15, p. 125005, 2013.

[28] A. Castellanos-Gomez, E. Navarro-Moratalla, G. Mokry, J. Quereda, E. Pinilla-Cienfuegos, N. Agraït, H. S. van der Zant, E. Coronado, G. A. Steele, and G. Rubio-Bollinger, "Fast and reliable identification of atomically thin layers of $TaSe_2$ crystals," *Nano Research*, vol. 6, pp. 191–199, 2013.

[29] A. Geim and I. Grigorieva, "Van der Waals heterostructures," *Nature*, vol. 499, pp. 419–425, 2013.

[30] T. Nagao, S. Yaginuma, T. Inaoka, and T. Sakurai, "One-dimensional plasmon in an atomic-scale metal wire," *Physical Review Letters*, vol. 97, pp. 1–4, 2006.

[31] M. Bosman, V. J. Keast, M. Watanabe, A. I. Maaroof, and M. B. Cortie, "Mapping surface plasmons at the nanometre scale with an electron beam," *Nanotechnology*, vol. 18, p. 165505, 2007.

[32] F. G. De Abajo, "Optical excitations in electron microscopy," *Reviews of Modern Physics*, vol. 82, p. 209, 2010.

[33] A. L. Koh, K. Bao, I. Khan, W. E. Smith, G. Kothleitner, P. Nordlander, S. A. Maier, and D. W. McComb, "Electron energy-loss spectroscopy (EELS) of surface plasmons in single silver nanoparticles and dimers: influence of beam damage and mapping of dark modes," *ACS Nano*, vol. 3, pp. 3015–3022, 2009.

[34] O. Nicoletti, M. Wubs, N. A. Mortensen, W. Sigle, P. A. Van Aken, and P. A. Midgley, "Surface plasmon modes of a single silver nanorod: An electron energy loss study," *Optics express*, vol. 19, pp. 15371–15379, 2011.

[35] B. S. Guiton, V. Iberi, S. Li, D. N. Leonard, C. M. Parish, P. G. Kotula, M. Varela, G. C. Schatz, S. J. Pennycook, and J. P. Camden, "Correlated optical measurements and plasmon mapping of silver nanorods," *Nano Letters*, vol. 11, pp. 3482–3488, 2011.

[36] W. Zhou, J. Lee, J. Nanda, S. T. Pantelides, S. J. Pennycook, and J.-C. Idrobo, "Atomically localized plasmon enhancement in monolayer graphene," *Nature Nanotechnology*, vol. 7, pp. 161–165, 2012.

[37] J. Kohanoff, *Electronic structure calculations for solids and molecules: theory and computational methods*. Cambridge University Press, 2006.

[38] P. Hohenberg and W. Kohn, "Inhomogeneous electron gas," *Physical Review*, vol. 136, p. B864, 1964.

[39] W. Kohn and L. J. Sham, "Self-consistent equations including exchange and correlation effects," *Physical Review*, vol. 140, p. A1133, 1965.

[40] G. Grosso and G. P. Parravicini, *Solid state Physics*. Academic Press, 2000.

[41] J. P. Perdew, K. Burke, and M. Ernzerhof, "Generalized gradient approximation made simple," *Physical Review Letters*, vol. 77, p. 3865, 1996.

[42] L. Hedin, "New method for calculating the one-particle green's function with application to the electron-gas problem," *Physical Review*, vol. 139, p. A796, 1965.

[43] E. Salpeter and H. A. Bethe, "A relativistic equation for bound-state problems," *Physical Review*, vol. 84, p. 1232, 1951.

[44] J. Enkovaara, C. Rostgaard, J. J. Mortensen, J. Chen, M. Dułak, L. Ferrighi, J. Gavnholt, C. Glinsvad, V. Haikola, H. Hansen, *et al.*, "Electronic structure calculations with GPAW: A real-space implementation of the projector augmented-wave method," *Journal of Physics: Condensed Matter*, vol. 22, p. 253202, 2010.

[45] J. J. Mortensen, L. B. Hansen, and K. W. Jacobsen, "Real-space grid implementation of the projector augmented wave method," *Physical Review B*, vol. 71, p. 035109, 2005.

[46] F. Hüser, T. Olsen, and K. S. Thygesen, "Quasiparticle gw calculations for solids, molecules, and two-dimensional materials," *Physical Review B*, vol. 87, p. 235132, 2013.

[47] J. Yan, K. W. Jacobsen, and K. S. Thygesen, "Optical properties of bulk semiconductors and graphene/boron nitride: The bethe-salpeter equation with derivative discontinuity-corrected density functional energies," *Physical Review B*, vol. 86, p. 045208, 2012.

[48] J. Yan, J. J. Mortensen, K. W. Jacobsen, and K. S. Thygesen, "Linear density response function in the projector augmented wave method: Applications to solids, surfaces, and interfaces," *Physical Review B*, vol. 83, p. 245122, 2011.

[49] H. Bruus and K. Flensberg, *Many-Body Quantum Theory in Condensed Matter physics: an introduction*. Oxford University Press, Oxford, 2004.

[50] R. Kubo, "Statistical-mechanical theory of irreversible processes. i. general theory and simple applications to magnetic and conduction problems," *Journal of the Physical Society of Japan*, vol. 12, pp. 570–586, 1957.

[51] J. M. Pitarke, V. M. Silkin, E. V. Chulkov, and P. M. Echenique, "Theory of surface plasmons and surface-plasmon polaritons," *Reports on Progress in Physics*, vol. 70, pp. 1–87, 2007.

[52] E. Gross and W. Kohn, "Time-dependent density-functional theory," *Advances in Quantum Chemistry*, vol. 21, pp. 255–291, 1990.

[53] P. Drude, "Zur elektronentheorie der metalle," *Annalen der Physik*, vol. 306, pp. 566–613, 1900.

[54] C. Kittel, *Introduction to Solid State Physics: 8th Ed.* John Wiley, 2005.

[55] S. L. Adler, "Quantum theory of the dielectric constant in real solids," *Physical Review*, vol. 126, pp. 413–420, 1962.

[56] N. Wiser, "Dielectric constant with local field effects included," *Physical Review*, vol. 129, pp. 62–69, 1963.

[57] "Linear dielectric response of an extended system: theory." `https://wiki.fysik.dtu.dk/gpaw/documentation/tddft/dielectric_response.html`, 2015.

[58] F. Hüser, T. Olsen, and K. S. Thygesen, "How dielectric screening in two-dimensional crystals affects the convergence of excited-state calculations: Monolayer MoS_2," *Physical Review B*, vol. 88, p. 245309, 2013.

[59] C. A. Rozzi, D. Varsano, A. Marini, E. K. Gross, and A. Rubio, "Exact Coulomb cutoff technique for supercell calculations," *Physical Review B*, vol. 73, p. 205119, 2006.

[60] R. Sundararaman and T. Arias, "Regularization of the Coulomb singularity in exact exchange by Wigner-Seitz truncated interactions: Towards chemical accuracy in nontrivial systems," *Physical Review B*, vol. 87, p. 165122, 2013.

[61] X. Fan, W. Zheng, and D. J. Singh, "Light scattering and surface plasmons on small spherical particles," *Light: Science & Applications*, vol. 3, p. e179, 2014.

[62] G. Mie, "Beiträge zur optik trüber medien, speziell kolloidaler metallösungen," *Annalen der Physik*, vol. 330, pp. 377–445, 1908.

[63] S. J. Leon, *Linear algebra with applications*. Pearson, 7th ed., 2006.

[64] E. Najafi, A. P. Hitchcock, D. Rossouw, and G. A. Botton, "Mapping defects in a carbon nanotube by momentum transfer dependent electron energy loss spectromicroscopy," *Ultramicroscopy*, vol. 113, pp. 158–164, 2012.

[65] J. Harl, *The linear response function in density functional theory.* PhD thesis, uniwien, 2008.

[66] B. M. Santoyo and M. Del Castillo-Mussot, "Plasmons in three, two and one dimension," *Revista Mexicana de Fìsica*, vol. 39, pp. 640–652, 1993.

[67] F. Stern, "Polarizability of a two-dimensional electron gas," *Physical Review Letters*, vol. 18, p. 546, 1967.

[68] A. Ramasubramaniam, "Large excitonic effects in monolayers of molybdenum and tungsten dichalcogenides," *Physical Review B*, vol. 86, p. 115409, 2012.

[69] R. A. Ferrell, "Predicted radiation of plasma oscillations in metal films," *Physical Review*, vol. 111, p. 1214, 1958.

[70] K.-D. Tsuei, E. Plummer, A. Liebsch, E. Pehlke, K. Kempa, and P. Bakshi, "The normal modes at the surface of simple metals," *Surface Science*, vol. 247, pp. 302–326, 1991.

[71] A. J. Bennett, "Influence of the electron charge distribution on surface-plasmon dispersion," *Physical Review B*, vol. 1, p. 203, 1970.

[72] W. Schaich and J. F. Dobson, "Excitation modes of neutral jellium slabs," *Physical Review B*, vol. 49, p. 14700, 1994.

[73] P. R. West, S. Ishii, G. V. Naik, N. K. Emani, V. M. Shalaev, and A. Boltasseva, "Searching for better plasmonic materials," *Laser & Photonics Reviews*, vol. 4, pp. 795–808, 2010.

[74] J. Yan, K. W. Jacobsen, and K. S. Thygesen, "First-principles study of surface plasmons on Ag (111) and H/Ag (111)," *Physical Review B*, vol. 84, p. 235430, 2011.

[75] M. Kuisma, J. Ojanen, J. Enkovaara, and T. Rantala, "Kohn-Sham potential with discontinuity for band gap materials," *Physical Review B*, vol. 82, p. 115106, 2010.

[76] P. W. Anderson, "Localized magnetic states in metals," *Physical Review*, vol. 124, p. 41, 1961.

[77] D. Newns, "Self-consistent model of hydrogen chemisorption," *Physical Review*, vol. 178, p. 1123, 1969.

[78] L. Song, L. Ci, H. Lu, P. B. Sorokin, C. Jin, J. Ni, A. G. Kvashnin, D. G. Kvashnin, J. Lou, B. I. Yakobson, *et al.*, "Large scale growth and characterization of atomic hexagonal boron nitride layers," *Nano letters*, vol. 10, pp. 3209–3215, 2010.

[79] L. Britnell, R. Ribeiro, A. Eckmann, R. Jalil, B. Belle, A. Mishchenko, Y.-J. Kim, R. Gorbachev, T. Georgiou, S. Morozov, *et al.*, "Strong light-matter interactions in heterostructures of atomically thin films," *Science*, vol. 340, pp. 1311–1314, 2013.

[80] F. Withers, O. Del Pozo-Zamudio, A. Mishchenko, A. P. Rooney, A. Gholinia, K. Watanabe, T. Taniguchi, S. J. Haigh, A. K. Geim, A. I. Tartakovskii, and K. S. Novoselov, "Light-emitting diodes by band-structure engineering in van der waals heterostructures," *Nature Materials*, vol. 14, pp. 301–306, 2015.

[81] "GPAW: DFT and beyond within the projector-augmented wave method." `https://wiki.fysik.dtu.dk/gpaw/index.html`, 2015.

[82] "Computational materials repository." `https://cmr.fysik.dtu.dk/`, 2015.

[83] E. Prodan, C. Radloff, N. J. Halas, and P. Nordlander, "A hybridization model for the plasmon response of complex nanostructures," *Science*, vol. 302, pp. 419–422, 2003.

[84] H. Wang, D. W. Brandl, P. Nordlander, and N. J. Halas, "Plasmonic nanostructures: Artificial molecules," *Accounts of Chemical Research*, vol. 40, pp. 53–62, 2007.

[85] E. Hwang and S. D. Sarma, "Plasmon modes of spatially separated double-layer graphene," *Physical Review B*, vol. 80, p. 205405, 2009.

[86] H. Ditlbacher, A. Hohenau, D. Wagner, U. Kreibig, M. Rogers, F. Hofer, F. R. Aussenegg, and J. R. Krenn, "Silver nanowires as surface plasmon resonators," *Physical Review Letters*, vol. 95, p. 257403, 2005.

[87] A. Huck, S. Kumar, A. Shakoor, and U. L. Andersen, "Controlled coupling of a single nitrogen-vacancy center to a silver nanowire," *Physical Review Letters*, vol. 106, p. 096801, 2011.

[88] U. Krieg, C. Brand, C. Tegenkamp, and H. Pfnür, "One-dimensional collective excitations in Ag atomic wires grown on si (557)," *Journal of Physics: Condensed Matter*, vol. 25, p. 014013, 2013.

[89] F. Haldane, "'luttinger liquid theory'of one-dimensional quantum fluids. i. properties of the luttinger model and their extension to the general 1d interacting spinless fermi gas," *Journal of Physics C: Solid State Physics*, vol. 14, p. 2585, 1981.

[90] J. Voit, "One-dimensional Fermi liquids," *Reports on Progress in Physics*, vol. 58, p. 977, 1995.

[91] M. Bockrath, D. H. Cobden, J. Lu, A. G. Rinzler, R. E. Smalley, L. Balents, and P. L. McEuen, "Luttinger-liquid behaviour in carbon nanotubes," *Nature*, vol. 397, pp. 598–601, 1999.

[92] A. Yacoby, H. L. Stormer, N. S. Wingreen, L. N. Pfeiffer, K. W. Baldwin, and K. W. West, "Nonuniversal conductance quantization in quantum wires," *Physical Review Letters*, vol. 77, p. 4612, 1996.

[93] Q. P. Li, S. D. Sarma, and R. Joynt, "Elementary excitations in one-dimensional quantum wires: Exact equivalence between the random-phase approximation and the Tomonaga-Luttinger model," *Physical Review B*, vol. 45, pp. 13713–13716, 1992.

[94] K. L. Jensen, *Quantum Theory of Plasmonic Jellium Nanostructures*. PhD thesis, Department of Physics, Technical University of Denmark, 2012. Master's Thesis.

[95] J. Gervasoni and N. Arista, "Plasmon excitations in cylindrical wires by external charged particles," *Physical Review B*, vol. 68, p. 235302, 2003.

[96] I. Romero, J. Aizpurua, G. W. Bryant, and F. J. García De Abajo, "Plasmons in nearly touching metallic nanoparticles: Singular response in the limit of touching dimers," *Optics Express*, vol. 14, pp. 9988–9999, 2006.

[97] K. J. Savage, M. M. Hawkeye, R. Esteban, A. G. Borisov, J. Aizpurua, and J. J. Baumberg, "Revealing the quantum regime in tunnelling plasmonics," *Nature*, vol. 491, pp. 574–577, 2012.

[98] J. A. Scholl, A. García-Etxarri, A. L. Koh, and J. A. Dionne, "Observation of quantum tunneling between two plasmonic nanoparticles," *Nano Letters*, vol. 13, pp. 564–569, 2013.

[99] A. Moradi, "Plasmon hybridization in parallel nano-wire systems," *Physics of Plasmas*, vol. 18, p. 064508, 2011.

[100] R. Esteban, A. G. Borisov, P. Nordlander, and J. Aizpurua, "Bridging quantum and classical plasmonics with a quantum-corrected model," *Nature Communications*, vol. 3, p. 825, 2012.

[101] J. Zuloaga, E. Prodan, and P. Nordlander, "Quantum description of the plasmon resonances of a nanoparticle dimer," *Nano Letters*, vol. 9, pp. 887–891, 2009.

[102] T. V. Teperik, P. Nordlander, J. Aizpurua, and A. G. Borisov, "Robust subnanometric plasmon ruler by rescaling of the nonlocal optical response," *Physical Review Letters*, vol. 110, p. 263901, 2013.

[103] S. Helveg, J. V. Lauritsen, E. Lægsgaard, I. Stensgaard, J. K. Nørskov, B. Clausen, H. Topsøe, and F. Besenbacher, "Atomic-scale structure of single-layer MoS_2 nanoclusters," *Physical Review Letters*, vol. 84, p. 951, 2000.

[104] M. Bollinger, K. W. Jacobsen, and J. K. Nørskov, "Atomic and electronic structure of MoS_2 nanoparticles," *Physical Review B*, vol. 67, p. 085410, 2003.

[105] C. Zhang, A. Johnson, C.-L. Hsu, L.-J. Li, and C.-K. Shih, "Direct imaging of band profile in single layer MoS_2 on graphite: quasiparticle energy gap, metallic edge states, and edge band bending," *Nano Letters*, vol. 14, pp. 2443–2447, 2014.

Papers

Paper I

Spatially resolved quantum plasmon modes in metallic nano-films from first-principles.
Kirsten Andersen, Karsten W. Jacobsen, and Kristian S. Thygesen, Phys. Rev. B 86, 245129 (2012)

Spatially resolved quantum plasmon modes in metallic nano-films from first-principles

Kirsten Andersen,[1] Karsten W. Jacobsen,[1] and Kristian S. Thygesen[1,2,*]

[1]*Center for Atomic-scale Materials Design (CAMD), Department of Physics, Technical University of Denmark, DK-2800 Kgs. Lyngby, Denmark*

[2]*Center for Nanostructured Graphene (CNG), Department of Physics, Technical University of Denmark, DK-2800 Kgs. Lyngby, Denmark*

(Received 14 August 2012; published 26 December 2012)

Electron energy loss spectroscopy (EELS) can be used to probe plasmon excitations in nanostructured materials with atomic-scale spatial resolution. For structures smaller than a few nanometers, quantum effects are expected to be important, limiting the validity of widely used semiclassical response models. Here we present a method to identify and compute spatially resolved plasmon modes from first-principles based on a spectral analysis of the dynamical dielectric function. As an example we calculate the plasmon modes of 0.5 to 4 nm thick Na films and find that they can be classified as (conventional) surface modes, subsurface modes, and a discrete set of bulk modes resembling standing waves across the film. We find clear effects of both quantum confinement and nonlocal response. The quantum plasmon modes provide an intuitive picture of collective excitations of confined electron systems and offer a clear interpretation of spatially resolved EELS spectra.

DOI: 10.1103/PhysRevB.86.245129 PACS number(s): 73.21.−b, 71.45.Gm, 73.22.Lp, 78.20.−e

I. INTRODUCTION

The dielectric properties of a material are to a large extent governed by the collective eigenmodes of its electron system known as plasmons.[1] Advances in spectroscopy and materials preparation have recently made it possible to study and control light-matter interactions at the nanometer length scale where particularly the surface plasmons play a key role.[2,3] While the ultimate goal of nanoplasmonics as a platform for ultrafast and compact information processing remains a challenge for the future, the unique plasmonic properties of metallic nanostructures have already been utilized in a number of applications including molecular sensors,[4,5] photocatalysis,[6] and thin-film solar cells.[7]

Electron energy loss spectroscopy (EELS) has been widely used to probe plasmon excitations in bulk materials and their surfaces. More recently, the use of highly confined electron beams available in transmission electron microscopes has made it possible to measure the loss spectrum of low-dimensional structures on a subnanometer length scale and with <0.1 eV energy resolution.[8] Because the loss spectrum is dominated by the plasmons this technique provides a means for visualizing the real-space structure plasmon excitations.[9]

All information about the plasmons of a given material is contained in its frequency-dependent dielectric function ϵ, which relates the total potential in the material to the externally applied potential to linear order,

$$\phi_{\text{ext}}(r,\omega) = \int \epsilon(r,r',\omega)\phi_{\text{tot}}(r',\omega)dr'. \qquad (1)$$

(We have specialized to the case of longitudinal fields which can be represented by scalar potentials.) In the widely used Drude model, one neglects the spatial variation of ϵ and describes the frequency dependence by a single parameter, the bulk plasmon frequency $\omega_p = \sqrt{ne^2/m\epsilon_0}$, where n is the average electron density of the material.[2] For metal surfaces the Drude model predicts the existence of surface plasmons with frequency $\omega_s = \omega_p/\sqrt{2}$. While the Drude model provides a reasonable description of plasmons in simple metal structures in the mesoscopic size regime, it fails to account for the dispersion (wave vector dependence) of the plasmon energy in extended systems and predicts a divergent field enhancement at sharp edges. These unphysical results are to some extent remedied by the semiclassical hydrodynamic models which can account for spatial nonlocality of ϵ and smooth charge density profiles at the metal-vacuum interface.[2,10,11] Still, for materials other than the simple metals and for truly nanometer sized structures, predictive modeling of plasmonic properties must be based on a full quantum mechanical description.[12,13] The calculation of plasmon energies and EELS spectra of periodic solids from first-principles is a well established discipline of computational condensed matter physics.[14–17] Here we apply these powerful methods to systematically map out the real space structure of plasmon excitations at the nanometer length scale.

In this paper we present a general method to calculate spatially resolved plasmon modes from first-principles. We apply the method to Na films of a few nanometer thickness where effects of quantum confinement and nonlocal response are expected to be important. The plasmon modes we find can be categorized as surface modes located mainly outside the metal surface, subsurface modes located just below the surface, and bulk modes. Very intuitively, the bulk plasmon modes resemble standing waves with nodes at the film surfaces. However, only plasmons with oscillation periods larger than 10 Å are found as a result of Landau damping which suppresses the strength of plasmon modes with smaller oscillation periods. Finally, we calculate the spatially resolved EELS spectrum of the metal films and show that all its features can be traced to excitation of specific plasmon modes.

II. METHOD

According to Eq. (1), a self-sustained charge density oscillation $\rho(r,\omega)$ can exist in a material if the related potential, satisfying the Poisson equation $\nabla^2\phi = -4\pi\rho$ (atomic units are used throughout), obeys the equation

$$\int \epsilon(r,r',\omega)\phi(r',\omega)dr' = 0. \qquad (2)$$

In general, this equation cannot be exactly satisfied because the dielectric function will have a finite imaginary part originating from single-particle transitions which will lead to damping of the charge oscillation.[18] We therefore require only that the real part of ϵ vanishes and use the following defining equation for the potential associated with a plasmon mode,

$$\int \epsilon(r,r',\omega_n)\phi_n(r',\omega_n)dr' = i\Gamma_n\phi_n(r,\omega_n), \tag{3}$$

where Γ_n is a real number. Mathematically, the plasmon modes are thus the eigenfunctions corresponding to purely imaginary eigenvalues of the dielectric function. Physically, they represent the potential associated with self-sustained charge-density oscillations damped by electron-hole pair formations at the rate Γ_n.

It is instructive to consider the dielectric function in its spectral representation

$$\epsilon(r,r',\omega) = \sum_n \epsilon_n(\omega)\phi_n(r,\omega)\rho_n(r',\omega), \tag{4}$$

where the left and right eigenfunctions satisfy the usual orthonormality relation

$$\langle\phi_n(\omega)|\rho_m(\omega)\rangle = \delta_{nm}. \tag{5}$$

In the Appendix we show that the left and right eigenfunctions are related through Poisson's equation

$$\nabla^2\phi_n(r,\omega) = -4\pi\rho_n(r,\omega), \tag{6}$$

and thus correspond to the potential and charge density of the dielectric eigenmode, respectively. Physically, the condition (5) expresses the fact that the different dielectric eigenmodes for a given frequency ω are electrodynamically decoupled. The inverse dielectric function $\epsilon^{-1}(r,r',\omega)$ is obtained by replacing the eigenvalues $\epsilon_n(\omega)$ in Eq. (4) by $1/\epsilon_n(\omega)$.

When the imaginary part of the eigenvalue $\epsilon_n(\omega)$ does not vary too much around the plasmon frequency ω_n, the condition (3) is equivalent to the condition that

$$\mathrm{Im}\epsilon_n(\omega_n)^{-1} \text{ is a local maximum.} \tag{7}$$

This is the case for most of the plasmon modes of the simple metal films studied in this work. However, for the high energy bulk modes we found that the variation in $\mathrm{Im}\epsilon_n(\omega)$ can shift the local maximum of $\mathrm{Im}\epsilon_n(\omega)^{-1}$ away from the point where $\mathrm{Re}\epsilon_n(\omega) = 0$. (The effect can be even stronger for more complex materials with interband transitions.[19]) In such cases the condition (7) rather than (3) should be used to define the plasmon energy. Importantly, however, the eigenfunctions $\phi_n(r,\omega)$ do not change significantly when ω is varied between the frequencies given by the two criteria, and thus the spatial form of the plasmon remains well defined.

In the case of metallic films where the in-plane variation of ϵ and ϕ_n can be assumed to have the forms $\exp(iq_\parallel\cdot(r_\parallel - r'_\parallel))$ and $\exp(iq_\parallel\cdot r_\parallel)$, respectively, Eq. (3) can be written

$$\int \epsilon(q_\parallel,z,z',\omega_n)\phi_n(z',\omega_n)dz' = i\Gamma_n\phi_n(z,\omega_n). \tag{8}$$

We stress that despite the atomic variation in the potential we have found that local field effects are negligible within the plane justifying this assumption.

All the calculations were performed with the electronic structure code GPAW[20,21] using the Atomic Simulation Environment.[22] The Na films were modeled in a supercell with periodic boundary conditions imposed in all directions. The minimal Na unit cell was used in the plane of the film, and 30 Å of vacuum was included in the direction perpendicular to the film to separate the periodic images. The single-particle wave functions and energies were computed on a real-space grid with a grid spacing 0.18 Å, and the Brillouin zone was sampled by 64×64 k points. The local density approximation (LDA) functional was used for exchange and correlation. The noninteracting density response function χ^0 was calculated from the single-particle states of a density functional theory (DFT) calculation using a 50 eV energy cutoff for the plane wave basis and including states up to 15 eV above the Fermi level. The frequency dependence of the dielectric function was sampled on the real frequency axis using a grid from 0 to 20 eV with a 0.1 eV spacing. We checked that our results were converged with respect to all the parameters of the calculation. The microscopic dielectric function was calculated from χ^0 using the random phase approximation (RPA). We note in passing that this DFT-RPA level of theory yields highly accurate bulk and surface plasmon energies (within a few tenths of an electron volt) of the simple metals.[17]

To obtain the plasmon modes, the dielectric function is diagonalized in a plane-wave basis on each point of a uniform frequency grid. To simulate an isolated film, the obtained eigenmode potentials were corrected to remove the effect of interactions with films in the other supercells, i.e., the periodic boundary conditions from the DFT calculation (this is most important for small $q_\parallel$ vectors). In general the eigenmodes were found to be complex valued, reflecting the spatial variation in the phase of the plasmon potential. This phase variation is, however, rather weak for the present system, and by a suitable choice of the overall phase the modes can be made almost real (>90%). For this reason only the real part of the plasmon modes are shown in this work.

III. RESULTS

In the left panel of Fig. 1 we show the plasmon modes $\phi_n(z)$ (red) and corresponding charge densities $\rho_n(z)$ (blue) obtained for a 10 atom thick Na film terminated by (100) surfaces. Figure 2 shows the real part of the eigenvalues of ϵ for the ten layer film. The red dots indicate the plasmon frequencies ω_n, where the real part of an eigenvalue crosses the real axis from below. Note that the point where an eigenvalue crosses the real axis from above corresponds roughly to the energy of the individual single-particle transitions contributing to the plasmon state. Thus the distance between the two crossing points, $\tilde{\alpha}$, represents the Coulombic restoring force of the plasma oscillation. The eigenfunctions of ϵ corresponding to the indicated eigenvalues are the plasmon modes shown in Fig. 1. The energies and strengths α_n of the plasmon modes are listed to the left. The strength is determined by fitting a single-pole model

$$\epsilon_{n,1p}(\omega) = 1 - \frac{\alpha_n}{\omega - \omega_{n,0} + i\gamma_n} \tag{9}$$

to the value and slope of the relevant eigenvalue branch of ϵ at the point $\omega = \omega_n$; see Fig. 2.

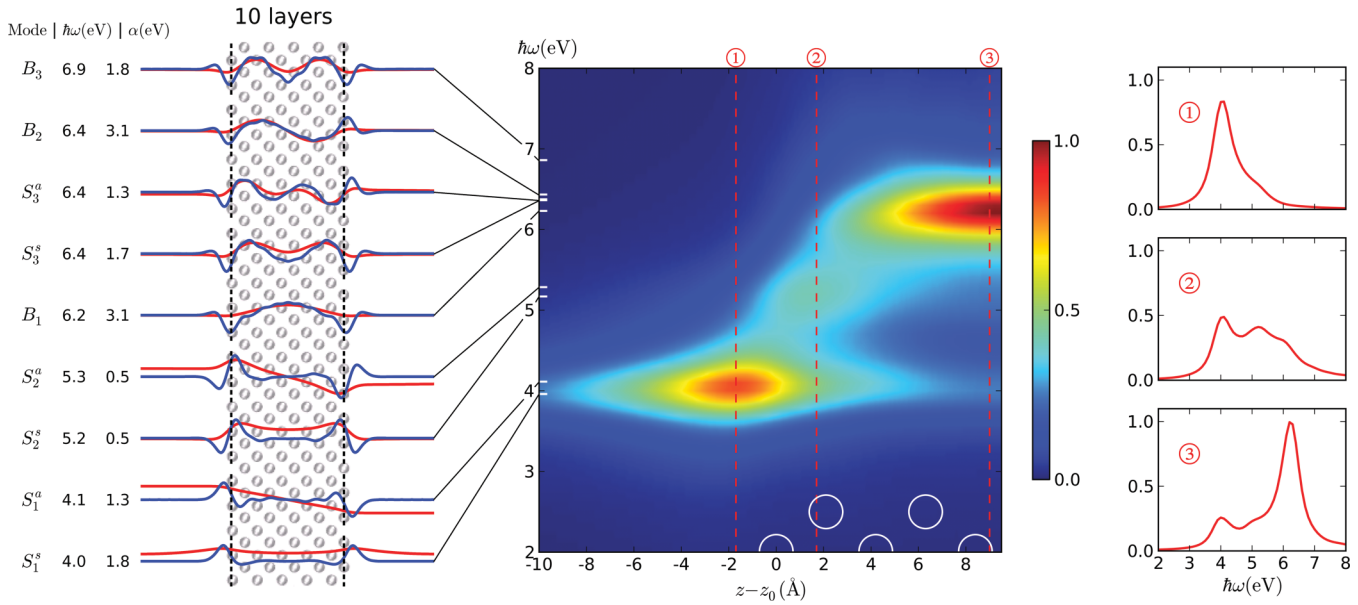

FIG. 1. (Color online) (Left) Spatial profile of the plasmon modes in the direction normal to the film for in-plane momentum transfer $q_\parallel = 0.1$ Å^{-1}. The red (blue) curves show the potential (density) associated with the plasmon excitation. Mode type, energy, and strength α are shown to the left. (Middle) Contour plot of the energy loss of an in-plane electron beam as it is scanned across the film. Only the left half of the film is shown, and the positions of the Na atoms are indicated by white circles at the bottom. The three bright features in the spectrum originate from energy loss due to excitation of three types of plasmons, namely, the surface plasmon mode S_1, the subsurface mode S_2, and the lowest bulk plasmon modes B_1, respectively. (Right) Calculated electron energy loss spectra along the dashed lines indicated in the middle panel.

Returning to Fig. 1, we see that the lowest lying plasmon modes S_1 are the symmetric and antisymmetric surface plasmons also predicted by the classical Drude model. The two sets of modes denoted S_2 and S_3 are also localized at the surface, although they penetrate more into the bulk, and we therefore refer to them as subsurface modes. For a very thin slab of three layers, see Fig. 3, only the first subsurface mode, S_2, is supported. The subsurface character of the S_3 mode is perhaps more evident for the twenty layer film where it is more clearly separated from the bulk modes; see Fig. 4. Experimental loss spectra of simple metal surfaces have shown a small peak between the surface and bulk peaks which was assigned to a subsurface plasmon (in that work denoted multipole surface mode).[23] Such a peak at intermediate energies was also observed in a previous RPA calculation for a jellium surface.[24] However, the complete analysis of the plasmons modes presented here shows that more than one subsurface mode exists.

The bulk plasmons B occur at higher energies and resemble standing waves across the film. The fact that only a discrete

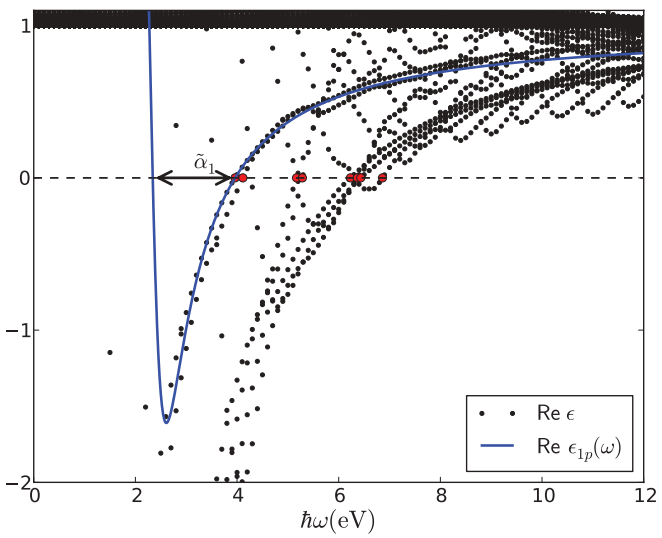

FIG. 2. (Color online) Real part of the eigenvalues of the microscopic dielectric function $\epsilon(\omega)$ for a ten layer Na film. The frequencies where an eigenvalue crosses the real axis from below (red dots) define the plasmon frequencies, and the corresponding eigenfunctions represent the plasmon modes shown by the red curves in the left panel of Fig. 1. The blue curve shows the real part of the single-pole model used to extract the strength of the plasmon. The distance between the zero points, $\tilde{\alpha} = \sqrt{\alpha^2 - 4\gamma^2}$, increases with increasing strength of the mode.

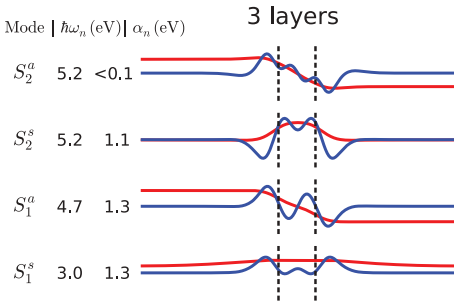

FIG. 3. (Color online) Spatial profile of the plasmon modes of a three layer Na film in the direction normal to the film for momentum transfer $q_\parallel = 0.1$ Å^{-1}. The red (blue) curves show the potential (density) associated with the plasmon excitation, and the mode type, energy, and strength α are shown to the left.

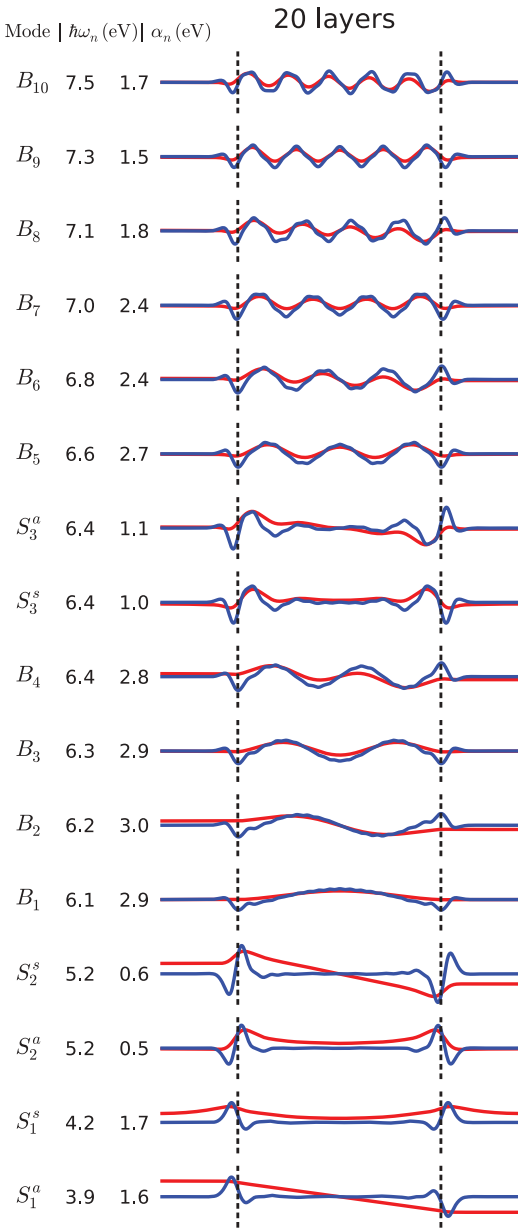

FIG. 4. (Color online) Spatial profile of the plasmon modes of a twenty layer Na film in the direction normal to the film for momentum transfer $q_\parallel = 0.1$ Å^{-1}. The red (blue) curves show the potential (density) associated with the plasmon excitation, and the mode type, energy, and strength α are shown to the left. In addition to the conventional surface modes S_1, the twenty layer slab supports two sets of subsurface plasmon modes (S_2,S_3) with energies between the surface and bulk modes.

set of bulk modes are observed is clearly a result of the confinement of the electron gas which requires the density to vanish at the boundaries of the film. The reason only a finite number of modes are found is that the damping of the modes due to single-particle transitions increases for smaller oscillation periods, i.e., larger wave number. Consequently, the strength of the bulk plasmons decreases with increasing wave number until the point where the real part of ϵ does not cross the real axis. This is evident in Fig. 2 where a series of local minima in the eigenvalue spectrum can be seen at higher frequencies. For all the films, the highest lying bulk mode has a wave number around 0.5 Å^{-1}. This is very close to the threshold q where Re$\epsilon(q,\omega)$ becomes positive for all ω in bulk Na.

As already mentioned, the main mechanism of energy loss of fast electrons propagating through a material is via excitation of plasmons. In general, the energy dissipated to the electron system due to an applied potential of the form $\phi_{\rm ext}(r,t) = \phi_{\rm ext}(r)\exp(i\omega t)$ is

$$P(\omega) = \int\int \phi_{\rm ext}(r)\chi_2(r,r',\omega)\phi_{\rm ext}(r')drdr'. \qquad (10)$$

Here χ_2 is the imaginary part of the density response function χ. In the case of a fast electron, the external potential is simply that of a point charge moving at constant velocity. We have calculated the loss function for high energy electron beams directed along lines parallel to the film. The resulting EELS spectrum is seen in the middle panel of Fig. 1. It is clear that the loss spectrum is completely dominated by three types of excitations corresponding to the surface, subsurface, and bulk plasmon modes shown to the left. The intensity of the subsurface modes is rather weak in agreement with the low strength α of these modes.

Figure 5 shows all the energies of the symmetric and antisymmetric surface plasmons (subsurface plasmons not included) found for four different film thicknesses as a function of the in-plane wave vector $q_\parallel$ (Ref. 25). The full curves are the classical Drude results for a two-dimensional (2D) metal film with the electron density of Na. For small $q_\parallel$ the agreement with the classical result is striking for the symmetric mode. On the other hand, the quantum results for the antisymmetric mode are significantly red shifted compared to the Drude result with deviations up to 1 eV for the thinnest film. For large $q_\parallel$ the quantum plasmons show a $q_\parallel^2$ dispersion whereas the classical result approaches the asymptotic value $\omega_p/\sqrt{2}$. This

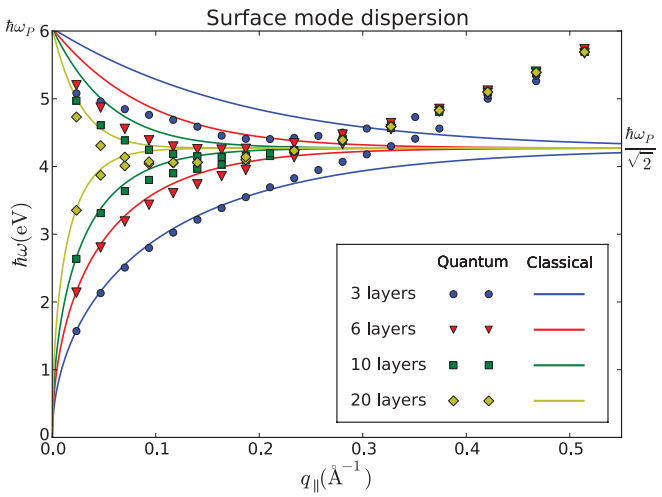

FIG. 5. (Color online) Dispersion of surface plasmon energies for different Na film thicknesses. The symbols represent the first-principles RPA results for the energy of the symmetric (lower branch) and antisymmetric (upper branch) surface plasmons as a function of the in-plane wave number $q_\parallel$. The full lines are the result of a classical Drude model.

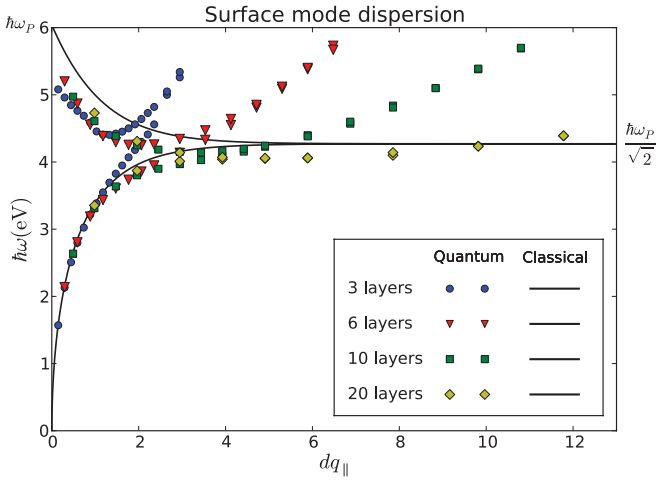

FIG. 6. (Color online) Like Fig. 5 but plotted as function of the dimensionless parameter $dq_\parallel$ where d is the thickness of the Na film.

failure of the classical model is due to the neglect of the spatial nonlocality of ϵ, i.e., the $(r - r')$ dependence.

We note that when exchange-correlation effects are included through the adiabatic local density approximation (ALDA) kernel, a larger deviation from the classical model is observed. In particular the antisymmetric mode is shifted even further down for small $q_\parallel$. A similar behavior, i.e., a downshift of plasmon energies, is observed for simple metal bulk systems where the ALDA also predicts a negative dispersion for small q (Ref. 2). The spatial form of the plasmon modes obtained with the ALDA is, however, identical to those obtained at the RPA level.

In Fig. 6 we show the same data as shown in Fig. 5 but with the plasmon energy plotted relative to the dimensionless parameter $dq_\parallel$, where d is the film thickness. When plotted in this way, all the classical dispersions fall on the same universal curve. In the regime $dq_\parallel < 2$, it is clear that the quantum results for the antisymmetric mode are not converged to the classical result even for the thickest slab.

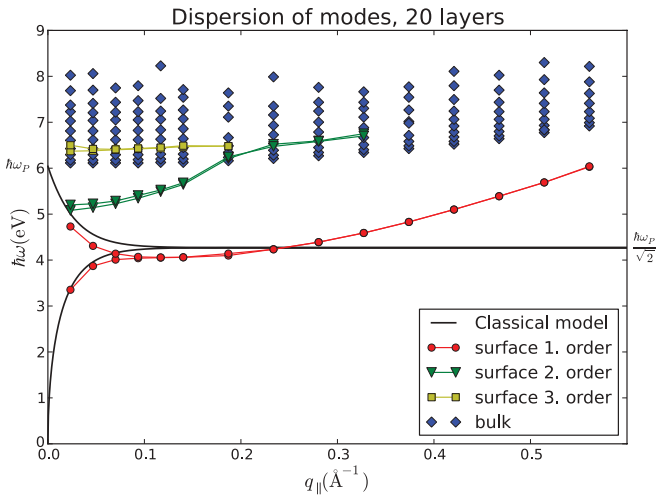

FIG. 7. (Color online) Dispersion of all the plasmon modes found for the twenty atomic layer Na film.

In Fig. 7 we present the dispersion of all plasmon modes (conventional surface, subsurface, and bulk modes) for the twenty layer film. The bulk modes show a weak $q_\parallel^2$ dispersion. The energy offset between the different bulk modes arises from the different wavelengths of the plasmons in the normal direction. The energy of the lowest bulk mode B_1 in the $q_\parallel = 0$ limit is <0.1 eV higher than the bulk value of $\hbar\omega_p$. This small deviation is due to the finite wavelength of the plasmon on the direction perpendicular to the film, and this indicates that quantum size effects have a very small influence on the bulk modes of the twenty layer film.

The first subsurface mode (green color) follows a $q_\parallel^2$ dispersion until around 0.2 $\mathrm{Å}^{-1}$ where it enters the bulk mode energy range. From this point the dispersion of the subsurface mode is reduced and follows that of the bulk modes. The dispersion of the second subsurface mode (yellow color) is very similar to the bulk dispersion. The second subsurface mode is rather weak and for $q_\parallel > 0.2$ $\mathrm{Å}^{-1}$ its eigenvalue $\epsilon_n(\omega)$ does not cross the real axis at any frequency. For both subsurface modes the splitting between the symmetric and antisymmetric modes is rather small. We ascribe this to the weaker strength of the electric field associated with the subsurface mode compared to the conventional surface mode: While the charge distribution ρ_n associated with the latter has monopole character in the direction perpendicular to the film, the subsurface modes have dipole character; see Fig. 4.

IV. CONCLUSION

We have demonstrated a method for calculating spatially resolved plasmon modes in nanostructured materials from first-principles. For the case of 2D Na films[19] of thicknesses 0.5 to 4 nm, we found that the modes could be classified as either surface modes, subsurface modes, or bulk modes. In contrast to other studies, the direct computation of eigenmodes revealed that several subsurface modes can exist at the surface of simple metals. We found clear effects of quantum confinement on the surface plasmon energies. In particular, the antisymmetric surface mode of the thinner films was significantly red shifted compared to the classical Drude result. Finally, it was demonstrated how the different features in the calculated spatially resolved EELS spectrum of the metal films could be unambiguously ascribed to the excitation of specific plasmon modes. Apart from providing an intuitive and visual picture of the collective excitations of a nanostructure, the spatially resolved plasmon modes should be useful as a basis for the construction of simple models for the full nonlocal dielectric function.

ACKNOWLEDGMENTS

K.S.T. acknowledges support from the Danish Research Council's Sapere Aude Program. The Center for Nanostructured Graphene CNG is sponsored by the Danish National Research Foundation. Support from The Catalysis for Sustainable Energy (CASE) initiative and the Center of Nanostructuring for Efficient Energy Conversion (CNEEC) at Stanford University, an Energy Frontier Research Center funded by the US Department of Energy, Office of Science, Office of Basic Energy Sciences under Grant No. DE-SC0001060, is also acknowledged.

APPENDIX: SPECTRAL REPRESENTATION OF ϵ

Let $|\phi_n(\omega)\rangle$ denote the eigenfunctions of the dielectric function,

$$\hat{\epsilon}(\omega)|\phi_n(\omega)\rangle = \epsilon_n(\omega)|\phi_n(\omega)\rangle. \tag{A1}$$

(We have suppressed the r dependence for notational simplicity.) Since $\hat{\epsilon}(\omega)$ is a non-Hermitian operator, the eigenvalues are complex and the eigenfunctions are nonorthogonal. In this case the spectral representation takes the form

$$\hat{\epsilon}(\omega) = \sum_n \epsilon_n(\omega)|\phi_n(\omega)\rangle\langle\rho_n(\omega)|. \tag{A2}$$

The set $|\rho_n(\omega)\rangle$ is the dual basis of $|\phi_n(\omega)\rangle$ and satisfies

$$\langle\phi_n(\omega)|\rho_n(\omega)\rangle = \delta_{nm}. \tag{A3}$$

From the spectral representation it follows directly that

$$\hat{\epsilon}(\omega)^\dagger|\rho_n(\omega)\rangle = \epsilon_n(\omega)^*|\rho_n(\omega)\rangle. \tag{A4}$$

In the following we show that the dielectric eigenfunction $|\phi_n(\omega)\rangle$ and its dual function $|\rho_n(\omega)\rangle$ constitute a potential-density pair, i.e.,

$$\nabla^2\phi_n(r,\omega) = -4\pi\rho_n(r,\omega). \tag{A5}$$

Within the RPA, the dielectric function is related to the noninteracting polarization function $\chi_0(r,r',\omega)$ by

$$\hat{\epsilon}(\omega) = \hat{1} - \hat{v}\hat{\chi}_0(\omega), \tag{A6}$$

where $\hat{v} = 1/|r-r'|$ is the Coulomb interaction, $\hat{1} = \delta(r-r')$. Exploiting that, under time reversal symmetry $\chi_0(r,r') = \chi_0(r',r)$, we have

$$\hat{\epsilon}(\omega)^\dagger = \hat{1} - \hat{\chi}_0(\omega)^*\hat{v}. \tag{A7}$$

We now make the ansatz $\rho_n(\omega) = \hat{v}^{-1}\phi_n(\omega)^*$ and evaluate

$$\epsilon(\omega)^\dagger\hat{v}^{-1}\phi_n(\omega)^* = v^{-1}\phi_n(\omega)^* - \hat{\chi}_0(\omega)^*\phi_n(\omega)^* \tag{A8}$$

$$= \hat{v}^{-1}[\hat{\epsilon}(\omega)\phi_n(\omega)]^* \tag{A9}$$

$$= \epsilon_n(\omega)^*\hat{v}^{-1}\phi_n^*, \tag{A10}$$

which concludes the proof.

*thygesen@fysik.dtu.dk

[1] D. Bohm and D. Pines, Phys. Rev. **92**, 609 (1953).
[2] J. M. Pitarke, V. M. Silkin, E. V. Chulkov, and P. M. Echenique, Rep. Prog. Phys. **70**, 1 (2007).
[3] K. A. Willets and R. P. Van Duyne, Annu. Rev. Phys. Chem. **58**, 267 (2007).
[4] K. Kneipp, Y. Wang, H. Kneipp, L. T. Perelman, I. Itzkan, R. R. Dasari, and M. S. Feld, Phys. Rev. Lett. **78**, 1667 (1997).
[5] E. M. Larsson, C. Langhammer, I. Zori, and B. Kasemo, Science **326**, 1091 (2009).
[6] T. Hirakawa and P. V. Kamat, J. Am. Chem. Soc. **127**, 3928 (2005).
[7] H. A. Atwater and A. Polman, Nat. Mater. **9**, 205 (2010).
[8] F. J. Garcia de Abajo, Rev. Mod. Phys. **82**, 209 (2010).
[9] B. S. Guiton, V. Iberi, S. Li, D. N. Leonard, C. M. Parish, P. G. Kotula, M. Varela, G. C. Schatz, S. J. Pennycook, and J. P. Camden, Nano Lett. **11**, 3482 (2011); O. Nicoletti, M. Wubs, N. A. Mortensen, W. Sigle, P. A. van Aken, and P. A. Midgley, Opt. Express **19**, 15371 (2011); W. Zhou, J. Lee, J. Nanda, S. T. Pantelides, S. J. Pennycook, and J. C. Idrobo, Nat. Nanotechnol. **7**, 161 (2012); J. Nelayah, M. Kociak, O. Stèphan, F. J. Garcia de Abajo, M. Tencè, L. Henrard, D. Taverna, I. Pastoriza-Santos, L. M. Liz-Marzàn, and C. Colliex, Nat. Phys. **3**, 348 (2007); A. L. Koh, A. I. Fernandez-Dominguez, D. W. McComb, S. A. Maier, and J. K. W. Yang, Nano Lett. **11**, 1323 (2011); M. Bosman, V. J. Keast, M. Watanabe, A. I. Maaroof, and M. B. Cortie, Nanotechnol. **18**, 165505 (2007); M. N'Gom, S. Li, G. Schatz, R. Erni, A. Agarwal, N. Kotov, and T. B. Norris, Phys. Rev. B **80**, 113411 (2009); J. A. Scholl, A. L. Koh, and J. A. Dionne, Nature (London) **483**, 421 (2012).
[10] C. David and F. J. Garcia de Abajo, J. Phys. Chem. C **115**, 19470 (2011).
[11] S. Raza, G. Toscano, A. P. Jauho, M. Wubs, and N. A. Mortensen, Phys. Rev. B **84**, 121412(R) (2011).
[12] T. Sokusin, A. Manjavacas, and F. J. Garcia de Abajo, ACS Nano **6**, 1766 (2012).
[13] J. Yan, Z. Yuan, and S. W. Gao, Phys. Rev. Lett. **98**, 216602 (2007).
[14] G. Onida, L. Reining, and A. Rubio, Rev. Mod. Phys. **74**, 601 (2002).
[15] C. Kramberger, R. Hambach, C. Giorgetti, M. H. Rümmeli, M. Knupfer, J. Fink, B. Büchner, L. Reining, E. Einarsson, S. Maruyama, F. Sottile, K. Hannewald, V. Olevano, A. G. Marinopoulos, and T. Pichler, Phys. Rev. Lett. **100**, 196803 (2008).
[16] A. Marini, R. Del Sole, and G. Onida, Phys. Rev. B **66**, 115101 (2002).
[17] J. Yan, K. W. Jacobsen, and K. S. Thygesen, Phys. Rev. B **84**, 235430 (2011).
[18] We note that exact solutions may be obtained for complex frequencies. However, this requires an analytical continuation of ϵ into the complex plane and will not be pursued in the present work.
[19] In the case of Ag films (results will be published elsewhere), we have found that the coupling to interband transitions can shift the peak of $\mathrm{Im}\epsilon_n(\omega)$ away from the point where $\mathrm{Re}\epsilon_n(\omega) = 0$. Importantly, however, the corresponding eigenfunction $\phi_n(r,\omega)$ does not change significantly when ω is varied between the frequencies given by the two criteria, and thus the spatial form of the plasmon remains well defined.
[20] J. Yan, J. J. Mortensen, K. W. Jacobsen, and K. S. Thygesen, Phys. Rev. B **83**, 245122 (2011).
[21] J. Enkovaara *et al.*, J. Phys.: Condens. Matter **22**, 253202 (2010).
[22] S. R. Bahn and K. W. Jacobsen, Comput. Sci. Eng. **4**, 56 (2002).
[23] K.-D. Tsuei, E. W. Plummer, A. Liebsch, E. Pehlke, K. Kempa, and P. Bakshi, Surf. Sci. **247**, 302 (1991).
[24] W. L. Schaich and J. F. Dobson, Phys. Rev. B **49**, 14700 (1994).
[25] To obtain the dispersion of the surface plasmons (Fig. 4) of an isolated film, the calculated plasmon energies were extrapolated to the limit of infinite distance between the repeated films using a classical model for the plasmon energies in an infinite array of films. The model is a straightforward generalization of the results in Ref. 26.
[26] R. A. Ferrell, Phys. Rev. **111**, 1214 (1958).

Paper II

Plasmons in metallic monolayer and bilayer transition metal dichalcogenides.
Kirsten Andersen and Kristian S. Thygesen, Phys. Rev. B 88, 155128 (2013)

Plasmons in metallic monolayer and bilayer transition metal dichalcogenides

Kirsten Andersen* and Kristian S. Thygesen†
Center for Atomic-scale Materials Design (CAMD) and Center for Nanostructured Graphene (CNG), Department of Physics Technical University of Denmark, DK-2800 Kgs. Lyngby, Denmark
(Received 2 July 2013; revised manuscript received 4 October 2013; published 23 October 2013)

We study the collective electronic excitations in metallic single-layer and bilayer transition metal dichalcogenides (TMDCs) using time dependent density functional theory in the random phase approximation. For very small momentum transfers (below $q \approx 0.02$ Å^{-1}), the plasmon dispersion follows the $\sqrt{q}$ behavior expected for free electrons in two dimensions. For larger momentum transfer, the plasmon energy is significantly redshifted due to screening by interband transitions. At around $q \approx 0.1$ Å^{-1}, the plasmon enters the dissipative electron-hole continuum and the plasmon dispersions flatten out at an energy around 0.6–1.1 eV, depending on the material. Using bilayer $NbSe_2$ as example, we show that the plasmon modes of a bilayer structure take the form of symmetric and antisymmetric hybrids of the single-layer modes. The spatially antisymmetric mode is rather weak with a linear dispersion tending to zero for $q = 0$, while the energy of the symmetric mode follows the single-layer mode dispersion with a slight blue shift.

DOI: 10.1103/PhysRevB.88.155128 PACS number(s): 73.43.Lp, 71.45.−d, 73.61.−r

I. INTRODUCTION

The success of graphene research has created a surge in interest for other types of atomically thin two-dimensional (2D) materials.[1,2] A particularly interesting class of 2D materials are the transition metal dichalcogenides (TMDC) whose electronic properties range from semiconducting to metallic and even superconducting. In combination with graphene and 2D insulators like hexagonal boron-nitride, the TMDCs could form the basis for artificially layered van der Waals structures with tailored electronic properties. While monolayers of semiconducting TMDCs have been fabricated and studied quite extensively,[3–5] metallic TMDCs have received less attention, possible due to stability issues.[6] However, exfoliation of atomically thin layers of $TaSe_2$, TaS_2, and $NbSe_2$ have been reported.[7–9]

The optical properties of a metallic system are to large extent governed by the collective excitations known as plasmons. In (doped) graphene, it was demonstrated that the energy of the so-called metallic plasmon, which is formed by intraband transitions within the π or π^* bands, can be varied by electrostatic gating or nanostructuring. Furthermore, the plasmons facilitate a strong spatial confinement of light making graphene interesting for applications within plasmonics.[10,11] However, the energy of the metallic plasmon is restricted by the achievable carrier concentration and this limits applications of graphene plasmonics to the tetrahertz regime. Metallic TMDCs have much higher charge carrier densities leading to plasmon energies of around 1 eV in bulk TMDCs.[12–15] Together with the possibility of tuning the plasmon energies and lifetimes through quantum confinement or plasmon hybridization,[16,17] this makes few-layer TMDCs interesting candidates for nanoplasmonic applications in the optical frequency regime. We mention that the efficient coupling of 2D plasmons and light generally requires some kind of scattering of the light to overcome the momentum mismatch.[18]

First-principles calculations of the $q = 0$ loss spectrum of several single- and bilayer TMDCs was recently reported in Ref. 19. While these calculations revealed the energy of the π and $\pi + \sigma$ interband plasmons, they did not address the nature of the intraband plasmons of the metallic systems, which are only seen for finite q due to the $\sqrt{q}$ dispersion in the small q limit.

In this paper, we study the intraband plasmons in monolayers of six different metallic TMDCs using first-principles calculations. For very small momentum transfer ($q < 0.02$ Å^{-1}), the plasmon energy follows the classical $\sqrt{q}$ behavior of free electrons in 2D. At larger q, the plasmons become screened by interband transitions leading to significant redshift compared to the free electron result, and the plasmon dispersions flatten out at an energy in the range 0.6–1.1 eV, depending on the material. At around $q = 0.1$ Å^{-1}, the plasmon enters the dissipative region of interband transitions and the plasmons acquire a finite lifetime. Using a recently developed method for visualizing the induced density associated with a plasmon mode, we study how the single-layer plasmons hybridize to form a symmetric and an (weak) antisymmetric plasmon in a bilayer structure. The symmetric mode of the bilayer is slightly blue shifted relative to the single-layer plasmon. This pushes it closer towards the dissipative interband continuum and reduces its strength compared to the single-layer plasmon.

II. METHOD

All density functional theory (DFT) calculations have been performed with the GPAW electronic structure code.[20] We study single layers of TMDCs with the chemical form MX_2, where M belongs to the group 5 transition metals V, Nb, and Ta and the chalcogen X is either S or Se, which results in six different combinations. The layers were modeled within periodic supercells with 20 Å of vacuum separating the periodic images in the perpendicular direction. The structures were relaxed with the Perdew-Burke-Ernzerhof (PBE) exchange-correlation functional.[21] The single-particle states used to construct the response function were calculated using the orbital-dependent GLLBSC (Gritsenko, Leeuwen, Lenthe, and Baerends potential[22] with the modifications from Kuisma *et al.*)[23] functional, which has been shown to give

accurate band energies of semiconductors. In the context of plasmons, correct band positions are important to describe the onset of interband transitions correctly. The 2D Brillouin zone (BZ) was sampled using 64×64 k points for most calculations, while a dense grid of 256×256 was used in order to study very small momentum transfers.

The dielectric matrix for in-plane wave vectors $\mathbf{q}$ was calculated in the random phase approximation (RPA)[24] following the implementation of Ref. 25:

$$\epsilon_{\mathbf{G},\mathbf{G}'}(\mathbf{q},\omega) = \delta_{\mathbf{G},\mathbf{G}'} - \frac{4\pi}{|\mathbf{q}+\mathbf{G}|^2}\chi^0_{\mathbf{G},\mathbf{G}'}(\mathbf{q},\omega). \quad (1)$$

For the reciprocal lattice vectors $\mathbf{G}$ and $\mathbf{G}'$, we used a cutoff of 50 eV to account for local field effects, and empty states up to 30 eV above the Fermi level were included in the noninteracting response function matrix $\chi^0_{\mathbf{G},\mathbf{G}'}(\mathbf{q},\omega)$. We have checked that the plasmon energies are well converged (to within 0.1 eV) with these parameters. We note that inclusion of the ALDA kernel was found to have negligible effect on the loss spectrum of bulk $NbSe_2$,[14] and based on this we expect the RPA to be valid also for the 2D TMDCs studied here. In order to remove the interaction between supercells, the Coulomb interaction was truncated in the direction perpendicular to the layers.[26] If this is not done, the plasmons in neighboring layers will interact for in-plane wave vectors $q < 2\pi/L$, where L is the distance between the layers. In particular, the plasmon energy will incorrectly tend to a finite energy in the $q \to 0$ limit.

The electron energy loss spectrum (EELS) was calculated from the inverse of the macroscopic dielectric function, $\epsilon_M(\mathbf{q},\omega) = 1/\epsilon^{-1}_{\mathbf{G}=\mathbf{G}=0}(\mathbf{q},\omega)$:

$$\mathrm{EELS}(\mathbf{q},\omega) = -\mathrm{Im}\epsilon^{-1}_M(\mathbf{q},\omega). \quad (2)$$

The plasmon energies are obtained as the peaks in the loss spectrum which is calculated for different momentum transfers parallel to the layer $\mathbf{q}$ and the integrated weight of the loss peaks is used as a measure of the strength of the plasmon mode.

A. Plasmon eigenmodes

A simple method to identify and compute the plasmon modes of a metallic nanostructure was introduced in Ref. 27. In the present work, the method has been used to analyze the plasmon excitations of the bilayer structure. An outline of the method is given below.

A self-sustained charge density oscillation, $\rho(\omega,\mathbf{r})$, can exist in a material if the related potential, satisfying Poisson's equation $\nabla^2\phi(\omega,\mathbf{r}) = -4\pi\rho(\omega,\mathbf{r})$, obeys the equation

$$\int \epsilon(\omega,\mathbf{r},\mathbf{r}')\phi(\omega,\mathbf{r}')d\mathbf{r}' = 0. \quad (3)$$

This corresponds to the case of having a finite induced potential in the absence of an external potential, which is the criterion for the existence of a plasmon. In general, this equation cannot be exactly satisfied due to a finite imaginary part originating from single-particle transitions, which will lead to damping of the charge oscillation. When the damping in the material is small, it is sufficient to require only that the real part of ϵ vanishes and use the following definition for the potential associated with a plasmon mode of frequency ω_n:

$$\int \epsilon(\omega_n,\mathbf{r},\mathbf{r}')\phi_n(\omega_n,\mathbf{r}')d\mathbf{r}' = i\Gamma_n\phi_n(\omega_n,\mathbf{r}), \quad (4)$$

where Γ_n is a real number. The plasmon modes are thus eigenfunctions corresponding to purely imaginary eigenvalues of the dielectric function. Physically, they represent the potential associated with self-sustained charge-density oscillations damped by electron-hole pair formations at the rate Γ_n. The right-hand-side eigenfunctions, ϕ_n, define the induced potential of the eigenmodes, and the corresponding induced density ρ_n can be obtained as the left-hand-side (dual) eigenfunctions of the dielectric function.[27] In the case of larger and frequency-dependent damping, a more accurate approach is to use the eigenvalues of $\epsilon(\omega,\mathbf{r},\mathbf{r}')$, denoted $\epsilon_n(\omega)$, and use the criterion

$$-\mathrm{Im}\epsilon_n(\omega)^{-1} \text{ is a maximum} \quad (5)$$

to define a plasmon mode. This definition takes into account that a finite imaginary part of ϵ may shift the plasmon peaks in the loss spectrum away from the zeros of $\mathrm{Re}\epsilon(\omega)$.

In contrast to the standard definition of the loss spectrum, Eq. (2), which measures the energy loss of a plane-wave perturbation, definition (5) provides a resolution of the loss spectrum into the intrinsic plasmon eigenmodes of the system. As a simple example we mention the resolution of the loss spectrum of a thin metal film into bulk and surface modes.[27]

In practice, the plasmon eigenmodes are obtained by diagonalizing the dynamical dielectric function (in the $\mathbf{G}$ and $\mathbf{G}'$ basis) for each point on a frequency grid. The dielectric eigenvalue spectrum results in a set of distinct eigenvalue curves that evolves smoothly with energy, each curve corresponding to a separate plasmon eigenmode, see Fig. 4 (left panel).

III. RESULTS

In the left panels of Fig. 1, we show the band structures for VS_2 and $TaSe_2$ obtained with the GLLBSC functional. We note that the band structures obtained with PBE are qualitatively similar. Compared to semiconducting TMDCs such as MoS_2, the reduced d-state occupation of the transition metal leads to a half-filled band. From the band structure plotted in Fig. 1 along the high symmetry Γ-M direction, it can be seen that the metallic band crosses the Fermi level along two curves in the 2D Brillouin zone. The band is situated in a gap of approximately 2.5–3 eV and stems from hybridization of the d state of the transition metal with the vertical p_z orbitals of the chalcogen. The band structures of the six materials are very similar, showing only minor variations in the width of the metallic band, and details in the position of the fully occupied or unoccupied bands. A comprehensive study of the electronic structure of several 2D TMDCs was reported in Ref. 28.

An example of an electron energy loss spectrum is shown in Fig. 1, here calculated for $TaSe_2$ for momentum transfers in the Γ-M direction. Momentum transfers along Γ-K and Γ-M were found to produce very similar results. The pronounced peaks in the loss spectrum are due to plasmon excitations. The plasmon dispersions of the six TMDCs are shown in Fig. 2, where the strength of the resonances is indicated by

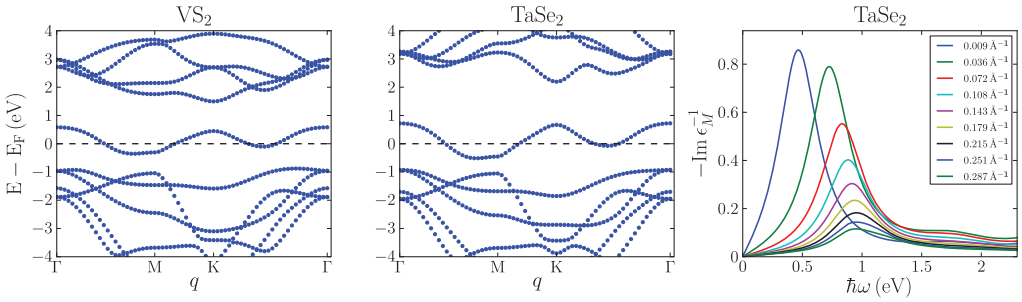

FIG. 1. (Color online) (Left and middle) Band structure of the transition metal dichalcogenides VS_2 and $TaSe_2$. The metallic band is seen to be separated from all other bands. (Right) Electron energy loss spectrum (EELS) calculated for $TaSe_2$ for increasing momentum transfers q along the Γ-M direction.

the size of the markers. In general, higher plasmon energies (for fixed momentum transfer) are found for the TMDCs with heavier transition metal ions. On the other hand, the TMDCs containing heavier species have larger lattice constants and thus lower density of free charge carriers. The trend in plasmon energy is therefore opposite to the free electron model, which predicts the plasmon energy to scale with the charge density as $\omega_P \propto \sqrt{n}$. As we show below, the TMDC plasmon dispersions deviate from the 2D free-electron model due to (i) the nonparabolic shape of the metallic band, and (ii) screening by interband transitions. We note that the $\sqrt{q}$ behavior of 2D free-electron plasmons in the small q limit is not directly seen from the figure. This is simply because the applied q-point grid is not fine enough to reveal this behavior around $q = 0$ (this is evident from Fig. 3 where a finer q-point mesh was used). We mention that crystal local field effects within the plane may be a third reason for deviations with the 2D free-electron model. However, the homogeneous nature of the 2D TMDC suggests that this will be a rather weak effect.

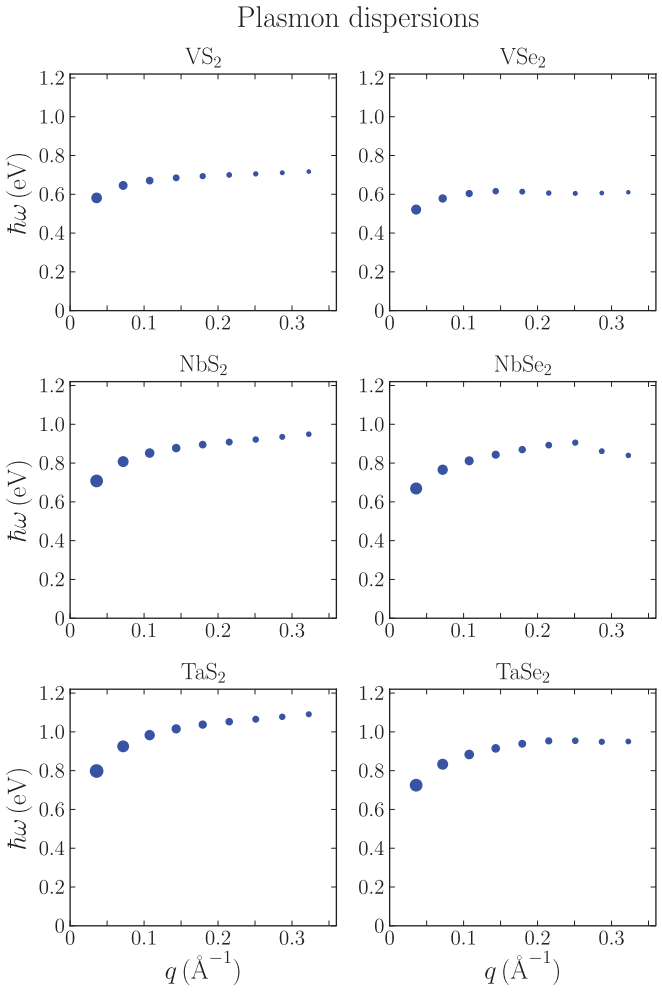

FIG. 2. (Color online) Plasmon dispersion of the six TMDCs along the Γ-M direction, obtained from the peaks in the loss spectra. The size of the markers represents the strength of the plasmon defined as the area under the loss peak. The energy dispersion tends towards zero for low momentum transfers as expected for a metallic 2D plasmon. At larger q, however, the dispersion is constant or in some case negative, and the strength of the plasmon is significantly reduced.

To investigate the origin of the deviation from free-electron behavior, we have studied the separate effects of intra and interband transitions on the plasmon resonances of monolayer $TaSe_2$. The noninteracting density response function can be divided into two contributions:

$$\chi^0_{\mathbf{G},\mathbf{G}'}(\mathbf{q},\omega) = \chi^{0,\mathrm{intra}}_{\mathbf{G},\mathbf{G}'}(\mathbf{q},\omega) + \chi^{0,\mathrm{inter}}_{\mathbf{G},\mathbf{G}'}(\mathbf{q},\omega), \qquad (6)$$

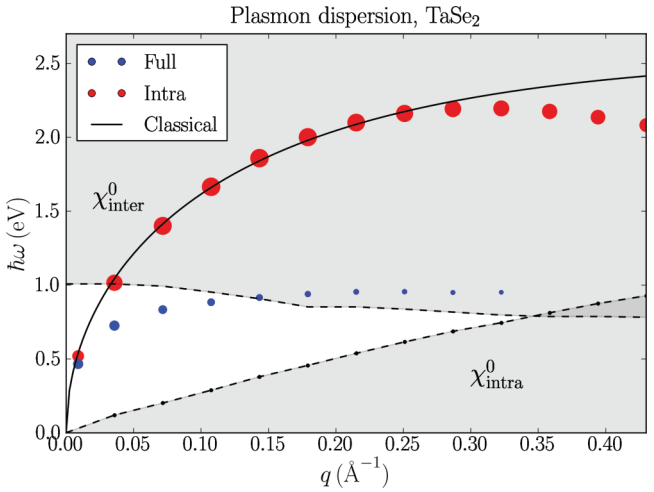

FIG. 3. (Color online) Plasmon dispersion along the Γ-M direction calculated from the full response function (red dots) and from a response function including only intraband transitions (blue dots). The result of a classical model for the plasmons in a 2D film is shown for comparison. The shaded areas indicate the dissipative regions of Landau damping by inter and intraband transitions, respectively.

where the first term is obtained by only including transitions within the metallic band in the response calculation, and the second term by including all transitions between separate bands. When the dielectric matrix is calculated from $\chi^{0,\text{intra}}_{\mathbf{G},\mathbf{G}'}(\mathbf{q},\omega)$ using Eq. (1), the pure intraband plasmon, i.e., neglecting screening by the interband transitions, is obtained. The result is shown in Fig. 3, where the dispersion of the pure intraband plasmon is plotted together with the dispersion obtained from the full calculation. The dispersion of the intraband plasmon is furthermore compared to a classical free-electron model for the 2D plasmon of a thin film:[29]

$$\omega = \frac{\omega_{\text{P}}}{\sqrt{2}}\sqrt{1-e^{-qd}}, \tag{7}$$

where d is the thickness of the film. The bulk plasmon frequency, ω_P, can be obtained from the free electron density, n, originating from the half-filled metallic band and the effective mass of the electron, m^*, through the relation: $\omega_{\text{P}}^2 = \frac{ne^2}{m^*\epsilon_0}$. For the film thickness, d, which is also used to define the free-electron density, we use $d = \frac{3}{2}d_{\text{Se-Se}}$, where $d_{\text{Se-Se}}$ is the distance between the two Se layers. This number agrees well with the *ab initio* result for the width of the ground-state electron density of the layer, however, the result of the classical model is relatively insensitive to variations in this parameter: if d is changed by 10%, the plasmon energy ω_P changes by around 5%. A good fit to the intraband *ab initio* results in the small q region is obtained when the effective mass is set to $m^* = 2m_e$ (see Fig. 3). We note that this value for the effective mass agrees reasonably well with the effective mass derived directly from the *ab initio* band structure, which lies in the range $1m_e - 3m_e$ depending on where along the Fermi curve it is evaluated. At higher q, the finite width of the metallic band (see Fig. 1) leads to deviations between the *ab initio* intraband plasmon and the free-electron result with the former showing a negative dispersion.

As seen in Fig. 3, the inclusion of interband transitions has a strong influence on the plasmons, which are significantly redshifted and weakened. To define the borders of the intra and interband continua, we have calculated the threshold energy where $\text{Im}\,\chi^{0,\text{intra}}_{\mathbf{G},\mathbf{G}'}(\mathbf{q},\omega)$ drops to zero and $\text{Im}\,\chi^{0,\text{inter}}_{\mathbf{G},\mathbf{G}'}(\mathbf{q},\omega)$ starts to increase from zero, respectively. The regions thus defined are indicated in the figure. The upper edge of the intraband continuum is well separated from the plasmon resonance, whereas the lower edge of the interband continuum is at approximately 1 eV at low q, and descends to lower energies as q increases. At $q \approx 0.1$ Å^{-1}, the plasmon enters the dissipative interband region and thus acquires a finite lifetime. Returning to the band structures, the onset of the interband continuum around 1 eV is seen to originate from transitions between the occupied bands just below the Fermi level and the metallic band. We note that transition from an undamped to a damped plasmon is not very clear in Fig. 1 where all the EELS peaks have a finite width. This is due to the numerical smearing, which introduces an artificial broadening of all spectral features. We mention that the effect of interband transitions on plasmons has been studied previously, e.g., for simple metals[30] and graphene.[31]

A. Bilayer NbS_2

Finally, we have studied a bilayer structure of NbS_2. The layers are hexagonally stacked and the separation set equal to half the experimental lattice constant of the bulk material ($c = 11.89$ Å). For such a bilayer system, classical plasmon hybridization theory predicts the existence of two plasmon modes for the combined structure, corresponding to the symmetric and antisymmetric, or bonding and antibonding, combinations of the uncoupled plasmon modes of the single layers.[16]

In order to investigate the spatial form of the plasmon modes of the bilayer, we follow a recently developed method.[27] As explained in Sec. II A, the full dielectric matrix is diagonalized for each frequency point to obtain its eigenvalues, $\epsilon_n(\mathbf{q},\omega)$ and left and right eigenfunctions, $\phi_n(\mathbf{q},\omega)$ and $\rho_n(\mathbf{q},\omega)$. The imaginary part of the inverse eigenvalues, $-\text{Im}\,\epsilon_n^{-1}(\mathbf{q},\omega)$, then provide a resolution the loss spectrum into independent dielectric eigenmodes. Modes corresponding to distinct peaks

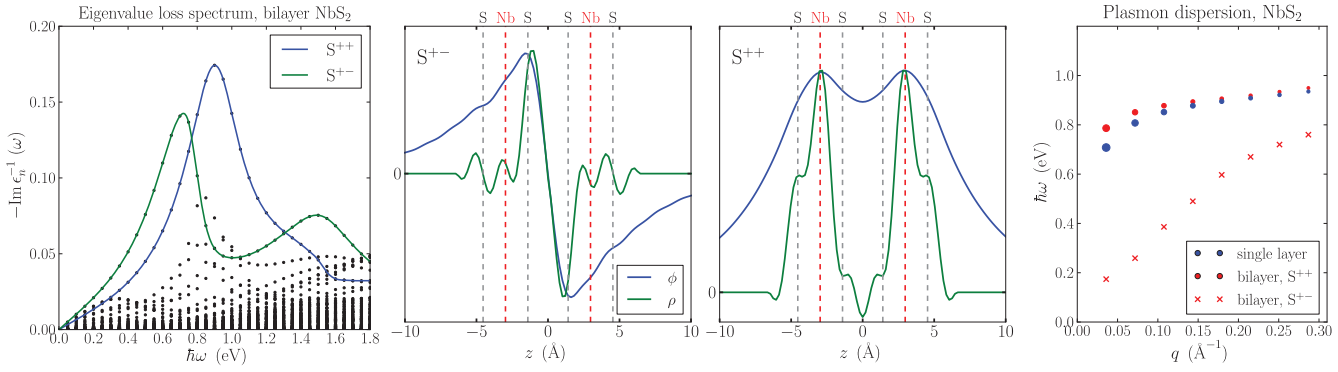

FIG. 4. (Color online) (Left) Eigenvalue loss spectrum for a bilayer NbS_2 structure. The imaginary parts of the inverse eigenvalues of the dielectric matrix $\epsilon_n(\omega)$ are plotted as a function of frequency. The two dominating eigenvalue curves, highlighted by the blue and green curves, correspond to the symmetric and antisymmetric plasmon modes, respectively. (Middle) Spatial shape of the symmetric (S^{++}) and antisymmetric (S^{+-}) plasmon modes plotted in the direction perpendicular to the layer. The charge density ρ and the corresponding potential ϕ are shown in green and blue, respectively. (Right) The energy dispersion of the two modes of the bilayer is shown together with the single-layer result for NbS_2. The S^{++} mode is slightly blue shifted compared to the single layer result as expected, whereas the S^{+-} mode is significantly redshifted and approaches the S^{++} mode with increasing q.

in the eigenvalue loss spectrum can be identified as the plasmon modes of the system, and the corresponding left and right eigenfunctions represent the potential and charge density of the plasmon excitation, respectively.[27]

In the left panel of Fig. 4, the eigenvalue loss spectrum is shown for a momentum transfer of $q \approx 0.25$ Å^{-1}. The spectrum is dominated by two eigenvalue curves, indicated by green and blue solid lines. For comparison, the eigenvalue loss spectrum for the monolayer systems (not shown) reveals a single peak very similar to both the blue curve in Fig. 4 (symmetric mode) and the EELS spectrum of the monolayer (shown in Fig. 1 for $TaSe_2$). Returning to Fig. 4, the eigenvectors belonging to the two peaks reveal an antisymmetric and a symmetric mode, labeled S^{+-} and S^{++}, respectively. The S^{+-} mode corresponds to an out-of-phase charge oscillation located on the two S atoms in the interface. The energy of this mode is significantly redshifted compared to the monolayer plasmon and shows a close to linear dispersion, see right panel of Fig. 4. However, the strength of this mode is vanishing at low q, which is possibly related to the close proximity of the two layers. The S^{++} mode can be characterized as an in-phase oscillation located on the transition metal atoms of the two layers. The induced density (ρ) of this mode within each layer is very similar to that found for the plasmon in monolayer $NbSe_2$ (not shown). The S^{++} mode is blue shifted relative to the single-layer result, particularly in the small q regime where the overlap between the potentials from the two layers is largest (recall the potential of a 2D charge density wave decays as e^{-qz}).[29]

IV. CONCLUSION

In conclusion, we have investigated the plasmonic properties of six monolayers of metallic transition metal dichalchogenides using first-principles calculations. Significant deviations from a 2D free-electron model were found due to coupling to interband transitions, which redshift the plasmon energy by up to 1 eV. For momentum transfers of $q \approx 0.1$ Å^{-1} the plasmon enters the dissipative electron-hole continuum. For a bilayer $NbSe_2$ structure, we found two plasmon modes, which can be regarded as symmetric and antisymmetric combinations of two unperturbed monolayer plasmons. The antisymmetric mode shows close to linear dispersion, but has very small strength, while the dispersion of the symmetric mode follows the monolayer plasmon with a slight blue shift.

ACKNOWLEDGMENTS

K.S.T. acknowledges support from the Danish Council for Independent Research's Sapere Aude Program through Grant No. 11-1051390. The Center for Nanostructured Graphene (CNG) is sponsored by the Danish National Research Foundation, Project DNRF58.

*kiran@fysik.dtu.dk
†thygesen@fysik.dtu.dk

[1] L. Britnell, R. V. Gorbachev, R. Jalil, B. D. Belle, F. Schedin, A. Mishchenko, T. Georgiou, M. I. Katsnelson, L. Eaves, S. V. Morozov *et al.*, Science **335**, 947 (2012).
[2] Q. Wang, K. Kalantar-Zadah, A. Kis, J. Coleman, and M. Strano, Nat. Nanotechnol. **7**, 699 (2012).
[3] B. Radisavljedic, A. Radenovic, J. Brivio, V. Giacometti, and A. Kis, Nat. Nanotechnol. **6**, 147 (2011).
[4] A. Splendiani, L. Sun, Y. Zhang, T. Li, J. Kim, C.-Y. Chim, G. Galli, and F. Wang, Nano Lett. **10**, 1271 (2010).
[5] K. F. Mak, C. Lee, J. Hone, J. Shan, and T. F. Heinz, Phys. Rev. Lett. **105**, 136805 (2010).
[6] A. K. Geim and I. V. Grigorieva, Nature (London) **499**, 419 (2013).
[7] A. Castellanos-Gomez *et al.*, Nano Res. **6**, 191 (2013).
[8] A. Ayari, E. Cobas, O. Ogundadegbe, and M. S. Fuhrer, J. Appl. Phys. **101**, 014507 (2007).
[9] N. E. Staley, J. Wu, P. Eklund, Y. Liu, L. J. Li, and Z. Xu, Phys. Rev. B **80**, 184505 (2009).
[10] L. Ju, B. Geng, J. Horng, C. Girit, M. Martin, Z. Hao, H. A. Bechtel, X. Liang, A. Zettl, Y. R. Shen *et al.*, Nat. Nanotechnol. **6**, 630 (2011).
[11] J. Chen, M. Badioli, P. Alonso-Gonzalez, S. Thongrattanasiri, F. Huth, J. Osmond, M. Spasenovic, A. Centeno, A. Pesquera, P. Godignon *et al.*, Nature (London) **487**, 77 (2012).
[12] Y. Liang and S. L. Cundy, Philos. Mag. **19**, 1031 (1969).
[13] A. König, K. Koepernik, R. Schuster, R. Kraus, M. Knupfer, B. Büchner, and H. Berger, Europhys. Lett. **100**, 27002 (2012).
[14] P. Cudazzo, M. Gatti, and A. Rubio, Phys. Rev. B **86**, 075121 (2012).
[15] M. N. Faraggi, A. Arnau, and V. M. Silkin, Phys. Rev. B **86**, 035115 (2012).
[16] E. Prodan, C. Radloff, N. J. Halas, and P. Nordlander, Science **302**, 419 (2003).
[17] H. Wang, D. W. Brandl, P. Nordlander, and N. J. Halas, Acc. Chem. Res. **40**, 53 (2007).
[18] X. Zhu, L. Shi, M. S. Schmidt, A. Boisen, O. Hansen, J. Zi, S. Xiao, and N. A. Mortensen, Nano Lett. **13**, 4690 (2013).
[19] P. Johari and V. B. Shenoy, ACS Nano **5**, 5903 (2011).
[20] J. Enkovaara, C. Rostgaard, J. J. Mortensen, J. Chen, M. Dulak, L. Ferrighi, J. Gavnholt, C. Glinsvad, V. Haikola, H. A. Hansen *et al.*, J. Phys.: Condens. Matter **22**, 253202 (2010).
[21] J. P. Perdew, K. Burke, and M. Ernzerhof, Phys. Rev. Lett. **77**, 3865 (1996).
[22] O. Gritsenko, R. van Leeuwen, E. van Lenthe, and E. J. Baerends, Phys. Rev. A **51**, 1944 (1995).
[23] M. Kuisma, J. Ojanen, J. Enkovaara, and T. T. Rantala, Phys. Rev. B **82**, 115106 (2010).
[24] D. Bohm and D. Pines, Phys. Rev. B **92**, 602 (1953).
[25] J. Yan, J. J. Mortensen, K. W. Jacobsen, and K. S. Thygesen, Phys. Rev. B **83**, 245122 (2011).
[26] C. A. Rozzi, D. Varsano, A. Marini, E. K. U. Gross, and A. Rubio, Phys. Rev. B **73**, 205119 (2006).
[27] K. Andersen, K. W. Jacobsen, and K. S. Thygesen, Phys. Rev. B **86**, 245129 (2012).
[28] C. Ataca, H. Sahin, and S. Ciraci, J. Phys. Chem. C **116**, 8983 (2012).
[29] R. A. Ferrell, Phys. Rev. **111**, 1214 (1958).
[30] F. Aryasetiawan and K. Karlsson, Phys. Rev. Lett. **73**, 1679 (1994).
[31] E. H. Hwang, S. Das Sarma, Phys. Rev. B **75**, 205418 (2007).

Paper III

The dielectric genome of van der Waals heterostructures.
Kirsten Andersen, Simone Latini, and Kristian S. Thygesen, submitted (2015).

The dielectric genome of van der Waals heterostructures

Kirsten Andersen,[*,†] Simone Latini,[†,‡] and Kristian S. Thygesen[*,†,‡]

Center for Atomic-scale Materials Design, Department of Physics, Technical University of Denmark, DK - 2800 Kgs. Lyngby, Denmark, and Center for Nanostructured Graphene, Technical University of Denmark, DK - 2800 Kgs. Lyngby, Denmark

E-mail: kiran@fysik.dtu.dk; thygesen@fysik.dtu.dk

KEYWORDS: van der Waals heterostructures, 2D materials, density-functional theory, dielectric function, excitons, plasmons

Abstract

Vertical stacking of two-dimensional (2D) crystals, such as graphene and hexagonal boron nitride, has recently lead to a new class of materials known as van der Waals heterostructures (vdWHs) with unique and highly tunable electronic properties. Ab-initio calculations should in principle provide a powerful tool for modeling and guiding the design of vdWHs, but in their traditional form such calculations are only feasible for commensurable structures with a few layers. Here we show that the dielectric properties of realistic, incommensurable vdWHs comprising hundreds of layers can be calculated with ab-initio accuracy using a multi-scale approach where the dielectric functions of the individual layers (the dielectric building blocks) are coupled simply

[*]To whom correspondence should be addressed

[†]Center for Atomic-scale Materials Design, Department of Physics, Technical University of Denmark, DK - 2800 Kgs. Lyngby, Denmark

[‡]Center for Nanostructured Graphene, Technical University of Denmark, DK - 2800 Kgs. Lyngby, Denmark

via their long-range Coulomb interaction. We use the method to illustrate the 2D-3D dielectric transition in multi-layer MoS_2 crystals, the hybridization of quantum plasmons in large graphene/hBN heterostructures, and to unravel the intricate effect of substrate screening on the non-Rydberg exciton series in supported WS_2. The dielectric building blocks for more than fifty different 2D materials are available in an open database allowing 2D materials researchers to efficiently predict and design the dielectric properties of realistic vdWHs.

The class of 2D materials which started with graphene is rapidly expanding and now includes metallic and semiconducting transition metal dichalcogenides[1] in addition to group III-V semi-metals, semiconductors and insulators.[2] These atomically thin materials exhibit unique opto-electronic properties with high technological potential.[3–7] However, the 2D materials only form the basis of a new and much larger class of materials consisting of vertically stacked 2D crystals held together by weak van der Waals forces. In contrast to conventional heterostructures which require complex and expensive crystal-growth techniques to epitaxially grow the single-crystalline semiconductor layers, vdWHs can be stacked in ambient conditions with no requirements of lattice matching. The latter implies a weaker constraint, if any, on the choice of materials that can be combined into vdWHs.

The weak inter-layer binding suggests that the individual layers of a vdWH largely preserve their original 2D properties modified only by the long range Coulomb interaction with the surrounding layers. Turning this argument around, it should be possible to predict the overall properties of a vdWH from the properties of the individual layers. In this Letter we show that this can indeed be achieved for the dielectric properties. Conceptually, this extends the Lego brick picture used by Geim and Grigorieva[8] for the atomic structure of a vdWH, to its dielectric properties. Specifically, we develop a semi-classical model which takes as input the dielectric functions of the individual isolated layers computed fully quantum mechanically and condensed into the simplest possible representation, and couple them together via the Coulomb interaction, see Figure 1. Despite the complete neglect of interlayer

hybridization, the model provides an excellent account of both the spatial and dynamical dielectric properties of vdWHs. The condensed representation of the dielectric function of all isolated 2D crystals can thus be regarded as the dielectric genome of vdWHs.

In addition to its conceptual value, our approach overcomes a practical limitation of conventional first-principles methods. Such methods are not only computationally demanding, but also rely on periodic boundary conditions which are incompatible with the incommensurable interfaces found in vdWHs. In fact, for many purposes, an in-plane lattice mismatch between neighbouring 2D crystals is preferred because it reduces the interlayer coupling and thus minimises the risk of commensurate-incommensurate transitions,[9] and to formation of Moire patterns[10] and associated band structure reconstructions[11] which are typical for systems with similar lattice constants. This emphasises the need for alternative approaches for modelling vdWHs.

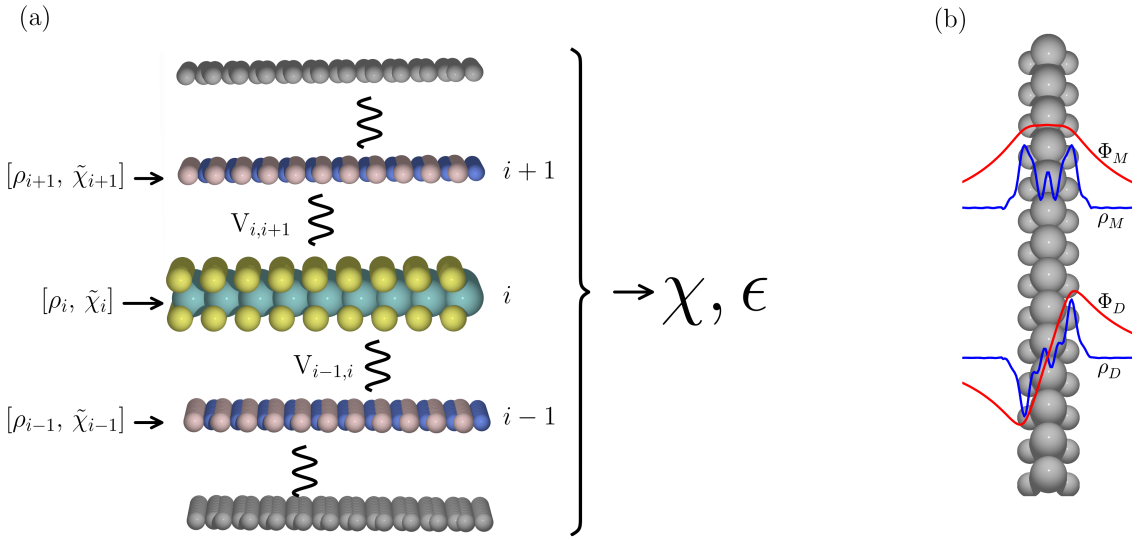

Figure 1: Schematic of the QEH model. (a) The density response function and dielectric function of the heterostructure are calculated from the dielectric building blocks of the individual layers assuming a purely electrostatic interaction between the layers. The dielectric building blocks are calculated ab-initio for the isolated layers. They comprise the monopole and dipole components of the density response function, $\tilde{\chi}_{M/D}$, together with the spatial shape of the electron density, $\rho_{M/D}(z)$, induced by a constant and linear applied potential, respectively. (b) Monopole and dipole induced densities (blue) together with the associated potentials (red) for monolayer MoS_2.

The dielectric function is one of the most important material response functions. It determines the effective interaction between charged particles in the material, contains information about the collective oscillations of the electron gas (plasmons),[12] and enters as a fundamental ingredient in many-body calculations of e.g. excitons and quasiparticle band structures.[13,14]

The (inverse) dielectric function is related to the electron density response function, χ, via

$$\epsilon^{-1}(\mathbf{r}, \mathbf{r}', \omega) = \delta(\mathbf{r} - \mathbf{r}') + \int \frac{1}{|\mathbf{r} - \mathbf{r}''|} \chi(\mathbf{r}'', \mathbf{r}', \omega) d\mathbf{r}''. \tag{1}$$

In our quantum-electrostatic heterostructure (QEH) model the calculation of the dielectric function is divided into two parts. In the first part the in-plane averaged density response function of each of the freestanding layers, $\chi_i(z, z', q_\parallel, \omega)$, are obtained from ab-initio calculations. Here $q_\parallel$ could be a vector, but we treat it as a scalar since most 2D materials are isotropic within the plane. From χ_i we calculate the magnitude of the monopole/dipole component of the density induced by a potential with a constant/linear variation across the layer and in-plane variation $\exp(ir_\parallel q_\parallel)$:

$$\tilde{\chi}_{i\alpha}(q_\parallel, \omega) = \int z^\alpha \chi_i(z, z', q_\parallel, \omega) z'^\alpha dz dz'. \tag{2}$$

Here $\alpha = 0, 1$ for the monopole and dipole components, respectively. In addition we calculate the spatial form of the induced density, $\rho_{i\alpha}(z, q_\parallel)$. With a proper normalization of $\rho_{i\alpha}$ we can then write

$$\int \chi_i(z, z', q_\parallel, \omega) z'^\alpha dz' = \tilde{\chi}_{i\alpha}(q_\parallel, \omega) \rho_{i\alpha}(z, q_\parallel) \tag{3}$$

We have found that while $\tilde{\chi}_{i\alpha}$ depends strongly on frequency, $\rho_{i\alpha}$ does not. The data set $(\tilde{\chi}_{i\alpha}, \rho_{i\alpha})$ with $\alpha = 0, 1$ or equivalently $\alpha = M, D$ constitutes the dielectric building block of layer i, as illustrated in Figure 1. According to Eq. (3) the dielectric building block allows

us to obtain the density induced in the (isolated) layer i by a constant/linear potential. It is straightforward to extend the dielectric building blocks to account for higher-order moments in the induced density described by $\alpha > 1$, but we have found the dipole approximation to be sufficient in all cases considered.

In the second part of the QEH model, the density response function of the vdWH in the discrete monopole/dipole representation is obtained by solving a Dyson equation that couples the dielectric building blocks together via the Coulomb interaction. The Dyson equation for the full density response function giving the magnitude of the monopole/dipole density on layer i induced by a constant/linear potential applied to layer j, reads (omitting the $q_\parallel$ and ω variables for simplicity)

$$\chi_{i\alpha,j\beta} = \tilde{\chi}_{i\alpha}\delta_{i\alpha,j\beta} \; + \tilde{\chi}_{i\alpha} \sum_{k\neq i,\gamma} V_{i\alpha,k\gamma}\, \chi_{k\gamma,j\beta} \tag{4}$$

The Coulomb matrices are defined as

$$V_{i\alpha,k\gamma}(q_\parallel) = \int dz \rho_{i\alpha}(z, q_\parallel)\Phi_{k\gamma}(z, q_\parallel) \tag{5}$$

where $\Phi_{k\gamma}$ is the potential of the induced density, $\rho_{k\gamma}$, which we calculate on a uniform grid by solving a 1D Poisson equation. Note that we leave out the self-interaction terms in Eq. (4) since the intralayer Coulomb interaction is already accounted for by the uncoupled $\tilde{\chi}_{i\alpha}$. The (inverse) dielectric function of Eq. (1) in the monopole/dipole basis becomes

$$\epsilon^{-1}_{i\alpha,j\beta}(q_\parallel, \omega) = \delta_{i\alpha,j\beta} + \sum_{k\gamma} V_{i\alpha,k\gamma}(q_\parallel)\, \chi_{k\gamma,j\beta}(q_\parallel, \omega). \tag{6}$$

More details on the method and computations are provided in the supporting information.

A database containing the dielectric building blocks of a large collection of 2D materials has been constructed.[15] It presently contains more than 50 transition metal dichalcogenides and oxides, graphene at different doping levels, and hBN, and more materials are being

added. From here the data files can be downloaded together with a Python module for calculating the dielectric function and associated properties of any combination of these materials. QEH model calculations for vdWHs containing a few hundred layers can be performed on a standard PC.

First-principles calculations were performed with the GPAW code.[16,17] Single-particle wave functions and energies were calculated within the local density approximation (LDA) using 400 eV plane wave cut-off and at least 45×45 sampling of the 2D Brillouin zone. Density response functions and dielectric functions were calculated within the random phase approximation (RPA). Except for MoS_2 bulk, we included at least 15 Å of vacuum in the super cells perpendicular to the layers and applied a truncated Coulomb kernel to avoid long range screening between periodically repeated structures. All response functions were calculated in a plane wave basis including reciprocal lattice vectors up to at least 50 eV. A similar cut off was used for the sum over empty states and convergence was carefully checked. The frequency dependence of the response functions was represented on a non-linear frequency grid ranging from 0 to 35 eV, with an initial grid spacing of 0.02 eV. All details of the calculations and atomic structure geometries are provided in the supporting information.

As a first application of the QEH model, we study how the (static) dielectric function of a 2D material evolves as the layer thickness increases towards the bulk. One of the most characteristic differences between 2D and 3D materials is the behaviour of the dielectric function in the long wave length limit: For a bulk semiconductor, the dielectric function $\epsilon(q)$ tends smoothly to a constant value larger than unity as $q \to 0$. In contrast $\epsilon(q_\parallel) = 1 + O(q_\parallel)$ for a 2D semiconductor implying a complete absence of screening in the long wave length limit.[18,19]

Ab initio calculations were performed for the dielectric function of MoS_2 monolayer, bilayer, and bulk, and the QEH model was used for multilayer structures up to 100 layers. Figure 2 (b) shows the dielectric functions averaged over the slabs as function of the in-plane

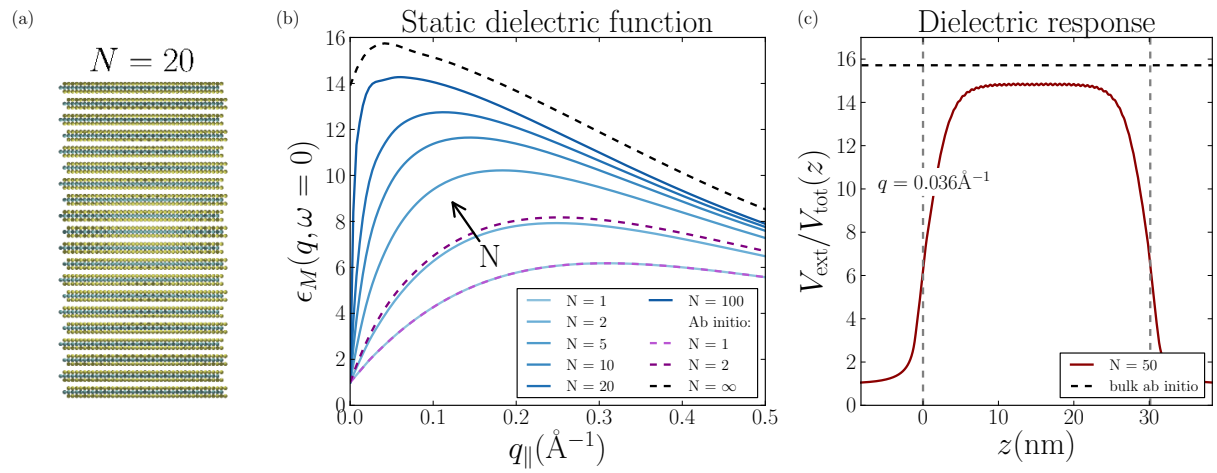

Figure 2: 2D-3D transition of the dielectric function. (a) Atomic structure of a 20 layer MoS_2 slab. (b) The macroscopic static dielectric function $\epsilon_M(q_\parallel, \omega = 0)$ as a function of the in-plane momentum transfer for different number of layers, N. The macroscopic dielectric function relates the total potential averaged over the width of the slab to an external potential of the form $V_{ext}(r_\parallel, z) = \exp(ir_\parallel q_\parallel)$. The dielectric functions increase monotonically with N converging slowly towards the dielectric function of bulk MoS_2 obtained from an ab-initio calculation. Excellent agreement between the QEH model and the ab initio results are seen for $N = 1, 2$. The slow convergence towards the bulk result is due to the strong spatial variation of the induced potential in the surface region of the slabs. This can be seen in panel (c) which shows $V_{ext}/V_{tot}(z)$, i.e. the local dielectric function, for an external potential constant across the slab and with in-plane wave vector $q_\parallel = 0.036\text{Å}^{-1}$ for $N = 50$.

momentum transfer. For large $q_\parallel$ the dielectric functions show similar behavior. However, whereas $\epsilon(0) = 14$ for the bulk, the dielectric functions of the slabs decrease sharply to 1 for small $q_\parallel$. This demonstrates that the dielectric properties of a vdWH of thickness L are 2D like for $q_\parallel \ll 1/L$ and 3D like for $q_\parallel \gg 1/L$.

The QEH model describes the change in the dielectric function from mono- to bilayer very accurately in spite of the well known differences between the mono- and bilayer band structures.[20] This shows that hybridisation driven band structure effects, i.e. quantum confinement, have negligible influence on the dielectric properties of a vdWH and is the main reason for the success of the QEH model. The model result seems to converge towards the ab initio bulk result, however, convergence is not fully reached even for $N = 100$. The slow convergence towards the bulk result is due to the spatial variation of the induced

potential across the slab. In Figure 2 (c) we show the z-dependent dielectric function defined as $\epsilon(z) = V_{ext}/V_{tot}(z)$, for a constant (along z) external potential and $N = 50$. Although $\epsilon(z)$ is close to the ab-initio bulk value (dashed line) in the middle of the slab, screening is strongly suppressed in the surface region. This is a direct consequence of the anisotropic nature of the layered MoS_2 crystals which limits the screening of perpendicular fields, and is expected to be a general property of vdWHs. Increasing the slab thickness beyond 50 layers brings the QEH result even closer to the bulk result in the middle of the slab, but a small underestimation remains originating from the difference in the band structures of the monolayer and bulk systems.

Next, we consider the hybridisation of plasmons in graphene sheets separated by hBN, see Figure 3(a). Plasmons in graphene on hBN were recently found to propagate with low loss,[6] and the close to perfect lattice match between the two layers enables full ab initio calculations for the thinnest heterostructures. Here we use doped graphene that has a finite density of states at the Fermi level, giving rise to two-dimensional plasmons with energies in the regime 0-2 eV. The plasmon energies goes to zero in the optical limit, $q_\parallel \to 0$ as is characteristic for plasmons in 2D metals.[21,22] We calculate the effect of hBN on the plasmons using the QEH model for up to 20 layers of hBN and compare to full ab-initio calculations for 1-3 layers of hBN.

To identify the plasmons of the heterostructure we follow Ref.[23] In brief, we compute the eigenvalues, $\epsilon_n(\omega)$, of the heterostructure dielectric function and identify a plasmon energy, $\hbar\omega_P$, from the condition $\mathrm{Re}\epsilon_n(\omega_P) = 0$, see Figure 3(b). The corresponding eigenvector, $\phi_n(\omega_P)$, represents the potential associated with the plasmon oscillation, see panel (c). This analysis identifies two plasmons corresponding to the symmetric $(++)$ and antisymmetric $(+-)$ combinations of the graphene plasmons as previously found for two freestanding graphene sheets.[24] For 1-3 hBN layers, the QEH model perfectly reproduces the ab-initio results for the dielectric eigenvalues, plasmon energy, and weight. The latter was defined as the area under the peaks in the loss function $-\mathrm{Im}\epsilon^{-1}(q_\parallel, \omega)$, see panel (b). The densities

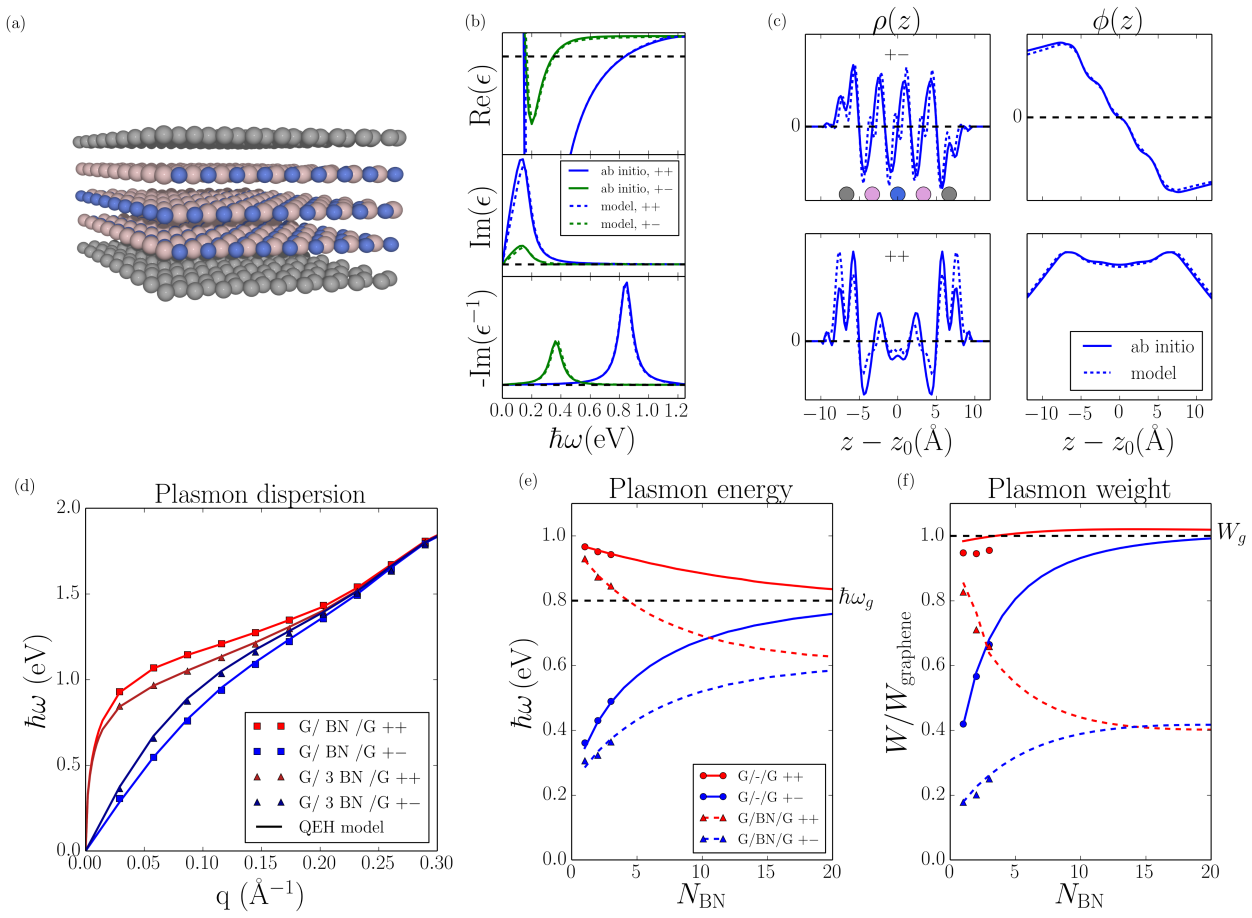

Figure 3: Plasmons in graphene/hBN heterostructures. (a) Two graphene sheets separated by three layers of hBN. (b) Eigenvalues of the heterostructure dielectric function $\epsilon(\omega)$. Only the two eigen value curves that fullfill the plasmon condition $\mathrm{Re}\epsilon_n(\omega_P) = 0$ are shown. (c) The eigen potential, $\psi(\omega_P)$, and associated density, $\rho(\omega_P)$, of the plasmon modes. The plasmons correspond to the antisymmetric $(+-)$ and symmetric $(++)$ combinations of the isolated graphene plasmons. (d) Plasmon dispersion for heterostructures containing 1 and 3 layers of hBN. Full lines denote the QEH model while ab-initio results are denoted by symbols. (e+f) Energy and weight of the plasmon modes for up to 20 layers hBN between the graphene sheets. Results for equivalent structures with vacuum filling the gap are also shown. Dashed black lines indicate the plasmon energy and weight in an isolated graphene sheet. Overall, the QEH model is in excellent agreement with the full ab initio calculations performed for up to 3 layers hBN.

and potentials of the plasmon eigen modes shown in panel (c) are also reproduced fairly accurately by the model. As can be seen in panels (e+f) the effect of the hBN buffer is to red shift and damp the plasmons compared to the result for two graphene sheets separated by the same amount of vacuum. This is also reflected by the relatively large amount of

electron density located on the hBN during the plasma oscillation, see panel (c).

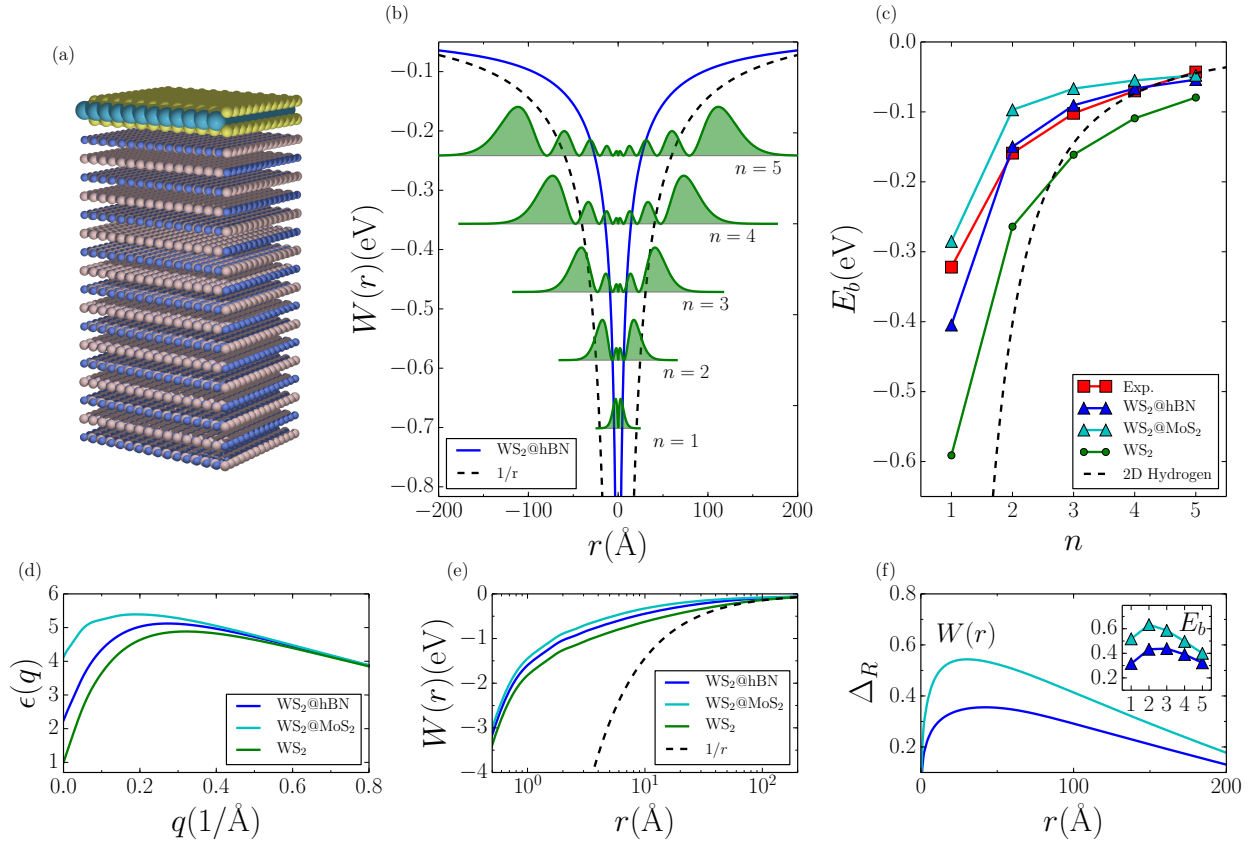

Figure 4: Excitons in supported WS_2. (a) Monolayer WS_2 adsorbed on a h-BN substrate. (b) The screened interaction between an electron and a hole localised within a WS_2 monolayer adsorbed on hBN. For comparison the unscreened $1/r$ potential is shown. The radial probability distribution of the first five excitons, $r|F(r)|^2$, are also shown (arbitrary normalization). (c) The calculated binding energies of the lowest five excitons in freestanding WS_2 (green dashed) and WS_2 on hBN (blue) and MoS_2 (cyan). Experimental values from Ref.[25] for WS_2 on SiO_2 are shown in red. The 2D hydrogen model with a $1/\epsilon r$ potential is shown for $\epsilon = 1.7$. (d) The dielectric function of the WS_2 layer defined as $\epsilon(q) = V(q)/W(q)$, where $V(q)$ and $W(q)$ are the bare and screened interaction in the WS_2 layer, respectively. (e) The screened interaction in the WS_2 layer as function of $\log(r)$. (f) The relative difference between the screened interaction in the supported and freestanding WS_2. Inset shows the relative difference between E_b for the supported and freestanding WS_2.

Finally, we explore some characteristic features of excitons in freestanding and supported 2D semiconductors. A straight forward generalisation of the well known Mott-Wannier

model[26] leads to the following eigenvalue equation for the excitons of a 2D semiconductor:[18,27]

$$\left[-\frac{\nabla_{2D}^2}{2\mu_{ex}} + W(\mathbf{r})\right] F(\mathbf{r}) = E_b F(\mathbf{r}), \tag{7}$$

where E_b is the exciton binding energy, $F(\mathbf{r})$ is the wave function, μ_{ex} is the effective mass, and $W(\mathbf{r})$ is the screened electron-hole interaction. Assuming that the electron and hole are localised in layer 1, the Fourier transformed screened electron-hole interaction is obtained from the static ($\omega = 0$) response function Eq. (4) and Coulomb interaction matrix Eq. (5) of the QEH model,

$$W(q_\parallel) = V_{1M,1M} + \sum_{i\alpha,j\beta} V_{1M,j\beta l}(q_\parallel)\chi_{j\beta,i\alpha}(q_\parallel)V_{i\alpha,1M}(q_\parallel). \tag{8}$$

The first term is the bare, i.e. unscreened, electron-hole interaction in layer 1 under the assumption that the electron and hole densities can be represented by the induced monopole density, $\rho_{1M}(z)$. Note that the above equation can be easily generalised to describe the screened interaction between charges localised in different layers (relevant for indirect excitons).

In Ref.[25] Chernikov et al. observed a peculiar non-hydrogenic Rydberg series for the excitons in a single layer of WS_2 adsorbed on a SiO_2 substrate. Here we use the QEH model to calculate the screened electron-hole interaction within the WS_2 layer from the dielectric function of the full heterostructure, see Methods. Since the QEH is applicable only to layered materials we place WS_2 on a 100 layer thick slab of hBN which has dielectric constant very similar to that of SiO_2 (both around 4). For comparison we performed similar calculations using MoS_2 as substrate (dielectric constant larger than SiO_2). Figure 4 (c) shows the five lowest s-excitons calculated from Eq. (7) for both freestanding and supported WS_2. For freestanding WS_2, we obtain $E_b = 0.59$ eV for the lowest exciton in good agreement with previous ab-initio calculations.[28] The enhanced screening from the substrate lowers the exciton binding energies bringing the entire series closer to the experimental values (red), in

particular for the hBN substrate.

Figure 4 (d) shows that the dielectric function of the supported WS_2 layer exceeds unity in the $q \to 0$ limit. This means that the nature of the screening within the layer is not strictly 2D because the bulk substrate is able to screen the long wave length fields. In real space, the screened potentials diverge as $\log(r)$ for small r and decay as $1/r$ for large r, see panel (e). In panel (f) we show how the substrate affects $W(r)$: The relative deviation from $W(r)$ of the freestanding layer vanishes for small and large r but becomes significant at intermediate distances. As a consequence, the substrate-induced change in the exciton binding energy is relatively larger for intermediate exciton sizes. These results clearly demonstrate the profound, nonlocal influence of substrates on the dielectric screening and excitations in 2D materials.

In conclusion, we have demonstrated that the spatial and dynamical dielectric properties of a vdWH can be accurately and efficiently obtained from the dielectric properties of its constituent 2D crystals. The presented quantum-electrostatic heterostructure model (QEH) exploits this feature and enables the calculation of the dielectric properties and collective electronic excitations of realistic incommensurable heterostructures with ab-initio precision.

Acknowledgement

The authors thank Karsten Jacobsen for inspiring discussions. The authors acknowledge support from the Danish Council for Independent Research's Sapere Aude Program through grant no. 11-1051390. The Center for Nanostructured Graphene (CNG) is sponsored by the Danish National Research Foundation, Project DNRF58.

Supporting Information Available

Detailed description of our quantum-electrostatic heterostructure (QEH) model and the computational details for all the ab-initio calculations. This material is available free of charge via the Internet at `http://pubs.acs.org/`.

The authors declare no competing financial interest.

References

(1) Wang, Q. H.; Kalantar-Zadeh, K.; Kis, A.; Coleman, J. N.; Strano, M. S. *Nature Nanotechnology* **2012**, *7*, 699–712.

(2) Şahin, H.; Cahangirov, S.; Topsakal, M.; Bekaroglu, E.; Akturk, E.; Senger, R. T.; Ciraci, S. *Physical Review B* **2009**, *80*, 155453.

(3) Britnell, L.; Ribeiro, R. M.; Eckmann, a.; Jalil, R.; Belle, B. D.; Mishchenko, a.; Kim, Y.-J.; Gorbachev, R. V.; Georgiou, T.; Morozov, S. V.; Grigorenko, a. N.; Geim, a. K.; Casiraghi, C.; Castro Neto, a. H.; Novoselov, K. S. *Science* **2013**, *340*, 1311–4.

(4) Choi, M. S.; Lee, G.-H.; Yu, Y.-J.; Lee, D.-Y.; Lee, S. H.; Kim, P.; Hone, J.; Yoo, W. J. *Nature Communications* **2013**, *4*, 1624.

(5) Shih, C. J.; Wang, Q. H.; Son, Y.; Jin, Z.; Blankschtein, D.; Strano, M. S. *ACS Nano* **2014**, *8*, 5790–5798.

(6) Woessner, A.; Lundeberg, M. B.; Gao, Y.; Principi, A.; Alonso-González, P.; Carrega, M.; Watanabe, K.; Taniguchi, T.; Vignale, G.; Polini, M.; Hone, J.; Hillenbrand, R.; Koppens, F. H. L. *Nature Materials* **2014**, 1–5.

(7) Withers, F. et al. *Nature Materials* **2015**, 1–6.

(8) Geim, a. K.; Grigorieva, I. V. *Nature* **2013**, *499*, 419–25.

(9) Woods, C. R. et al. *Nature Physics* **2014**, *10*, 451–456.

(10) Kang, J.; Li, J.; Li, S. S.; Xia, J. B.; Wang, L. W. *Nano Letters* **2013**, *13*, 5485–5490.

(11) Lu, C.-P.; Li, G.; Watanabe, K.; Taniguchi, T.; Andrei, E. *Physical Review Letters* **2014**, *113*, 156804.

(12) Pitarke, J. M.; Silkin, V. M.; Chulkov, E. V.; Echenique, P. M. *Reports on Progress in Physics* **2007**, *70*, 1–87.

(13) Onida, G.; Reining, L.; Rubio, A. *Reviews of Modern Physics* **2002**, *74*, 601–659.

(14) Hybertsen, M. S.; Louie, S. G. *Physical Review B* **1986**, *34*, 5390.

(15) The dielectric building blocks and QEH software can be downloaded at https://cmr.fysik.dtu.dk/c2dm/c2dm.html.

(16) Enkovaara, J.; et al., *Journal of Physics: Condensed Matter* **2010**, *22*, 253202.

(17) Yan, J.; Mortensen, J. J.; Jacobsen, K. W.; Thygesen, K. S. *Physical Review B* **2011**, *83*, 245122.

(18) Cudazzo, P.; Tokatly, I. V.; Rubio, A. *Physical Review B* **2011**, *84*, 085406.

(19) Hüser, F.; Olsen, T.; Thygesen, K. S. *Physical Review B* **2013**, *87*, 1–14.

(20) Cheiwchanchamnangij, T.; Lambrecht, W. R. L. *Physical Review B* **2012**, *85*, 1–4.

(21) Hwang, E.; Sarma, S. *Physical Review B* **2007**, *75*, 205418.

(22) Shin, S. Y.; Kim, N. D.; Kim, J. G.; Kim, K. S.; Noh, D. Y.; Kim, K. S.; Chung, J. W. *Applied Physics Letters* **2011**, *99*, 082110.

(23) Andersen, K.; Jacobsen, K.; Thygesen, K. *Physical Review B* **2012**, *86*, 245129.

(24) Hwang, E.; Das Sarma, S. *Physical Review B* **2009**, *80*, 205405.

(25) Chernikov, A.; Berkelbach, T. C.; Hill, H. M.; Rigosi, A.; Li, Y.; Aslan, O. B.; Reichman, D. R.; Hybertsen, M. S.; Heinz, T. F. *Physical Review Letters* **2014**, *113*, 076802.

(26) Wannier, G. H. *Physical Review* **1937**, *52*, 191.

(27) Berkelbach, T. C.; Hybertsen, M. S.; Reichman, D. R. *Physical Review B* **2013**, *88*, 045318.

(28) Shi, H.; Pan, H.; Zhang, Y.-W.; Yakobson, B. I. *Physical Review B* **2013**, *87*, 155304.

Supplementary material for paper III

Supplementary material for: The dielectric genome of van der Waals Heterostructures

Kirsten Andersen and Simone Latini
Center for Atomic-scale Materials Design, Department of Physics
Technical University of Denmark, DK - 2800 Kgs. Lyngby, Denmark

Kristian S. Thygesen*
Center for Atomic-scale Materials Design, Department of Physics, and Center for Nanostructured Graphene
Technical University of Denmark, DK - 2800 Kgs. Lyngby, Denmark

In this supplementary material we provide a detailed description of our quantum-electrostatic heterostructure (QEH) model including the precise definition of the dielectric building blocks. In addition we detail the spectral analysis used to identify the plasmon eigen modes for the graphene/hBN structures and describe the calculation of the screened electron-hole interaction used in the 2D exciton model. Finally, we provide computational details for all the ab-initio calculations presented in the Letter.

I. FORMAL MATTERS

Within linear response theory, the induced density due to an external field of the form $V_{ext}(\mathbf{r},t) = V_{ext}(\mathbf{r},\omega)e^{i\omega t}$, is described by the density response function, $\chi(\mathbf{r},\mathbf{r}',\omega)$:

$$n_{\rm ind}(\mathbf{r},\omega) = \int dr' \chi(\mathbf{r},\mathbf{r}',\omega) V_{ext}(\mathbf{r}',\omega), \tag{1}$$

The density response function can be obtained from its non-interacting counterpart, $\chi^0(\mathbf{r},\mathbf{r}',\omega)$, that gives the response to the *total* field, by solving the Dyson equation in the random phase approximation (RPA):

$$\chi(\mathbf{r},\mathbf{r}',\omega) = \chi^0(\mathbf{r},\mathbf{r}',\omega) + \int\int d\mathbf{r}_1 d\mathbf{r}_2 \chi^0(\mathbf{r},\mathbf{r}_1,\omega)\frac{1}{|\mathbf{r}_1-\mathbf{r}_2|}\chi(\mathbf{r}_2,\mathbf{r}',\omega). \tag{2}$$

For modelling of vdWHs, this equation is favourably split into two parts, namely the intra-layer and inter-layer parts, as described below.

We are assuming a basis set consisting of layer centred functions, $\{\phi_{i\alpha}\}$, where i denotes the layer. Defining the Coulomb matrix as

$$\mathbf{V}_{i\alpha,j\beta} = \int d\mathbf{r} d\mathbf{r}' \phi_{i\alpha}(\mathbf{r})\frac{1}{|\mathbf{r}-\mathbf{r}'|}\phi_{j\beta}(\mathbf{r}') \tag{3}$$

we can divide the Coulomb interaction into its intra- and interlayer parts: $\mathbf{V} = \tilde{\mathbf{V}} + \mathbf{V^I}$. The Dyson equation 2 can then be separated into the following two matrix equations

$$\tilde{\boldsymbol{\chi}} = \boldsymbol{\chi^0} + \boldsymbol{\chi^0}\tilde{\mathbf{V}}\tilde{\boldsymbol{\chi}} \tag{4}$$

$$\boldsymbol{\chi} = \tilde{\boldsymbol{\chi}} + \tilde{\boldsymbol{\chi}}\mathbf{V^I}\boldsymbol{\chi}. \tag{5}$$

To see this, simply insert Eq. 4 into Eq. 5

$$\boldsymbol{\chi} = \boldsymbol{\chi^0} + \boldsymbol{\chi^0}\tilde{\mathbf{V}}\tilde{\boldsymbol{\chi}} + \boldsymbol{\chi^0}\mathbf{V^I}\boldsymbol{\chi} + \boldsymbol{\chi^0}\tilde{\mathbf{V}}\tilde{\boldsymbol{\chi}}\mathbf{V^I}\boldsymbol{\chi} \tag{6}$$

$$= \boldsymbol{\chi^0} + \boldsymbol{\chi^0}\mathbf{V^I}\boldsymbol{\chi} + \boldsymbol{\chi^0}\tilde{\mathbf{V}}(\tilde{\boldsymbol{\chi}} + \tilde{\boldsymbol{\chi}}\mathbf{V^I}\boldsymbol{\chi}) \tag{7}$$

$$= \boldsymbol{\chi^0} + \boldsymbol{\chi^0}\mathbf{V^I}\boldsymbol{\chi} + \boldsymbol{\chi^0}\tilde{\mathbf{V}}\boldsymbol{\chi} \tag{8}$$

$$= \boldsymbol{\chi^0} + \boldsymbol{\chi^0}(\tilde{\mathbf{V}} + \mathbf{V^I})\boldsymbol{\chi}, \tag{9}$$

which is the original Dyson equation.

At this point no approximations, except for the RPA, have been introduced. In particular, $\boldsymbol{\chi^0}$ in Eq. 4 is the non-interacting response function of the full vdWH. To make progress we make the assumption that the overlap/hybridization between wave functions (not to be confused with the basis functions) on neighbouring layers can be neglected. This allows us to replace χ^0 of the heterostructure by the sum of χ^0_i for the individual isolated layers. In practice this means that Eq. 4 can be solved for each layer separately.

We calculate χ^0 for the isolated layers within the RPA using single-particle wave functions and energies from density functional theory (DFT) as described in Ref.[1]. The interacting density response function, $\tilde{\chi}$, for the monolayer is obtained by solving the Dyson equation in a plane-wave basis with a 2D truncated Coulomb Kernel, $\tilde{V}^{2D}_{\mathbf{G}}$:

$$\tilde{V}^{2D}_{\mathbf{G},G_z} = \frac{4\pi}{G^2}\big[1-\cos(G_z L/2)\big]. \tag{10}$$

The use of a truncated Coulomb interaction is essential to avoid interaction between periodically repeated layers[2]. The truncation length is set to half the unit cell height, L. In the plane wave basis, the Dyson equation for the density response function, $\tilde{\chi}$, is then written:

$$\tilde{\chi}_{\mathbf{G},\mathbf{G}'}(\mathbf{q}_\parallel,\omega) = \chi^0_{\mathbf{G},\mathbf{G}'}(\mathbf{q}_\parallel,\omega) + \sum_{\mathbf{G}_1}\chi^0_{\mathbf{G},\mathbf{G}_1}(\mathbf{q}_\parallel,\omega)\tilde{V}^{2D}_{\mathbf{G}_1}(\mathbf{q}_\parallel)\tilde{\chi}_{\mathbf{G}_1,\mathbf{G}'}(\mathbf{q}_\parallel,\omega), \tag{11}$$

where $\mathbf{q}_\parallel$ belongs to the 2D Brillouin zone.

II. QEH MODEL

A. The dielectric building blocks

We start by defining the density response function for the individual layers, where the macroscopic average is

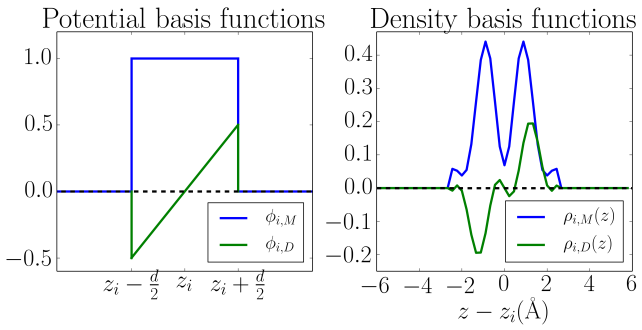

FIG. 1: Basis functions used to represent potentials (left) and induced densities (right) in the QEH model. The example is for graphene.

taken in the parallel directions. The response function is then expressed in terms of the perpendicular coordinates z and z', and the magnitude of the momentum transfer parallel to the layer, $q_\parallel$ (we assume isotropic materials, where the response does not depend on the direction of $q_\parallel$, but the method can be straightforwardly generalized to non-isotropic 2D materials):

$$\begin{aligned}\tilde{\chi}(z,z',q_\parallel,\omega) &= \frac{1}{A}\int_A\int_A d\mathbf{r}_\parallel d\mathbf{r}'_\parallel \tilde{\chi}(\mathbf{r},\mathbf{r}',q_\parallel,\omega)\\ &= \frac{1}{L}\sum_{\mathbf{G}_z,\mathbf{G}'_z} e^{i\mathbf{G}_z z}\tilde{\chi}_{\mathbf{G}_z,\mathbf{G}'_z}(q_\parallel,\omega)e^{-i\mathbf{G}'_z z'},\end{aligned} \tag{12}$$

where the integration is over the in-plane coordinates, A is the in-plane area of the supercell, and L is the height of the supercell perpendicular to the layer. Integrating over the in-plane coordinates corresponds to taking the zero components $\mathbf{G}_\parallel = \mathbf{G}'_\parallel = 0$ in the plane-wave representation of $\tilde{\chi}_{\mathbf{G},\mathbf{G}'}(\mathbf{q},\omega)$. Working with $\tilde{\chi}$ instead of $\tilde{\chi}^0$ ensures that local field effects within the isolated layer are exactly taken into account.

For an efficient representation of the response functions and solution of the Dyson equation we need a small yet accurate basis set to represent the induced densities in the layers and the potentials created by these induced densities. To represent potentials we simply use a constant and linear potential corresponding to a first order expansion of the induced potentials, see Fig 1(left). We refer to these as monopole (M) and dipole (D) potentials. The potential basis functions of layer i at position z_i are thus

$$\phi_{i,M}(z) = 1_{[z_i-d/2,z_i+d/2]} \tag{13}$$

$$\phi_{i,D}(z) = (z-z_i)\,1_{[z_i-d/2,z_i+d/2]} \tag{14}$$

$$1_C = \begin{cases} 1 & \text{if } z \in C \\ 0 & \text{if } z \notin C \end{cases} \tag{15}$$

where d is a localisation parameter that is set equal to the interplane distance. Since the density response is already confined to the layer, the precise value of d is not essential and in calculating the matrix elements of the intralayer response function we integrate over all space:

$$\tilde{\chi}_{i\alpha}(q_\parallel,\omega) = \int\int dz dz' \phi_{i,\alpha}(z)\tilde{\chi}(z,z',q_\parallel,\omega)\phi_{i,\alpha}(z') \tag{16}$$

$$\approx \int\int dz dz' (z-z_i)^\alpha \tilde{\chi}_i(z,z',q_\parallel,\omega)(z'-z_i)^\alpha, \tag{17}$$

where $\alpha = \{M,D\}$ or equivalently $\alpha = \{0,1\}$.

The basis functions can be interpreted as potentials that act on χ. In order to represent the induced densities produced by these potentials, we introduce two density basis functions defined as

$$\rho_{i,\alpha}(z,q_\parallel) = \frac{\int dz' \tilde{\chi}(z,z',q_\parallel,\omega=0)\,\phi_{i,\alpha}(z')}{\tilde{\chi}_{i,\alpha}(q_\parallel,\omega=0)}. \tag{18}$$

As an example, the monopole and dipole density basis functions for monolayer graphene are shown in Fig. 1(right). We have found that the frequency dependence of the basis functions can in general be omitted, while the $q_\parallel$-dependence is not always negligible. Dividing by $\tilde{\chi}_{i,\alpha}(q_\parallel,\omega=0)$ in Eq. 18 ensures that the density basis function is normalized such that the overlap with the potential basis is unity: $\langle\phi_{i,\alpha}|\rho_{i,\alpha}(q_\parallel)\rangle = 1$, where integration over z is implied. To ease the derivation of the Dyson equation in the monopole/dipole basis, we make the approximation that the potential and density basis functions form a dual basis, i.e.

$$\langle\phi_{i,\alpha}|\rho_{j,\beta}(q_\parallel)\rangle \;= \delta_{\alpha\beta}\delta_{ij}, \tag{19}$$

where $\alpha,\beta = \{M,D\}$, and i,j are layer indices. This implies that, within the subspace spanned by the basis functions, we have the completeness relation

$$\mathrm{P} = \sum_{i,\alpha}|\rho_{i,\alpha}\rangle\langle\phi_{i,\alpha}| = \hat{1} \tag{20}$$

We note that Eq. (19) is not exact because of the small but finite overlap between potential and density basis functions on neighbouring layers. However, taking this into account gives very small modifications to the resulting vdWH dielectric properties. Finally, we note that working with a dual basis is natural as, in general, the spectral representation of the dielectric function is written in a dual basis of potential and density eigenfunctions[3].

B. Electrostatic Dyson equation

The Dyson equation (5) for the heterostructure density response function $\chi(z,z',q_\parallel,\omega)$ is now written in the potential basis of dimension $2N\times 2N$, where N is the number of layers. In the following the $(q_\parallel,\omega)$ variables are omitted from the expressions for simplicity. Response functions $\tilde{\chi}$, χ and Coulomb kernel V are regarded as operators and integration over $\mathbf{r},\mathbf{r}'$ is implied in the inner

products. The matrix elements of χ are written in the potential basis:

$$\langle\phi_{i,\alpha}|\chi|\phi_{j,\beta}\rangle = \langle\phi_{i,\alpha}|\tilde{\chi}|\phi_{j,\beta}\rangle + \langle\phi_{i,\alpha}|\tilde{\chi}\, V^I\, \chi|\phi_{j,\beta}\rangle. \quad (21)$$

The first term on the right hand side is simply the response function of the isolated layers for which we have $\langle\phi_{i,\alpha}|\tilde{\chi}|\phi_{j,\beta}\rangle = \tilde{\chi}_{i,\alpha}\delta_{i\alpha,j\beta}$. In the second term, applying $\langle\phi_{i,\alpha}|$ to $\tilde{\chi}$ returns $\tilde{\chi}_{i,\alpha}\langle\rho_{i,\alpha}|$ (this follows from Eq. 18 and the symmetry of $\tilde{\chi}(z,z')$). Now the completeness relation (20) is inserted between V^I and χ, leading to

$$\langle\phi_{i,\alpha}|\chi|\phi_{j,\beta}\rangle = \tilde{\chi}_{i,\alpha}\delta_{i\alpha,j\beta} + \tilde{\chi}_{i,\alpha}\sum_{k,\alpha'}\langle\rho_{i,\alpha}|V^I|\rho_{k,\alpha'}\rangle\langle\phi_{k,\alpha'}|\chi|\phi_{j,\beta}\rangle$$

This leads to the final Dyson equation for the heterostructure:

$$\chi_{i\alpha,j\beta}(q_\parallel,\omega) = \tilde{\chi}_{i,\alpha}(q_\parallel,\omega)\delta_{i\alpha,j\beta} + \tilde{\chi}_{i,\alpha}(q_\parallel,\omega)\sum_{k\neq i,\gamma} V_{i\alpha,k\gamma}(q_\parallel)\,\chi_{k\gamma,j\beta}(q_\parallel,\omega). \quad (22)$$

The Coulomb kernel is here defined in the density basis as: $V_{i\alpha,k\alpha'} = \langle\rho_{i,\alpha}|V|\rho_{k,\alpha'}\rangle$. The term $V|\rho_{k,\alpha'}\rangle$ is the potential at z from the density basis function in layer k, which is found by solving Poisson's equation for $|\rho_{k,\alpha'}\rangle$ on a real space grid. Since the density parallel to the layer just shows periodic oscillations with wave vector $q_\parallel$, Poisson's equation reduces to a 1D differential equation:

$$\frac{\partial^2}{\partial z^2}\Phi_{k\alpha'}(z) - q_\parallel^2\Phi_{k\alpha'}(z) = -4\pi\rho_{k\alpha'}(z). \quad (23)$$

The elements of the V matrix are then: $V_{i\alpha,k\alpha'} = \langle\rho_{i,\alpha}|\Phi_{k,\alpha'}\rangle$.

C. The dielectric matrix

The inverse dielectric function is related to χ through: $\epsilon^{-1} = \mathrm{I} - V\chi$. Due to the non-symmetric nature (in $\mathbf{r}$ and $\mathbf{r}'$) of the dielectric function, the elements of ϵ^{-1} are naturally written using a mixed density/potential basis:

$$\langle\rho_{i,\alpha}|\epsilon^{-1}|\phi_{j,\alpha}\rangle = \delta_{i\alpha,j\beta} + \langle\rho_{i,\alpha}|V\,\chi|\phi_{j,\beta}\rangle. \quad (24)$$

Upon insertion of the completeness relation (20) this gives

$$\epsilon^{-1}_{i\alpha,j\beta}(q_\parallel,\omega) = \delta_{i\alpha,j\beta} + \sum_{k,\gamma} V_{i\alpha,k\gamma}(q_\parallel)\chi_{k\gamma,j\beta}(q_\parallel,\omega). \quad (25)$$

III. PLASMONS EIGENMODES

By following a previously developed method for identifying plasmon eigenmodes in nanostructures from ab initio[3], the dielectric matrix for the heterostructure, Eq. 25, is diagonalized to solve the eigenvalue equation:

$$\sum_{j\beta}\epsilon_{i\alpha,j\beta}(q_\parallel,\omega)f_{n,j\beta}(q_\parallel,\omega) = \epsilon_n(q_\parallel,\omega)f_{n,i\alpha}(q_\parallel,\omega), \quad (26)$$

which returns the eigenvalues, $\epsilon_n(q_\parallel,\omega)$, and eigenvectors, $f_{n,i\alpha}(q_\parallel,\omega)$ of the dielectric matrix in the monopole/dipole basis. A plasmon eigenmode fullfills that:

$$\mathrm{Re}\sum_{j\beta}\epsilon_{i\alpha,j\beta}(q_\parallel,\omega)f_{n,j\beta}(q_\parallel,\omega) = 0, \quad (27)$$

corresponding to $\mathrm{Re}\epsilon_n(q_\parallel,\omega) = 0$. In practice, the plasmon energies are identified from the peaks in the eigenvalue loss-spectrum $-\mathrm{Im}\epsilon_n(q_\parallel,\omega)$ since this includes the finite imaginary part which can shift the plasmon energy. The right eigenfunctions $f_{n,i\alpha}$ give the induced potential of the plasmon in the basis of $\phi_{i,M/D}$. The left eigenfunctions, $f^n_{i\alpha}$, correspond to the induced density of the plasmon in the basis of $\rho_{i,M/D}$[3]. The induced density is thus given by

$$\rho_n(z,q_\parallel) = \sum_{i\alpha} f^n_{i\alpha}\rho_{i\alpha}(z,q_\parallel) \quad (28)$$

with the corresponding induced potential

$$\phi_n(z,q_\parallel) = \sum_{i\alpha} f^n_{i\alpha}\Phi_{i\alpha}(z,q_\parallel) \quad (29)$$

IV. EXCITONS

The Mott-Wannier model, widely used to model excitons in bulk semiconductors, can be straightforwardly generalised to 2D semiconductors. This leads to a 2D hydrogenic Hamiltonian of the form

$$\left[-\frac{\nabla^2_{2D}}{2\mu_{ex}} + W(\mathbf{r})\right]F(\mathbf{r}) = E_b F(\mathbf{r}), \quad (30)$$

where $F(\mathbf{r})$ is the exciton wave-function, μ_{ex} the exciton effective mass and $W(\mathbf{r}_\parallel)$ is the screened Coulomb potential which includes the screening coming from the 2D material itself and the environment, e.g. a substrate.

Now, consider electron and hole charge distributions given by (the in-plane variation is a plane wave of wave vector $q_\parallel$)

$$\rho^{e/h}(z,q_\parallel) = \sum_{i\alpha}\rho^{e/h}_{i\alpha}(q_\parallel)\rho_{i\alpha}(z,q_\parallel) \quad (31)$$

We can then calculate the screened interaction between the electron and hole charge distributions according to

$$W(q_\parallel) = \sum_{k\alpha,i\beta,j\gamma}\rho^e_{k\alpha}(q_\parallel)\epsilon^{-1}_{k\alpha,i\beta}(q_\parallel)V_{i\beta,j\gamma}(q_\parallel)\rho^h_{j\gamma}(q_\parallel). \quad (32)$$

In the case of excitons located in the layer 1 we can approximate $\rho^{e/h}(z, q_\parallel) = \rho_{1M}(z, q_\parallel)(z)$ and we recover the expression in the Methods section. We can describe a general charge distribution, e.g. using conduction/valence band charge distributions $\rho^{e/h}(z, q_\parallel) = |\psi_{c/v}(z, q_\parallel)|^2$, by a simple redefinition of the Coulomb matrix elements in Eq. 32.

Performing a 2D Fourier transform of $W(q_\parallel)$ yields the screened potential in real space:

$$W(\mathbf{r}_\parallel) = -\frac{1}{2\pi}\int_0^\infty dq_\parallel q_\parallel J_0(q_\parallel \mathbf{r}_\parallel) W(q_\parallel), \qquad (33)$$

where $J_n(x)$ is the Bessel function of the first kind. The exciton mass can be obtained e.g. from an ab-initio band structure calculation. We solve Eq. 30 using polar coordinates and a logarithmic radial grid.

V. COMPUTATIONAL DETAILS

A. Multilayer MoS_2

Ab initio calculations were performed for monolayer MoS_2 to obtain the monolayer density response functions and induced densities used as input for the heterostructure model. The single-particle energies and wave functions were calculated with the PBE exchange correlation functional, with a plane-wave basis set with an energy cutoff of 400 eV. A dense k-point sampling of $(128, 128)$ in the 2D Brillouin zone was used in order to calculate the response at low momentum transfers. In the linear response RPA calculation we used an energy cutoff of 50 eV for the reciprocal lattice vectors. We used a nonlinear frequency grid from 0 to 35 eV, with an initial grid spacing of 0.02 eV and a broadening of 0.04 eV. Corresponding ab initio calculations were performed for bulk and bilayer MoS_2, but with a k-point sampling of $(64, 64, 1)$ for the bilayer and $(64, 64, 8)$ for bulk. For the monolayer and bilayer calculations the truncated Coulomb kernel, see Eq. 10, was used while the full, i.e. non-truncated kernel, was used for the bulk calculation. We used an in-plane lattice constants of 3.18 Å, and A-B stacking with 6.15 Å separation between layers. For the monolayer and bilayer calculation the unit cells contained 20 Å of vacuum to separate the periodic images in the z-direction. For the heterostructure calculation we used the same separation between the layers as for the ab initio calculations ($d = 6.15$ Å). We note that the effect of stacking arrangement (A-A or A-B) cannot be accounted for within the model.

B. Graphene/hBN heterostructures

Ab initio calculations were performed to obtain the dielectric building blocks of monolayer doped graphene and hBN. Also, full ab initio calculations were done for entire heterostructures, including up to three layers of hBN, or the equivalent amount of vacuum, separating the doped graphene layers. An in plane lattice-constant of 2.5 Å was used for both graphene and hBN, so that the heterostructure could be represented a 1×1 unit cell. The layers were stacked in A-B configuration, with 3.326 Å separation (c-lattice constant of 6.653). We used PBE exchange-correlation, a 340 eV energy cutoff for the plane waves in the ground state calculations, and (100,100) k-point sampling in the 2D Brillouin zone. In the response calculation doped structures were obtained by shifting the Fermi-level 1 eV upwards. An energy cutoff of 70 eV was used for the reciprocal lattice vectors, and unoccupied bands were included up to 35 eV above the Fermi level. All the calculations employed the truncated Coulomb interaction and 20 Å vacuum to separate the repeated structures. A non-linear frequency-grid with an initial grid spacing of 0.02 eV and a broadening of 0.05 eV was used to represent the dynamic response function. Plasmon eigenmodes were obtained by diagonalizing the dielectric matrix in Bloch representation as described in ref.[3].

C. Excitons in supported WS_2

The dielectric building blocks of the WS_2, hBN, and MoS_2 monolayers were calculated as follows. Single-particle energies and wave functions were calculated using LDA, a plane wave cut-off of 500 eV, and $(45, 45)$ k-points. The density response function was calculated within RPA using an energy cut-off of 300 eV and including empty states up to 50 eV above the Fermi level. The truncated Coulomb kernel was employed and 20 Å vacuum was included in the supercell to separate repeated layers. In setting up the heterostructure we used a separation of 3.22 Å between the 100 layers of h-BN and 5.08 Å between WS_2 and h-BN. For WS_2 on 50 layers of MoS_2 we used a uniform separation of 6.3 Å between all layers. We then calculated the screened interaction from Eq. 32 for $q_\parallel$ up to (and including) the second Brillouin zone. For calculating the exciton Rydberg series we solved Eq. 30 for spherical states on a radial logarithmic grid and verified that the exciton energies were converged to within 0.01 eV.

D. 2D Database

The dielectric building blocks were calculated for 51 transition metal dichalcogenides and oxides, hBN, and graphene at 10 different doping levels from 0.1 to 1 eV. For the single particle wave functions and energies obtained from DFT, we used PBE exchange-correlation and a plane-wave basis with a energy cutoff equal to 500 eV. The 2D Brillouin zone was sampled by (200,200) k-points for graphene, and for the remaining materials we used a k-point density corresponding to (100,100) k-points.

For the density response functions we used a cutoff of 100 eV for the transition metal dichalcogenides and oxides and 150 eV for graphene and hBN. The truncated Coulomb kernel was employed and 20 Å vacuum was included in the supercell to separate the repeated layers. All materials were represented on the same frequency grid from 0 to 35 eV, with an initial spacing of 0.01 eV and a broadening of 0.05 eV. The response functions were calculated for a range of in-plane momentum transfers, $q_\parallel$, within the first Brillouin zone of graphene. At small $q_\parallel$ below 0.3 Å^{-1} we use a denser sampling with a grid spacing of 0.015 Å^{-1} in order to capture the strong $q_\parallel$-dependence of the plasmon energies and the dielectric function in this region. After this limit the grid spacing is increased to 0.029 Å^{-1}. In order to obtain all response functions on the same $q_\parallel$-grid, the data for the remaining materials was interpolated to the grid for graphene using conventional 2D spline interpolation.

---

* Electronic address: thygesen@fysik.dtu.dk

[1] Yan, J., Mortensen, J. J., Jacobsen, K. W. & Thygesen, K. S. Linear density response function in the projector augmented wave method: Applications to solids, surfaces, and interfaces. *Physical Review B* **83**, 245122 (2011).

[2] Rozzi, C., Varsano, D., Marini, A., Gross, E. & Rubio, A. Exact Coulomb cutoff technique for supercell calculations. *Physical Review B* **73**, 205119 (2006).

[3] Andersen, K., Jacobsen, K. & Thygesen, K. Spatially resolved quantum plasmon modes in metallic nano-films from first-principles. *Physical Review B* **86**, 245129 (2012).

Paper IV

Visualizing hybridized quantum plasmons in coupled nanowires: From classical to tunneling regime.
Kirsten Andersen, Kristian L. Jensen, N. Asger Mortensen, and Kristian S. Thygesen, Phys. Rev. B 87, 235433 (2013)

Visualizing hybridized quantum plasmons in coupled nanowires: From classical to tunneling regime

Kirsten Andersen,[1,*] Kristian L. Jensen,[1] N. Asger Mortensen,[2,3] and Kristian S. Thygesen[1,3,†]

[1]*Center for Atomic-scale Materials Design, Department of Physics, Technical University of Denmark, DK-2800 Kongens Lyngby*

[2]*Department of Photonics Engineering, Technical University of Denmark, DK-2800 Kongens Lyngby*

[3]*Center for Nanostructured Graphene, Technical University of Denmark, DK-2800 Kongens Lyngby*

(Received 23 March 2013; revised manuscript received 22 May 2013; published 26 June 2013)

We present full quantum-mechanical calculations of the hybridized plasmon modes of two nanowires at small separation, providing real-space visualization of the modes in the transition from the classical to the quantum tunneling regime. The plasmon modes are obtained as certain eigenfunctions of the dynamical dielectric function, which is computed using time-dependent density functional theory (TDDFT). For freestanding wires, the energy of both surface and bulk plasmon modes deviate from the classical result for low wire radii and high momentum transfer due to effects of electron spill-out, nonlocal response, and coupling to single-particle transitions. For the wire dimer, the shape of the hybridized plasmon modes are continuously altered with decreasing separation, and below 6 Å, the energy dispersion of the modes deviate from classical results due to the onset of weak tunneling. Below 2–3 Å separation, this mode is replaced by a charge-transfer plasmon, which blue shifts with decreasing separation in agreement with experiment and marks the onset of the strong tunneling regime.

DOI: 10.1103/PhysRevB.87.235433 PACS number(s): 73.20.Mf, 73.22.−f, 81.07.Gf, 31.15.E−

I. INTRODUCTION

Plasmons are collective oscillatory modes of the electron system that are found in solids, at extended surfaces, and at the surface of confined metal structures.[1] The localized surface plasmon resonances sustained by metallic nanoparticles[2] have found widespread use in applications ranging from molecular spectroscopy[3] and chemical sensing,[4] to photocatalysis[5] and photovoltaics.[6] Applications of plasmons in next generation nanoelectronics[7] and quantum information technology[8,9] have also been envisioned. Advances in nanofabrication techniques and transmission electron microscopy have recently enabled the study of plasmon excitations on a subnanometer length scale.[10] In particular, the use of highly confined electron beams can provide spatial resolution of the electron energy loss spectrum (EELS) yielding unprecedented information about the dynamical properties of confined electron systems.[11–15]

When the size of a plasmonic structure reaches the nanoscale, quantum effects begin to play a dominant role and the widely used classical models of electronic response become insufficient.[16,17] In this size regime, the theoretical description must be refined to account for quantum effects such as surface scattering, electron spill-out at the surface, coupling of plasmons to single-particle excitations, and the nonlocality of the electronic response. We note that some of these effects, in particular the non-local response and spill-out, can be incorporated into semi-classical hydrodynamic models.[1,18,19] However, the validity and predictive power of such an approach in the true quantum regime is not fully clarified, and the standard hydrodynamic approximation, not including spill-out, has been found to fail for calculations on small nanometric gabs due to a insufficient description of induced charges in the interface.[20]

One important hallmark of the quantum regime is electron tunneling, which occurs when two systems are brought into close proximity. In fact, tunneling leads to a break down of the local field enhancement predicted by the classical theory at subnanometer separations, and leads to the formation of a charge-transfer plasmon.[21–24] Classically, the plasmon modes of a composite system can be obtained as even/odd combinations of the plasmon modes of the individual subsystems.[25,26]

Recent experiments by Savage *et al.*[27] on coupled nanoparticles at finely controlled separation, found that the onset of the quantum regime is marked by a beginning blue shift of the hybridized modes, followed by the entrance of charge-transfer modes at conductive contact. Through the use of a quantum corrected model, they predict the onset of quantum tunneling effects at around 0.3-nm particle separation. This conclusion is supported by experiments by Scholl *et al.*[28] on silver nanoparticles, where the bonding dipole plasmon was replaced by a charge-transfer plasmon below 0.27 nm. Other experiments on film-coupled nanoparticles[29] found the energy of hybridized modes to be blue shifted relative to the classical result at separations less than 1 nm, a similar blue shifting is anticipated for nanowire dimers within a hydrodynamic description.[30] However, until now, the influence of quantum effects on the spatial shape of the hybridized modes has not been explored.

In this work, we apply a recently developed method[31] to compute and visualize the hybridization of the quantum plasmons of two parallel metallic nanowires at separations between 0 and 2 nm. The evolution of the spatial form of the hybrid modes and their energies is used to determine the regimes where quantum effects are of importance. We first show that the plasmon modes of single wires can be classified as surface or bulk modes with a specific angular symmetry index m and radial node index n. The maximum number of modes found for a given wire radius is limited by Landau damping, which increases with n and m. For the double wire system, we find several hybridized plasmon modes. The induced potential of the hybrid modes changes in shape in a continuous manner with decreasing separation and below 6 Å the energies deviate from the classical result, in agreement with the observed blue shift of the bonding dipole plasmon with decreasing dimer separation. We explain this by a beginning weak tunneling below 6 Å where the electron densities start to overlap. At separations below 2–3 Å, the onset depending

slightly on wire diameter, we enter the regime of strong tunneling where the bonding dipole plasmon is quenched and replaced by a charge-transfer mode.

II. METHOD

A. Theory of plasmon eigenmodes

The plasmonic properties of a given material are contained in its frequency-dependent dielectric function, which relates the total and the externally applied potential to linear order:

$$\phi_{\text{ext}}(r,\omega) = \int \epsilon(r,r',\omega)\phi_{\text{tot}}(r',\omega)dr'. \quad (1)$$

A self-sustained charge density oscillation $\rho(r,\omega)$ can exist in a material if the related potential, satisfying the Poisson equation $\nabla^2\phi = -4\pi\rho$, obeys the equation

$$\int \epsilon(r,r',\omega)\phi(r',\omega)dr' = 0. \quad (2)$$

This corresponds to the case of having a finite induced potential in the absence of an external potential, which is the criterion for the existence of a plasmon eigenmode. In general, this equation cannot be exactly satisfied due to a finite imaginary part originating from single-particle transitions, which will lead to damping of the charge oscillation. When the damping in the material is small, it is sufficient to require only that the real part of ϵ vanishes and use the following definition for the potential associated with a plasmon mode:

$$\int \epsilon(r,r',\omega_n)\phi_n(r',\omega_n)dr' = i\Gamma_n\phi_n(r,\omega_n), \quad (3)$$

where Γ_n is a real number. The plasmon modes are thus the eigenfunctions corresponding to purely imaginary eigenvalues of the dielectric function. Physically, they represent the potential associated with self-sustained charge-density oscillations damped by electron-hole pair formations at the rate Γ_n. The right-hand-side eigenfunctions, $\phi_n(r',\omega_n)$, define the induced potential of the eigenmodes, and the corresponding induced density $\rho_n(r',\omega_n)$ can be obtained as the left-hand-side (dual) eigenfunctions of the dielectric function.[31] In the case of larger and frequency-dependent damping, a more accurate approach is to use the eigenvalues of $\epsilon(r,r',\omega)$, denoted $\epsilon_n(\omega)$, and use the criterion

$$-\text{Im}\epsilon_n(\omega)^{-1} \text{ is a local maximum}, \quad (4)$$

to define the plasmon energies. This definition takes into account that a finite imaginary part of ϵ may shift the plasmon peaks in the loss spectrum away from the zeros of $\text{Re}\epsilon_n(\omega)$.

In practice, the plasmon eigenmodes are obtained by diagonalizing the dynamical dielectric function for each point on a frequency grid. This approach bears some similarities with the concept of dielectric band structure introduced by Baldereshi,[32] but opposed to calculating the static dielectric band structure, this method enables us to identify plasmon modes and their energy. The dielectric eigenvalue spectrum results in a set of distinct eigenvalue curves that evolves smoothly with energy, each curve corresponding to a separate plasmon eigenmode, see Fig. 1. The eigenvalue curves each resembles a Drude-Lorentz-like model for the dielectric

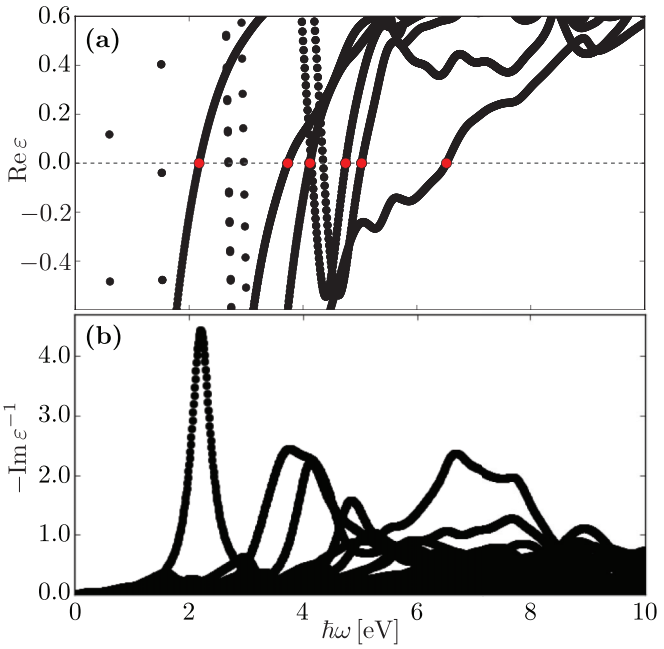

FIG. 1. (Color online) (a) Real part of the eigenvalues of the dielectric function $\epsilon(r,r',\omega)$ for a 5 Å radius jellium wire. Each eigenvalue curve that extends to negative values defines the existence of a plasmon eigenmode and the crossing with zero from below (red points) approximates the plasmon energy of the current mode. (b) For a more correct description of the mode energies in the presence of large damping, maxima in $-\text{Im}\epsilon_n(\omega)^{-1}$ are used to define the plasmon frequencies, ω_n.

function, and has been fitted to a single-pole model:

$$\epsilon_n(\omega) = 1 - \frac{\alpha_n}{\omega - \beta_n + i\gamma_n}, \quad (5)$$

where only the real part is fitted, and used to find the mode strength, α_n. The parameter β_n corresponds to the average energy of the single-particle transitions contributing the given eigenmode, and γ_n is the damping of the mode.

B. Computational approach

The DFT calculations have been carried out with the electronic structure code GPAW[33,34] using the atomic simulation environment.[35] We study metallic Na wires with radii in the range 2 to 8 Å modeled within the jellium approximation, that gives a good description of simple, free-electron-like metals such as Na. The atomic nuclei of the nanowire are modeled with a constant positive background density that terminates abruptly at the wire edges, while the electron density is converged self-consistently, see Fig. 2, showing the unit cell and the calculated densities within the jellium model. Electron spill-out extends approximately 3 Å outside the jellium edge and should be included for a correct description of surface plasmon modes in particular. This jellium approach thus includes the confinement of the electrons to the wire, and spill-out from the surface, but neglects the local field effects from the atomic nuclei. This allows us to study simple metals such as Na, where local field effects have been found to be negligible.[31] We note that for the study of noble metals such as Ag and Au this jellium approach will not be justified since the

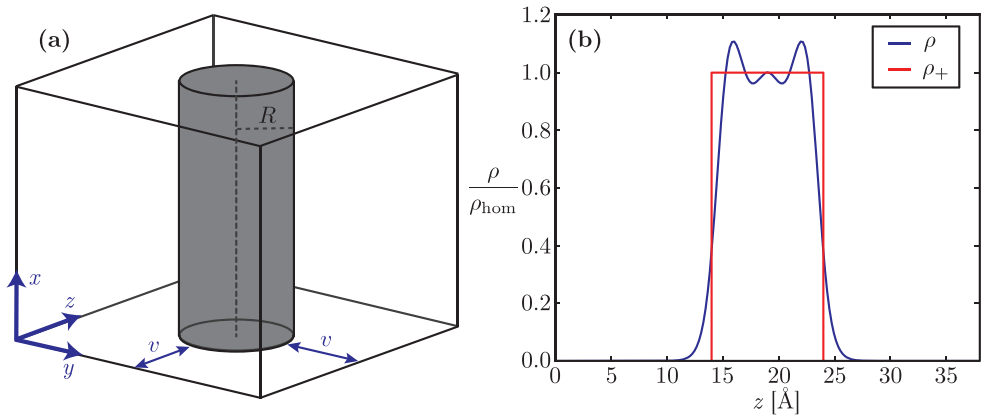

FIG. 2. (Color online) (a) Sketch of the unit cell with gray region indicating the positive charge density of a cylindrical jellium wire, surrounded by vacuum $2v = 28$ Å. R is varied from 1 to 8 Å and the unit cell is 3 Å along the wire. (b) Cross-sectional view of the wire showing the fixed positive background density profile ρ_+ (red) and the converged electron density ρ (blue), plotted relative to the free electron density of bulk Na, ρ_{hom}.

$3d$ and $4d$ bands of these metals play a large role in screening the plasmon excitations and therefore must be included. The local density approximation (LDA) was used for exchange correlation. The unit cell was sampled on grid points of 0.2 Å spacing, and 20 k points were used to map the 1D Brillouin zone along the wire, except for the study of small momentum transfers in the response calculation where 80 k points were used.

The microscopic dielectric matrix, $\epsilon_{\mathbf{G},\mathbf{G}'}(\mathbf{q},\omega)$ was calculated in a plane-wave basis, using linear response TDDFT within the random phase approximation (RPA):[36]

$$\epsilon_{\mathbf{G},\mathbf{G}'}(\mathbf{q},\omega) = \delta_{\mathbf{G},\mathbf{G}'} - \frac{4\pi}{|\mathbf{q}+\mathbf{G}|^2}\chi^0_{\mathbf{G},\mathbf{G}'}(\mathbf{q},\omega), \tag{6}$$

where the exchange correlation kernel f_{xc} is neglected. The RPA level, in general, gives a good description of plasmon resonances but fails for the description of bound excitons. It performs well for the calculation of plasmon energies in simple metals, for example, the surface plasmon energy of Mg(1000) is reproduced within 0.2 eV from the experimental value.[36] The RPA is exact in the high density limit, but is also expected to give a good description for simple metals with intermediate electron densities such as Na. The nonlocality of the dielectric matrix is ensured by including off-diagonal matrix elements in the reciprocal lattice vectors, $\mathbf{G}$ and $\mathbf{G}'$, where we used a 15 eV energy cutoff perpendicular to the wire. Electronic states 10 eV above the Fermi level were included, and the dielectric function was sampled on an energy grid ranging from 0 to 10 eV with a spacing of 0.01 eV and a broadening of 0.2 eV. The wave vector along the wire, $q_\parallel$, was varied between 0.03 Å^{-1} and 0.8 Å^{-1} in order to study the energy dispersion. Convergence has been checked with respect to all parameters, including the applied vacuum perpendicular to the wires, where a vacuum of 20 Å ensures that there is no overlap of single-particle states from neighboring supercells. However, special care must be taken in the response calculation where the Coulomb kernel, $v(\mathbf{G}) = \frac{4\pi}{|\mathbf{G}+\mathbf{q}|^2}$, diverges for $\mathbf{q}+\mathbf{G} \to 0$ and gives a long ranged potential for small q that can not be compensated by adding vacuum in a realistic calculation. In order to avoid the overlap of induced potentials from neighboring supercells, we use a truncated version of $v(\mathbf{G})$, that goes to zero as a step function at radial cutoff distance R_c:[37]

$$\tilde{v}^{1D}(G_\parallel, G_\perp) = \frac{4\pi}{|G+q|^2}[1 + G_\perp R_c J_1(G_\perp R_c)K_0(|G_\parallel|R_c) - |G_\parallel|R_c J_0(G_\perp R)K_1(|G_\parallel|R_c)], \tag{7}$$

where J and K are the ordinary and modified cylindrical Bessel functions, and $G_\perp$ and $G_\parallel$ refer to components of the reciprocal lattice vectors perpendicular and parallel to the wire respectively. R_c is set equal half of the width of the supercell, and this approach thus requires that the vacuum distance exceeds the diameter of the wire.

The use of the truncated Coulomb potential was found to be important for a correct description of the plasmon mode energies for $q < 0.1$ Å^{-1}, and in particular for modes with large macroscopic ($\mathbf{G} = 0$) component. For the study of two coupled cylinders, we chose a q that is sufficiently large that the energy shift of the modes is less than 0.03 eV, and the truncation is not applied.

III. RESULTS

A. Single wires

The obtained plasmon eigenmodes for single wires of radius 2, 5, and 7.5 Å is shown in Figs. 3(a)–3(c), where the induced potential (first row) and density (second row) is plotted for increasing energy going left to right. The modes are characterized as surface S or bulk B determined by the relative weight outside and inside the jellium perimeter, sketched in Fig. 3(d). The potential and density of surface modes has a large contribution in the spill-out region outside the jellium edge, and has lower energy than the bulk modes. The modes are labeled according to their angular quantum number m, accounting for the $e^{im\theta}$ angular symmetry, easily visualized for the surface modes as the number of standing waves along the wire perimeter. For the thinnest wire, only modes up to $m = 1$ are sustained, whereas modes with larger m are found for increasing radii. This corresponds to a minimum plasmon wavelength, $\lambda_{\text{min}} \approx 10$ Å that can be sustained by the surface, which is obtained by defining an effective wave-vector for the

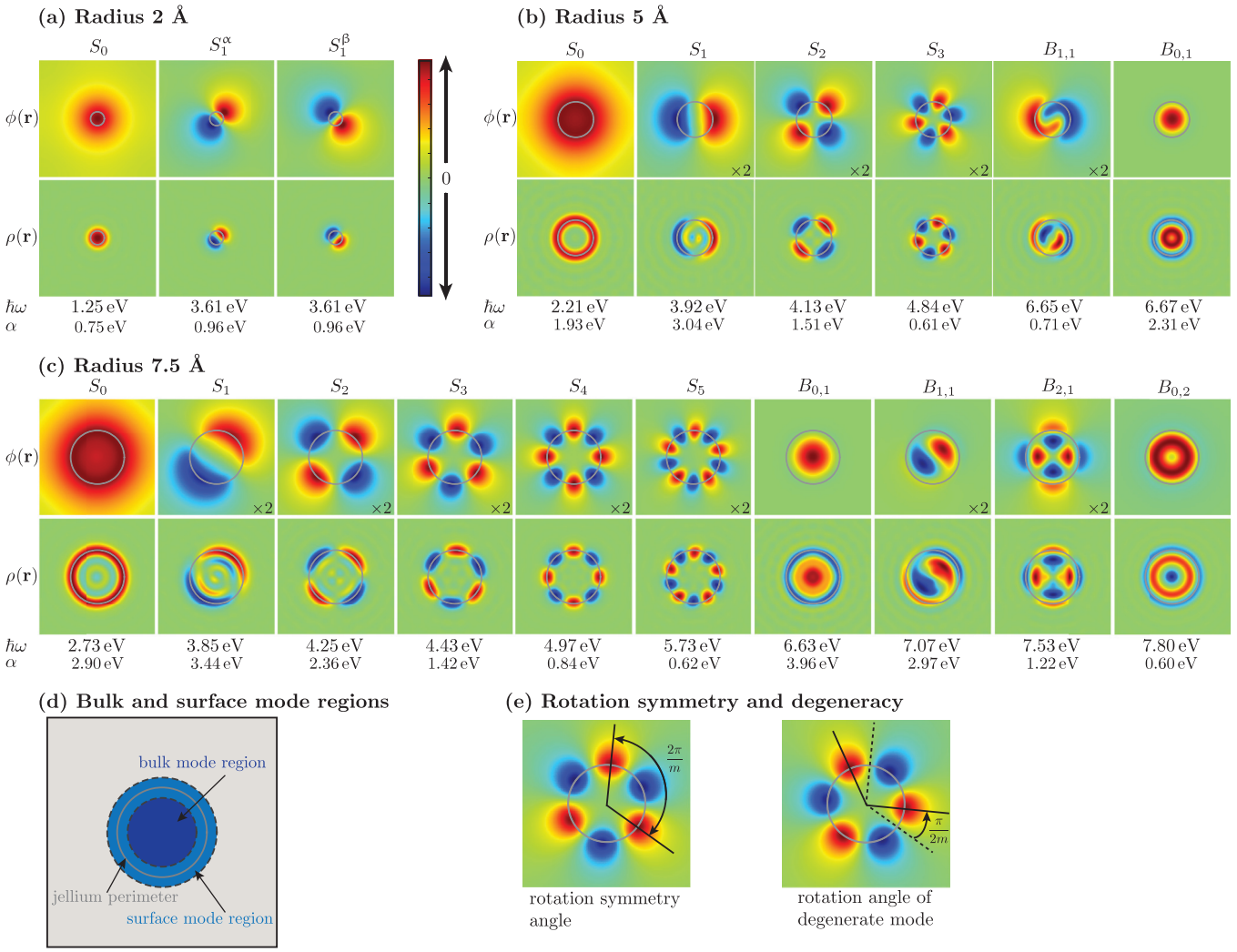

FIG. 3. (Color online) Plasmon eigenmodes of Na jellium wires of radii: (a) 2, (b) 5, and (c) 7.5 Å, corresponding to induced potential $\phi(\mathbf{r})$ and density $\rho(\mathbf{r})$. The strength, α, and energy, $\hbar\omega$, is given for each mode. Modes with surface as well as bulk character are found, labeled S and B, respectively, where the surface modes has a significant contribution in the spill-out region outside the jellium edge, see (d). The first subscript denotes the angular quantum number m, describing the $e^{im\theta}$ rotational symmetry. The increase in m leads to a larger effective wave vector for the plasmon, q_{eff}, resulting in an increase in energy with m. Also the Landau damping increases with q_{eff}, which is why a larger number of modes can be sustained by wires with larger radius. As explained in (e), modes with $m > 0$ appear as degenerate pairs, rotated with $\pi/2m$ (plots labeled $\times 2$ when both are not shown).

modes, $q_{\text{eff}}^2 = q_\parallel^2 + q_\perp^2$. The parallel momentum transfer $q_\parallel$ is fixed in the calculation, and $q_\perp$ can be written as

$$q_\perp = \frac{2\pi}{\lambda_\perp} = \frac{m}{R}, \tag{8}$$

where $\lambda_\perp$ is the wavelength associated with the shape of modes perpendicular to the wire. When m is sufficiently large, or R small, the effective wave vector becomes large enough for the mode to enter the regime of Landau damping (coupling to intraband transitions with large q), until the point where the mode can no longer be sustained. This is also reflected in a mode strength, α, that decreases with $m > 1$ for the surface modes.

For the bulk modes an additional quantum number, n, is required to account for radial dependence, where $B_{0,2}$ has an extra node in the induced density compared to $B_{0,1}$. From a group-theoretical analysis of the possible symmetries within the point-group $D_{\infty h}$, the modes with $m > 0$ are expected to appear in degenerate pairs. This is exactly found for the calculated modes, where pairwise identical eigenvalue-curves results in identical modes with a relative rotation of $\pi/2m$, see Fig. 3(e). We have investigated the energy dispersion of the modes with R and $q_\parallel$, shown in Fig. 4, where the result from our quantum calculation has been plotted together with the classical result obtained from solving Laplace's equation and using a local Drude model for the dielectric function.[38] The classical model yields a dispersion relation for the surface modes that depends on a single dimensionless parameter, qR, where q is the wave vector parallel to the wire:

$$\omega_m^2 = \omega_p^2 \, qR \, I_m'(qR) \, K_m(qR), \tag{9}$$

where I_m is the modified Bessel's functions of order m, and ω_p is the bulk plasmon frequency. The acoustic character of the S_0 mode leads to an energy that goes to zero as a function

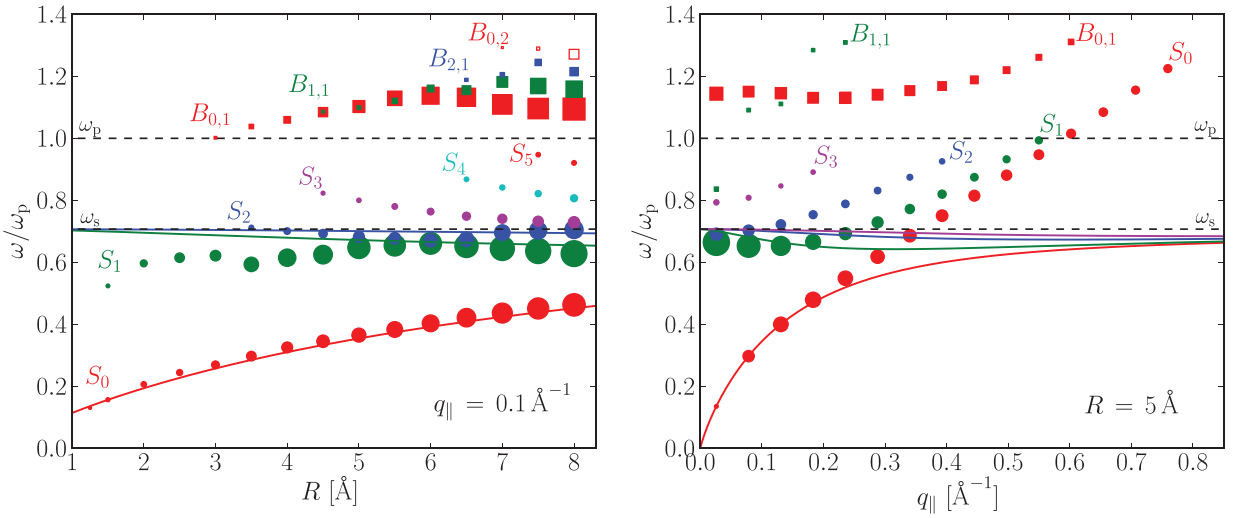

FIG. 4. (Color online) Energy dispersion of plasmon eigenmodes for the quantum calculations (circles and squares) and the classical results for the surface modes (solid lines). The energy is plotted against (a) the wire radius for fixed $q_\parallel = 0.10$ Å^{-1} and (b) the wave vector $q_\parallel$ for fixed $R = 5$ Å. Circles and squares represent surface and bulk modes, respectively, and the diameter/height of the points indicate the mode strength α, obtained by fitting the eigenvalues to a single-pole model, Eq. (5). The S_0 mode, which has acoustic character, tends to zero energy for vanishing R or q, where there is a good agreement with the classical result. For large q, the quantum model produces a positive dispersion for all modes, which is not captured by local models. For surface modes with $m > 0$, there is an overall poor agreement due to effects from a larger q_{eff} and spill-out.

of $q_\parallel R$, whereas the $S_{m>0}$ modes tends towards the classical surface plasmon frequency $\omega_P/\sqrt{2}$ for low $q_\parallel R$. For large $q_\parallel R$ all modes tends towards $\omega_P/\sqrt{2}$.

When comparing to our quantum results, a very good agreement is seen for the S_0 mode at low $q_\parallel$, which breaks down for larger $q_\parallel$. Since the Drude model assumes the electronic response to be local in space, it cannot capture the dispersion with q which explains the significant deviation for large $q_\parallel$, where the quantum result for the energy continues to increase. This q dependence explains why the energy of the surface modes increases with larger m (due to a larger q_{eff}), opposed to the classical result where the energy does not exceed $\omega_P/\sqrt{2}$. This deviation from the classical result is also observed in semiclassical hydrodynamic models for waveguiding on nanowires.[39] However, S_1 and S_2, are seen to be redshifted with respect to the classical value in the limit $q \to 0$, and for S_1 the redshift increases further with decreasing R. A redshift is expected for decreasing size of simple metal nanostructures due to electron spill-out; as the surface to bulk ratio increases, the spill-out will lead to a decrease in the mean electron density, which results in a lower plasmon frequency. This redshift was also observed for the plasmon eigenmodes of thin slabs of sodium,[31] and for quantum calculation on small Na clusters.[40] This is opposed to the behavior of silver nanostructures, where coupling to single-particle transitions originating from the $3d$ states leads to blue shift with decreasing size.[16,40] Thus there are two competing factors affecting the energy of the $S_{m>0}$ modes for decreasing R; the increase due to a larger perpendicular q, and the decrease due to spill-out, which might explain the oscillatory behavior of the S_1 mode for small R.

When considering the strength of the modes (represented by the width of the labels in Fig. 4), there is a clear tendency for weakening of modes for small R and large $q_\parallel$. This is due to a smaller number of electronic bands crossing the Fermi level for the thin wires, which gives a smaller number of transitions contributing to the plasmon in this limit. The weakening with increasing q can be explained by increasing Landau damping as discussed previously.

Even though the wires modeled in this work are thin compared to a realistic setup, the results allow us to make some generalizations to thicker wires. For larger R, the number of surface modes S_m is expected to increase according to the wire perimeter and the minimum plasmon wavelength, $\lambda_{\text{min}} \approx 10$ Å, such that $m_{\text{max}} = 2\pi R/\lambda_{\text{min}}$. These higher-order modes will not couple to optical fields, i.e., they are so-called dark modes but should be observable in a scanning EELS experiment. As seen from the energy dispersion in Fig. 4, the energies for the surface modes approach the result of the classical model for increasing R, however, the energy of the $S_{m=1}$ mode is still noticeably redshifted compared to the classical value at $R = 8$ Å. Thus, for this mode, the impact of spill-out exceeds the size quantization effects, which leads to an overall redshift in energy.[41] For calculations on thin Na slabs,[31] a redshift of the dipole plasmon mode was observed at 5-nm film thickness, and since spill-out will have a larger impact on 1D structures this indicates that the redshift should be observable for much thicker wires. The magnitude of the q dispersion is expected to be independent on R for large q, and interestingly, we find an apparent linear dispersion of the surface modes with q in this range.

B. Coupled nanowires

After establishing an understanding of the quantum modes of single wires, we are ready to study the hybridization of modes between two parallel wires of small separation.

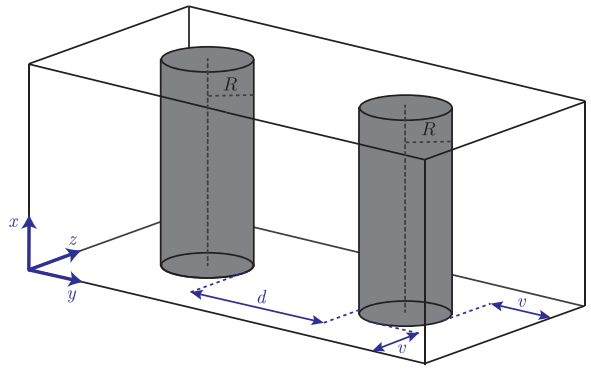

FIG. 5. (Color online) The unit cell containing two jellium wires of distance d. We consider separations in the range 0 to 20 Å, and choose R = 2.5 Å for both wires, in order to study the case where only three modes exist for the individual wires.

The unit cell is sketched in Fig. 5, where the separation, d, is varied from 20 Å down to zero measured from the jellium edge, and the amount of vacuum separating the wires of neighboring supercells are kept constant at 20 Å. The hybridization of plasmon modes is not unlike the formation of molecular orbitals as bonding and antibonding combinations of atomic orbitals,[25,26] where the new hybridized modes correspond to the even and odd combinations of isolated modes of the individual structures. At very small separations, however, this simplified description no longer holds since overlap of the electronic states and eventual tunneling will alter the resonances. We have applied our quantum approach to provide real-space visualization of the hybridized modes in the transition from the nonoverlap to the overlap regime.

In order to limit the number of hybridized modes, we choose both wire radii equal to 2.5 Å, where only the S_0 and the two degenerate S_1 modes exists. Though the wires used in this study are thinner than a realistic experimental setup, it allows us to perform a qualitative study of the evolution of the hybridized modes with separation and give a quantitative discussion on the onset of quantum effects.

Only modes of similar symmetry with respect to the y axis will couple to form hybridized modes; for example, an S_0 mode at one wire will be unable of inducing a S_1-like potential at a neighboring wire, and no self-sustained oscillation can occur. Therefore the modes only couple to those of the same type (S_1 couple to the S_1 mode of same rotation), and six hybridized modes are predicted to exists for this structure.

Six modes are found in the quantum calculation as shown in Fig. 6(a), with eigenmodes calculated for a 20 Å separation of the wires. In this regime of zero overlap between the electronic states, the modes can be classified according to conventional hybridization theory as even or odd combinations of the initial modes, labeled ++ and +− respectively, where the four S_1-types are further divided into vertical, v, and horizontal, h, according to the direction of polarization. As can be seen in Fig. 7, showing the induced potential and density for 8-, 2 -, and 1-Å separations, this description is no longer valid for small separations.

The energy dispersion of the modes as a function of d is shown in Fig. 6(b), where the +− and ++ combinations split in energy for intermediate separations. A redshift is found for the bonding modes where opposite charges face each other, i.e., S_0^{+-}, $S_1^{\mathrm{h}++}$, and $S_1^{\mathrm{v}+-}$. This energy shift can be explained by the electrostatic attraction between induced charges of opposite sign that leads to a lowering of the plasmon frequency (and in reverse for the remaining antibonding modes). The resonance of largest technological importance is the S_0^{+-} mode, also known as the bonding dipole plasmon, which has a large cross-section for coupling to optical fields.

The interaction between the wires increases for decreasing separations which leads to a larger splitting, until the weak tunneling regime is entered around 6 Å. The shift is more distinct for the S_0 types that also has the most long-ranged

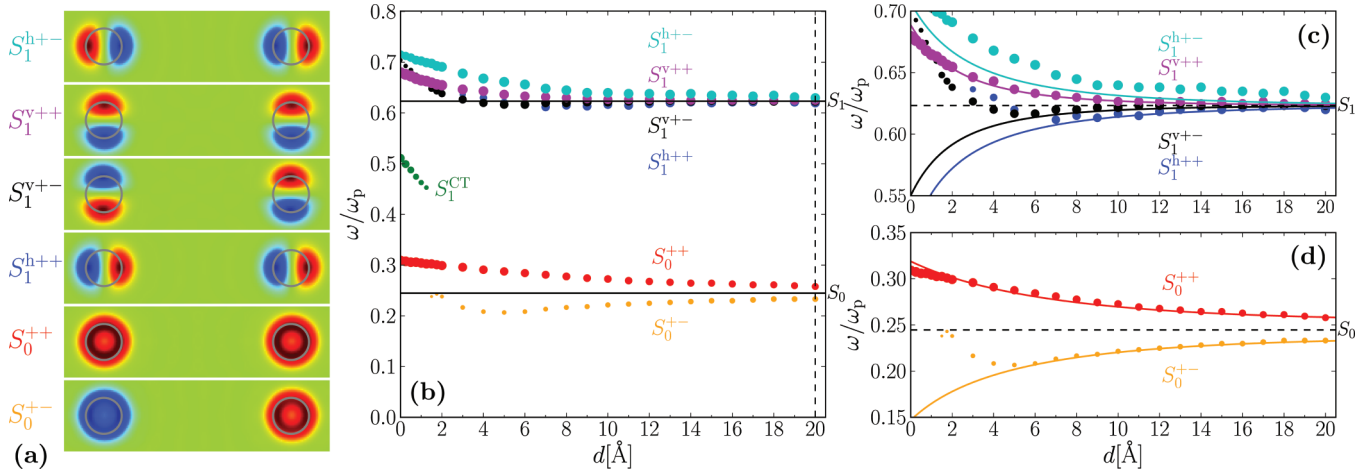

FIG. 6. (Color online) (a) Induced density of hybridized modes of two parallel wires with R = 2.5 Å at 20-Å separation. The modes can be identified as hybridization between the S_0, S_1^{α}, and S_1^{β} modes of the individual wires, where only modes of the same type couple due to symmetry restrictions. (b) The mode energies as a function of wire separation, d, with the mode strength indicated by the diameter of the points. The hybridization leads to a split in energy of the even, ++, and odd, +− mode-combinations, plotted together with the classical result (solid curves) in (c) and (d). At 2-Å separation, the S_0^{+-} and $S_1^{\mathrm{h}++}$ modes are quenched out due to tunneling and a charge-transfer mode S_1^{CT} appears.

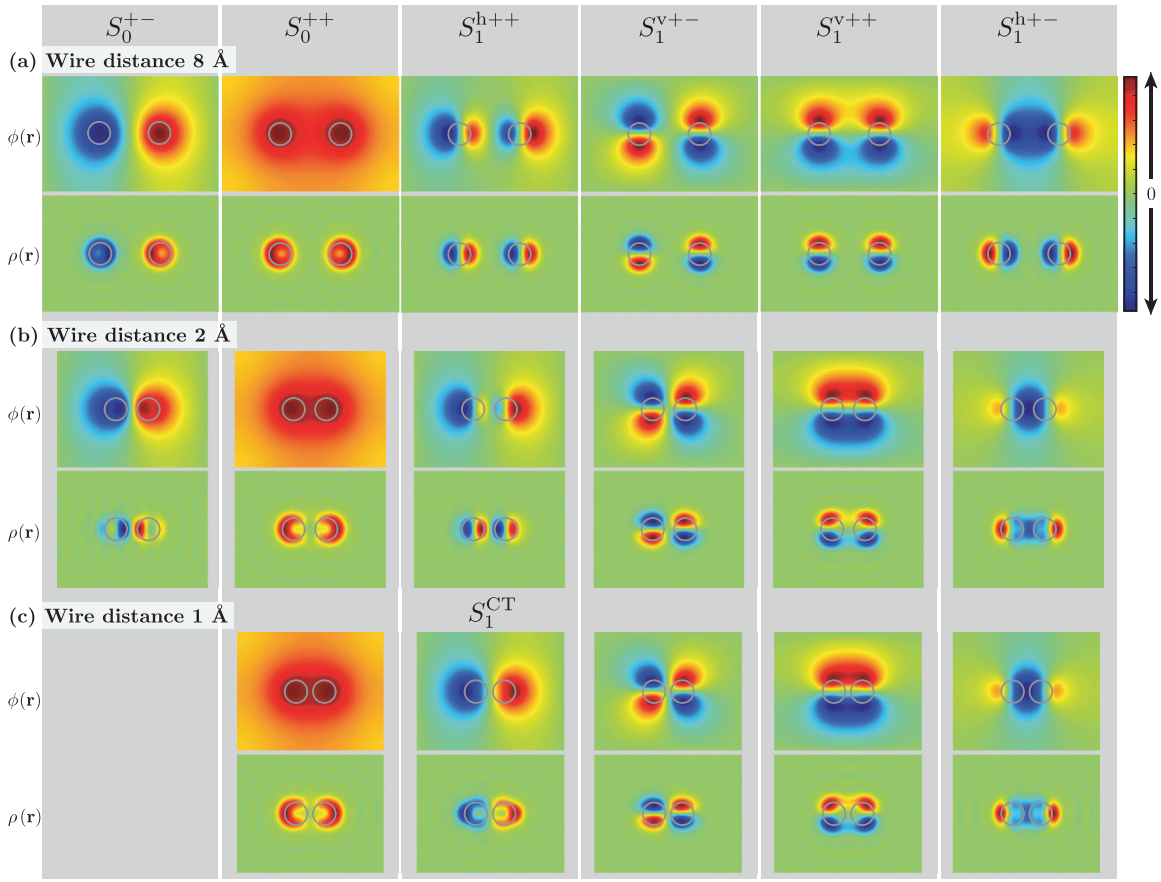

FIG. 7. (Color online) The plasmon eigenmodes for two parallel nanowires with $R = 2.5$ Å for separations (a) 8, (b) 2, and (c) 1 Å. Already at 8-Å separation, the potential $\phi(r)$ and density $\rho(r)$ of the modes are slightly modified, the change being most dominant for the S_1^{h++} and S_0^{+-} modes. At 2 Å, these modes are almost quenched out due to tunneling, and the induced density is shifted into the bulk. Below 2 Å, a new charge-transfer mode S_1^{CT}, where the density oscillates between the wires, appears. For the other modes, there is a continuous evolution in shape from the nontouching to the touching regime, as seen for the mode energies as well.

potential that explains the stronger coupling and larger splitting of bonding and antibonding modes. The potential from the electric dipole of the S_1 modes decreases faster along y, in particular for the vertical modes, which again shows a smaller splitting than the horizontal modes.

In Figs. 6(c) and 6(d), the quantum results have been plotted together with the results of a classical model. The later has been obtained by solving Laplace's equation for a system of two cylinders of equal radii R and dielectric constant $\epsilon = 1 - \frac{\omega_p^2}{\omega^2}$. Following a general approach by Moradi,[42] we have derived the expressions for hybridized S_0 and S_1 modes for this system, see Appendix.

Above the regime of weak tunneling, there is a good agreement between the classical and quantum results for the energy splitting. Below $d \approx 6$ Å, however, the bonding modes, S_0^{+-}, S_1^{h++}, and S_1^{v+-}, are blue shifted with respect to the classical model as can be explained by a reduction of the induced charges in the interface due to tunneling.

Our approach for visualizing the eigenmodes from a quantum calculation provides a clear picture of how the plasmon modes are altered due to this quantum effect. As can be seen in Fig. 7, already at 8-Å separation some eigenmodes are modified compared to the large separation limit shown in Fig. 6(a). The modes are seen to be gradually altered with decreasing separation, with the S_0^{+-} and S_1^{h++} modes being most seriously affected due to the facing of opposite charges. The potential between the wires decreases in amplitude going from 8 to 2-Å separation, and the induced density is shifted further into the bulk. A decrease in mode strength (indicated by the marker diameter in Fig. 6) is also found for these modes upon approaching 2-Å separation. At 1 Å, both modes are quenched due to tunneling and have been replaced by a dipolar charge-transfer mode, here named S_1^{CT}, and the induced density is now located at the other side of the wires, away from the interface. That this mode is different in nature than the S_1^{h++} and S_0^{+-} is also clear from Fig. 6(b), where it appears as a separate line in the energy dispersion below 2 Å, and increases in strength for smaller separations. In this touching regime with large degree of tunneling, the structure can be regarded as one (noncylindrical) wire; however, for the other modes, there is a continuous transition from the nontouching to the touching regime. The S_1^{v++} and S_1^{h+-} modes gradually build up induced density in the region between the wires, and S_1^{v+-} ends up resembling a quadropolar ($m = 2$) mode for the joint structure.

We note that small thickness of nanowires used in this study should be considered when making quantitative conclusions about the onset of quantum effects. For a dimer consisting of thicker wires realistic for experimental studies, the overlap of the electronic states could increase due to a lower surface curvature, which is expected to give rise to an earlier onset of quantum effects. For very thick wires, the result should approach that of an bimetallic interface of two planar surfaces. Our corresponding calculations on such an interface, modeled by two infinite Na jellium films of varying separation, yielded the presence of a charge-transfer mode already at 3-Å separation. This should be compared to the onset just below 2 Å for the small dimer; hence, for thicker wires, the onset of the charge-transfer mode is expected to shift slightly to larger separations and approach that of a bimetallic interface. Quantum calculations on a corresponding Na nanowire dimer or diameters up to 9.8 Å have recently been presented[43] that find an onset of the charge transfer plasmon close to 2-Å separation measured from the jellium edge, in good agreement with our results.

Another factor that could potentially affect the onset of tunneling is the r_s parameter defining the electron density in the jellium model. We note that choosing a smaller r_s parameter than the one of Na will lead to a larger plasmon frequency due to the increase in density, but could also increase the work function of the surface and potentially shift the onset of tunneling to smaller separations.[44] However, our calculations on a dimer of Al jellium films did not change the onset of the charge-transfer plasmon compared to Na jellium films, so we do not expect this parameter to give large quantitative differences for simple metals.

IV. CONCLUSION

We have given a visual demonstration of the plasmon eigenmodes in nanowires and shown how the hybridized plasmon modes of a two-wire system is modified due to quantum effects for decreasing separation. For wire separations above 10 Å, the modes are well characterized according to conventional hybridization theory, and a good correspondence was found with a classical theory for the mode energies until the onset of tunneling around 6-Å separation. Below this limit, our quantum calculations produced a blue shift of the bonding plasmon modes with decreasing separation, due to the decrease in induced charge at the interface caused by tunneling. However, only for separations below 2–3 Å was the tunneling sufficiently strong for a true charge-transfer plasmon to appear.

ACKNOWLEDGMENTS

K.S.T acknowledges support from the Danish Council for Independent Research's Sapere Aude Program through grant No. 11-1051390. The Center for Nanostructured Graphene (CNG) is sponsored by the Danish National Research Foundation, Project DNRF58.

APPENDIX: CLASSICAL HYBRIDIZATION MODEL FOR A TWO-WIRE SYSTEM

We have derived the classical expression for the energy of the hybridized modes of a system of two cylinders of equal radii R of separation d_c between the two centers, where the general approach by Moradi[42] simplifies to finding the zeros of the determinant of the matrix: $(\mathbf{M}^2 - I)$, where the elements of $\mathbf{M}$ are written as

$$M_{mn} = \frac{\omega_m^2}{\omega^2 - \omega_m^2} \frac{K_{m+n}(qd_c) I_m(qR)}{K_n(qR)}, \tag{A1}$$

where the m,n indices corresponds to angular quantum numbers, and ω_m is the energy of the S_m mode of a single wire given in Eq. (9). For the coupling of two S_0 modes, both $m,n = 0$, and solving for omega yields two solutions:

$$\omega_\pm^2 = \omega_0^2 \left[1 \pm K_0(qd_c) \frac{I_0(qR)}{K_0(qR)} \right], \tag{A2}$$

accounting for the splitting of the S_0^{+-} and S_0^{++} modes. Due to the small discrepancy between the quantum results and the classical model for a single wire (due to dispersion with q and R), we have set ω_0 equal to the result from the quantum calculation for S_0 for a clearer comparison. For coupling of S_1 modes, $m,n = \pm 1$, and $(\mathbf{M}^2 - I)$ is a 2×2 matrix, which leads to a total of four solutions for ω:

$$\omega_{\{h,v\},\{\pm\}}^2 = \omega_1^2 \left[1\{\pm,\mp\} \frac{I_1(qR)}{K_1(qR)} \times \sqrt{K_2(qd_c)^2 + K_0(qd_c)^2 \pm 2K_0(qd_c)K_2(qd_c)} \right], \tag{A3}$$

where ω_1 has been set equal to the quantum result for S_1.

*kiran@fysik.dtu.dk
†thygesen@fysik.dtu.dk

[1] J. M. Pitarke, V. M. Silkin, E. V. Chulkov, and P. M. Echenique, Rep. Prog. Phys. **70**, 1 (2007).
[2] K. A. Willets and R. P. Van Duyne, Annu. Rev. Phys. Chem. **58**, 267 (2007).
[3] K. Kneipp, Y. Wang, H. Kneipp, L. T. Perelman, I. Itzkan, R. R. Dasari, and M. S. Feld, Phys. Rev. Lett. **78**, 1667 (1997).
[4] E. M. Larsson, C. Langhammer, I. Zorić, and B. Kasemo, Science **326**, 1091 (2009).
[5] T. Hirakawa and P. V. Kamat, J. Am. Chem. Soc. **127**, 3928 (2005).
[6] H. A. Atwater and A. Polman, Nat. Mater. **9**, 205 (2010).
[7] K. F. MacDonald, Z. L. Sámson, M. I. Stockman, and N. I. Zheludev, Nat. Photon. **3**, 55 (2008).
[8] D. E. Chang, A. S. Sørensen, P. R. Hemmer, and M. D. Lukin, Phys. Rev. Lett. **97**, 053002 (2006).
[9] A. Huck, S. Kumar, A. Shakoor, and U. L. Andersen, Phys. Rev. Lett. **106**, 096801 (2011).
[10] F. J. García de Abajo, Rev. Mod. Phys. **82**, 209 (2010).

[11]M. Bosman, V. J. Keast, M. Watanabe, A. I. Maaroof, and M. B. Cortie, Nanotechnology **18**, 165505 (2007).
[12]A. L. Koh, K. Bao, I. Khan, W. E. Smith, G. Kothleitner, P. Nordlander, S. A. Maier, and D. W. McComb, ACS Nano **3**, 3015 (2009).
[13]O. Nicoletti, M. Wubs, N. A. Mortensen, W. Sigle, P. A. Van Aken, and P. A. Midgley, Opt. Express **19**, 15371 (2011).
[14]B. S. Guiton, V. Iberi, S. Li, D. N. Leonard, C. M. Parish, P. G. Kotula, M. Varela, G. C. Schatz, S. J. Pennycook, and J. P. Camden, Nano Lett. **11**, 3482 (2011).
[15]I. Alber, W. Sigle, F. Demming-Janssen, R. Neumann, C. Trautmann, P. A. van Aken, and M. E. Toimil-Molares, ACS Nano **6**, 9711 (2012).
[16]J. A. Scholl, A. L. Koh, and J. A. Dionne, Nature (London) **483**, 421 (2012).
[17]S. Raza, N. Stenger, S. Kadkhodazadeh, S. V. Fischer, N. Kostesha, A.-P. Jauho, A. Burrows, M. Wubs, and N. A. Mortensen, Nanophotonics **2**, 131 (2013).
[18]S. Raza, G. Toscano, A.-P. Jauho, M. Wubs, and N. A. Mortensen, Phys. Rev. B **84**, 121412 (2011).
[19]C. David and F. J. García de Abajo, J. Phys. Chem. C **115**, 19470 (2011).
[20]L. Stella, P. Zhang, F. J. García-Vidal, A. Rubio, and P. Garcia-Gonzalez, J. Phys. Chem. C **117**, 8941 (2013).
[21]I. Romero, J. Aizpurua, G. W. Bryant, and F. J. García de Abajo, Opt. Express **14**, 9988 (2006).
[22]J. B. Lassiter, J. Aizpurua, L. I. Hernandez, D. W. Brandl, I. Romero, S. Lal, J. H. Hafner, P. Nordlander, and N. J. Halas, Nano Lett. **8**, 1212 (2008).
[23]J. Zuloaga, E. Prodan, and P. Nordlander, Nano Lett. **9**, 887 (2009).
[24]R. Esteban, A. G. Borisov, P. Nordlander, and J. Aizpurua, Nat. Commun. **3**, 825 (2012).
[25]E. Prodan, C. Radloff, N. J. Halas, and P. Nordlander, Science **302**, 419 (2003).
[26]H. Wang, D. W. Brandl, P. Nordlander, and N. J. Halas, Acc. Chem. Res. **40**, 53 (2007).
[27]K. J. Savage, M. M. Hawkeye, R. Esteban, A. G. Borisov, J. Aizpurua, and J. J. Baumberg, Nature (London) **491**, 574 (2012).
[28]J. Scholl, A. Garcia-Etxarri, A. L. Koh, and J. A. Dionne, Nano Lett. **13**, 564 (2013).
[29]C. Ciracì, R. T. Hill, J. J. Mock, Y. Urzhumov, A. I. Fernández-Domínguez, S. A. Maier, J. B. Pendry, A. Chilkoti, and D. R. Smith, Science **337**, 1072 (2012).
[30]G. Toscano, S. Raza, A.-P. Jauho, N. A. Mortensen, and M. Wubs, Opt. Express **20**, 4176 (2012).
[31]K. Andersen, K. W. Jacobsen, and K. S. Thygesen, Phys. Rev. B **86**, 245129 (2012).
[32]A. Baldereschi and E. Tosatti, Solid State Commun. **29**, 131 (1979).
[33]J. J. Mortensen, L. B. Hansen, and K. W. Jacobsen, Phys. Rev. B **71**, 035109 (2005).
[34]J. Enkovaara *et al.*, J. Phys.: Condens. Matter **22**, 253202 (2010).
[35]S. R. Bahn and K. W. Jacobsen, Comput. Sci. Eng. **4**, 56 (2002).
[36]J. Yan, J. J. Mortensen, K. W. Jacobsen, and K. S. Thygesen, Phys. Rev. B **83**, 245122 (2011).
[37]C. A. Rozzi, D. Varsano, A. Marini, E. K. U. Gross, and A. Rubio, Phys. Rev. B **73**, 205119 (2006).
[38]J. L. Gervasoni and N. R. Arista, Phys. Rev. B **68**, 235302 (2003).
[39]G. Toscano, S. Raza, W. Yan, C. Jeppesen, S. Xiao, M. Wubs, A.-P. Jauho, S. I. Bozhevolnyi, and N. A. Mortensen, arXiv:1212.4925.
[40]A. Liebsch, Phys. Rev. B **48**, 11317 (1993).
[41]R. C. Monreal, T. J. Antosiewicz, and S. P. Apell, arXiv:1304.3023.
[42]A. Moradi, Phys. Plasmas **18**, 064508 (2011).
[43]T. V. Teperik, P. Nordlander, J. Aizpurua, and A. G. Borisov, arXiv:1302.3339 [Phys. Rev. Lett. (to be published)].
[44]N. D. Lang and W. Kohn, Phys. Rev. B **1**, 4555 (1970).

Paper V

Plasmons on the edge of MoS_2 nanostructures.
Kirsten Andersen, Karsten W. Jacobsen, and Kristian S. Thygesen, Phys. Rev. B 90, 161410(R) (2014).

PHYSICAL REVIEW B **90**, 161410(R) (2014)

Plasmons on the edge of MoS_2 nanostructures

Kirsten Andersen,[1,*] Karsten W. Jacobsen,[1] and Kristian S. Thygesen[1,2]
[1]*Center for Atomic-scale Materials Design, Department of Physics Technical University of Denmark, DK - 2800 Kgs. Lyngby, Denmark*
[2]*Center for Nanostructured Graphene Technical University of Denmark, DK - 2800 Kgs. Lyngby, Denmark*
(Received 21 July 2014; published 29 October 2014)

Using *ab initio* calculations we predict the existence of one-dimensional (1D), atomically confined plasmons at the edges of a zigzag MoS_2 nanoribbon. The strongest plasmon originates from a metallic edge state localized on the sulfur dimers decorating the Mo edge of the ribbon. A detailed analysis of the dielectric function reveals that the observed deviations from the ideal 1D plasmon behavior result from single-particle transitions between the metallic edge state and the valence and conduction bands of the MoS_2 sheet. The Mo and S edges of the ribbon are clearly distinguishable in calculated spatially resolved electron energy loss spectrum owing to the different plasmonic properties of the two edges. The edge plasmons could potentially be utilized for tuning the photocatalytic activity of MoS_2 nanoparticles.

DOI: 10.1103/PhysRevB.90.161410 PACS number(s): 73.20.Mf, 73.22.Lp, 71.45.Gm

Plasmons are collective electronic excitations that couple strongly to external fields such as light or fast propagating charges. In metals, their excitation gives rise to charge oscillations, which can be localized either in the interior of the metal or at its surface. Localized surface plasmon resonances (LSPR) in metal nanoparticles have been utilized for chemical sensing [1], cancer treatment [2], and to increase solar cell performance [3]. Two-dimensional (2D) plasmons are found at metal surfaces and thin films [4], in graphene [5–8], and other atomically thin 2D materials such as metallic transition metal dichalcogenides [9].

Compared to their 2D counterparts, one-dimensional plasmons have been much less studied. So far, true atomically confined 1D plasmons have only been observed in self-assembled atomic chains on semiconducting substrates [10,11]. One peculiar fundamental aspect of 1D metals is the break down of Fermi-liquid theory and the transition to Luttinger liquid behavior [12,13]; at low energies, the spectral weight of the quasiparticle peak approaches zero and the lifetime broadening becomes of the same order as the excitation energy [14,15]. This implies that for (ideal) 1D metals, the plasmons adopt a special status as the only excitations that can couple to external fields.

Recently, the interest in novel 2D materials, such as graphene and monolayer MoS_2, has been accelerated by the prospects of utilizing their unique electronic properties for nanoscale (opto)electronics [16,17]. While graphene has shown great potential as a material for terahertz plasmonics [18], the finite band gap of MoS_2 makes it unsuitable for applications within this field. In a rather different context, MoS_2 nanoparticles are used industrially as hydrodesulphurization catalysts [19] and are considered as promising alternative to Pt as low-cost catalysts for hydrogen evolution [20]. The high catalytic activity of the MoS_2 nanoparticles has been directly linked to the presence of metallic edge states on the otherwise semiconducting MoS_2 nanoparticles [21]. Very recently, an observed extraordinary photocatalytic behavior of metallic nanoparticles has been shown to originate from the excitation of LSPRs [22,23]. As we predict here, the metallic edge states on MoS_2 nanostructures can lead to the formation of highly localized 1D plasmons—a result that adds edge plasmonics to the list of this material's unique properties with potential applications within nanoplasmonics and photocatalysis.

In this communication, we use time-dependent density functional theory (DFT) to demonstrate the existence of a set of highly localized plasmons on the edges of a MoS_2 nanoribbon, see Fig. 1. The fundamental properties of this new type of edge plasmon are investigated through a spectral analysis of the dielectric function, which allows us to identify the plasmonic eigenmodes of the system in an unambiguous way. The deviations of the edge plasmon properties from those of an ideal 1D plasmon are shown to arise from interband transitions between the metallic edge state and the MoS_2 conduction and valence bands. The distinctly different plasmonic properties of the Mo and S edges are clearly seen in the spatially resolved loss spectrum suggesting that high-resolution transmission electron microscopy could be used to probe the atomic structure of nanoribbon edges.

All calculations were performed with the GPAW electronic structure code, which is a grid-based implementation of the projector-augmented wave method [24]. We considered a 1.5-nm wide sulfur terminated zigzag MoS_2 nanoribbon, see Fig. 1 for a front view of the structure, and Supplemental Material [35] for a detailed image of the structure. This edge structure should be favorable at high chemical potential of sulfur, which can be tuned by the choice of sulfiding agent [25]. The ribbon was placed in a supercell including 20 and 12 Å of vacuum in the two perpendicular directions. The wave functions were represented in a plane-wave basis set with an energy cutoff of 340 eV. The structure was relaxed using the Perdew-Burke-Ernzerhof (PBE) exchange-correlation functional, while the GLLB-SC functional, including GLLB type exchange by Gritsenko *et al.* and PBEsol correlation [26], was applied to calculate the single-particle states used as an input for the linear response calculation. The GLLB-SC functional has been shown to improve the PBE band gaps of semiconductors [26] and yield better descriptions of plasmon resonances in noble metals [27] due to its improved description of the *d*-band energies. However, for the MoS_2 nanoribbon, GLLB-SC gives only minor corrections to the PBE band

*kiran@fysik.dtu.dk

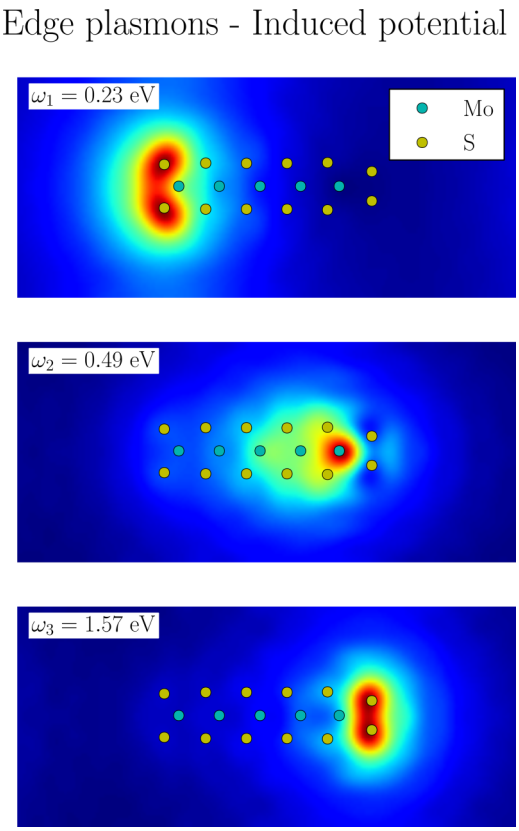

FIG. 1. (Color online) Induced electric potential of the three plasmon eigenmodes at $q = 0.2$ Å^{-1}, calculated as the eigenvectors of $\epsilon_q(\mathbf{r},\mathbf{r}',\omega)$. The structure of the ribbon is shown in front view, with the ribbon running into the plane of the page. The Mo and S edge, covered by sulfur dimers, is found to the right and left of the ribbon, respectively.

energies. The 1D Brillouin zone was sampled with 128 k points along the ribbon axis. A spin polarized calculation yielded zero magnetic moment for the structure.

The dielectric matrix was calculated in the random phase approximation (RPA) following reference [28]:

$$\epsilon_{\mathbf{G},\mathbf{G}'}(\mathbf{q},\omega) = \delta_{\mathbf{G},\mathbf{G}'} - \frac{4\pi}{|\mathbf{q}+\mathbf{G}|^2}\chi^0_{\mathbf{G},\mathbf{G}'}(\mathbf{q},\omega). \qquad (1)$$

For the calculation of the noninteracting density response function χ^0, empty states were included up to 12 eV above the Fermi level, which was sufficient to converge the low-energy plasmon peaks of interest. An energy cutoff of 30 eV was used for the reciprocal lattice vectors $\mathbf{G}$ and $\mathbf{G}'$. We used a nonlinear frequency grid from 0 to 12 eV, with an initial grid spacing of 0.01 eV at $\omega = 0$ and a smearing of 0.02 eV. The dense frequency sampling and small broadening was necessary at low energies in order to resolve all intra-band transitions. The Wigner-Seitz truncated Coulomb approximation [29] was used in order to avoid interaction between supercells, which would otherwise give a significant energy shift at low momentum transfers.

The calculated band structure of the nanoribbon shown in Fig. 2 reveals three metallic edge states (labeled I–III) in agreement with previous calculations on a MoS_2 nanoribbon with S-terminated edges [25]. The remaining bands produce a

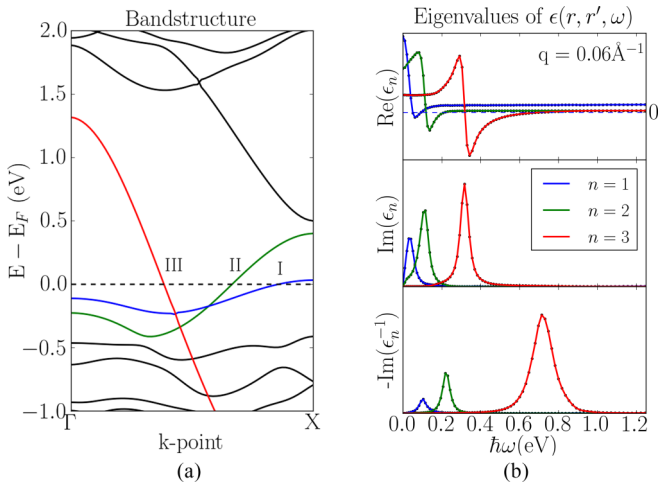

FIG. 2. (Color online) (a) Electronic band structure revealing three metallic edge states (I–III). (b) The three eigenvalues for the dielectric matrix fulfilling $\mathrm{Re}\,\epsilon_n(q,\omega) = 0$ plotted for $q = 0.06$ Å^{-1}. The color (red, blue, green) illustrates the one-to-one connection between the electronic bands and the plasmon eigenmodes.

band gap of approximately 2 eV. When the width of the ribbon is doubled to 3.3 nm, the edge states are unaffected while the band gap is decreased to 1.8 eV, which agrees with the value we find for the infinite single-layer MoS_2. The Kohn-Sham wave functions I and III are almost completely localized on the S dimers on the S and Mo edge of the ribbon, respectively. The wave functions are linear combinations of p_x orbitals, forming the one-dimensional metallic states along the edge. State III has a large Fermi velocity and is close to linear up to 1 eV away from the Fermi level. The wave function of state II resides at the outermost Mo atom at the Mo edge, and extends a few atoms into the ribbon. The number of edge states and their properties depend on the particular edge configuration. In this case, the presence of sulfur dimers on the Mo edge is crucial for obtaining the state III. However, zigzag MoS_2 nanoribbons are in general found to be metallic opposed to armchair types [30]. We note that MoS_2 nanostructures could also have topologically protected metallic edge states due to strong spin-orbit coupling in MoS_2, which was not included in the present study. In the following, we show that the metallic states give rise to plasmon states at the ribbon edges.

The plasmon modes of the system were investigated following a recently developed spectral analysis method for the dielectric function [31]. The eigenvalue equation

$$\sum_{\mathbf{G}'} \epsilon_{\mathbf{G},\mathbf{G}'}(\mathbf{q},\omega)\phi^n_{\mathbf{G}'}(\mathbf{q},\omega) = \epsilon_n(q,\omega)\phi^n_{\mathbf{G}}(\mathbf{q},\omega), \qquad (2)$$

is solved to obtain the frequency-dependent eigenvalues, ϵ_n, and eigenvectors, ϕ^n, of the microscopic dielectric function. The plasmon energies are identified as those frequencies where the real part of an eigenvalue vanishes, $\mathrm{Re}\,\epsilon_n(\mathbf{q},\omega_P) = 0$. When $\mathrm{Im}\,\epsilon_n(\mathbf{q},\omega)$ does not vary too much around the plasmon frequency, a vanishing real part coincides with a maximum in $-\mathrm{Im}\,\epsilon_n^{-1}(\mathbf{q},\omega)$. The corresponding eigenvector $\phi^n(\mathbf{q},\omega_P)$ gives the spatial form of the induced potential associated with the plasmon oscillation.

For the MoS_2 nanoribbon, we find three distinct plasmon eigenmodes in the low-energy regime. The dielectric eigenvalue curves corresponding to these modes are shown in Fig. 2(b) for momentum transfer $q = 0.2$ Å^{-1}. Each mode arises from intraband transitions within one of the three metallic edge bands as indicated by the color code. The plasmons are clearly observed as peaks in $\mathrm{Im}\,\epsilon_n^{-1}(\omega)$ shown in the lower panel. In contrast, the imaginary parts, $\mathrm{Im}\,\epsilon_n$, have peaks at the energy of the intraband transitions associated with the edge states and occur at qv_F. The $n = 3$ plasmon has a higher energy than the other two modes, partially due to the larger Fermi velocity of electrons in state III. The induced potentials of the plasmon eigenmodes, given as the eigenvectors of the dielectic matrix, are shown in Fig. 1. The edge plasmon corresponding to $n = 3$, is clearly localized on the S dimers of the Mo edge, and stems from the electronic state III. The extend of the induced charge density of the edge plasmons are thus limited by the extend of the electronic edge states, so that the plasmons will be atomically localized independently of the size of the MoS_2 ribbon.

In Fig. 3(a), the plasmon energies are plotted for increasing momentum transfers, and are clearly seen to be blue-shifted compared the single-particle intra-band transitions (dashed lines) that disperse linear with q. In order to map out the effect of Landau damping in (q,ω) space, the sum of single-particle transitions, $\sum_n \mathrm{Im}\,\epsilon_n(q,\omega) = \mathrm{Im\,Tr}\,\epsilon(\mathbf{q},\omega)$, has been indicated in gray contours. The damping is becoming significant around 2 eV, where interband transitions between the valence- and conduction-band states of the MoS_2 sheet set in.

At vanishing momentum transfers, the weight of single-particle transitions decreases significantly, since the number of single-particle transitions scales as q. For an ideal 1D electron gas, the weight of the plasmon resonance should also go to zero in the limit $q \to 0$ [32]. However, our calculations predict that the plasmon weight is almost constant in the considered q range, and actually increases slightly for small momentum transfers. In order to explain this behavior, the result is compared to the pure intraband plasmon, obtained by including only the single metallic band III (see Fig. 2) in the calculation of $\chi^0_{\mathbf{GG}'}(\omega,\mathbf{q})$. This allows us to compare to the case of an undamped plasmon. As seen in Fig. 3(b), this approach yields a plasmon mode that is blue shifted in energy compared to the full calculation and a weight that approaches zero for small q as expected for an ideal 1D metal. Therefore we conclude that the stagnant weight of the plasmon in the full calculation is due to damping from coupling to interband transitions. The effect of interband transitions can be described by an effective dielectric constant of the medium that screens the Coulomb interaction: $V(q) \to \epsilon^{-1}_{\mathrm{inter}}(q,\omega)V(q)$. The screened interaction will be reduced in magnitude compared to $V(q)$ and will have a finite imaginary part at energies corresponding to the interband transitions. These properties lead to a reduction of energy and life time of the full plasmon compared to the bare intraband result. However, for very low momentum transfers, the plasmon is well separated from single-particle transitions, and a sharp resonance is obtained. Therefore the plasmon coincides with the undamped result, and is expected to have a long lifetime in this regime. For the other two modes, we expect the damping by single-particle transitions to be less significant due to separation in energy.

Following reference [32], a simple model for the plasmon dispersion in the long wavelength limit can be obtained by approximating χ_0 as that of a 1D linear band with transitions at qv_F:

$$\chi_0(q,\omega) = \frac{q}{\pi}\left(\frac{1}{\omega - qv_F + i\eta} - \frac{1}{\omega + qv_F + i\eta}\right). \quad (3)$$

The dielectric function is obtained from the RPA expression $\epsilon = 1 - V(q)\chi_0$, where $V(q)$ is the 1D Coulomb potential.

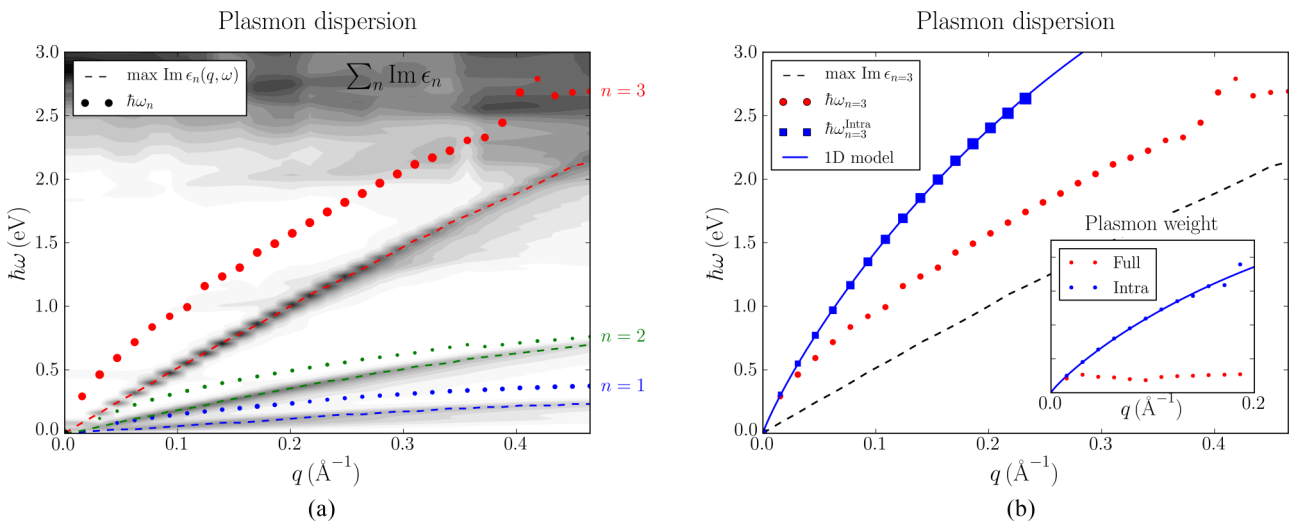

FIG. 3. (Color online) (a) Energy dispersion of the three edge plasmons, showing plasmon energy (dots) as well as intraband transitions (dashed lines). The dot size indicates the plasmon weight, defined as the integral over the loss peak. The gray contours map the regions of single-particle transitions, which contribute to the damping of the plasmons. (b) Comparison of the dispersion of the S-dimer plasmon to the undamped intraband mode obtained by only including the metallic state (III) in the response calculation. The inset shows the evolution of plasmon weight with q for the undamped and the full calculation. A 1D RPA model valid at low q, identical to the Tamonaga-Luttinger result, has been fitted to the intraband results.

The inverse dielectric function can then be cast on the form

$$\epsilon^{-1}(q,\omega) = 1 + \frac{\alpha}{\omega - \omega(q) + i\eta} - \frac{\alpha}{\omega + \omega(q) + i\eta}. \quad (4)$$

The pole of ϵ^{-1} for positive frequencies and in the limit of $\eta = 0$ yields the plasmon dispersion

$$\omega(q) = q v_F \sqrt{1 + \frac{2V(q)}{\pi v_F}}, \quad (5)$$

and the weight of the resonance equals $\alpha = qV(q)/(\pi\sqrt{1+\frac{2V(q)}{\pi v_F}})$. This result is identical to the eigenenergies obtained from the interacting Tomonaga-Luttinger model with a 1D Coulomb interaction. In this sense, the RPA is exact for a 1D system [33]. The Coulomb interaction for a thin wire of confinement a can be written for small q as $V(q) = V_0|\ln(qa)|$, where V_0 is a system dependent interaction strength accounting for, e.g., the screening due to interband transitions. The expressions for the plasmon frequency and spectral weight derived from the linear band RPA model were fitted to the pure intraband results in Fig. 3(b). As expected from the highly linear form of band III, the quality of the fit is excellent. From the fit, we obtained $a = 1.34$ Å, which is in the same order as the radius of the orbitals of the edge state. Comparing the dispersion and weight of the model to the results of the full *ab initio* calculation, we find agreement for small (q,ω), after which the plasmon energy and, in particular, the plasmon weight start to deviate in a nonlinear way. This shows that the screening varies as a function of q and ω as is generally the case, such that the interaction strength cannot be written as a constant V_0 as assumed in the model.

Experimentally, plasmon excitations can be probed by electron energy loss spectroscopy (EELS). When performed with a highly confined electron beam, the spatial form of the loss spectrum can be obtained with few angstrom resolution [34].

The loss spectrum is defined as the power dissipated in the medium due to an external potential, $\phi_{\text{ext}}(\mathbf{r})e^{i\omega t}$:

$$P(\omega) = \int\int d\mathbf{r}d\mathbf{r}'\phi_{\text{ext}}(\mathbf{r})\chi(\mathbf{r},\mathbf{r}',\omega)\phi_{\text{ext}}(\mathbf{r}'). \quad (6)$$

Here, χ is the interacting density response function. In the case of EELS, the external potential corresponds to the Coulomb potential of a fast electron moving at constant velocity $\mathbf{v}_e$ emitted at point $\mathbf{r}_0$:

$$\phi_{\text{ext}}(\mathbf{r},t) = \frac{4\pi e^2}{|\mathbf{r} - \mathbf{r}_0 - \mathbf{v}_e t|}. \quad (7)$$

The final expression for the loss spectrum is given in the Supplemental Material [35]. In Fig. 4, the spatially resolved EELS spectrum is plotted for two different values of q_x for a beam position that is varied across the ribbon. The spectrum is dominated by the S-dimer plasmon on the Mo edge, which reflects the large coupling strength of this mode. The other two edge plasmons are also visible in the spectrum, particularly at larger momentum transfers where the Coulomb potential is less long ranged, which results in more localized features. Furthermore, the modes can be distinguished by their difference in energy and dispersion with q. We suggest this approach could be applied to verify the existence of the edge-plasmons in MoS_2 nanoribbons or clusters.

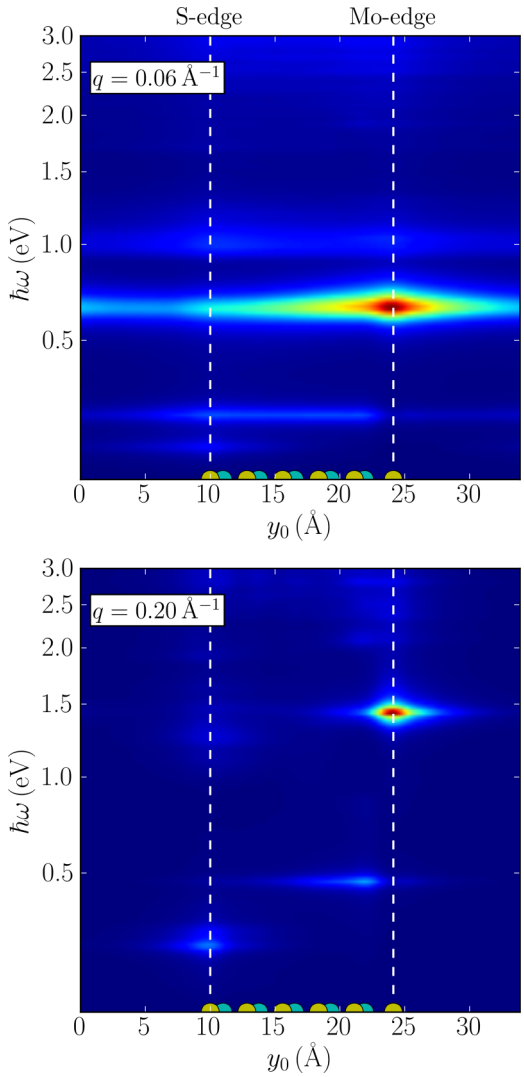

FIG. 4. (Color online) Spatially resolved electron energy loss spectrum calculated for two different values of momentum transfer, q_x. We observe a strong signal associated with the S-dimer plasmon at the Mo edge, while the two other plasmon modes give a weaker response. At low momentum transfers, the signal is less localized due to the long range of the Coulomb potential.

In conclusion, our first-principles calculations predict the existence of a unique type of plasmon localized on the edge of a zigzag MoS_2 nanoribbon. The fundamental properties of this plasmon were investigated in detail and its clear signature in the spatially resolved electron energy loss spectrum was demonstrated. Finally, we proposed that the edge plasmons could be utilized to tune the photocatalytic activity of MoS_2 nanoparticles as was recently demonstrated for metal nanoparticles [22,23].

K.S.T. acknowledges support from the Danish Council for Independent Research's Sapere Aude Program through Grant No. 11-1051390. The Center for Nanostructured Graphene (CNG) is sponsored by the Danish National Research Foundation, Project DNRF58.

[1] K. Kneipp, Y. Wang, H. Kneipp, L. T. Perelman, I. Itzkan, R. R. Dasari, and M. S. Feld, Phys. Rev. Lett. **78**, 1667 (1997).
[2] L. Au, D. Zheng, F. Zhou, Z.-Y. Li, X. Li, and Y. Xia, ACS Nano **2**, 1645 (2008).
[3] H. A. Atwater and A. Polman, Nat. Mater. **9**, 205 (2010).
[4] J. M. Pitarke, V. M. Silkin, E. V. Chulkov, and P. M. Echenique, Rep. Prog. Phys. **70**, 1 (2007).
[5] J. Chen, M. Badioli, P. Alonso-González, S. Thongrattanasiri, F. Huth, J. Osmond, M. Spasenović, A. Centeno, A. Pesquera, P. Godignon, A. Zurutuza Elorza, N. Camara, F. J. García de Abajo, R. Hillenbrand, and F. H. L. Koppens, Nature (London) **487**, 77 (2012).
[6] A. Grigorenko, M. Polini, and K. Novoselov, Nat. Photon. **6**, 749 (2012).
[7] B. Wunsch, T. Stauber, F. Sols, and F. Guinea, New J. Phys. **8**, 318 (2006).
[8] E. H. Hwang and S. Das Sarma, Phys. Rev. B **75**, 205418 (2007).
[9] K. Andersen and K. S. Thygesen, Phys. Rev. B **88**, 155128 (2013).
[10] T. Nagao, S. Yaginuma, T. Inaoka, and T. Sakurai, Phys. Rev. Lett. **97**, 116802 (2006).
[11] U. Krieg, C. Brand, C. Tegenkamp, and H. Pfnür, J. Phys.: Condens. Matter **25**, 014013 (2013).
[12] F. Haldane, J. Phys. C **14**, 2585 (1981).
[13] J. Voit, Rep. Prog. Phys. **58**, 977 (1995).
[14] A. Yacoby, H. L. Stormer, N. S. Wingreen, L. N. Pfeiffer, K. W. Baldwin, and K. W. West, Phys. Rev. Lett. **77**, 4612 (1996).
[15] M. Bockrath, D. H. Cobden, J. Lu, A. G. Rinzler, R. E. Smalley, L. Balents, and P. L. McEuen, Nature (London) **397**, 598 (1999).
[16] K. F. Mak, C. Lee, J. Hone, J. Shan, and T. F. Heinz, Phys. Rev. Lett. **105**, 136805 (2010).
[17] B. Radisavljevic, A. Radenovic, J. Brivio, V. Giacometti, and A. Kis, Nat. Nanotechnol. **6**, 147 (2011).
[18] L. Ju, B. Geng, J. Horng, C. Girit, M. Martin, Z. Hao, H. A. Bechtel, X. Liang, A. Zettl, Y. R. Shen *et al.*, Nat. Nnanotechnol. **6**, 630 (2011).
[19] R. R. Chianelli, M. H. Siadati, M. P. De la Rosa, G. Berhault, J. P. Wilcoxon, R. Bearden, Jr., and B. L. Abrams, Catal. Rev.: Sci. Eng. **48**, 1 (2006).
[20] T. F. Jaramillo, K. P. Jørgensen, J. Bonde, J. H. Nielsen, S. Horch, and I. Chorkendorff, Science **317**, 100 (2007).
[21] J. V. Lauritsen, M. Nyberg, R. T. Vang, M. Bollinger, B. Clausen, H. Topsøe, K. W. Jacobsen, E. Lægsgaard, J. Nørskov, and F. Besenbacher, Nanotechnol. **14**, 385 (2003).
[22] P. Christopher, H. Xin, A. Marimuthu, and S. Linic, Nat. Mater. **11**, 1044 (2012).
[23] A. Marimuthu, J. Zhang, and S. Linic, Science **339**, 1590 (2013).
[24] J. Enkovaara *et al.*, J. Phys.: Condens. Matter **22**, 253202 (2010).
[25] M. V. Bollinger, K. W. Jacobsen, and J. K. Nørskov, Phys. Rev. B **67**, 085410 (2003).
[26] M. Kuisma, J. Ojanen, J. Enkovaara, and T. T. Rantala, Phys. Rev. B **82**, 115106 (2010).
[27] J. Yan, K. W. Jacobsen, and K. S. Thygesen, Phys. Rev. B **84**, 235430 (2011).
[28] J. Yan, J. J. Mortensen, K. W. Jacobsen, and K. S. Thygesen, Phys. Rev. B **83**, 245122 (2011).
[29] R. Sundararaman and T. A. Arias, Phys. Rev. B **87**, 165122 (2013).
[30] H. Pan and Y.-W. Zhang, J. Mater. Chem. **22**, 7280 (2012).
[31] K. Andersen, K. W. Jacobsen, and K. S. Thygesen, Phys. Rev. B **86**, 245129 (2012).
[32] S. DasSarma and E. H. Hwang, Phys. Rev. B **54**, 1936 (1996).
[33] Q. P. Li, S. Das Sarma, and R. Joynt, Phys. Rev. B **45**, 13713 (1992).
[34] F. J. García de Abajo, Rev. Mod. Phys. **82**, 209 (2010).
[35] See Supplemental Material at http://link.aps.org/supplemental/10.1103/PhysRevB.90.161410 for the derivation of the expression for the spatially resolved electron energy loss spectrum, shown in Fig. 4. Furthermore, we have included a detailed figure of the atomic structure of the MoS_2 nanoribbon used for the DFT calculations.